

# **SECONDARY INTERACTIONS WHICH MODIFY REDOX AND OTHER PROPERTIES OF ORGANOMETALLIC SYSTEMS**

A thesis submitted to the University of East Anglia

For the Degree of Doctor of Philosophy

Submitted February 2016

**Faizah Salah Aljohani**

Energy Materials Laboratory

School of Chemistry, UEA

Norwich

This copy of this thesis has been supplied on the condition that anyone who consults it is understood to recognise that its copyright rests with the author and that no quotation from the thesis, nor any information derived there from, may be published without the author's prior written consent. ©

## Abstract

Second coordination sphere interactions of metal centres involving hydrogen bonding, ion-pairing or dipolar bonding can play an important role in determining the physical and chemical properties of molecular and biomolecular systems. For example, the redox potentials of cubane iron-sulfur clusters in a redox protein or enzyme can range between -700mV and -400mV *versus* the standard hydrogen electrode as a consequence of the nature of the second-coordination sphere environment. Whilst this is largely explained in terms of hydrogen-bonding ionic, dipolar or other interactions may have a role in this. The first part of this thesis examines a model system in which a ligand based isomerism controls the redox potentials of two interconverting couples. Specifically this is a bis(cyclopentadienyl) Mo<sup>V/IV</sup> system possessing a cysteinyl N,S coordinated metallocycle ring in which deployment of the amide O away or towards the metal centre by rotation is shown to lead to a *ca* 200 mV difference in the isomer redox potentials. The activation enthalpy for this rotation process is 18kcal mole<sup>-1</sup> in MeCN. It is further shown that second coordination sphere interactions with an exogenous Lewis acid, Eu(fod)<sub>3</sub> can control the isomer population, favouring the trans-amide conformation.

The second part of this thesis examines second coordination sphere interactions of coordinated cyanide in a model for the diiron subsite of [FeFe]-hydrogenase. The natural subsite in its protein environment catalyses hydrogen evolution (or uptake) at very fast rates *ca* 10<sup>4</sup> s<sup>-1</sup> near the reversible potential of the H<sup>+</sup>/1/2 H<sub>2</sub> couple but such rates have yet to be attained in model systems. Controlling the electronic and geometric

properties of synthetic diiron subsites by hydrogen bonding or other interactions might provide a means of attaining the turnover rates of the natural system. This work takes some first steps towards introducing second coordination sphere interactions to modify subsite properties. Firstly, a metal Lewis acid  $\text{Eu}(\text{fod})_3$  is shown to bridge to CN ligands in the model subsite to change its spectroscopic and electrochemical behavior. Secondly, it is shown that hydrogen bonding interactions with the ligated cyanide using certain activated amides also perturbs spectroscopic and redox properties and importantly, the rate of protonation at the metal-metal bond and the stability of the resulting  $\mu$ -hydride.

## **Acknowledgements**

I have to first thank my advisor Professor Christopher Pickett who every day approaches chemistry with a high level of enthusiasm. He has challenged me to dig deeper into a result not only when the unexpected occurs but also when things go as planned.

I want to thank Dr. Saad Ibrahim and Dr. Joseph Wright for regularly putting up with my asking of seemingly dumb questions and providing helpful advice. Also, I want to thank a fantastic group of people who I work with in Energy Material Lab. I want to also thank my friends here who celebrated with me the good days and encouraged me through the bad , Ashah Alharbi, Badreh Al-shammari , Amani Al-sayri and Tahani Almutiri.

Finally, A big thanks go to my husband Saleh Almarwani who support me with love , help me to be there and make my life enjoyable. I want to thank my parents for all of their encouragement and support.

This work has funded by Tabiah University in Saudi Arabia.

*To my husband and my children Abdulmalik, Sarah and coming baby with  
my love.*

## List of Abbreviations

$\text{BAr}^{\text{F}}_3$	Tris-(pentafluorophenyl)borane, $\text{B}(\text{C}_6\text{F}_5)_3$
$\text{BAr}^{\text{F}\#}_3$	Tris-(2,4,6-trifluorophenyl)borane, $\text{B}(2,4,6\text{-F}_3\text{C}_6\text{H}_2)_3$
Bn	Benzyl, $\text{CH}_2\text{Ph}$
Bu	Butyl, $\text{C}_4\text{H}_{10}$
Cp	Cyclopentadienyl, $[\text{C}_5\text{H}_5]$
Et	Ethyl, $\text{C}_2\text{H}_5$
$\text{Fc}^{0/+}$	Ferrocene/ferrocenium couple, $[(\text{C}_5\text{H}_5)_2\text{Fe}]^{0/+}$
Me	Methyl, $\text{CH}_3$
pdt	1,3-propaneditholate, $(\text{S}_2\text{C}_3\text{H}_6)^{2-}$
Ph	Phenyl, $\text{C}_6\text{H}_5$
CV	cyclic voltammetry
DFT	Density Functional theory
DMF	<i>N,N</i> -Dimethylformamide
MeCN	Methyl cyanide
MeOH	Methyl hydroxide

EI	Electron ionisation
ESI	Electrospray ionisation
Fc	Ferrocene
FTIR	Fourier transform infrared
IR	Infrared
MS	Mass spectroscopy
NMR	Nuclear magnetic resonance
ORTEP	Oak Ridge thermal ellipsoid program
RT	Room temperature
THF	Tetrahydrofuran
UV-vis	Ultraviolet-visible

## Contents

Abstract.....	ii
Acknowledgements .....	iv
List of abbreviations .....	vi
1. Introduction .....	1
1.1. General introduction.....	1
1.2. Hydrogen bonding in metal–ligand coordination.....	4
1.3. Cyanide-bridged complexes of transition metal.....	9
1.3.1. General overview.....	9
1.3.2. IR Spectroscopy of Cyanide-bridged Complexes.....	14
1.4. Experimental methods and techniques.....	19
1.4.1. General synthetic methodology.....	19



1.4.1.1.Solvent purification.....	19
1.4.1.2. Handling methodology.....	19
1.4.1.3. Electrolyte preparation.....	19
1.4.1.4. Microanalysis .....	19
1.4.2. Background to experimental techniques.....	20
1.4.2.1. FTIR spectroscopy.....	20
1.4.2.2. NMR spectroscopy.....	24
1.4.2.3. Mass spectrometry.....	26
1.4.2.4.X-ray crystallography.....	28
1.4.2.5. Stopped-flow FTIR.....	29
1.4.2.6. Electrochemical measurements.....	31
1.4.3..Background to theoretical and simulation methods.....	38
1.4.3.1. Simulation of electrochemical data.....	38
1.4.3.2..Density functional theory.....	38
1.5... Aims and objectives.....	39
2. Intramolecular redox isomerism.....	40

2.1.Introduction.....	40
2.1.1 Overview.....	44
2.1.2. Redox – linked cis-trans isomerism .....	41
2.1.3. Cyclic voltammetric characteristics of the square scheme.....	43
2.1.4. A redox linked ligand rotamer system.....	48
2.2. Result and discussion.....	52
2.2.1.Synthesis and characterisation of bis(cyclopentadienyl)molybdenum(IV)-N-(3-phenylpropanyl)-L-cysteine methyl ester (Complex 1).....	52
2.2.2.Spectroscopic properties of Complex 1.....	56
2.2.3.Electrochemistry of Complex 1.....	62
2.2.4 Comparison of thermodynamic and kinetic parameters of isomerism with related systems.....	74
2.2.5 Synthesis of a Mo(IV) complex possessing a thiolate – amine metallocycle ring(Complex 2).....	77
2.2.6. Second coordination sphere effects on the redox linked isomerism of Complex 1.....	82
2.2.7. Final Remarks.....	93

2.3 Experimental.....	93
3. Interaction of Eu(fod) <sub>3</sub> with coordinated cyanide in an analogue of the sub-site of [FeFe]-hydrogenase .....	102
3.1. Introduction.....	102
3.1.1. General aspects.....	102
3.1.2. [FeFe]-hydrogenase chemistry.....	103
3.1.3. Synthesis, structural and spectroscopic aspects of the sub-site analogue [Fe <sub>2</sub> (CO) <sub>4</sub> (CN) <sub>2</sub> pdt] <sup>2-</sup> .....	107
3.1.4. Second coordination sphere interactions of [Fe <sub>2</sub> (CO) <sub>4</sub> (CN) <sub>2</sub> pdt] <sup>2-</sup> with triaryl boranes.....	111
3.2. Results and discussion .....	114
3.2.1. The binding of Eu(fod) <sub>3</sub> , ( <i>tris</i> -6,6,7,7,8,8,8-hepta-fluor-2,2-dimethyl-3,5-octanedionato-europium), to [Fe <sub>2</sub> (CO) <sub>4</sub> (CN) <sub>2</sub> (pdt)] <sup>2-</sup> , A <sup>2-</sup> .....	114
3.2.1.1. FTIR spectroscopy .....	114
3.2.1.2. Isolation and characterisation of (Et <sub>4</sub> N) <sub>2</sub> [Fe <sub>2</sub> (CO) <sub>4</sub> (CN) <sub>2</sub> (pdt)(Eu(fod) <sub>3</sub> ) <sub>2</sub> ] by mass spectroscopy.....	118
3.2.1.3. Further spectroscopic characterisations of (Et <sub>4</sub> N) <sub>2</sub> [Fe <sub>2</sub> (CO) <sub>4</sub> (CN) <sub>2</sub> (pdt)(Eu(fod) <sub>3</sub> ) <sub>2</sub> ].....	120

3.2.1.4. Comparative infra-red spectroscopy.....	129
3.2.1.5. Electrochemistry studies .....	133
3.2.1.6. Protonation of $[\text{Fe}(\text{CO})_4(\text{CN})_2\text{pdt}(\text{Eu}(\text{fod})_3)_2]^{2-}$ .....	138
3.3. Experimental.....	150
4... Hydrogen bonding interactions of tris- and bis- urea and thioureas with cyanide ligands in an analogue of the sub-site of [FeFe]-hydrogenase.....	153
4.1. Introduction.....	153
4.1.1. General aspects.....	153
4.1.2. Hydrogen bonding of substituted (thio)ureas to simple anions.....	154
4.1.3. Probing H-bonding interactions by FTIR spectroscopy.....	160
4.2. Results and discussion.....	161
4.2.1. Solvent effects on $\nu(\text{CN})$ and $\nu(\text{CO})$ in $[\text{Et}_4\text{N}]_2[\text{Fe}_2(\text{CO})_4(\text{CN})_2\text{pdt}]$ .....	161
4.2.2. Interaction of $\text{A}^{2-}$ with substituted tris-(thio)ureas 5 and 9.....	166
4.2.3. Interaction of $\text{A}^{2-}$ with substituted tris- and bis-(thio)ureas.....	187
4.2.4. Stopped – flow FTIR studies of the protonation of $\text{A}^{2-} \rightarrow 9$ with $\text{HBF}_4 \cdot (\text{Et}_2\text{O})_2$ in MeCN.....	198
4.2.5. Cyclic voltammetry of receptor complexes.....	210

4.4.3. Experimental.....	215
5. Concluding remarks.....	217
References.....	219

## CHAPTER 1. INTRODUCTION

This chapter will first give a general survey of the background to this work, followed by a description of the techniques employed, and conclude with an outline of the specific aims and objectives of the research.

### 1.1 General Introduction

#### *First- and second- coordination sphere interactions.*

The concept that a transition metal complex can interact orderly with neutral molecules to give an outer-sphere complex dates back over 100 years to Alfred Werner's original description of coordination chemistry. Werner found, how metal complex affected by surrounding environment, primary and secondary valance, now called second-sphere coordination. Three of the most important postulates are: The number of groups attached to an atom, something that he refer to as its secondary valency, need not equal its oxidation number (primary valency). The chemistry of the cobalt(III)-ammonia compounds could be rationalised if in them cobalt had a primary valency of three, as in  $\text{CoCl}_3$ , but a secondary valency of six, as in  $[\text{Co}(\text{NH}_3)_6]\text{Cl}_3$ . The term secondary valency has now been replaced by coordination number and primary valency by oxidation his greatest state but Werner's ideas otherwise stand largely unchanged.

Every element tends to satisfy both primary and secondary valencies. Werner postulated that in the series of cobalt-ammonia-chloride compound, the cobalt exhibits

## CHAPTER 1 | INTRODUCTION

a constant coordination number of 6 and, as ammonia molecules are removed, they are replaced by chloride ions which tend to act as covalently bound to cobalt rather than as free chloride ion. For Werner, to describe the complex chemistry of cobalt, one must consider not only the oxidation state but also its coordination number.

The secondary valence is directed towards a fixed position in space and therefore can be treated by applications of structural principles. Werner was able to assign the correct geometric structures to many coordination compounds long before any direct experimental method was available for structural determination. <sup>1</sup>

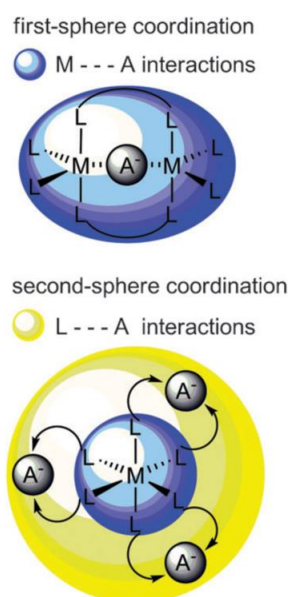


**Figure 1.1** Schematic representations of the binding of anionic substrates using a metal-based anion receptor design. Top: interaction in the first sphere of coordination. Bottom: interaction in the second-sphere of coordination (first-sphere = blue, second-sphere = yellow). <sup>2</sup>

## CHAPTER 1 | INTRODUCTION

Nowadays, second-sphere coordination is well-understood in terms of noncovalent bonding of chemical entities constituting the second coordination sphere to a ligated metal ion in the first coordination sphere. The chemical entities in the second coordination sphere can consist of ionic or molecular receptors and even portions of a ligand backbone.<sup>3</sup> Shook and Borovik<sup>4</sup> mentions the fundamental differences between the two coordination spheres, which can be understood within the context of chemical bonding. The primary coordination sphere is dominated by covalent interactions between donor atoms on ligands and metal ions. Experimental and theoretical investigations have provided detailed structure function relationships that have improved the understanding of key properties, such as correlations between electronic and molecular structures and chemical reactivity, and the development of organometallic catalysts. In contrast, the secondary coordination sphere normally utilizes non-covalent interactions and is associated with determining chemical selectivity.<sup>4</sup>

A number of synthetic and naturally occurring macrocyclic receptors<sup>5</sup> (host compounds) such as crown ethers<sup>6,7</sup> calixarenes<sup>8</sup>, and cyclophanes<sup>9</sup> have been shown to act as efficient second-sphere ligands. Stoddart *et al*<sup>10</sup> report that ,in general, the first-sphere ligands generate second-sphere adducts by harnessing the entire range of noncovalent bonding interactions, such as electrostatic, hydrogen bonding, charge transfer, and van der Waals interactions. Second-sphere coordination has been shown to exercise significant influence upon various scientific phenomena, including biological recognition<sup>11</sup> and supramolecular assembly<sup>12</sup>. The idea that metal complexes



could be recognised by other molecules via binding to the coordinated ligands (and not the metal centers) was found soon after the realisation that host compounds could bind anions and small molecules [13,14,15](#). These findings led to several reports of secondary sphere coordination complexes, examples of which are species formed with crown ethers and metal complexes containing amine or aqua ligands (**Figure 1.2**) [4,16](#). Note that the intermolecular forces used to form these host-guest species are hydrogen bonds (H-bonds).

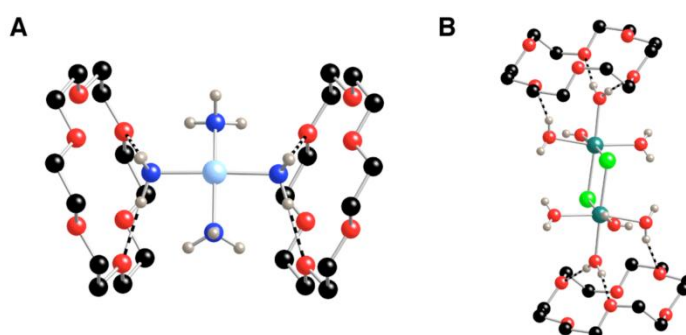


**Figure 1.2.** Two examples of secondary coordination sphere interactions with crystalline lattices: (A)  $(18\text{-crown-}6)_2[\text{Cu}^{\text{II}}(\text{NH}_3)_4]$  and (B)  $(18\text{-crown-}6)_2[\text{Mn}^{\text{II}}(\text{H}_2\text{O})_4(\text{Cl})_2]$ . Only amine and aqua hydrogen atoms are shown for clarity. [4, 16](#)

### 1.2. Hydrogen bonding in metal–ligand coordination

One of the most important aspects of supramolecular chemistry is that preorganisation of a binding site leads to enhanced recognition. For metal-based anion receptors, it is coordination of the ligands to the metal centre that play to pre organise hydrogen bond donor functional groups for anion binding. This pre organisation can take two different

forms, first, as described by Hamilton et al. in 1995, Metal–ligand coordination can be used to bring together the hydrogen-bond donor groups from individual ligands via complexation, **Figure 1.3**.<sup>17</sup> Second, more subtly, metal–ligand coordination can be used to induce a conformational change of a single ligand that will result in a beneficial reorganization of hydrogen-bond donor groups. In either case, metal–ligand bonding reduces the entropic cost required to reach the particular conformation needed to bind the anion and any entropic loss associated with stiffening the system is overbalanced by the enthalpic gain accumulated by formation of a set of strong metal–ligand bonds<sup>2</sup>. Examples illustrating these two different designs are presented below on how to apply second-sphere coordination to create an effective anion receptor.

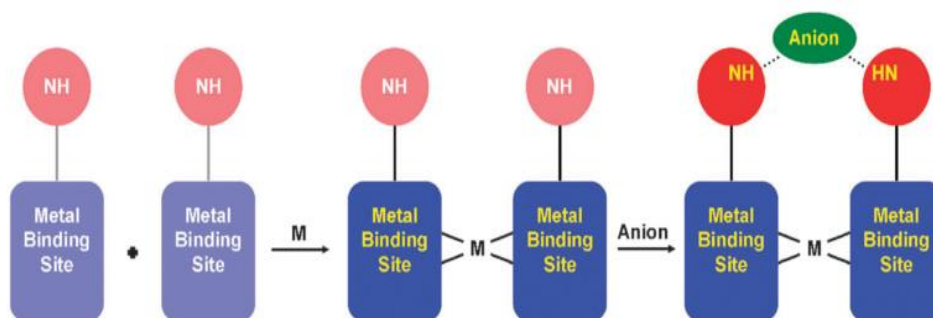


**Figure 1.3** . Schematic representation of Hamilton’s original idea for utilising metal-templated self-assembly to arrange functional groups for recognition of anions. From left to right: in the free ligands, neither the metal binding site donors nor hydrogen-bonding donors are used (pale colours). Utilisation of the metal-binding sites (blue) to form a complex organises the hydrogen bond donor NH groups (red) for anion binding (green).<sup>2,17</sup>

## CHAPTER 1 | INTRODUCTION

Mohamadou *et al* reported that hydrogen bond system of interaction of *N,N*-bis(2-pyridylmethyl)-1,3-propanediamine hydrochloride (pypn.4HCl) with iron(III) nitrate trihydrate. The lattice structure is stabilized by a medium strong hydrogen bond between the N18 hydrogen atom to a neighbouring chloride anion (N...Cl distance 3.288(2) Å) and between the N28 hydrogen atom to the oxygen atoms of the nitrate anion (N...O distances 2.919(2) and 3.183(3) Å), **Figure 1.4**. Details of the hydrogen bond geometries are given in **Table 1.1** The bond distances and angles of this structure are comparable to a related type of structure, [Fe(pypn)Cl<sub>2</sub>](ClO<sub>4</sub>)<sup>18</sup>, which gives also the same type of hydrogen bonds <sup>19</sup>.

D–H...A	D–H (Å)	H...A (Å)	D...A (Å)
N(18)–H(18A)...Cl(1)	0.93	2.47	3.288(2)
N(28)–H(28A)...O(1)	0.93	2.08	2.919(2)
N(28)–H(28A)...O(3)	0.93	2.41	3.183(3)

**Table 1.1.** Hydrogen bonding parameters distances of [Fe(pypn)Cl<sub>2</sub>](NO<sub>3</sub>), The labeling refers to those shown in **Figure 1.4**.<sup>19</sup>

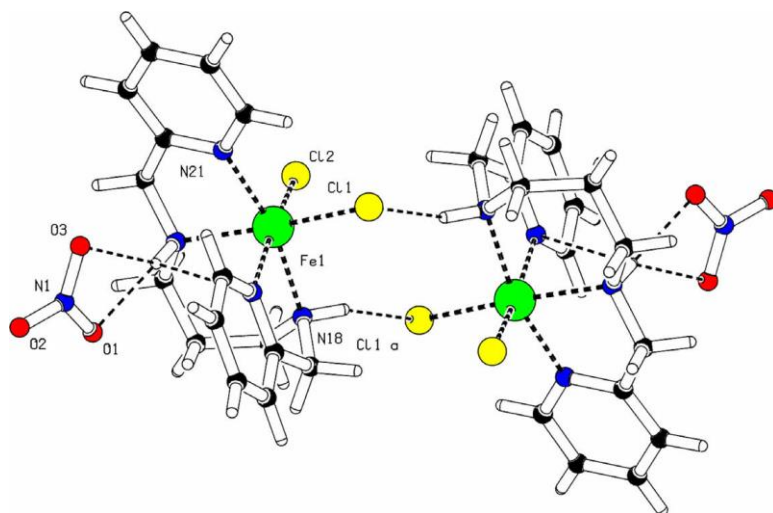


**Figure 1.4.** The hydrogen bond system of  $[\text{Fe}(\text{pypn})\text{Cl}_2](\text{NO}_3)$ , showing a dimerisation with both Cl and  $\text{NO}_3$  displayed <sup>19</sup>.

The huge development in spectroscopic and X-ray diffraction analysis of metalloproteins is arguably the most important advance in understanding how to integrate the primary and secondary coordination sphere in inorganic chemistry. Findings obtained from these studies illustrate in striking clarity that control of both the primary and secondary coordination spheres can be effected in an intramolecular manner. Shook and Borovik (2010)<sup>4</sup> highlight that protein active sites have numerous “architectural” features which aid in regulating function, including 1) metal binding sites utilizing endogenous ligands from amino acid side-chains to regulate the primary coordination spheres; 2) site isolation (when necessary) to avoid unwanted metal ion–metal ion interactions; 3) channels or paths to allow external reagents access to the

## CHAPTER 1 | INTRODUCTION

functionally vital metal center(s); and 4) control of the secondary coordination sphere through protein-derived architectures. These findings have challenged chemists to design and prepare synthetic systems that control both the primary and secondary coordination spheres<sup>4</sup>. The best example of intramolecular hydrogen bonding networks are biomolecules. H-bonds have bond strengths ranging from 5 to 15 kcal/mol in the condensed phase, which are generally much weaker than covalent interactions found within the primary spheres<sup>20</sup>. For example, SyrB2, a non-heme Fe(II)/ $\alpha$ -ketoglutarate ( $\alpha$  KG)-dependent halogenase, catalyzes the conversion of L-Thr to 4-Cl-L-Thr, a modification that is essential for the antifungal activity of syringomycin E.21, The proposed mechanism involves Cl<sup>-</sup>,  $\alpha$  KG, and O<sub>2</sub>, and proceeds through an [(Cl)Fe(IV)=O] intermediate, **Figure 1.5**. XRD studies on the reduced form of SyrB2 revealed that a Cl<sup>-</sup> is coordinated to the Fe(II) center, replacing a carboxylate ligand that is normally found in this class of enzymes<sup>21</sup>. The Fe(II)—Cl distance is unusually long at 2.44 Å<sup>22</sup> in part because of two intramolecular H-bond involving Cl<sup>-</sup>, **Figure 1.5**.<sup>23</sup>

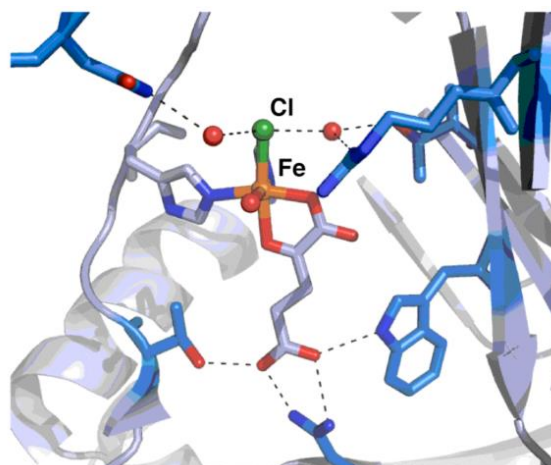


**Figure 1.5.** Active site structure of SyrB2 showing the H-bond network surrounding the chloride ion. The red spheres represent water molecules. <sup>23</sup>

### 1.3 Cyanide-bridged complexes of transition metal

#### 1.3.1 General overview

The research in the field of cyanide bridged complexes has been a subject of several reviews. The simple dinuclear cyanide-bridged complexes are present by Beauvais and Long <sup>24</sup>,  $(\text{Et}_4\text{N})_5[\text{Mo}_2^{\text{III}}(\text{CN})_{11}]$ , another example is  $(\text{Et}_4\text{N})_8[\text{Cr}^{\text{II}}(\text{CN})_5][\text{Cr}_2^{\text{II}}(\text{CN})_9]$  <sup>25</sup> (**Figure 1.6**), Nelson *et al* reported that the Cr center in the distorted square-pyramidal  $[\text{Cr}^{\text{II}}(\text{CN})_5]^{3-}$  unit lies  $0.40\text{Å}$  from the plane formed by the four basal carbon atoms, and the apical Cr-C bond length is  $2.23\text{Å}$ , while the average basal Cr-C bond length is  $2.12\text{Å}$ .  $[\text{Cr}_2^{\text{II}}(\text{CN})_9]$  is composed of two square-pyramidal moieties bridged by a cyanide ion. The bridging cyanide is disordered, with average Cr-C and Cr-N bond lengths of  $2.20\text{Å}$  observed. <sup>25</sup>

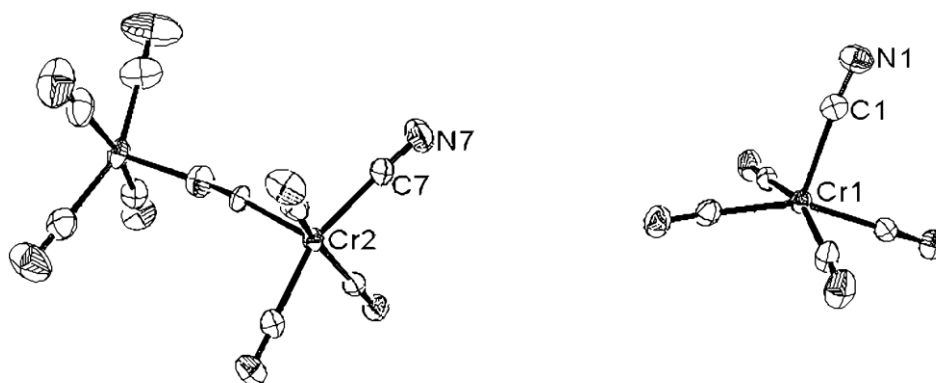


**Figure 1.6** . ORTEP labeling diagram of  $(\text{Et}_4\text{N})_8[\text{Cr}^{\text{II}}(\text{CN})_5][\text{Cr}_2^{\text{II}}(\text{CN})_9].2\text{MeCN}$ . cations and solvent molecules are omitted for clarity [25](#).

X-ray structure of combining of aqueous solution of  $\text{K}_3[\text{Fe}^{\text{III}}(\text{CN})_6]$  and  $\text{Na}_2[\text{Fe}^{\text{III}}(\text{CN})_5(\text{NH}_3)].3\text{H}_2\text{O}$  show that a single  $[(\text{NC})_5\text{Fe}-\text{NC}-\text{Fe}(\text{CN})_4(\text{NH}_3)]^{4-}$  formation for complex [26](#). Diaz et al [27](#) synthesised and studied of *trans*- $[\text{M}(\text{CN})_4(\mu\text{-CN})_2\text{Ln}(\text{H}_2\text{O})_4(\text{bpy})]_n, \text{XnH}_2\text{O}, 1.5\text{nbp}$  (M)  $\text{Fe}^{3+}$  or  $\text{Co}^{3+}$ ; Ln  $\text{Sm}^{3+}, \text{Gd}^{3+}, \text{or Yb}^{3+}$ ; X = 4 or 5. An ORTEP view of  $[\text{Fe}^{3+}\text{-Yb}^{3+}]$  complex with the atom-labeling scheme is given in **Figure 1.7**.

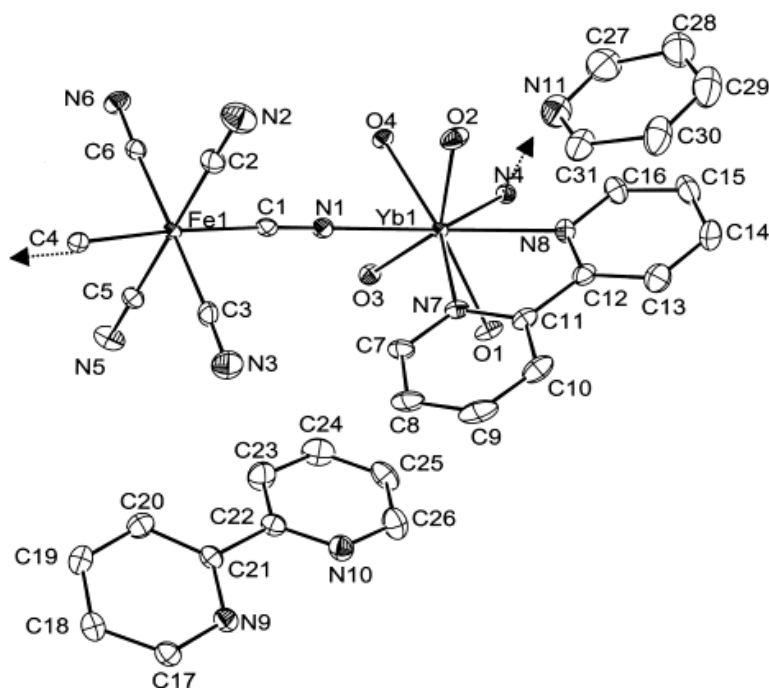


**Figure 1.7** ORTEP view of complex *trans*-[Fe(CN)<sub>4</sub>(*f*-CN)<sub>2</sub>Yb(H<sub>2</sub>O)<sub>4</sub>-(bpy)]·4*n*H<sub>2</sub>O 1.5*nbpy* (3) with atom labeling scheme.

Selected bond lengths and angles for 1-5 are listed in **Table 1.2**. The chains show an alternation of Ln<sup>3+</sup> ion and [M(CN)<sub>6</sub>]<sup>3-</sup> (M = Fe, Co) units linked by cyanide bridges in the *trans* geometry. The coordination sphere around the Ln<sup>3+</sup> ion comprises two nitrogen atoms of 2,2-bipyridine ligand, four oxygen atoms of four water molecules, and two nitrogen atoms of the cyanide bridges. The eight-coordinated Ln<sup>3+</sup> ion lies in a distorted dodecahedral environment. The distances Ln-O range from 2.45 to 2.27 Å. The lowest values are observed for Yb<sup>3+</sup> in accordance with the variation of the radius of the lanthanide ions. Six cyanide ligands surround the M<sup>3+</sup> (Co, Fe) ion in a distorted octahedral environment. The M-C distances range from 1.88 to 1.96 Å, and the lowest correspond to the [Co(CN)<sub>6</sub>]<sup>3-</sup>. The Ln-M (M = Fe, Co) intramolecular distances are:



## CHAPTER 1 | INTRODUCTION

5.612 Å for [Fe<sup>3+</sup>Sm<sup>3+</sup>] , 5.564 Å for [Fe<sup>3+</sup>Gd<sup>3+</sup>] , 5.421 Å for [Fe<sup>3+</sup>Yb<sup>3+</sup>] , 5.555 Å for [Co<sup>3+</sup>Gd<sup>3+</sup>], and 5.515 Å for [Co<sup>3+</sup>Yb<sup>3+</sup>] . The Ln-M-Ln angle are 159.55° for [Fe<sup>3+</sup>Sm<sup>3+</sup>], 159.40° for [Fe<sup>3+</sup>Gd<sup>3+</sup>] , 159.17° for [Fe<sup>3+</sup>Yb<sup>3+</sup>] , 159.40° for [Co<sup>3+</sup>Gd<sup>3+</sup>], and 159.27° for [Co<sup>3+</sup>Yb<sup>3+</sup>], indicating the trans geometry. [27](#)

	[Fe <sup>3+</sup> Sm <sup>3+</sup> ]	[Fe <sup>3+</sup> -Gd <sup>3+</sup> ]	[Fe <sup>3+</sup> -Yb <sup>3+</sup> ]	[Co <sup>3+</sup> -Gd <sup>3+</sup> ]	[Co <sup>3+</sup> -Yb <sup>3+</sup> ]
Ln(1)-O(1)	2.434(2)	2.404(2)	2.356(2)	2.417(2)	2.365(3)
Ln(1)-N(1)	2.529(2)	2.488(2)	2.426(3)	2.508(2)	2.449(3)
M(1)-C(1)	1.939(3)	1.936(3)	1.948(3)	1.905(2)	1.918(4)
C(1)-N(1)	1.154(3)	1.151(3)	1.163(4)	1.153(3)	1.159(5)
Ln(1)-N(1)-C(1)	175.5(2)	175.4(2)	175.9(2)	175.3(2)	175.5(3)
M(1)-C(1)-N(1)	176.2(2)	175.8(2)	175.5(3)	175.8(2)	175.6(3)

**Table1.2.** Selected bond lengths (Å) and angles (deg) . Taken from Reference 27. [27](#)

Guo *et al* [28](#) report that the structure of [EuFe(CN)<sub>6</sub>(DMF)<sub>4</sub>(H<sub>2</sub>O)<sub>3</sub>] complex molecules and solvent water molecules. **Figure 1.8.** The Fe<sup>III</sup> and Eu<sup>III</sup> ions are bridged by a cyanide group to form a dinuclear complex. The Eu<sup>III</sup> ion is eightfold coordinated by one N atom of the bridging cyanide group [Eu-N = 2.495 (4) Å ], four O atoms of DMF molecules [Eu-O<sub>DMF</sub> = 2.353 (3)±2.649 (3) Å , with an average distance of 2.469 (3) Å], and three water molecules, for which the three Eu-O<sub>water</sub> distances are in the range

## CHAPTER 1 | INTRODUCTION

2.204 (3)±2.589 (3) Å, with an average distance of 2.362 (3) Å. The coordination polyhedron can be described as a slightly distorted square antiprism. A similar situation was found in [Ln(Fe(CN)<sub>6</sub>(DMF)<sub>4</sub>(H<sub>2</sub>O)<sub>3</sub>].H<sub>2</sub>O <sup>29</sup>. The Eu1-N1-C1 angle is 165.7 (4) Å, deviating slightly from linearity, as was the case in its analog. A three-dimensional framework is formed through O-H.....O and O-H.....N hydrogen-bonding interactions, with O.....O distances of 2.748 (3) Å and average O.....N separations of 2.706 (3) Å.

[28](#)

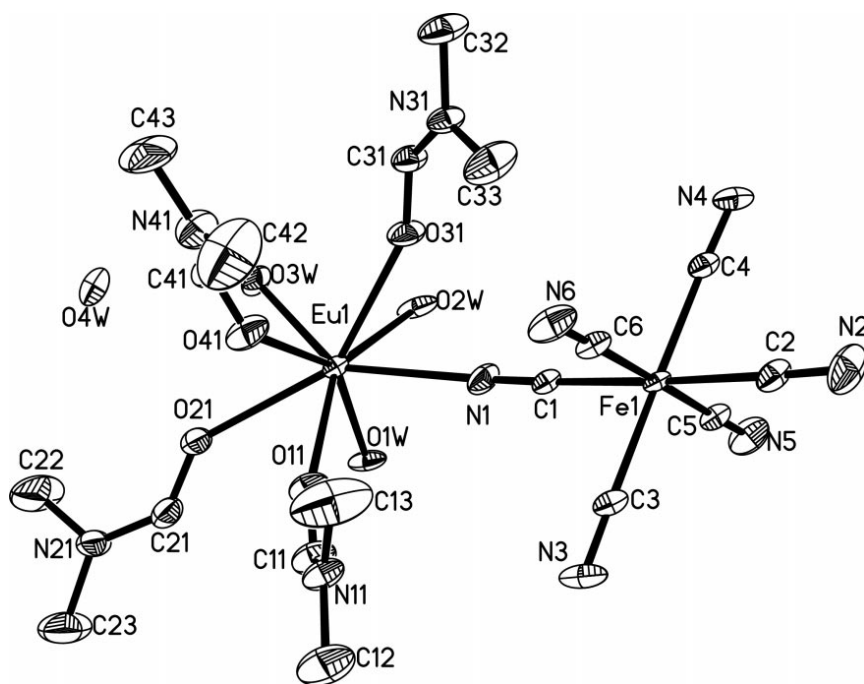


**Figure 1.8** Structure of neutral bimetallic  $\text{EuFe}(\text{CN})_6(\text{DMF})_4(\text{H}_2\text{O})_3$  showing ligated solvent and water molecules. Reproduced from Reference <sup>28</sup>.

### 1.3.2 IR Spectroscopy of cyanide-bridged Complexes.

Nakamoto <sup>30</sup> gave more details for the carbon end of cyanide ligand after coordinating to metal behaving as  $\sigma$ -donor by donating electron density from the highest occupied 5  $\sigma$  MO. This led to an increase in  $\nu(\text{CN})$  as the oxidation state of the metal increased. However, the opposite trend observed on d- $\pi$  back-bonding interaction requiring electron donation from the  $d$  orbital in metal ion to the  $2\pi^*$  MO of cyanide, this led to shift  $\nu(\text{CN})$  to lower frequencies<sup>30</sup>, for example, comparing IR of  $[\text{Fe}^{\text{III}}(\text{CN})_6]^{3-}$  and  $[\text{Fe}^{\text{II}}(\text{CN})_6]^{4-}$  <sup>31</sup>, the  $\nu(\text{CN})$  stretch of  $[\text{Fe}^{\text{III}}(\text{CN})_6]^{3-}$  is shifted to higher frequency at 2101  $\text{cm}^{-1}$  compared by free CN at 2080  $\text{cm}^{-1}$  while CN of  $[\text{Fe}^{\text{II}}(\text{CN})_6]^{4-}$  shifted to lower frequency at 2050  $\text{cm}^{-1}$  <sup>31</sup>. Another important observation on cyanide-bridged complexes is that the formation of bridge between two metal ion leads to a shift in  $\nu(\text{CN})$  to higher frequency compared to the starting material.<sup>32</sup> This increase in  $\nu(\text{CN})$  is assigned to the ‘mechanical constraint’ on CN ligand produced by the second metal center, however, it may be the electrostatic more important in this case. <sup>33</sup> IR  $\nu(\text{CN})$  stretches for different M-CN-M’ is shown in **Table 1.3**.

Karlin <sup>34</sup> reported that IR spectroscopy is a useful probe for discerning the nature of the cyanide linkage. A compilation of  $\nu(\text{CN})$  stretching frequencies in various cyanide-bridged complexes is given in **Table 1.3**. Nakamoto <sup>30</sup> reported that the factors that influence the shift of  $\nu(\text{CN})$  stretches of the cyanide-bridged complexes relative to those of the free  $\text{CN}^-$  ligand with  $\nu(\text{CN}) = 2080 \text{ cm}^{-1}$ . These can be understood from the molecular orbital (MO) diagram of the  $\text{CN}^-$  anion **Figure 1.9**. <sup>34</sup>

CHAPTER 1 | INTRODUCTION

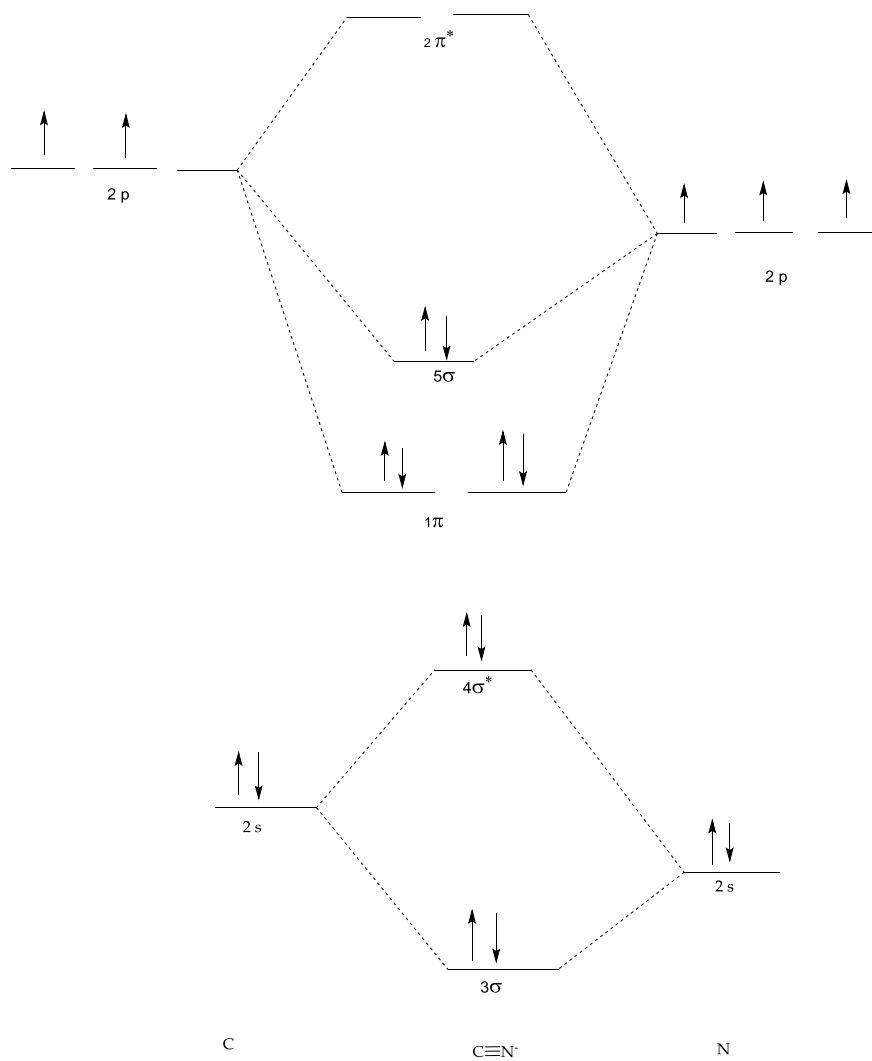


**Figure 1.9** Molecular orbital diagram of  $\text{CN}^-$ .

M	M'	v(CN) cm <sup>-1</sup>	
		Bridging	Terminal
V <sup>III</sup> (d <sup>2</sup> ,mTP)	V <sup>III</sup> (d <sup>2</sup> ,mTP)	2156 <a href="#">35</a>	
Mn <sup>I</sup> (d <sup>6</sup> ,-LS,Oct)	Fe <sup>III</sup> (d <sup>5</sup> ,Td)	2017 <a href="#">36</a>	
Fe <sup>II</sup> (d <sup>6</sup> ,-LS,Oct)	Mn <sup>II</sup> (d <sup>5</sup> ,- HS,Oct)	2053	2046 <a href="#">37</a> , <a href="#">38</a>
Fe <sup>II</sup> (d <sup>6</sup> ,-LS,Oct)	Fe <sup>II</sup> (d <sup>6</sup> ,-LS,Oct)	2083-208 <a href="#">39</a> , <a href="#">40</a>	
Fe <sup>II</sup> (d <sup>6</sup> ,-LS,Oct)	Fe <sup>III</sup> (d <sup>5</sup> ,-LS,Oct)	2009-2025 <a href="#">41</a>	
Fe <sup>III</sup> (d <sup>5</sup> ,-LS,Oct)	Fe <sup>II</sup> (d <sup>6</sup> ,-HS,Oct)	2150-2131	2122-2127 <a href="#">31</a> , <a href="#">42</a> , <a href="#">43</a>
Fe <sup>III</sup> (d <sup>5</sup> ,-LS,Oct)	Eu <sup>III</sup> (SAP)	2145	2138-2121 <a href="#">28</a>

**Table 1.3** Cyanide stretching frequencies of various cyanide-bridged complexes. HS = high spin, LS = low spin, mTP = monocapped trigonal prismatic, Td = tetrahedral, Oct = octahedral and SAP = square antiprismatic.

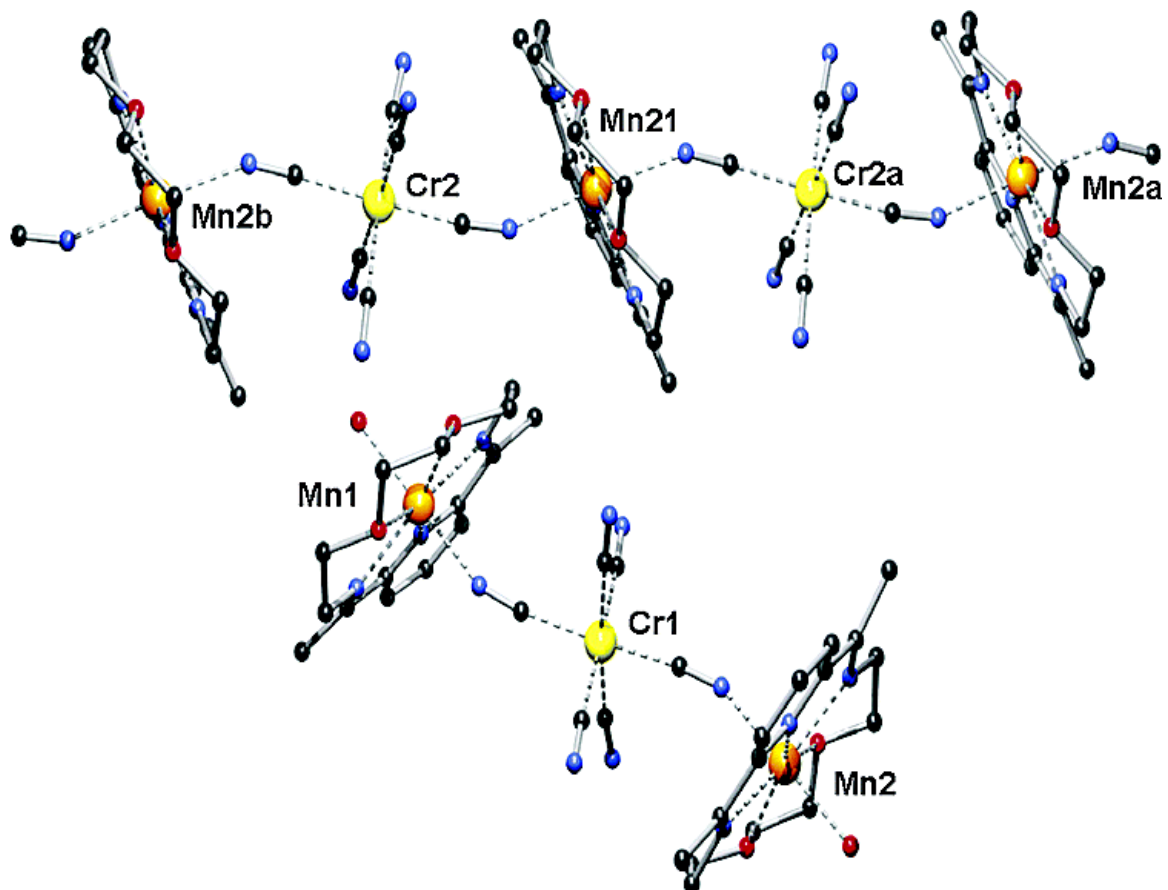


**Figure 1.10** ORTEP representation of  $n[(\text{Mn}^{\text{II}}(\text{azaoxamacrocyclo})\text{H}_2\text{O}))_2(\text{Cr}^{\text{III}}(\text{CN})_2(\text{CN})_4)] [(\text{Mn}^{\text{II}}(\text{azaoxamacrocyclo})\text{Cr}^{\text{III}}(\text{CN})_2(\text{CN})_4) 7.5n\text{H}_2\text{O}$  (**5**). H atoms and solvent molecules are omitted for clarity.<sup>38</sup>

## CHAPTER 1 | INTRODUCTION

In a biological context, bridging cyanide has recently come to the fore as an area of research because it is thought to be involved in the biosynthetic pathway to the active site of [FeFe]-hydrogenase. In this pathway a ‘maturase’ of ‘scaffold’ protein HydF is believed to transfer a diiron unit **Figure 1.11 (a)** to the *apo*-hydrogenase, **Figure 1.11 (b)** to give the active H-cluster of HydA , **Figure 1.11 (c)** . Remarkably, it is proposed that HydF possesses a bridging cyanide but this is formed by a CN linkage isomerism from the diiron dicyanide precursor. <sup>44</sup> This has yet to be fully substantiated although such linkage isomerism has been established with the flipping of the CN modifying the complex properties. <sup>34</sup>

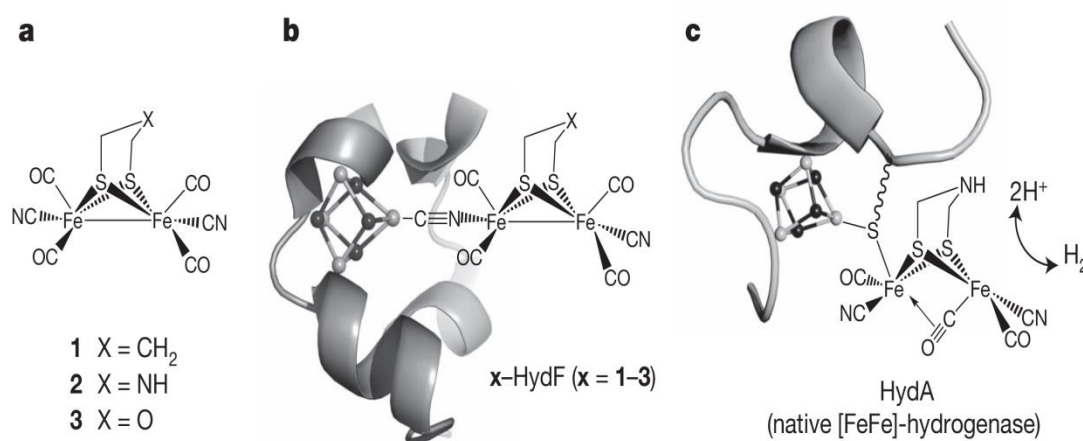


**Figure 1.11** Synthetic subsites (a), their binding to the maturase with linkage isomerism of the CN bridge, and (c) the re-flipped CN after transfer to form an active hydrogenase. <sup>44</sup>

## **1.4 Experimental methods and techniques**

### **1.4.1 General synthetic methodology**

#### **1.4.1.1 Solvent purification**

Solvents were freshly distilled under an inert atmosphere of dinitrogen from an appropriate drying agent using standard laboratory procedures.<sup>45</sup>

#### **1.4.1.2 Handling methodology**

Unless otherwise stated chemicals were handled under an inert atmosphere of dinitrogen or argon using standard Schlenk line techniques.<sup>46</sup> Chemicals (starting materials, electrode materials, solvents, specialist gases) were generally purchased from Sigma-Aldrich, Alfa Aesar or specialist suppliers without further purification.

#### **1.4.1.3 Electrolyte preparation**

[NBu<sub>4</sub>][BF<sub>4</sub>] was the electrolyte used in electrochemistry experiments. It was prepared by a standard laboratory procedure.<sup>47</sup>

#### **1.4.1.4 Microanalysis**

Elemental analysis was carried out at London Metropolitan University using a Thermo Scientific Flash 2000 Elemental Analyser configured for %CHN.



## 1.4.2. Background to experimental techniques

### 1.4.2.1. FTIR spectroscopy

In infrared spectroscopy (IR) a sample is irradiated with infrared light and certain frequencies are absorbed as bonds within molecules move to higher vibrational levels. Different types of bonds within molecules will absorb IR radiation of different frequencies. The strength of a bond can also be approximated from the frequency of IR light it absorbs. IR spectroscopy is therefore a valuable technique in characterizing functional groups within molecules.<sup>48</sup>

Sampling techniques in IR spectroscopy vary in consideration of the sample state. IR radiation has a limited transmittance depth in molecular solid samples to circumvent this a number of approaches are taken to produce finely dispersed solids which will give a useful signal. By far the most common approach is to produce a dilute paste of the solid by grinding with Nujol (paraffin oil). The Nujol mull is then thinly applied between single-crystal NaCl discs or a similar ionic solid that will not absorb IR radiation in the region of interest. A second approach is to intimately mix the solid with KBr and create a disc using a hydraulic press. Solid samples can also be analyzed by attenuated total reflectance (ATR). In ATR the solid is pressed against a single crystal sample head, commonly diamond. IR light is passed through the crystal making use of total internal reflectance; a small amount of this light escapes the crystal as an evanescent wave which penetrates a short distance into the sample (typically less than one micrometer). This has the advantage of not having to add anything extra to the sample.

## CHAPTER 1 | INTRODUCTION

For liquids and solutions the absorption of the light by the sample is less problematic. Samples can be applied directly to the IR discs or an ATR, or can be injected into an IR transmission cell (for air sensitive samples).

FTIR spectroscopy of diatomic molecules on organometallics

A useful equation for predicting the wavenumber of vibration of a diatomic molecule is given by

$$\tilde{\nu} = \frac{1}{2\pi c} \sqrt{\frac{k_f}{\mu}} \quad \text{Eq 1.1}$$

where  $k_f$  is the force constant in  $\text{N m}^{-1}$ ,  $\mu$  is the reduced mass in kg, and  $c$  is the speed of light measured in  $\text{cm s}^{-1}$ . The reduced mass can be calculated by

$$\mu = \frac{m_1 m_2}{m_1 + m_2} \quad \text{Eq 1.2}$$

where  $m_1$  is the mass of atom 1 in kg and  $m_2$  is the mass of atom 2 in kg. These equations can also be useful when applied to multi-atom molecules in the context of isotopic labelling. The bond strength and therefore the IR vibrational frequency of a bond depends on the mass of the atoms that make it up. Isotopic substitution of one of the components will result in a change in the reduced mass. Therefore we can make a prediction of the size of the shift in vibrational frequency based on the equations above. This relies on the assumption that each bond behaves as an isolated diatomic.

## CHAPTER 1 | INTRODUCTION

IR spectroscopy is a particularly useful technique to probe  $\text{C}\equiv\text{N}^-$  and  $\text{C}\equiv\text{O}$  containing molecules. This is because of the dipole moment of these functional groups which give rise to strong absorptions in a region largely free of other signals.

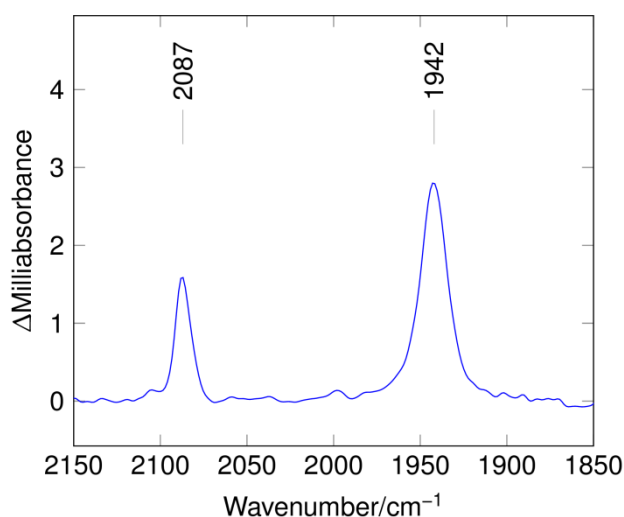


**Figure 1.13** Example of an IR spectrum. Two strong bands can be seen, one in the region of  $\text{CN}^-$  ( $2087 \text{ cm}^{-1}$ ) one in the region of  $\text{CO}$  ( $1942 \text{ cm}^{-1}$ ).

The positions of  $\text{C}\equiv\text{O}$  absorptions are characteristic of the type of  $\text{C}\equiv\text{O}$  functional group and are influenced by the electronic environment of the atom to which they are attached (particularly in metal-carbonyl complexes). In  $\text{C}\equiv\text{O}$  complexes with metals, the  $\text{C}\equiv\text{O}$  binds to the metal via  $\sigma$  donation into a vacant metal  $d$  orbital. In addition to a  $\sigma$  bond, a metal carbonyl bond is further strengthened through the overlap of antibonding  $\pi^*$  molecular orbital of  $\text{C}\equiv\text{O}$  and the  $d$  atomic orbitals of the metal (known as back-bonding). Commonly,  $\text{C}\equiv\text{O}$  in metal carbonyl complexes vibrates at frequencies lower than that found for free  $\text{C}\equiv\text{O}$ . This means that the  $\text{C}\equiv\text{O}$  bond is weakened by binding

to the metal, consistent with the idea that back-bonding between the metal and  $\text{C}\equiv\text{O}$  takes place.

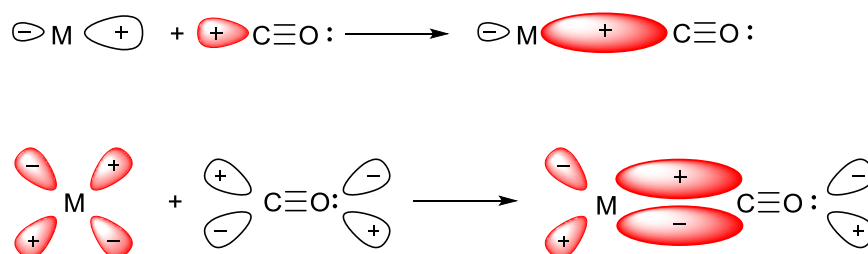


**Figure 1.14** Top: Bonding between the empty  $d$  orbital of a metal centre and the  $\sigma$  bonding orbital of  $\text{C}\equiv\text{O}$ . Bottom: bonding between the filled  $d$  orbital of a metal and the  $\pi^*$  unoccupied molecular orbital of  $\text{C}\equiv\text{O}$ .

The occupation of the  $\pi^*$  molecular orbital of  $\text{C}\equiv\text{O}$  with electron density leads to a destabilizing of the  $\text{C}\equiv\text{O}$  bond. The more electron-rich the metal centre to which  $\text{C}\equiv\text{O}$  is bound the greater the extent of the weakening of the  $\text{C}\equiv\text{O}$  bond. A weaker bond will vibrate at a lower frequency than a stronger bond therefore the vibrational frequency of a  $\text{C}\equiv\text{O}$  stretch can give information about the electronic environment of the metal centre. Equally, predictions of the direction of the shift vibrational frequency can be made when altering the electron richness of the metal in a metal carbonyl by changing the ligand environment.

The number of bands observed in an infrared spectrum is related to the symmetry of the complex. This can be analysed by group theory or in current methodology by analysis of structures by DFT. Group theory will predict the number of bands only and is most

## CHAPTER 1 | INTRODUCTION

useful for a molecule of higher symmetry. DFT will predict positions and intensities too, and although one can argue about accuracy this information is often as useful as a predicted number of bands.

The bond angle  $2\theta$  between *cis* carbonyls on an organometallic is related to the relative intensities of the symmetric and asymmetric stretch as shown in **Eq 1.3**.<sup>49</sup>

Relation of relative intensities of the symmetric and asymmetric stretch of *cis* carbonyls on a metal complex to the bond angle between them  $2\theta$ .

$$\frac{I_{\text{sym}}}{I_{\text{asym}}} = \cotan 2\theta \quad \text{Eq 1.3}$$

### 1.4.2.2. NMR spectroscopy

Nuclear magnetic resonance (NMR) spectroscopy is a technique commonly used to determine the structure of organic molecules.<sup>48</sup> In NMR spectroscopy a sample is placed in a powerful magnetic field and irradiated with a pulse of radiowaves. This produces a signal that is then converted into an NMR spectrum. Some nuclei have a non-zero spin and NMR exploits their interaction with an external magnetic field. A spinning atom (such as a proton) generates its own magnetic field in proportion to the magnitude of the spin. When an external magnetic field is applied  $(2S + 1)$  spin states exist. For a proton  $S = 1/2$ , and therefore two spin states exist, one parallel and one antiparallel to the external magnetic field. The greater the external magnetic field applied the greater the energy difference in energy between the states. The NMR sample

## CHAPTER 1 | INTRODUCTION

is irradiated with radiowaves and this causes the spin to transition from one state to the other. This transition occurs because the radiowaves absorbed have the same energy as the energy difference between the two spin states, this is known as resonance. A signal is generated from the energy released when the spin population of the nuclei returns to equilibrium. Processing of the signal leads to a peak of frequency  $\nu$  where  $\Delta E = h\nu$ .

A naïve prediction might be that we would only see one peak per kind of nucleus (e.g. C, H, B). However, nuclei of the same kind in a compound will not necessarily resonate at the same frequency. For example, protons in a compound may be in different chemical environments: this dictates the electron density around the nuclei. Electrons generate a local magnetic field which opposes the applied magnetic field. Therefore, where electron density is higher the net magnetic field will be weaker, lowering the frequency of the signal produced. The frequency of a given NMR signal is converted into a chemical shift from a given reference in ppm. This gives us a value that is independent from the magnetic field strength. Nuclei in different chemical environments will give different chemical shifts and therefore give rise to separate signals.

$$\text{chemical shift, } \delta, \text{ in ppm} = 10^6 \times \frac{\nu_{\text{resonance}} - \nu_{\text{reference}}}{\nu_{\text{reference}}}$$

In addition to the external and local magnetic field contributions, spins from neighbouring nuclei can interact with one another. This imparts a further magnetic contribution if the neighbouring nuclei have non-zero spin. A spin 1/2 nucleus can either exist as “spin up” or “spin down” and each state acts on a neighbouring nucleus

to either increase or decrease the net magnetic field, respectively. This has the effect of splitting the signal seen into two peaks (or more depending on the number of neighbouring nuclei with non-zero spin). This splitting is known as the coupling constant ( $J$ ) and is reported in Hz.

The combination of chemical shift and coupling information makes NMR a powerful spectroscopic technique for the modern synthetic chemist.

### 1.4.2.3. Mass spectrometry

Mass spectrometry is a useful analytical technique that measures the mass of an ionised molecule or fragment.<sup>48</sup> This is typically done by ionizing a chemical sample, separating the ions and fragments created according to their mass and having a means of detecting them. The general scheme for this is shown in **Figure 1.15** .

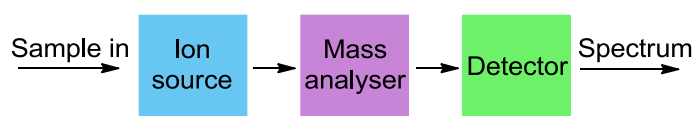


**Figure 1.15** Basic schematic of mass spectrometer.

This then produces a mass spectrum, a plot of ion signal as a function of mass to charge ratio. Samples are introduced into the spectrometer as a solution or solid and then vaporised under vacuum. There are a variety of techniques used to then ionise the sample. One such technique is electron ionization (EI), where high energy electrons are fired at the sample. The high energy electrons create positively charged ions by

## CHAPTER 1 | INTRODUCTION

knocking off electrons from the sample. The resulting positively charged ions are then electrostatically repelled into the mass analyser. The main disadvantage of electron ionization is that direct bombardment of the sample with electrons can lead to fragmentation of ions before they reach the detector.

Electrospray ionization is now a commonly used ionization technique. In this technique the sample is made into a solution which can sometimes have added ionic compounds such as carboxylate or sodium alkoxide. This is then sprayed through a fine capillary at a potential of several thousand volts. The aerosol produced consists of charged droplets of solution. The droplets are then swept into a high vacuum, evaporating the solvent and eventually causing the droplets to explode. This gives sample molecules with ions attached. These are then accelerated into the mass analyzer.

In contrast to a classical quadrupole analyser, the orbitrap method relies on ions trapped in a cylindrical electric field. The trapped ions orbit a central spindle-like electrode under the influence of an oscillating electric field. The frequency of orbit is dependent upon the mass of the ion in question and can be extracted by Fourier transform. As the ions are trapped during analysis it is possible to selectively extract them for hyphenated analysis. The orbitrap technique combines the soft ionization technique of ESI with the ability to obtain high-resolution results it thus becoming the standard technique for molecular identification for mass spectrometry.<sup>50</sup>



#### 1.4.2.4 X-ray crystallography

X-ray crystallography is the definitive technique for determining the exact structure and shape of a molecule.<sup>48</sup> Unlike spectroscopic techniques, which give qualitative data concerning functional groups and connectivity, X-ray crystallography gives a defined structure. One drawback is the need to obtain a good quality crystal of the compound of interest, which is often difficult. A crystal is composed of ions, or molecules arranged in a regular order throughout the solid forming a lattice, in which the smallest repeating subunit is called the unit cell.

In order for diffracted X-rays to be observed, there must be constructive interference between them. **Figure 1.16** illustrates the diffraction of X-rays from lattice planes. In order to have constructive interference the path difference between these X-rays must be equal to an integer number of wavelengths.

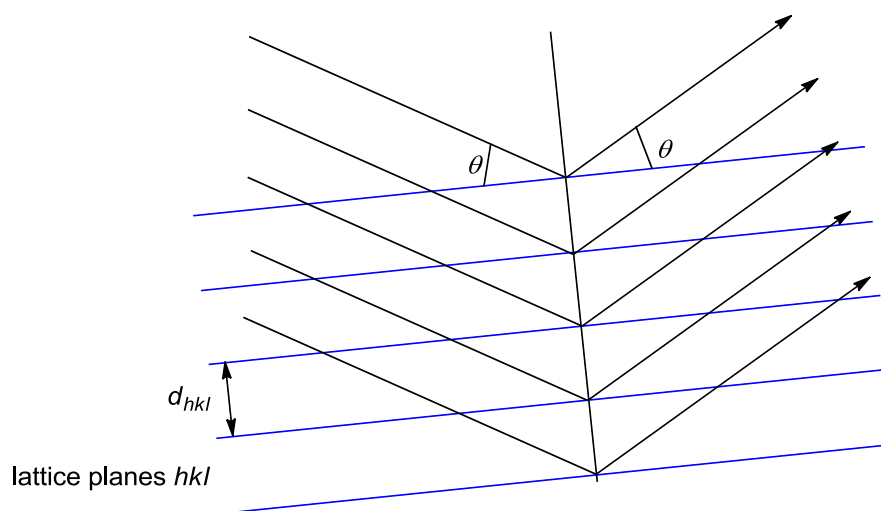


**Figure 1.16** Diffraction of X-rays from crystal lattice planes.

## CHAPTER 1 | INTRODUCTION

This leads onto Bragg's law

$$2d \sin \theta = n\lambda$$

where  $\theta$  is known as the Bragg angle,  $\lambda$  is the wavelength of the X-rays and  $d$  is the distance between adjacent planes in a parallel set.

Bragg's Law is a fundamental law in diffraction that gives the conditions under which a diffracted beam of radiation may be observed.<sup>51</sup> When a good quality crystal is irradiated with X-rays, the radiation will be diffracted in a regular pattern. The diffraction is strongest in regions of high electron density as it is the electrons that diffract the X-rays. The diffraction pattern is used to discern the location of the atoms in a molecule as most electron density is centred around the nuclei. It is possible to not only determine the spatial arrangement of the atoms but also how the molecules pack within the cell. To obtain this information the electron density is mapped out, with heavier atoms placed in regions of higher electron density. The experimental information is compared to a computer model of the suspected structure and refined until good agreement is obtained. One measure of the agreement between the experimental data and the computer model is known as the *R*-factor, the smaller the *R*-factor: the better the agreement.

### 1.4.2.5 Stopped-flow FTIR

Stopped-flow is a useful technique for detecting the presence of short lived intermediates in solution and for gathering kinetic data about a reaction. In a stopped-flow experiment two syringes are used each loaded with one of two reactive partners.

## CHAPTER 1 | INTRODUCTION

The two syringes are connected to a mixing chamber and then to a spectroscopic cell. At the start of the reaction the two syringes are injected simultaneously into the mixing chamber. Rapid mixing occurs and the product solution moves into the cell. The FTIR then starts scanning the mixture and follows the progress of the reaction from time zero. It can thus be seen that stopped-flow can give information about reaction rates and show the presence of any intermediates formed.<sup>52</sup> A schematic of a stopped-flow IR is shown below.

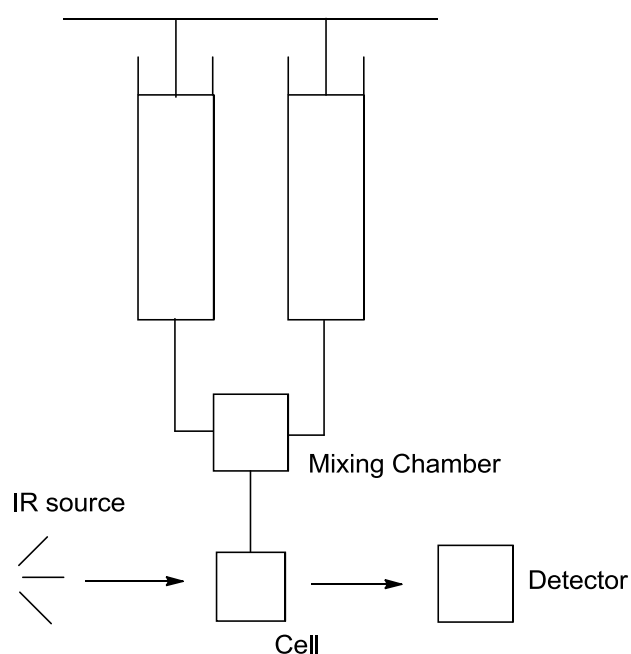


**Figure 1.19** Basic cross-section of stopped-flow IR.

In practice the distance between the mixing chamber and the cell needs to be minimised to reduce the “dead time”: the time interval between mixing and the first observable signal. There is also a time-scale requirement for acquisition of Fourier transform

## CHAPTER 1 | INTRODUCTION

infrared data as this involves a mechanical component (interferometer). For systems in use today the dead time of roughly 50 ms is less significant than the requirements for the acquisition of infra red data which limit time resolution to at best tens of milliseconds.

Stopped-flow IR is particularly powerful when the observed bands fall in an otherwise unpopulated region of the spectrum. Organometallic compounds that contain CO and CN bands are therefore favourable for study using this method as the distinct chromophores fall in a unique spectral window.

Data obtained from absorption-time data is analyzed to provide kinetic information on the rate of consumption of starting material and growth of product(s).

### **1.4.2.6 Electrochemical measurements**

Where the chemistry of compounds involves their ability to undergo redox changes, electrochemical techniques can offer a unique insight into the intimate detail. Perhaps the most versatile electrochemical technique is cyclic voltammetry (CV). In CV a potential applied to the solution is swept over a controlled range and the current response is recorded. By varying factors such as the temperature, scan rate and potential range analysis of a set of CV experiments can give information about the kinetics and thermodynamics of a chemical system. Cyclic voltammetry is a particularly useful technique as an experiment requires very little compound (milligrams) and is essentially non-destructive since the chemistry occurs in a small volume in the diffusion layer at the surface of the electrode, leaving the bulk concentration essentially unchanged.

## CHAPTER 1 | INTRODUCTION

During a basic CV experiment a redox active compound (the subject of the experiment) is dissolved in a solution containing a non-redox active electrolyte. The electrolyte is present to reduce resistance and allow charge to flow. Electrolytes used in non-aqueous solvents feature large ions to give good solubility and thus conductivity. For example  $[\text{Bu}_4\text{N}][\text{BF}_4]$  is a common electrolyte in a solvent such as acetonitrile. The solution of subject compound and electrolyte are contained within an electrochemical cell which typically has three chambers, each of which contains an electrode.

A common three electrode arrangement is made up of a working electrode, typically made of vitreous carbon (platinum, gold or amalgamated gold can also be used), a secondary electrode made of platinum and a reference electrode of silver wire or  $\text{Ag}/\text{AgCl}$ .<sup>53</sup>

In a cyclic voltammetry experiment there is a variable potential difference between the working and secondary electrodes and a fixed potential difference between the working and reference electrodes. Over the time-course of the experiment the variable potential difference is swept over a controlled range in the manner depicted **Figure 1.17**

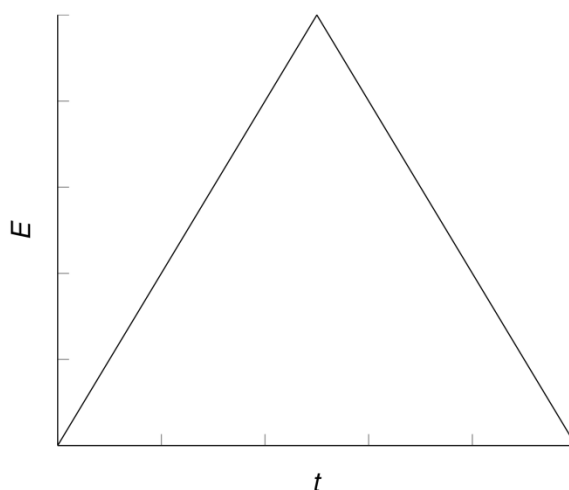


**Figure 1.17** The potential difference sweep during a typical CV experiment, where the slope is equal to the scan rate.<sup>54</sup>

**Figure 1.18** below shows the key features of a typical cyclic voltammogram for a reversible couple. On the forward sweep, the current passed rises to a maximum  $i_p^{\text{ox}}$  at the oxidation potential  $E_p^{\text{ox}}$ , before falling away in the reverse direction the absolute value of the current again rises to a maximum  $i_p^{\text{red}}$  at the reduction potential  $E_p^{\text{red}}$ . The average of  $E_p^{\text{ox}}$  and  $E_p^{\text{red}}$  is  $E_{1/2}^o$  for the redox couple being examined. For an ideal one electron reversible couple, the difference between  $E_p^{\text{ox}}$  and  $E_p^{\text{red}}$  is close to 60 mV at room temperature (theoretically 59 mV at 25 °C), and  $i_p^{\text{ox}}/i_p^{\text{red}} = 1$ .

The diagram on the right illustrates the effect of scan rate on the cyclic voltammogram. For a fully reversible process, the peak positions are unaffected whilst the peak current scales linearly with the square root of the scan rate.

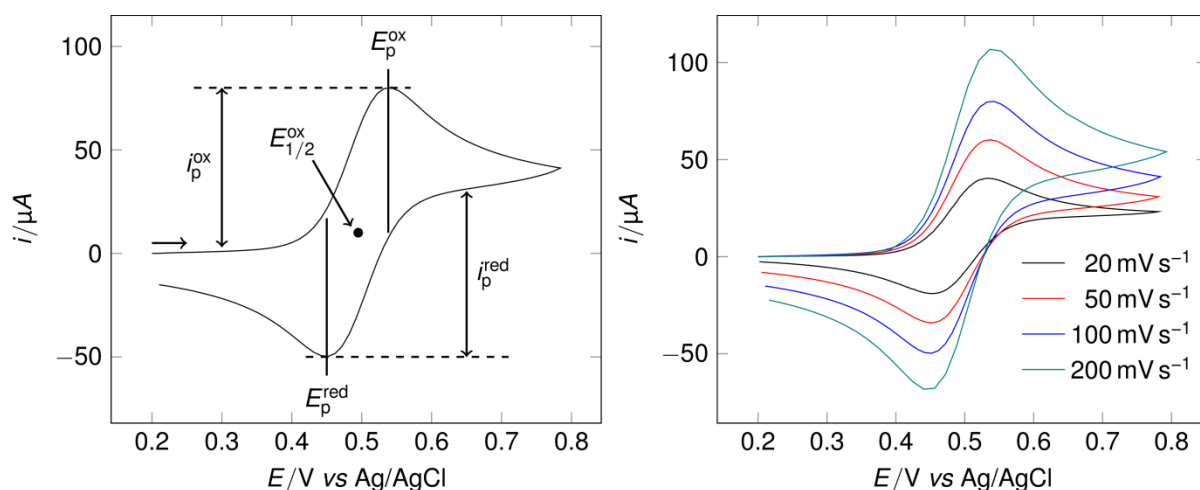


**Figure 1.18** Left: CV of 3.5 mM ferrocene recorded at  $100 \text{ mV s}^{-1}$  vs Ag/AgCl in 0.1 M  $[\text{Bu}_4\text{N}][\text{BF}_4]$ - MeCN at  $25^\circ\text{C}$ ; Right: CV of 3.5 mM ferrocene recorded at various scan rates vs Ag/AgCl in 0.1 M  $[\text{Bu}_4\text{N}][\text{BF}_4]$ - MeCN at  $25^\circ\text{C}$ . Reproduced from ref. [55](#)

The information contained in the cyclic voltammogram above tells us that ferrocene is a reversible, one-electron system. In addition, for a reversible system, it can be shown that the magnitude of the forward peak current is given by the Randles-Sevcik equation

$$i_p = 2.69 \times 10^5 n^{3/2} A D^{1/2} C^* \nu^{1/2}$$

where  $n$  is the number of electrons associated with the oxidation or reduction step of the parent species,  $A$  is the area of the electrode in  $\text{cm}^2$ ,  $D$  is the diffusion coefficient of the species in  $\text{cm}^2 \text{ s}^{-1}$ ,  $C^*$  is the bulk concentration expressed in  $\text{mol}^3 \text{ dm}^{-3}$ , and  $\nu$  is the potential scan rate in  $\text{V s}^{-1}$ .

A linear plot of the peak current vs the square root of the scan rate over a range of scan rates establishes that the electrochemical process is controlled by diffusion rather than involving the species being bound to the electrode surface.

*The thermodynamic significance of cyclic voltammetric  $E_{1/2}$  values*

It was shown by Nernst that the potential established at the electrode under equilibrium conditions is given by

$$E_e = E^\circ + \frac{RT}{nF} \ln \frac{[O]}{[R]}$$

where the potential at equilibrium ( $E_e$ ) of the electrode results from the standard electrode potential ( $E^\circ$ ) of the reaction and the concentrations of O and R, which, under equilibrium conditions are the same as the bulk solution. Thermodynamic parameters such as free energies, entropies, enthalpies, equilibrium constants, activities and solution pH can be obtained from equilibrium chemical measurements.<sup>56</sup>

In this work the potential at which redox couples are reported are given as the  $E_{1/2}$  (the mid potential between  $E_p^{\text{ox}}$  and  $E_p^{\text{red}}$  as shown in **Figure 1.18** .

The Nernst equation defines the equilibrium potential  $E_e$  for a system as:

$$E = E^0 + \frac{RT}{nF} \ln \frac{a^{\text{ox}}}{a^{\text{red}}}$$

where  $a^{\text{ox}}$  and  $a^{\text{red}}$  are the thermodynamic activities of the redox partners and  $E^0$  is the *standard potential*. This can be re-written as:

$$E = E^0 + \frac{RT}{nF} \ln \frac{\gamma^{\text{ox}} C^{\text{ox}}}{\gamma^{\text{red}} C^{\text{red}}}$$



## CHAPTER 1 | INTRODUCTION

where  $\gamma^{\text{ox}}$ ,  $\gamma^{\text{red}}$ ,  $C^{\text{ox}}$ ,  $C^{\text{red}}$  are the respective activity coefficients and concentrations of the oxidised and reduced species. Rearranging this equation gives:

$$E = E^0 + \frac{RT}{nF} \ln \frac{\gamma^{\text{ox}}}{\gamma^{\text{red}}} + \frac{RT}{nF} \ln \frac{C^{\text{ox}}}{C^{\text{red}}}$$

Letting

$$E^{0'} = E^0 + \frac{RT}{nF} \ln \frac{\gamma^{\text{ox}}}{\gamma^{\text{red}}}$$

and, defining  $E^{0'}$  as the *formal potential* we have an alternative form of the Nernst equation:

$$E = E^{0'} + \frac{RT}{nF} \ln \frac{C^{\text{ox}}}{C^{\text{red}}}$$

$E_{1/2}$  is related to  $E^{0'}$  by the expression:<sup>57</sup>

$$E_{1/2} = E^{0'} + \frac{RT}{nF} \ln \sqrt{\frac{D^{\text{red}}}{D^{\text{ox}}}}$$

The diffusion coefficients ( $D$ ) of the redox partners of systems of moderate molecular mass (>200) are usually quite similar. If we consider a case where the reduced form of the redox pair has a diffusion coefficient as much as 20 % greater than that of the oxidised species, then it can be shown that for a one electron couple:

$$E_{1/2} = E^{0'} + 2.34 \text{ mV}$$

## CHAPTER 1 | INTRODUCTION

Thus to a reasonable approximation:

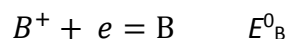
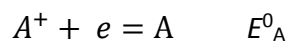
$$E_{1/2} \approx E^{0'}$$

Using similar arguments for activity coefficients we can use the approximation:

$$E_{1/2} \approx E^{0'} \approx E^0$$

Variation in  $E_{1/2}$  for series of closely related compounds

Consider the two Nernstian equilibrium shown in below Equations for two closely related species A and B which have associated formal potentials  $E^0_A$  and  $E^0_B$  respectively.



If  $E^0_A$  is positive of  $E^0_B$  relative to the same reference electrode then  $A^+$  is clearly easier to reduce than  $B^+$ . The direct collorary of course is that B is easier to oxidise than A because the potential  $E^0_B$  is negative of  $E^0_A$ .

### 1.4.3 Background to theoretical and simulation methods

### 1.4.3.1 Simulation of electrochemical data

There is a strong theoretical understanding of the behaviour of electroactive species in solution. Cyclic voltammograms can be simulated by calculation of the current which flows as a consequence of changing the concentrations of species at the electrode. These time dependent changes are determined by Nernstian, diffusional and chemical reactions in the diffusion layer. The equations underlying these processes can be solved analytically for the simplest of systems such as reversible electron transfer but iterative numerical simulation can be successfully applied for analysis of more complex system.<sup>58</sup>

### 1.4.3.2 Density functional theory

Density functional theory (DFT) is a computational modelling technique used to simulate the structure and properties of relatively small molecules. DFT has become an increasingly popular technique in the last 20 years as it has been shown to give useful information for a range of chemical systems, whilst being less computationally intensive than *ab initio* techniques. The key concept in density functional theory is to calculate the electron density of the simulated system rather than a series of wavefunctions. DFT can be used to predict a range of spectroscopic properties particularly those for ground state electron configurations, for example infrared and Raman data.<sup>59</sup>

Collaboration with Joseph Wright

## CHAPTER 1 | INTRODUCTION

The detailed DFT calculations were performed by Dr. Joseph Wright and involved advanced consideration of spin states associated with the [FeFe] with (thio)ureas receptors used in this study. The author used these results in the analysis of the likely structures of products and of their experimental spectra, specifically FTIR.

### 1.5 Aims and objectives

The first part of the research described in **Chapter 2** sets out to further explore a model system in which a ligand based isomerism controls the redox potentials of two interconverting couples. Specifically, a bis(cyclopentadienyl)  $\text{Mo}^{\text{V/IV}}$  system possessing a cysteinyl N,S coordinated metallocycle ring is studied and the effects of second coordination sphere interactions with a Lewis acid probed.

The aim and objectives of the second part of the research was to establish the possibility of altering the physical and chemical properties of a synthetic analogue of the diiron subsite of [FeFe] through second coordination sphere interactions of the ligated cyanide ligands. This was first explored by examining the binding of the Lewis acid  $\text{Eu}(\text{fod})_3$  to a synthetic subsite (**Chapter 3**) and secondly by probing its hydrogen-bonding interactions with certain activated ureas (**Chapter 4**).

## CHAPTER 2. INTRAMOLECULAR REDOX ISOMERISM

### 2.1 Introduction:

#### 2.1.1 Overview

This chapter sets out to describe the redox properties of a metallo-system in which an intramolecular ligand based rotational isomerism <sup>60</sup> is linked to electron transfer. Such systems can be viewed as a mechanical change in the conformation of a ligand brought about by a change in oxidation state. Whereas *cis-trans* and to a lesser extent *mer-fac* redox dependent isomerisms (that is ligand position or geometric isomerism) are well – established, those involving ligand based rotational isomerisms are rare. There are examples of changes in hapticity, for example  $\eta^2$  to  $\eta^1$  – of ligated carboxylate ligand,<sup>61</sup> and bonding isomerism involving the cyclooctatriene ligand at Co centres and S and U isomeric interconversions of  $\eta^5$  – pentadienyl Cr closed-shell complexes.<sup>62</sup> In this introduction a classical case of *cis-trans* isomerism is discussed, this is then followed by a general description of the cyclic voltammetry of systems involving interconverting redox pairs and then by a summary of the behaviour of a molybdenum system in which rotation about an amide bond is linked to redox isomerism. It is the further exploration of this system which is the focus of the research described in this chapter.

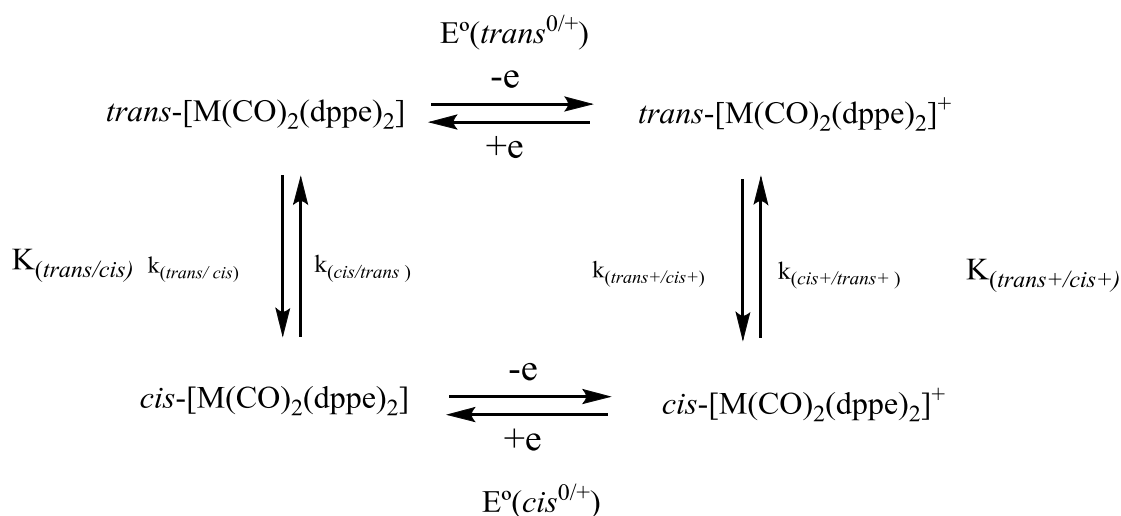
**2.1.2 Redox – linked cis-trans isomerism.**

Ligand positional isomers of coordination complexes can exhibit quite distinct redox properties. The classic example of this is the behavior of *cis* and *trans* isomers of  $[M(\text{CO})_2(\text{dppe})_2]$  where  $M = \text{Cr}, \text{Mo}$  or  $\text{W}$  and  $\text{dppe} = \text{Ph}_2\text{PCH}_2\text{CH}_2\text{PPh}_2$ . The *trans* isomer of these species undergo reversible one electron oxidation at potentials 200 to 300 mV negative of their *cis* isomer counterparts. Moreover, upon oxidation of the *cis* isomers to the mono-cations undergo rapid equilibration to give the more stable *trans* mono-cations. This redox linked isomerism also involves equilibria between the neutral and cationic species and can be represented by the ‘Square-Scheme’ shown in **Scheme 2.1**. In this scheme the four thermodynamic parameters  $E^\circ_{(\text{trans}+/0)}$ ,  $E^\circ_{(\text{cis}+/0)}$ , and the equilibrium constants  $K_{(\text{trans}/\text{cis})}$  and  $K_{(\text{trans}+/\text{cis}+)}$  are interlinked by the equation shown in **Eq 2.1**.

$$(K_{(\text{trans}/\text{cis})})/ K_{(\text{trans}+/\text{cis}+)} = \exp [ F/RT\{ E^\circ_{(\text{trans}+/0)} - E^\circ_{(\text{cis}+/0)} \}] \quad \text{Eq 2.1}$$

Cyclic voltammetry can be used to measure the  $E_{1/2}^{\text{ox}}$  potentials of the two isomers and these closely approximate to  $E^\circ$  as discussed in **Chapter 1**. This allows determination of the ratio of the equilibrium constants associated with interconversion of the oxidized and reduced species. Measurement of one of the equilibrium constants, for example  $K_{(\text{trans}/\text{cis})}$  by  $^1\text{H}$  or  $^{31}\text{P}\{^1\text{H}\}$ -nmr, taken together with the two  $E^\circ$  allows complete definition of the thermodynamics of the system. The rate constants for the forward and back interconversion of the isomeric neutral and cationic pairs can also be determined by simulation of the cyclic voltammetry at various scan-rates as also described in

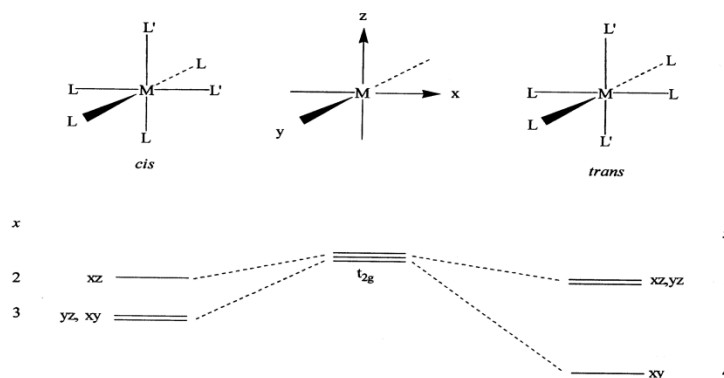
**Chapter 1.** For the *cis/trans* -  $[M(CO)_2(dppe)_2]^{0/+}$  redox systems, the 18-electron *cis* – isomer is generally much more stable than the *trans*-isomer and equilibration between the two forms is kinetically slow. However, as noted above, upon oxidation to the 17-electron *cis* cation there is a rapid isomerisation to the 17-electron *trans*-cation which then undergoes reversible reduction to the *trans*-neutral 18-electron species. The isomerization of which back to the neutral *cis* – species is slow on the cyclic voltammetry time-scale.



**Scheme 2.1.** ‘Square-scheme’ for a redox-linked isomerism of the *cis/trans* -  $[M(CO)_2(dppe)_2]^{0/+}$  system. The equilibrium (K) and standard potentials ( $E^0$ ) are related by Equation 2.1; k values are the rate-constants associated with the isomerization. Adapted from reference 63. [63](#)

An explanation for the difference in oxidation potentials of the *cis* and *trans* isomers has been discussed in simple terms of d-orbital splitting by Pombeiro and coworkers as

represented in **Scheme 2.2**. Studies of redox linked isomerism to *cis* and *trans* arrangements in closed-shell octahedral complexes and also in certain *mer* and *fac* isomers have been reviewed [63](#).

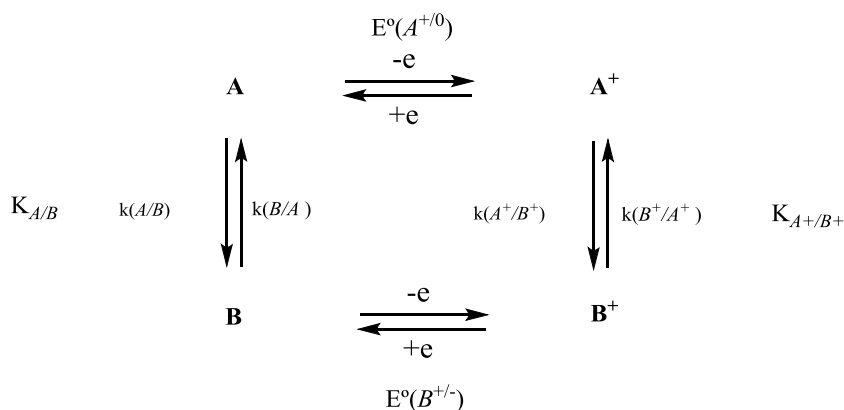


**Scheme 2.2.** Splitting of the d-orbitals for the *cis* and *trans* isomers of  $[ML_4L']_2$ . L is a better  $\pi$ -electron acceptor than  $L'$  and x is the number of the ligands that can interact with a given metal  $d_n$  orbital. [63](#)

### 2.1.3 Cyclic voltammetric characteristics of the ‘square scheme’.

The square scheme shown in **Scheme 2.1** and the relationship given by **Equation 2.1** can of course be generalized to any system involving redox linked interconversions as represented in **Scheme 2.3** where, as before, K and k are equilibrium and rate constants respectively.





**Scheme 2.3:** Generalised square-scheme representing redox linked interconverting forms.

Here it is useful to describe how such systems behave when interrogated by cyclic voltammetry by simulating the response pattern as the thermodynamic and kinetic parameters are varied. This will aid in the discussion of the experimental results described in this chapter which specifically relate to a Mo(IV) rotamer system.

To illustrate the range of cyclic voltammetric responses for the square scheme system shown in **Figure 2.1** simulations were performed for  $E^\circ(\mathbf{A}^{+/0}) = 0 \text{ V}$  versus SHE,  $E^\circ(\mathbf{B}^{+/0}) - E^\circ(\mathbf{A}^{+/0}) = 0.15 \text{ V}$  [*i.e.*  $E^\circ(\mathbf{B}^{+/0}) = 0.15 \text{ V}$ ]  $K_{A/B} = 0.1, 1.0$  and  $10$ ,  $k_{(A/B)} = 100, 0.01, 0.00001 \text{ s}^{-1}$  for a  $1 \text{ mM}$  solution of **A** before equilibration. Diffusion coefficients were all set at  $10^{-5} \text{ cm}^2 \text{ s}^{-1}$  at  $298 \text{ K}$ , the scan-rate at  $100 \text{ mV s}^{-1}$  and the electrode area at  $1 \text{ cm}^2$ . The nine panels in **Figure 2.1** show how the CV changes as the equilibrium and rate constants are adjusted.

If equilibration of the isomers is fast on the CV timescale of seconds, then the system will appear as a single reversible one-electron couple because the kinetics of

interconversion can keep up with the Nernstian equilibrium, **Figure 2.1, panels h, i, j.** If the interconversion is very slow, then the CV will show both couples  $\mathbf{A}^{+/0}$  and  $\mathbf{B}^{+/0}$ . Moreover, the peak currents will be in a ratio which corresponds to the ‘frozen’ equilibrium concentrations of **A** and **B**, **Figure 2.1 panels a, b and c.** At intermediate rates of interconversion then both the kinetics and equilibrium constants will determine the shape of the CVs, **Figure 2.1 panels d,e,f.** For example, **panel e**, shows the case where the forward peak for the  $\mathbf{A}^{+/0}$  couple is less than that for the return reduction peak because  $\mathbf{B}^+$  that is generated from **B** near 0.15V is rapidly converted to  $\mathbf{A}^+$ . This fast conversion is also apparent in the irreversibility of the  $\mathbf{B}^{+/0}$  couple, i.e the loss of the return reduction peak.

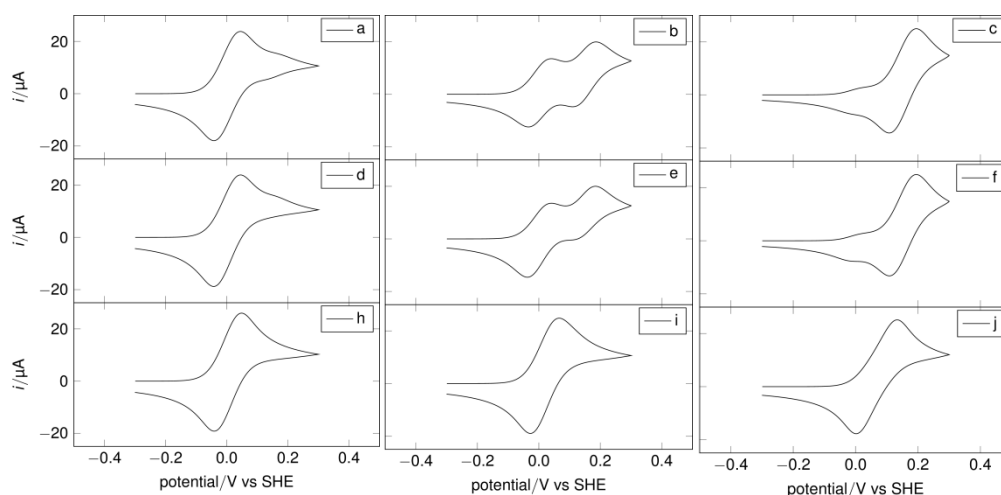


**Figure 2.1** Simulations of the CV response for a square – scheme system with interconverting redox partners  $\mathbf{A}^{+/0}$  and  $\mathbf{B}^{+/0}$ . The panels **a** to **j** show simulations at three different equilibrium constants  $K_{A/B}$  (horizontal) and three different rate constants  $k_{A/B}$  as indicated for a fixed scan-rate of  $100 \text{ mVs}^{-1}$ . These were undertaken by the author.

In a cyclic voltammetry experiment varying the scan-rate will adjust the time window in which interconversions can take place. **Figure 2.2** shows the response for the system in which  $K_{A/B} = 1.0$  and  $k_{(A/B)} = 0.01 \text{ s}^{-1}$  at scan-rates of 20, 100 and 500  $\text{mVs}^{-1}$ , **panels a, b** and **c** respectively. At the slowest scan-rate, the kinetics can keep up with the Nerstian response **Figure 2.2 panel a**. At the faster scan-rate the kinetics are ‘out run’, **Figure 2.2 panel c**.

At low temperatures the rate constants are decreased and this will have a similar effect on the voltammetry as increasing the scan-rate. Variable temperature CV also allows activation energy for the interconversions to be estimated from the temperature dependence of the rate constants.

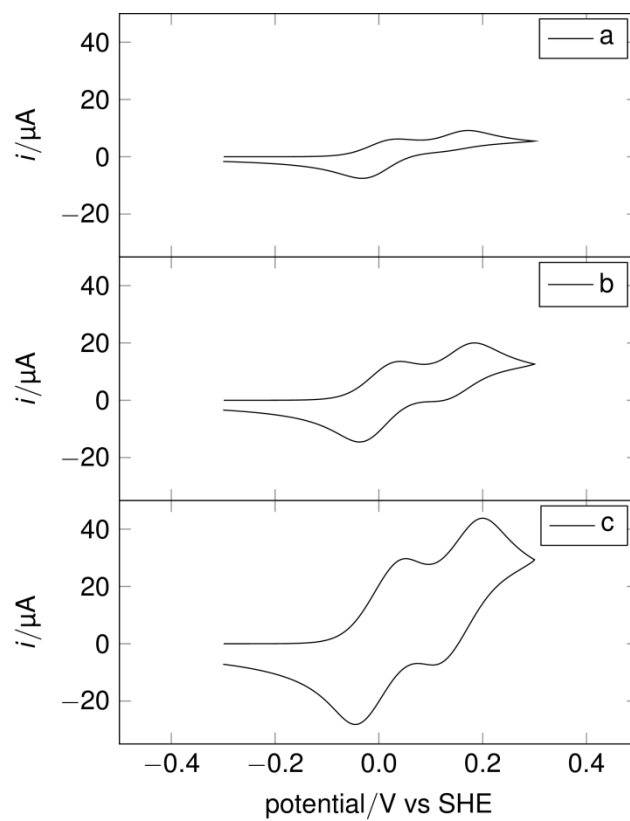


**Figure 2.2** Simulated CV response for the system in which  $K_{A/B} = 1.0$  and  $k_{(A/B)} = 0.01 \text{ s}^{-1}$  at scan-rates of (a) 20, (b) 100 and (c) 500  $\text{mVs}^{-1}$ .

### 2.1.4 A redox linked ligand rotamer system

In earlier work it was shown that the complex  $[\text{Mo}(\eta^5\text{-C}_5\text{H}_5)_2\text{Cl}_2]$  reacts with N-(3-pyrrole-1-yl)propanoyl-L-cysteine methyl ester  $\text{L}_{\text{pyrrole}}\text{NH}(\text{SH})$  in ethanol in the presence of the base triethylamine to give the metallo-cycle amide complex  $[\text{Mo}(\eta^5\text{-C}_5\text{H}_5)_2][\text{L}_{\text{pyrrole}}\text{N}(\text{S})]$ . A poor quality X-ray crystallographic structure from weak intensity measurement was nevertheless sufficient to establish the bonding connectivity in the complex as consisting of a metallocyclic ring involving the cysteinyl S and the deprotonated amide N. The amide carbonyl group was co-planar with the S, Mo, N and the the chiral carbon of the metallocycle ring with its oxygen atom deployed *trans* to the metal atom as shown in **Figure 2.3**. The unit cell showed two structural arrangements which differed only in the conformation of the  $\text{CH}_2\text{CH}_2(\text{N-pyrrole})$  group. <sup>60</sup>

$^1\text{H}$  NMR [ $\text{CD}_3\text{CN}$ ,  $\text{CD}_2\text{Cl}_2$  or  $(\text{CD}_3)_2\text{NCDO}$ ] spectroscopy of the  $[\text{Mo}(\eta^5\text{-C}_5\text{H}_5)_2][\text{L}_{\text{pyrrole}}\text{N}(\text{S})]$  showed two distinct sets of resonances in each solvent, indicative of the presence of two isomeric forms of the complex.  $^1\text{H}$  NMR ( $\text{CD}_2\text{Cl}_2$ ) exchange spectroscopy (EXSY) showed that the isomers interconvert.

Cyclic voltammetry of  $\text{Mo}(\eta^5\text{-C}_5\text{H}_5)_2[\text{L}_{\text{pyrrole}}\text{N}(\text{S})]$  in MeCN, DMF or  $\text{CH}_2\text{Cl}_2$ -0.2M  $[\text{NBu}_4][\text{BF}_4]$  at a vitreous carbon electrode also confirmed that two interconverting isomeric forms (**A** and **B**) are present, each of which undergoes reversible one-electron oxidation at distinct  $E^\circ$  potentials,  $\text{A}/\text{A}^+ = 0.58\text{V}$  and  $\text{B}/\text{B}^+ = 0.73\text{V}$ .

The activation energy calculated for the interconversion of the two crystallographic

forms was found to be  $\Delta H^*_{\text{calc}} < 5 \text{ kcal mol}^{-1}$  whereas the experimental enthalpy of activation for the conversion of **A** to **B** in the DMF electrolyte is  $\Delta H^*_{\text{exp}} = 20 \text{ kcal mol}^{-1}$ . Thus the observed activation energy is not consistent with the two forms that are observed in the crystal structure. Another explanation of the isomeric processes was therefore sought. The observed activation energy is similar to that measured for processes involving restricted rotation about C–N amide bonds. For example, dimethylformamide has a barrier for internal rotation of 19.6 kcal mol<sup>-1</sup>. Support for this type of rotation being responsible for the observed spectroscopy and electrochemistry was provided by Nuclear Overhauser effect (NOE) difference spectroscopy. (NOE) CD<sub>2</sub>Cl<sub>2</sub> showed that the irradiation of the  $\beta$  methylene protons of isomer **A** caused enhancement of the  $\gamma$ -H resonance of the chiral centre but no enhancement of the cyclopentadienyl ring proton resonances. However, (NOE) CD<sub>3</sub>CN showed irradiation of the  $\beta$  methylene protons of isomer **B** caused enhancement of the cyclopentadienyl ring proton resonances but absence of NOE enhancement of the  $\gamma$ -H resonance, **Figure 2.3** This is consistent with the oxygen atom of an amide group displaced towards or away from a neighbouring metal centre, as would be expected for **A** and **B** being the *cis* and *trans*-amide isomers, respectively.<sup>60</sup>

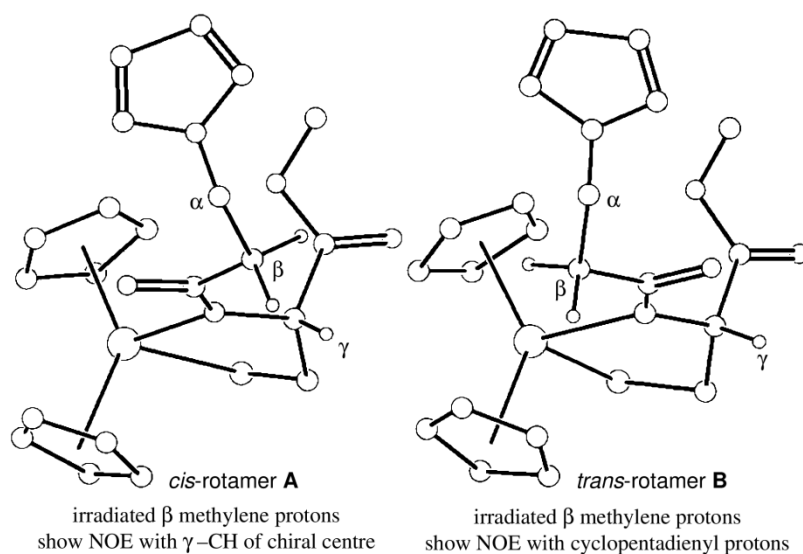


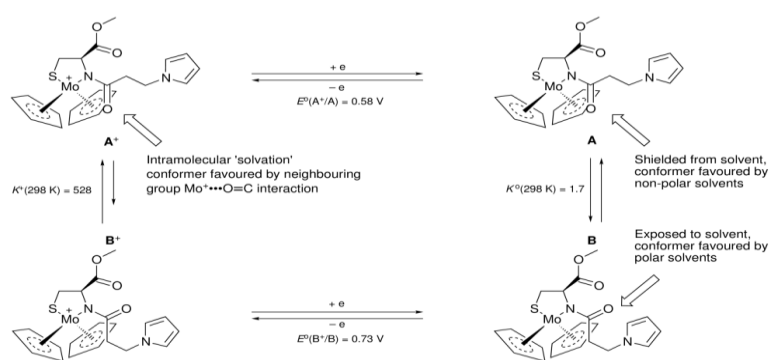
**Figure 2.3 :** Nuclear Overhauser Enhancements (NOE) observed on irradiation of  $\beta$ -methylene protons. Taken from reference 60.<sup>60</sup>

The *cis*–*trans* amide bond isomerisation provides a rationale for other properties of the system. In the *cis* conformation the oxygen atom of the carbonyl is deployed towards the molybdenum atom (A calc. Mo $\cdots$ O distance, 3.23 Å) and through space interaction could contribute towards the stabilisation of the positive charge on the oxidised metal centre. The observation that  $E^\circ$  (*cis*-rotamer **A**<sup>+</sup>/**A**) is negative of  $E^\circ$  (*trans*-rotamer **B**<sup>+</sup>/**B**) is consistent with this and the calculated Mo $\cdots$ O distance in **B** of 4.3 Å. Stabilisation of **A**<sup>+</sup> by what might be considered as intramolecular solvation by the amide oxygen explains why **A**<sup>+</sup> is the thermodynamically favoured cation.

The equilibrium constant  $K^0$  in DMF for the interconversion of **A** and **B** was determined from cyclic voltammetry to be 1.7 at 298K. Similarly, the equilibrium constant  $K^+$  for

the interconversion of **B**<sup>+</sup> to **A**<sup>+</sup> was estimated from the electrochemical data to be 528 at 298K in DMF, **Scheme 2.4**.

The equilibrium between **A** and **B** is markedly solvent dependent: in polar solvents such as MeCN or DMF the *trans*-amide rotamer **B** is the more stable species, in the less polar solvent CH<sub>2</sub>Cl<sub>2</sub> (or CHCl<sub>3</sub>) the converse is true, for example,  $K^\circ(298\text{ K}) (\text{CH}_2\text{Cl}_2) = 0.5$  for the conversion of **A** to **B**. In the *trans* configuration, the amide oxygen of **B** is exposed on the surface of the molecule whereas in the *cis* configuration of **A** it is shielded by the cyclopentadienyl rings. Thus polar interactions of the amide carbonyl group presumably stabilise **B** with respect to **A**. Consistent with this, IR spectroscopy in MeCN shows two distinct amide CO bands with that for the major isomer **B** at a significantly lower energy, 1562 cm<sup>-1</sup>, than that for **A**, 1582 cm<sup>-1</sup>. Polar interactions with the carbonyl oxygen are expected to weaken the CO bond and decrease  $\nu(\text{CO})$ .<sup>60</sup> The overall interpretation of this reported rotamer system is summarised in by **Scheme 2.4** which is adapted from reference 60.



**Scheme 2.4** Redox linked amide rotamer system for a Mo(V/IV) couple taken from reference 60. Equilibrium constants are those determined in DMF. <sup>60</sup>

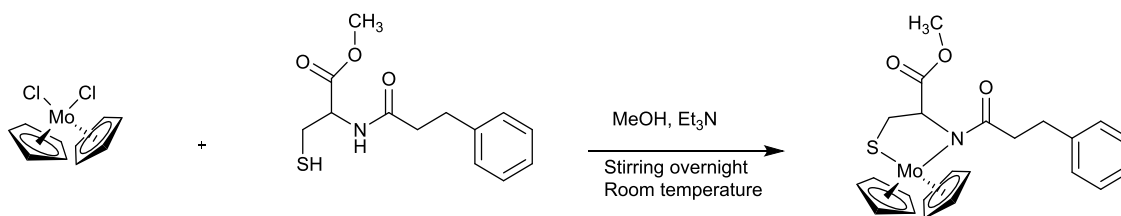


The experimental work described below sets out to examine a related isomer system in which the N-pyrrole substituent group is formally replaced by phenyl group. This has allowed collection of higher quality X-ray crystallographic data and has allowed the examination of second coordination sphere interactions uncomplicated by the presence of the pyrrole group. The factors which govern the thermodynamics and kinetics of these systems are perhaps of some interest in the context of a molecular machine in which a redox process induces a ‘second-coordination’ conformational switch of a ligand rather than of the inner-sphere geometric rearrangement of ligands.

## 2.2 Result and discussion

### 2.2.1 Synthesis and characterisation of bis(cyclopentadienyl)molybdenum(IV)-N-(3-phenylpropyl)-L-cysteine methyl ester (Complex1)

This complex was prepared by treatment of a methanol solution of  $\text{MoCp}_2\text{Cl}_2$  with one equivalent of N-phenylpropyl-L-cysteine methyl ester as the hydrochloride salt with excess of triethylamine at room temperature, **Scheme 2.5** (see Experimental Section).



**Scheme 2.5.** Synthesis of **Complex 1**.

Orange-red crystals suitable for an X-ray structure determination were obtained and this was undertaken by the National Crystallographic Service, Southampton. The structure was modelled as two distinct isomeric forms of approximately equal occupancy; these two forms differed in the conformation of the metallo-cyclic ring. Thus the ester group and alkyl chain linking this to the sulfur are disordered over two positions, neither of these features an interaction with the metal centre. The R-factor was 0.060.

The two conformers are shown by the crystallographic structures in **Figure 2.4**. In this figure, the views (a) and (b) show the two flipped configurations of the metallo-cyclic ring and the views (c) and (d) show the essential co-planarity of the amide group with the C2, N1, Mo1 and S1 for both structures. The selected bond distances and angles about the metal centre are summarised in **Table 2.1**. The C1A – S1 and C1-S bond distances are 1.808(12) and 1.854(13) but the difference is not statistically significant at the accepted two standard deviations ( $2\sigma$ ) level.

In a study of the reactions of  $[\text{Mo}(\eta^5\text{-C}_5\text{H}_5)_2(\text{H}_2\text{O})_2]^+$  with cysteinyl peptides and the ability of this type of moiety to promote amide hydrolysis, Erxleben <sup>64</sup> reported a similar type of metallo-cycle structure. The X-ray crystallographic structure of this species is shown in **Figure 2.5** together with selected bond lengths and angles, these are quite similar to those of **Complex 1** given in **Table 2.1**.

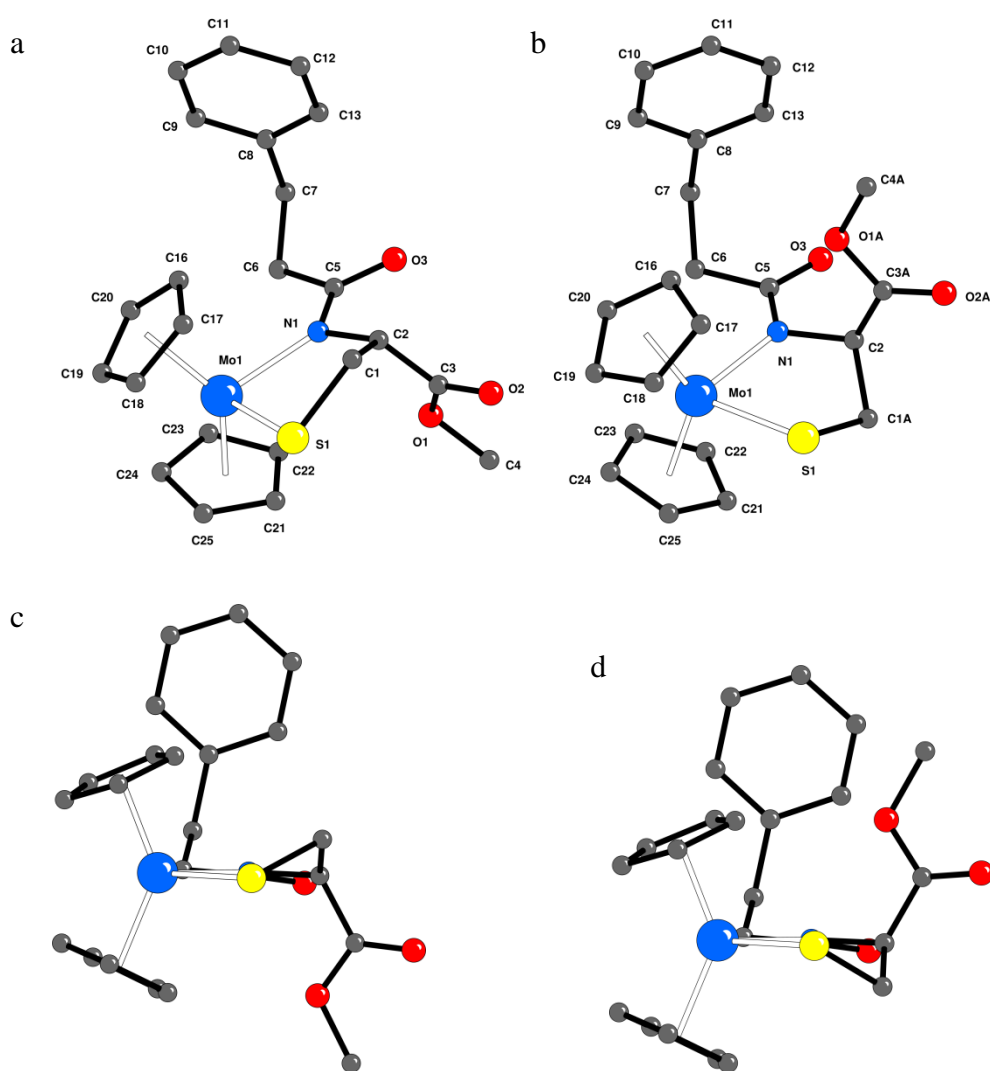


**Figure 2.4.** X-ray structure of bis(cyclopentadienyl)molybdenum(IV)-N-(3-phenylpropanoyl)-L-cysteine methyl ester showing spheres of arbitrary size; hydrogen atoms have been omitted for clarity. The views (a) and (b) show the inversion at the optical centre C2 in which the C1 carbon is flipped up towards the C16-C20 cyclopentadienyl ring or C1A down relative to this ring. The views (c) and (d) show the essential co-planarity of C2,N1,Mo1 and S1 in both conformers.

Mo(1)–N(1)	2.188(5)
Mo(1)–S(1)	2.4337(15)
C(1)–S(1)	1.854(13)
C(1A)–S(1)	1.808(12)
C(2)–N(1)	1.478(8)
C(1)–C(2)	1.522(14)
N(1)–Mo(1)–S(1)	79.58(13)
C(18)–Mo(1)–C(23)	128.4(2)

**Table 2.1** Selected bond lengths (Å) and angles (deg) for **Complex 1**.

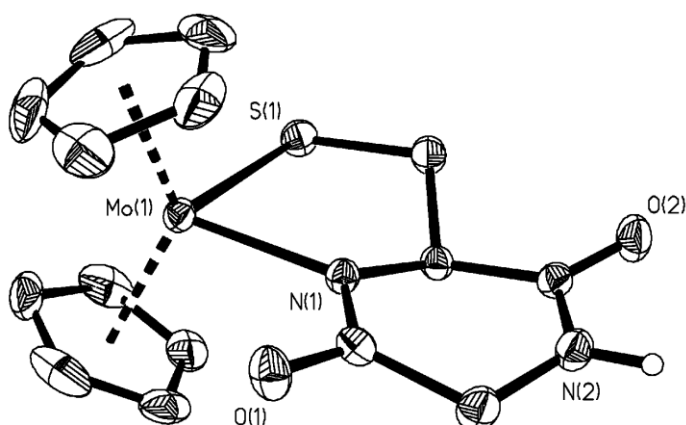


**Figure 2.5.** X-ray structure of  $[(\eta^5\text{-C}_5\text{H}_5)_2\text{Mo}\{\text{cyclo-(Gly-Cys)}\}]. 2\text{H}_2\text{O}$ . Selected bond lengths ( $\text{\AA}$ ) and angles (deg) : Mo1-N1 2.178(3) ; Mo1-S1 2.455(1) ; N1-Mo1-S1 79.82(9). Taken from reference 64. [64](#)

### 2.2.2 Spectroscopic properties of Complex 1.

**Infra-red spectroscopy.** Solution infra-red spectroscopy of **Complex 1** in MeCN shows two distinct amide I (CO) bands at  $1582\text{cm}^{-1}$  and  $1574\text{cm}^{-1}$  which are similar to those reported for the pyrrole analogue  $\text{Mo}(\eta^5\text{-C}_5\text{H}_5)_2[\text{L}_{\text{pyrroleN(S)}}]$ . In this case two amide I bands were observed at  $1582\text{cm}^{-1}$  and  $1562\text{cm}^{-1}$  and which were assigned to *cis*- and *trans*- amide isomers respectively. **Complex 1** also shows two distinct bands for the ester group at  $1743\text{cm}^{-1}$  and  $1728\text{cm}^{-1}$ . The *cis* or *trans* orientation of the amide group away or towards the metal centre presumably has an electronic effect on the ester and affects the frequencies of the CO stretch.

***<sup>1</sup>H-nmr spectroscopy.*** The <sup>1</sup>H-nmr spectrum of **Complex 1** in CD<sub>2</sub>Cl<sub>2</sub> (298K) is shown in **Figure 2.6** and clearly shows the presence of two isomeric forms. This is most apparent from the two sets of resonances for the two types of cyclopentadienyl ring and the presence of two distinct Me resonances of the ester group. The <sup>1</sup>H-nmr spectrum of **Complex 1** in CD<sub>3</sub>CN (298K) is similar except that the ratio of the two sets of cyclopentadienyl resonances and correspondingly the two Me resonances are significantly different and this represents a major influence of the solvent on the position of the equilibrium, **Figure 2.7**. Thus values of the equilibrium constant K<sub>1</sub> at 298K for the interconversion of the **A<sub>1</sub>** and **B<sub>1</sub>** as represented in **Scheme 2.6** were 1.28 in MeCN and 0.22 in CH<sub>2</sub>Cl<sub>2</sub> indicative of **B<sub>1</sub>** being more stable in the more polar solvent. The corresponding estimation of ΔG° the free energy difference between the isomeric forms **A<sub>1</sub>** / **B<sub>1</sub>** as in the two solvents calculated from the equilibrium constants is summarised in **Table 2.2**. The free energy differences are small, all are less the 5 kcal mole<sup>-1</sup>.

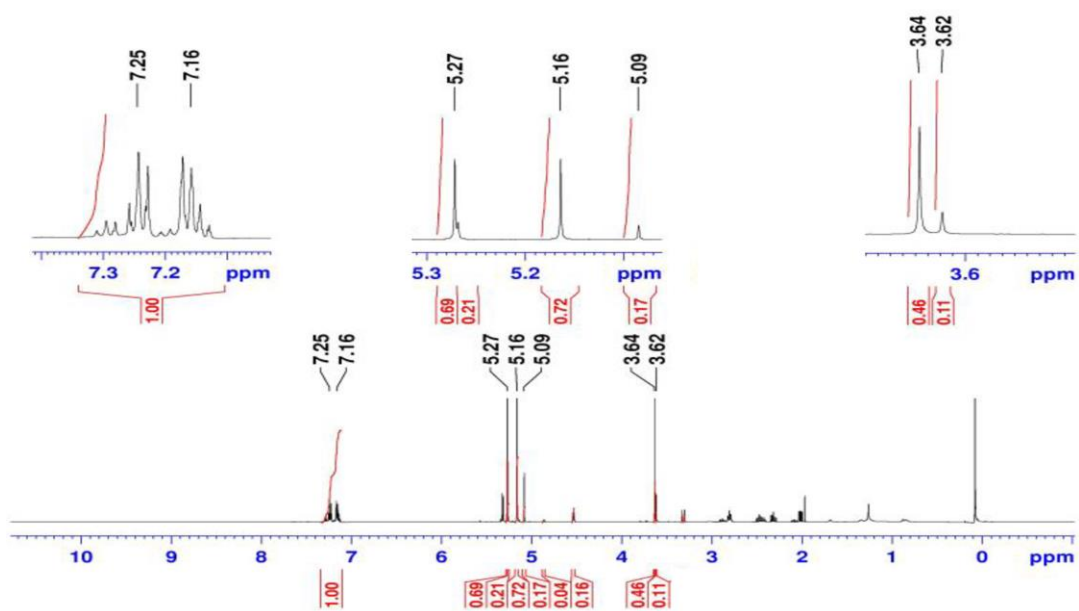


**Figure 2.6.**  $^1\text{H}$  NMR of **Complex 1** in  $\text{CD}_2\text{Cl}_2$ . The regions of the phenyl, cyclopentadienyl and methyl resonances are expanded.

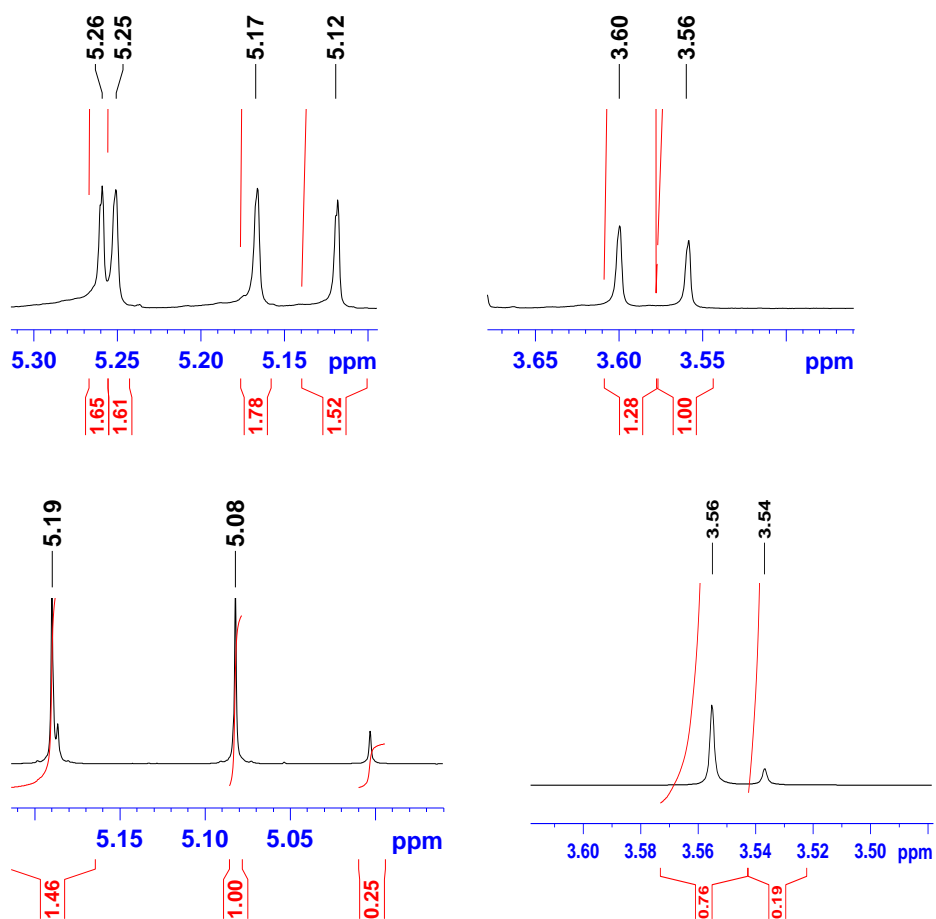
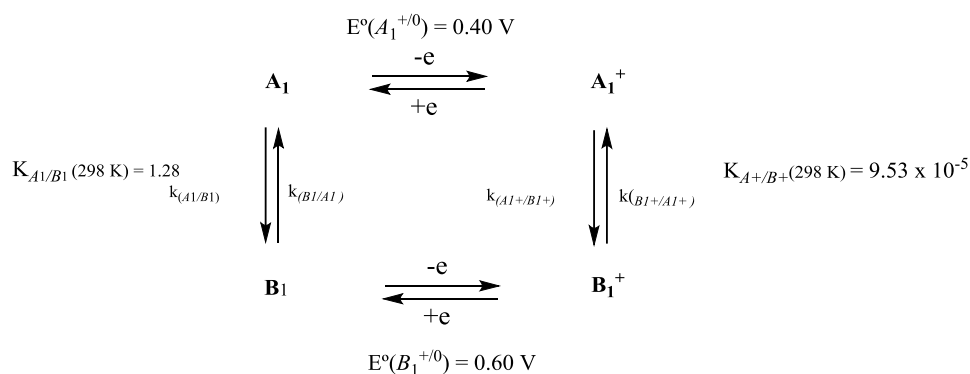


**Figure 2.7.**  $^1\text{H}$  NMR spectrum of the  $\text{CH}_3$  and  $\text{Cp}$  resonances of **Complex 1** in  $\text{CD}_3\text{CN}$  at 298K (above) and similarly in  $\text{CD}_2\text{Cl}_2$  (below) showing the different isomer distribution in the two solvents.





**Scheme 2.6** Square-scheme representing interconverting forms of  $A_1/A_1^+$  and  $B_1/B_1^+$  for complex **1**.

		MeCN	CH <sub>2</sub> Cl <sub>2</sub>
<b>Neutral A<sub>1</sub>/B<sub>1</sub> system</b> <b>298K</b>	$K_{A_1/B_1}$	1.28	0.22
	$\Delta G^\circ_{A_1/B_1}$ (kcal/ mol <sup>-1</sup> )	-0.15	+0.90
	$k_{A_1/B_1}$	0.9	0.8
<b>Cationic A<sub>1</sub><sup>+</sup>/B<sub>1</sub><sup>+</sup> system</b> <b>298K</b>	$K_{A_1^+/B_1^+}$	$9.53 \times 10^{-5}$	$1.34 \times 10^{-5}$
	$\Delta G^\circ_{A_1^+/B_1^+}$ (kcal/ mol <sup>-1</sup> )	+ 2.667	+1.26
	$k_{A_1^+/B_1^+}$	0.009	0.1

**Table 2.2.** The corresponding estimation of  $\Delta G^\circ$  free energy difference between the isomeric forms  $A_1 / B_1$  in MeCN and CH<sub>2</sub>Cl<sub>2</sub>.

The temperature dependence of  $K_1$  was also measured by  $^1\text{H}$  NMR in MeCN and the Van't Hoff plot is shown in **Figure 2.8**. From this plot  $\Delta H_1^\circ$  for the conversion **A**<sub>1</sub> / **B**<sub>1</sub> was estimated from the slope to be  $0.9 \pm 0.2$  kcal mole<sup>-1</sup> and  $\Delta S_1^\circ = 3.4 \pm 0.5$  cal mole<sup>-1</sup> K<sup>-1</sup>.  $^1\text{H}$  NMR measurements were complicated at the higher temperatures by some decomposition of the parent material. The small positive (endothermic)  $\Delta H_1^\circ$  value indicates the conversion of **A**<sub>1</sub> to **B**<sub>1</sub> is close to being thermally neutral, the positive  $\Delta S_1^\circ$  value suggests entropy marginally favours the formation of **B**<sub>1</sub> ( $T\Delta S_1^\circ$  ca 1 kcal at 298K) but the extrapolation error is large.

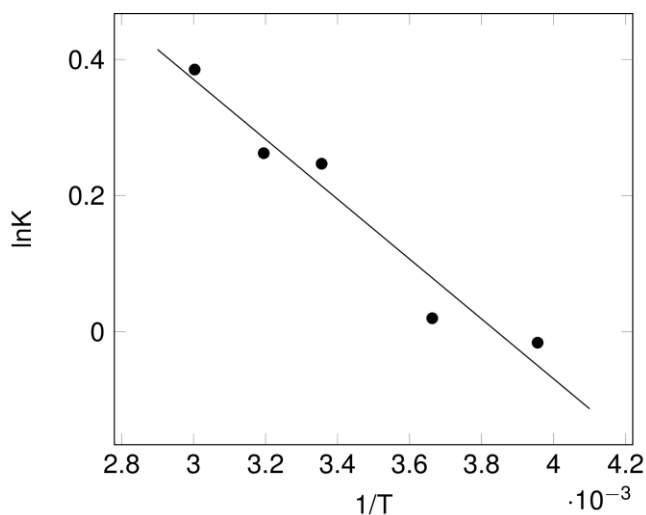


**Figure 2.8.** Van 't Hoff plot for interconversion of the isomers in  $\text{CD}_3\text{CN}$ . Correlation coefficient,  $R = 0.94$ .

### 2.2.3 Electrochemistry of Complex 1

#### *Cyclic voltammetric of the behavior of the A<sub>1</sub> / B<sub>1</sub> system at low and high temperature.*

The overall behavior of **Complex 1** in the MeCN-0.2M [NBu<sub>4</sub>][BF<sub>4</sub>] electrolyte at 241 and 323K was examined at a scan-rate of 50mVs<sup>-1</sup>. **Figure 2.9** shows the voltammetric plot for these two temperatures but with the current-scale normalized by division by the square route of the diffusion-coefficient at the two different temperatures, D<sup>1/2</sup><sub>241K</sub> and D<sup>1/2</sup><sub>323K</sub>. The plot of  $i_p / D^{1/2}$  conveniently shows the temperature behavior of the voltammetry on comparable scales. It is generally very reasonable to assume that the diffusion coefficients for all the reduced and oxidised species in a coordination complex are closely similar and show the same dependence on temperature.<sup>65, 66</sup> The two global values for the D<sup>1/2</sup><sub>241K</sub> and D<sup>1/2</sup><sub>323K</sub> were estimated by simulation.<sup>67</sup> **Figure 2.9** dramatically shows the extremes of the behaviour of the system as the kinetics interconversion of the redox partners in the square scheme are altered. At the low temperature 241K the equilibrium concentration of **A<sub>1</sub>/B<sub>1</sub>** and **A<sup>+</sup><sub>1</sub>/B<sup>+</sup><sub>1</sub>** are essentially frozen with no interconversion and two distinct reversible couples are observed. At 323K the interconversion of **A<sub>1</sub>** and **B<sub>1</sub>** is fast and can keep up with the Nernstian equilibrium at the electrode, thus the behavior approaches that of a single reversible one-electron system. This has been exemplified by the simulations shown in the introduction to this Chapter, **Figure 2.1** which illustrated the effect of changing the rate constants.

On the cyclic voltammetry time-scale the cations  $\mathbf{A}^{+1}$  and  $\mathbf{B}^{+1}$  are moderately stable at low temperature but on a preparative electrolysis time-scale these species are unstable, precluding isolation. A minor pathway has been modelled into the voltammetry above 298K to account for the decay of  $\mathbf{B}^{+1}$  as also observed for the  $\mathbf{B}^{+}$  system.

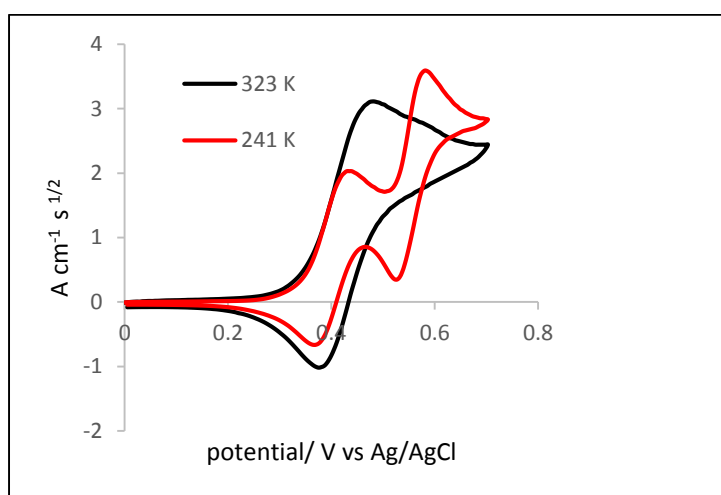


**Figure 2.9** The voltammetric plot for **complex 1** at two temperatures, 323 K and 241 K, with the current-scale normalized by  $D^{1/2}$ .

*The effect of scan-rate dependence on the cyclic voltammetric of the behavior of the  $\mathbf{A}_1 / \mathbf{B}_1$  system at 293K.*

The experimental scan-rate dependence of the cyclic voltammetry **Complex 1** in the methyl cyanide electrolyte at a vitreous carbon electrode at 293K is shown by the overlaid voltammograms **Figure 2.10(a)** for potential scan-rates ranging from 10 - 300mVs<sup>-1</sup>. It can be seen that at the slowest scan-rate, which provides the greatest time-

window for interconversion of  $\mathbf{A}_1$  /  $\mathbf{B}_1$  the primary  $\mathbf{A}_1^+$  /  $\mathbf{A}_1$  couple dominates the response. At the fastest scan-rate the current associated with the  $\mathbf{B}_1^+$  /  $\mathbf{B}_1$  is greatly enhanced. Importantly the peak current associated with the reduction of  $\mathbf{A}_1^+$  generated in part from the fast isomerization of  $\mathbf{B}_1^+$  is greater than the peak current for the oxidation of  $\mathbf{A}_1$ , that is  $i_p^{\text{ox}}_{\mathbf{A}} < i_p^{\text{red}}_{\mathbf{A}^+}$ . The overall scan-rate behavior is fully consistent with interconverting redox pairs as discussed in the introduction to this chapter and illustrated by **Figure 2.2**. Compellingly, the set of experimental cyclic voltammograms can be closely simulated using the measured values for the redox couples  $E^{\circ}_{\mathbf{A}_1^+ / \mathbf{A}_1}$  and  $E^{\circ}_{\mathbf{B}_1^+ / \mathbf{B}_1}$  and  $K_{\mathbf{A}_1 / \mathbf{B}_1}$  determined by  $^1\text{H-nmr}$  in MeCN as shown in **Figure 2.10(b)**.

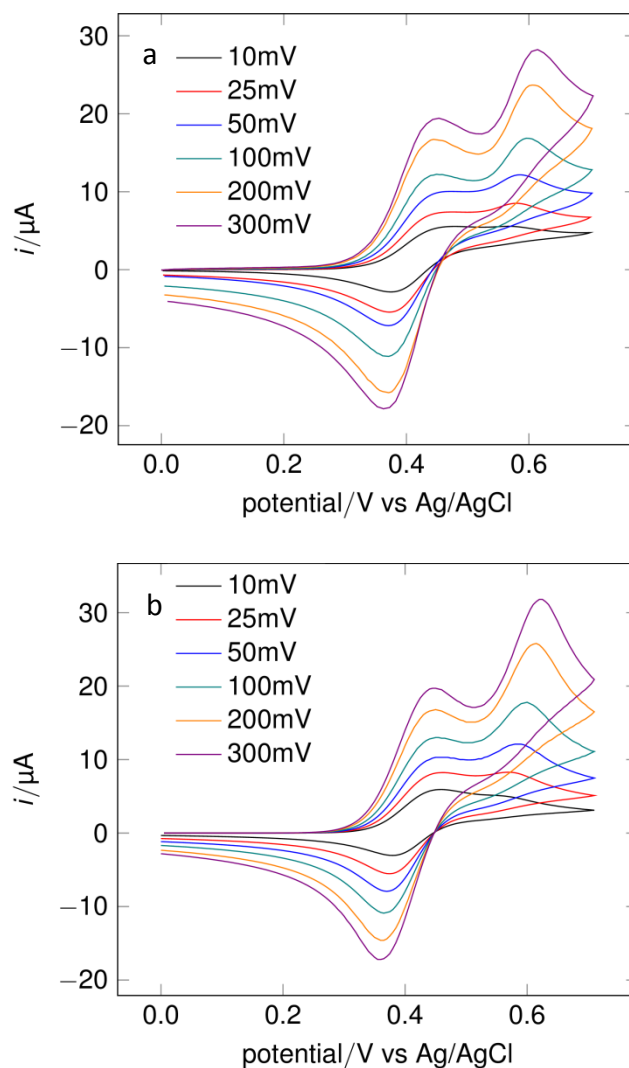


**Figure 2.10 (a)** Experimental cyclic voltammetry of **Complex 1** 0.9 mM in 0.2M  $[\text{Bu}_4\text{N}][\text{BF}_4]$  - MeCN at various scan-rates at 293K temperature. **(b)** simulation.

The quality of the fit of simulated and experimental data is shown by the overlay in **Figure 2.11** for the scan-rate  $100\text{mVs}^{-1}$ . The forward rate constant at 293K for the conversion of **A<sub>1</sub>** to **B<sub>1</sub>** used in the simulation was  $0.9\text{ s}^{-1}$ , that for the conversion of **B<sub>1</sub><sup>+</sup>** to **A<sub>1</sub><sup>+</sup>** was  $94.4\text{ s}^{-1}$  with the associated equilibrium constant  $K_{\text{B}_1^+/\text{A}_1^+} = 1.05 \times 10^4$ . Thus we have a greater stability of the **A<sup>+</sup>** isomer over the **B<sup>+</sup>** with  $\Delta G_{293\text{K}}^0 \text{ ca} - 5.4$

kcal mole<sup>-1</sup> and a fast conversion of the latter cation to the former. **Scheme 2.6** summarises the thermodynamic and rate constant data in the square-scheme for the system at 293K determined from the simulation. All parameters used in the simulation are given in **Table 2.3** and equilibrium, rate, thermodynamic and activation energy data for these measurements at 293K **Table 2.2**.

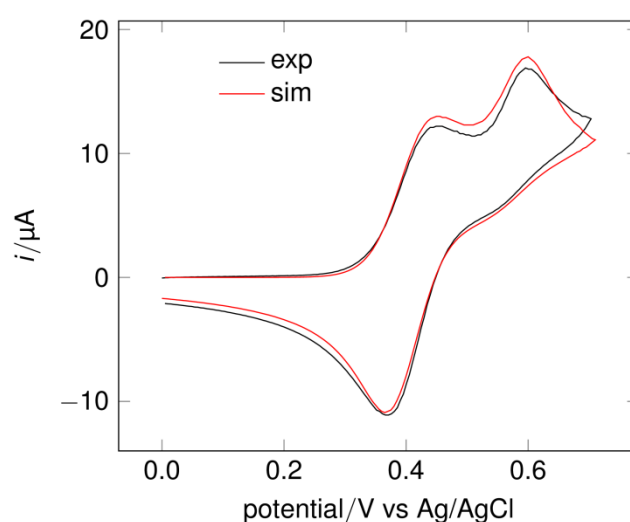


**Figure 2.11** Cyclic voltammetry of **Complex 1** 0.9 mM in 0.2M [Bu<sub>4</sub>N][BF<sub>4</sub>] - MeCN at 100mV s<sup>-1</sup> at 293K temperatures

		$A_1/B_1$			$A_1^+/B_1^+$			
T (K)	$K_{eq}$	$k_f$	$k_b$	$k_f^+$	$k_b^+$	$K_{eq}^+$	Diffusion coefficient, $D / \text{cm}^2\text{s}^{-1}$	
323	1.38	11	7.97	0.03	120.76	$2.48 \times 10^{-4}$	$4.8 \times 10^{-5}$	
298	1.28	0.9	0.703	0.009	94.43	$9.53 \times 10^{-5}$	$2 \times 10^{-5}$	
273	1.02	0.05	0.049	0.0007	7.903	$8.86 \times 10^{-5}$	$1.2 \times 10^{-5}$	
Experimental condition:  Scan rate = $50 \text{ mV s}^{-1}$ ,  Electrode area= $0.0707 \text{ cm}^2$ ,  Complex 1 = $0.9 \text{ mM}$  in $0.2 \text{ M } [\text{Bu}_4\text{N}][\text{BF}_4] - \text{MeCN}$ .				Simulation :  Heterogeneous electron transfer $1000 \text{ cm/s}$  $E^\circ (A^+/A) = 0.40 \text{ V}$ , $E^\circ (B^+/B) = 0.60 \text{ V}$ .  $R_u = 500 \Omega$				

**Table 2.3** Parameters used for simulation of the variable temperature cyclic voltammetry of **complex 1** in MeCN.



*Determination of activation energy parameters from the temperature dependence of the cyclic voltammetric response.*

The temperature dependence of the cyclic voltammetric response for **Complex 1** in MeCN and CH<sub>2</sub>Cl<sub>2</sub> was measured. **Figure 2.12** shows a set of four voltammograms recorded between 197K and 293K in CH<sub>2</sub>Cl<sub>2</sub> – 0.2M [NBu<sub>4</sub>][BF<sub>4</sub>] at a vitreous carbon electrode together with the simulated voltammograms. The kinetic parameters used to fit the experimental data allowed the estimation of activation energy parameters. **Figure 2.13** and **2.14** shows the Eyring plot from which the activation enthalpies  $\Delta H^*_{A_1/B_1}$  and  $\Delta H^*_{A_1^+/B_1^+}$  were calculated for the **A<sub>1</sub>/B<sub>1</sub>** and **A<sup>+</sup><sub>1</sub>/B<sup>+</sup><sub>1</sub>** isomerisations together with the corresponding entropy of activation data. These activation energy parameters are summarised in **Table 2.4**.

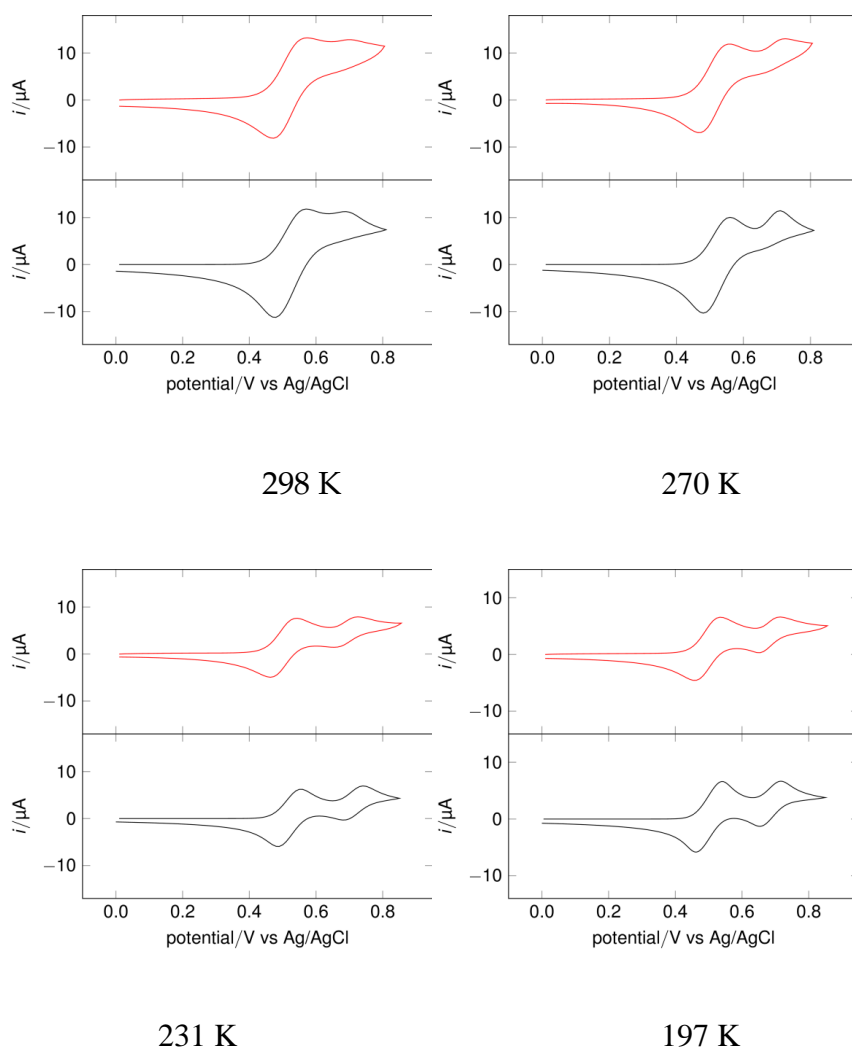


**Figure 2.12** . Experimental (red) and simulated (black) CVs of 1.6 mM **Complex1** in 0.2M [Bu<sub>4</sub>N][BF<sub>4</sub>] CH<sub>2</sub>Cl<sub>2</sub> at various temperature.

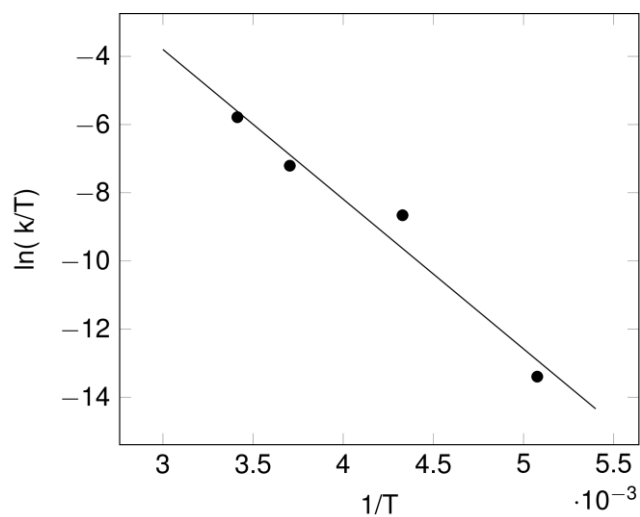


**Figure 2.13** Eyring plot for conversion of  $\mathbf{A}_1$  to  $\mathbf{B}_1$  in  $\text{CH}_2\text{Cl}_2$ . The rate constant  $k$  is that for the forward reaction  $\mathbf{A}_1 \rightarrow \mathbf{B}_1$ . Correlation coefficient,  $R^2 = 0.96$ .

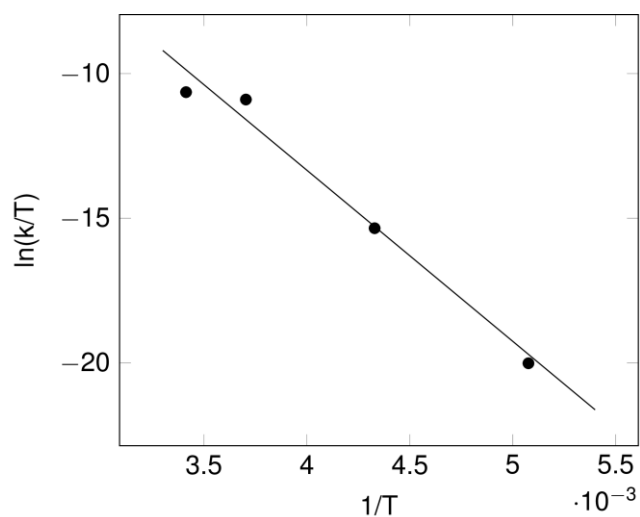


**Figure 2.14** Eyring plot for conversion of  $\mathbf{A}_1^+$  to  $\mathbf{B}_1^+$  in  $\text{CH}_2\text{Cl}_2$ . The rate constant  $k$  is that for the forward reaction  $\mathbf{A}_1^+ \rightarrow \mathbf{B}_1^+$ . Correlation coefficient,  $R^2 = 0.98$ .

	<b>A<sub>1</sub> to B<sub>1</sub></b>		<b>A<sub>1</sub><sup>+</sup>to B<sub>1</sub><sup>+</sup></b>	
Solvent	$\Delta H^*$ (kcal/mol)	$\Delta S^*$ ((cal /mol K)	$\Delta H^*$ (kcal/mol)	$\Delta S^*$ (cal /mol K)
CH <sub>2</sub> Cl <sub>2</sub>	8.7 ± 2.5	-29 ± 14	12 ± 2	-3.2 ± 1
MeCN	18 ± 4	2.0 ± 0.5	12 ± 5	-26 ± 10

**Table 2.4.** The thermodynamic parameters of **Complex 1** from electrochemistry experiments in CH<sub>2</sub>Cl<sub>2</sub> and MeCN.

Similarly, the temperature dependence of the cyclic voltammetry was examined in MeCN – 0.2M [NBu<sub>4</sub>][BF<sub>4</sub>] at three temperatures and the kinetic data determined by simulation. **Figure 2.15** shows the set of voltammograms together with the simulated data and **Table 2.4** also summarises the activation energy parameters determined in this way in MeCN.

The activation enthalpy in MeCN for the conversion **A<sub>1</sub> to B<sub>1</sub>** is greater than in CH<sub>2</sub>Cl<sub>2</sub> which is consistent with the contribution of solvation to the enthalpy of activation being more important in MeCN. For the **A<sub>1</sub><sup>+</sup>to B<sub>1</sub><sup>+</sup>** conversion the enthalpies of activation are similar and this may be explained by dipolar interactions between Mo<sup>+</sup> and ligand (amide) groups being balanced by solvation energy changes being to a smaller extent in CH<sub>2</sub>Cl<sub>2</sub>. The entropies of activation suggest a greater ordering of solvent molecules for the conversion **A<sub>1</sub> to B<sub>1</sub>** in CH<sub>2</sub>Cl<sub>2</sub> than in MeCN and the converse for the **A<sub>1</sub><sup>+</sup>to B<sub>1</sub><sup>+</sup>**

conversion. This is perhaps surprising in the context of the proposed *cis*-amide and *trans*-amide conformations where in the latter case the solvent ordering might be expected to be more important. However, some caution is needed in the interpretation of the entropy of activation data because extrapolation to  $1/T = 0$  has a wide error.

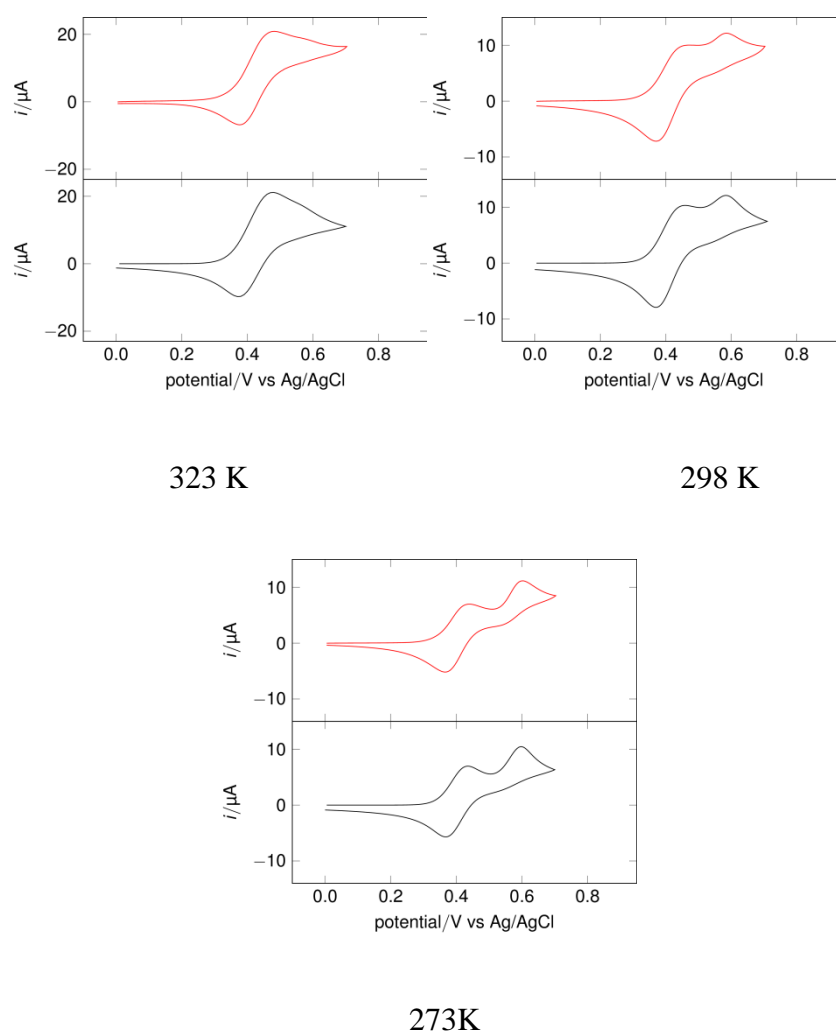


**Figure 2.15** . Experimental (red) and simulated (black) CVs of 0.9mM **Complex1** in 0.2M  $[\text{Bu}_4\text{N}][\text{BF}_4]$  MeCN at various temperature.

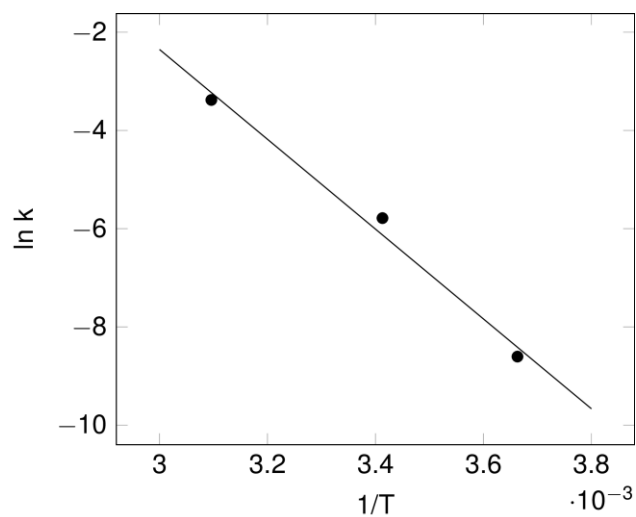


**Figure 2.16.** Eyring plot for conversion of **A<sub>1</sub>** to **B<sub>1</sub>** in MeCN. The rate constant  $k$  is that for the forward reaction **A<sub>1</sub>** → **B<sub>1</sub>**. Correlation coefficient,  $R^2 = 0.98$

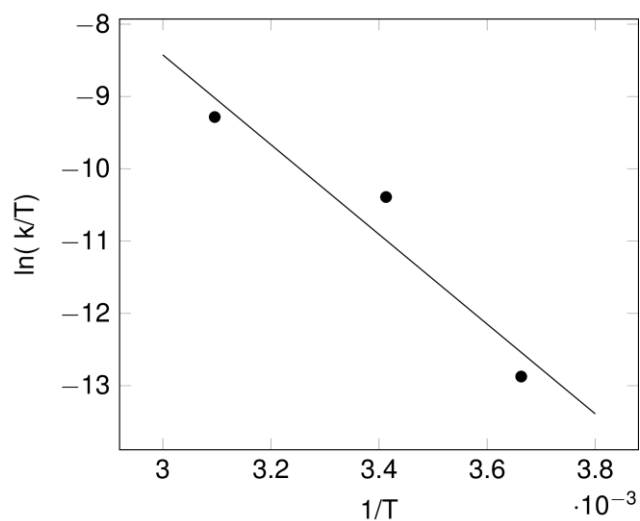


**Figure 2.17.** Eyring plot for conversion of **A<sub>1</sub><sup>+</sup>** to **B<sub>1</sub><sup>+</sup>** in MeCN. The rate constant  $k$  is that for the forward reaction **A<sub>1</sub><sup>+</sup>** → **B<sub>1</sub><sup>+</sup>**. Correlation coefficient,  $R^2 = 0.92$ .

#### 2.2.4 Comparison of thermodynamic and kinetic parameters of isomerism with related systems.

##### *General overview.*

The spectroscopic and electrochemical data described in **sections 2.2.1** and **2.2.2** above from which thermodynamic and kinetic data were determined are entirely consistent with a square scheme involving interconversion of isomeric pairs as shown in **Scheme 2.6** irrespective of the molecular nature of chemical rearrangements involved. The interpretation of data for the pyrrole system **A/A<sup>+</sup>** and **B/B<sup>+</sup>** in the earlier work, in particular the NOE information strongly supported an isomerization involving rotamers with the *cis-trans* deployment of the amide group in the metallo-cycle ring explaining the observed spectroscopic and electrochemical data. In this section the data obtained for the pyrrole system is compared with that obtained for **A<sub>1</sub>/A<sub>1</sub><sup>+</sup>** and **B<sub>1</sub>/B<sub>1</sub><sup>+</sup>** summarised in **Table 2.2**.

##### *The cis/trans amide isomerism model.*

In simple primary amides the *trans*-form is significantly favoured over the *cis*-form and this is a dominant feature of secondary structure in peptide chemistry. However, for secondary amides *ie* with two substituents on the N –atom, steric repulsion between the groups attached to the C and to the N are similar in *cis* or *trans*-configurations and differences in steric repulsion are less important in stabilization of one form over the other. Thus the relatively small values of  $\Delta H$  observed for both the **A/B** , and **A<sub>1</sub> / B<sub>1</sub>** systems accords with the behavior of secondary amides in which the energy differences

are small with equilibrium constants at 298K small (0.2 – 2.0). The effect of solvent on the equilibrium parameters in the **A/B**, and **A<sub>1</sub>/B<sub>1</sub>** systems is similar. In both cases in CH<sub>2</sub>Cl<sub>2</sub> the **A** or **A<sub>1</sub>** isomer is favoured whereas in the more polar solvent MeCN the opposite is true. This was explained by the C=O amide group ‘facing’ outward towards the solvent in the *trans*-configuration favouring stronger dipolar interactions with the more polar MeCN solvent. The consequence of changing the pyrrole group for phenyl on the ester side chain as might be expected is small. Thus the equilibrium constant  $K_{A_1/B_1}$  (298K) is 0.7 in 0.2M [Bu<sub>4</sub>N][BF<sub>4</sub>]- CH<sub>2</sub>Cl<sub>2</sub> and that for  $K_{A/B}$  in the same solvent system is 0.50.

In simple amides the enthalpies of activation for interconversion of *cis*- and *trans*-isomers are significant and in the order of 20 kcal mole<sup>-1</sup>. For example, the activation enthalpy for rotation about the C-N bond in dimethyl formamide is 19.6 kcal mole<sup>-1</sup> which is close to that measured for both the **A<sub>1</sub>/B<sub>1</sub>** system (18.7 kcal mole<sup>-1</sup> in MeCN) and for the **A/B** system ( 20.1 kcal mole<sup>-1</sup> in DMF).<sup>60</sup> The activation enthalpy estimated for the **A<sub>1</sub><sup>+</sup>/B<sub>1</sub><sup>+</sup>** interconversion in MeCN is of the same order, 12.3 kcal mole<sup>-1</sup>.

In summary, the thermodynamic data for the **A<sub>1</sub>/B<sub>1</sub>** and the **A/B** and their cationic partners is very similar and consistent with the *cis-trans* rotamer interconversion. However, given the crystallographic data which shows two conformations of **Complex 1** in which the CH<sub>2</sub> group in the metallo-cyclic ring is ‘flipped’ up or down relative to the position of the CH<sub>2</sub>CH<sub>2</sub>Ph with the ester group deployed down or up, the thermodynamic and redox consequences of this need to be considered as a possible explanation for square-scheme redox isomerism.



The arguments against these conformers determining the redox isomerism is as follows. In solution free rotation about the carbons of the  $\text{CH}_2\text{CH}_2\text{Ph}$  would be enabled and thus the geometric distinction of the conformers as observed in the solid state would be lost. Even in the unlikely event there was an activation energy barrier to this, the deployment of the other functionality with respect to the redox active Mo centre is essentially the same in the two conformers and cannot explain the considerable difference in redox potential nor the stabilization of the  $\mathbf{A}^+$  and  $\mathbf{A}_1^+$  isomeric forms. In particular, inversion of the sulfur lone pairs in the metallocycle does not change their relative position with respect to the Mo centre which might otherwise induce an electronic discrimination. There is an example of conformeric inversion of sulfur atoms in a tetrathioether macrocyclic ring which does lead to observation of a square scheme redox isomerism at low temperature. However, in this case there is a marked change of the position of the Mo(III)/Mo(II) centre relative to the plane of the sulfur atoms. This system is shown in **Figure 2.18**.<sup>68</sup>

Further experiments showing certain second coordination sphere interactions can switch the position of the isomer equilibrium and which support the amide bond redox isomerism scheme are described below.

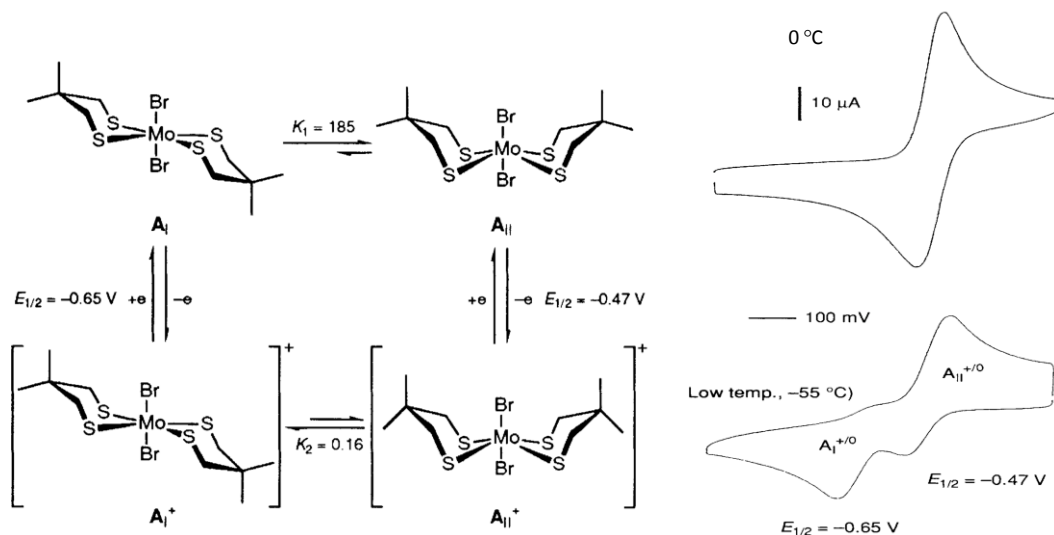
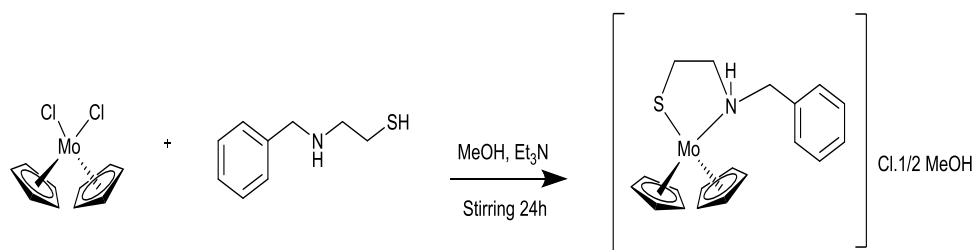


**Figure 2.18** Conformational and redox equilibria of tetrathioether macrocyclic ring.

Taken from reference 68. [68](#)

### 2.2.5 Synthesis of a Mo(IV) complex possessing a thiolate – amine metalocycle ring( Complex 2)

In order to further explore the metallo-cyclic ring system and the conformational role of the amide group, a complex with a five-membered N,S - metallo-cyclic was synthesized in which the amide function was absent. This was partially achieved in a straightforward fashion by the route shown in **Scheme 2.7**. A crystalline yellow orange material was obtained suitable for X-ray diffraction. The structure was determined by the National Crystallographic Service and is shown in **Figure 2.19** below with selected bond lengths and angles given in **Table 2.5**.



**Scheme 2.7** Synthesis of **Complex 2**.

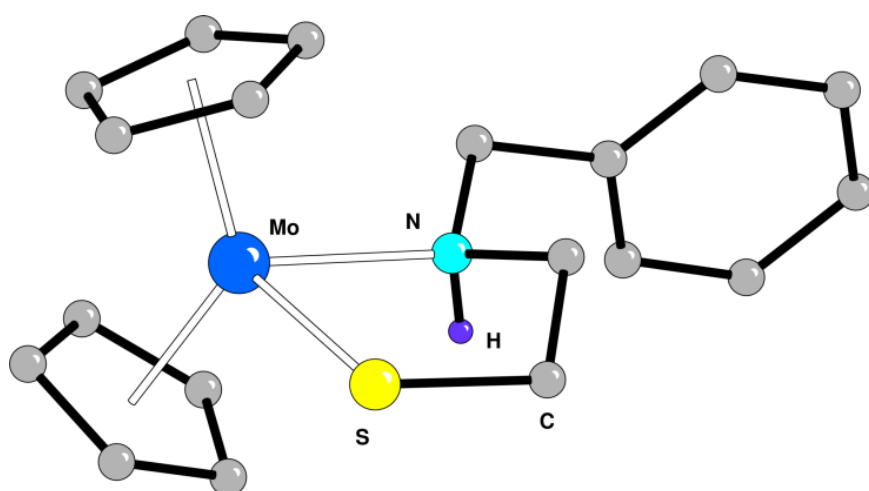


**Figure 2.19.** Structure of  $[\text{MoCp}_2(\text{SCH}_2\text{CH}_2\text{NHBn})]\text{Cl}\cdot\frac{1}{2}(\text{MeOH})$  showing spheres of arbitrary size; hydrogen atoms except for H(1), half a molecule of methanol and the chloride counter ion have been omitted for clarity.

Mo(1)–N(1)	2.277 (3)
Mo(1)–S(1)	2.4605 (9)
C(11)–S(1)	1. 1.830 (3)
C(12)–N(1)	1.499 (4)
C(11)–C(12)	1.508 (5)
N(1)–Mo(1)–S(1)	78.44 (7)

**Table 2.5** Selected bond lengths (Å) and angles (deg) for **Complex 2**.

Mo-N distance is significantly longer in **Complex 2** than in **Complex 1** as would be expected for a  $sp^3$  donor ligand rather than a  $sp^2$  hybridised anionic N-atom. The Mo-S distance is comparable with that of **Complex 1** as is the N(1)–Mo(1)–S(1) bond angle, 78.44 (7) *versus* 79.58 (7) °. The Mo-S-CH<sub>2</sub> and Mo-N atoms lie approximately in a plane as is shown in **Figure 2.20**. The <sup>1</sup>H-nmr shows two resonances for the cyclopentadienyl rings consistent with the presence of a single type of molecule in solution, that is there is no evidence for isomeric forms.

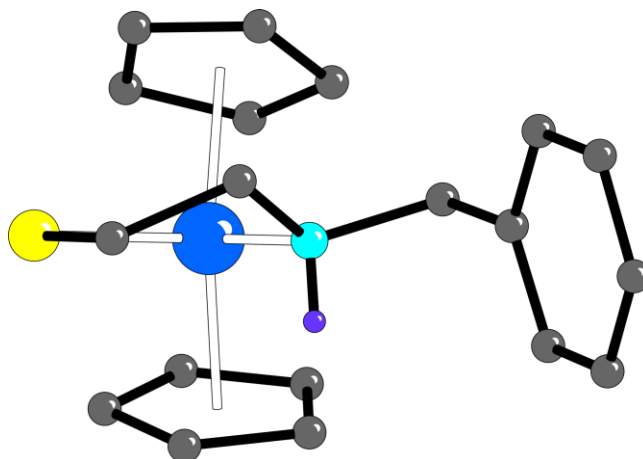


**Figure 2.20** Perspective view of **Complex 2** showing co-planarity of four atoms of the metallo-cycle ring, Mo, N, S and C.

The comparison of **Complex 1** and **Complex 2** has limitations because as mentioned above the bonding of the N-atom in the complexes differs. In the former case the N-atom is  $sp^2$  -hybridised in the latter it is  $sp^3$  -hybridized. In addition, **Complex 1** is neutral whereas **2** is cationic. Attempts were made to deprotonate the NH group in **Complex 2** with various bases but this led to decomposition rather than the isolation of a clean imide product.

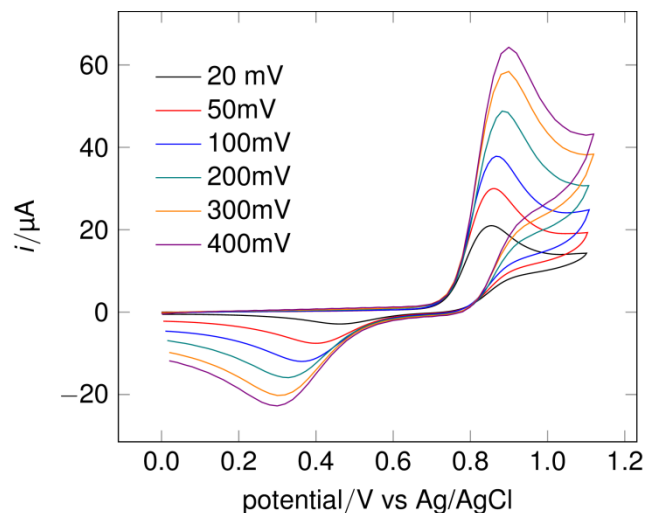


**Figure 2.21.** Cyclic voltammetry of **Complex 2** 1.8 mM in 0.2M [Bu<sub>4</sub>N][BF<sub>4</sub>] - MeCN at variable scan rate.

The cyclic voltammetry of **Complex 2** in a MeCN electrolyte shows an irreversible oxidation near 0.8V *versus* Ag/AgCl at all scan-rates, **Figure 2.21**. The oxidation process is diffusion-controlled as is evident from the plot of  $i_p$  *versus*  $v^{1/2}$  as shown in **Figure 2.22** and the peak current function  $i_p/v^{1/2}$  [**Complex2**] has a magnitude consistent with a two electron oxidation, the product of this oxidation is detected near 0.3V *versus* Ag/AgCl.

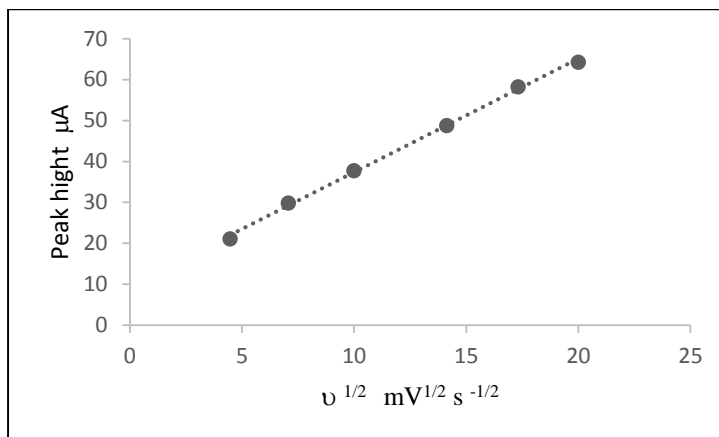


**Figure 2.22** Plot of  $i_p$  versus  $v^{1/2}$  and the peak current function  $i_p/v^{1/2}$  for **Complex 2**.

### 2.2.6 Second coordination sphere effects on the redox linked isomerism of **Complex 1**.

#### *Interaction with protons.*

It was thought that the kinetics and thermodynamics of the redox isomerism of **Complex 1** might be modified by protic interactions with the basic sites on the molecule. The amide N and carbonyl, the S atom and the ester are potential sites for proton binding or hydrogen bonding interactions. **Figure 2.23** shows the effect of addition of acetic acid on the voltammetry of **Complex 1**. The clear effect is that in the CH<sub>2</sub>Cl<sub>2</sub> electrolyte the primary **A<sub>1</sub><sup>+</sup>/A<sub>1</sub>** system switches progressively from a reversible one – electron process to a two – electron process. Thus the forward peak height is nearly doubled at five equivalents of acid whilst the back peak height is lost. This indicates that it is not protonation by a weak acid that takes place, rather it is the effect

of acetate ion attacking the  $A_{11}^+$  species that occurs resulting in an ‘ece’ process in which the product of nucleophilic attack undergoes a second-electron transfer.

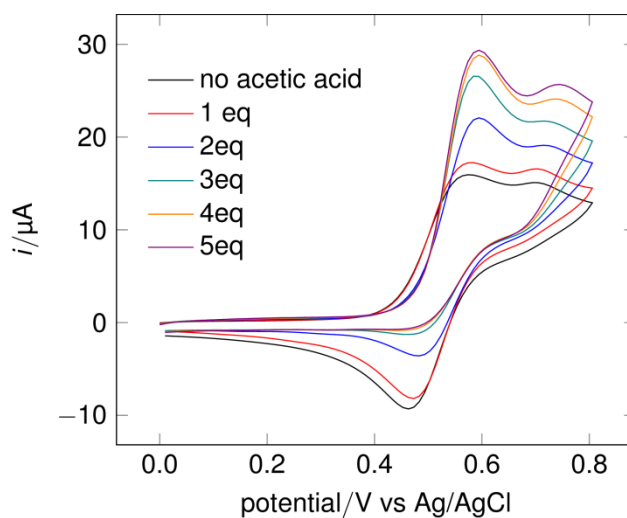


**Figure 2.23.** Cyclic voltammetry of **Complex 1** with acetic acid in 0.2M  $[Bu_4N][BF_4]$  -  $CH_2Cl_2$  at  $100mV s^{-1}$

To test this further the cyclic voltammetry was examined in the presence of a non-coordinating acid,  $\mu$ -amido-hexakis(2,3,4,5,6-pentafluorophenyl)di-borate(1-),<sup>69</sup> the structure of which is shown below, **Figure 2.24**. The effect of this relatively strong acid on the voltammetry was quite dramatic. With two equivalents the primary oxidation process is lost, a minor reversible couple is observed near 0.75V *versus* Ag/AgCl and a major oxidation occurred near 1.2V *versus* Ag/AgCl. On the reverse scan a sharp desorption peak was apparent, typical of that for the reduction of an electrode (surface) bound product, **Figure 2.25**.



Since the effect of both acids was to introduce complexity into the chemistry rather than perturb the redox linked isomerism, another approach was taken.

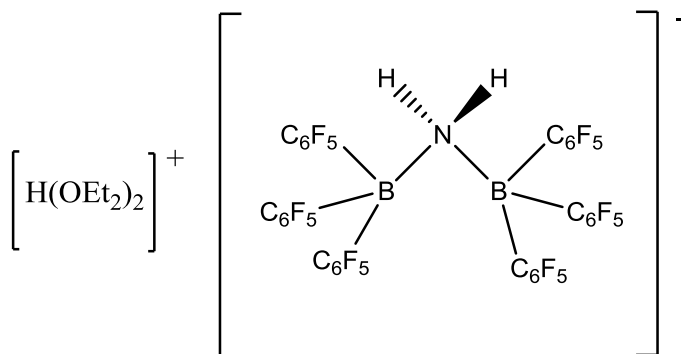


**Figure 2.24** Structure of  $[\text{H}(\text{OEt}_2)_2][\text{H}_2\text{N}(\text{B}(\text{C}_6\text{F}_5)_3)_2]$ .

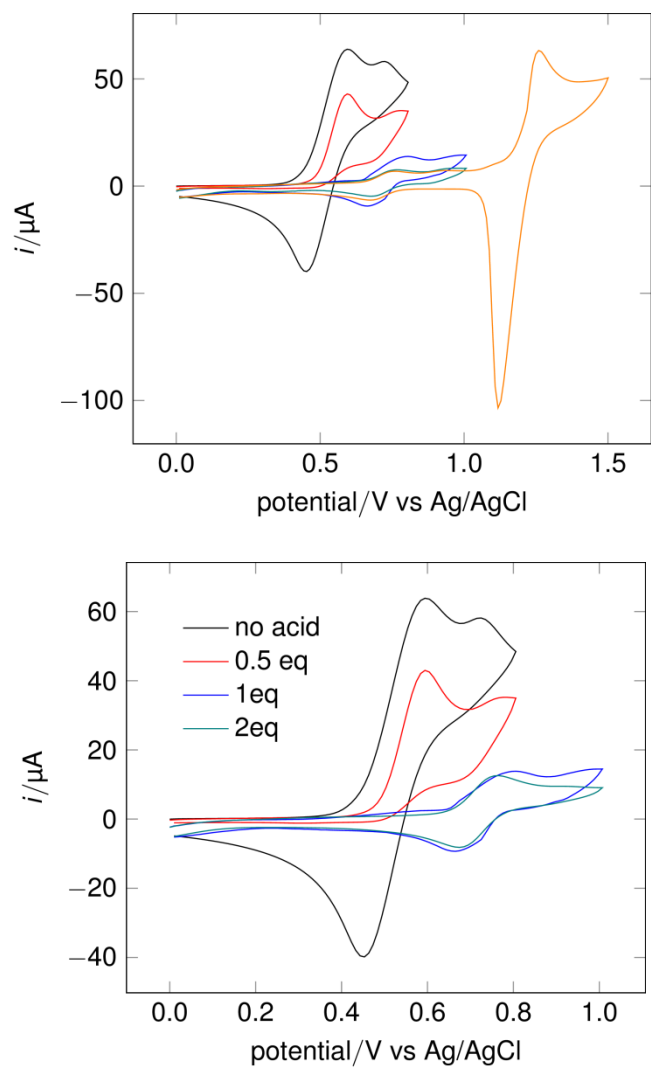


**Figure 2.25.** Cyclic voltammetry of **Complex 1** with  $[\text{H}(\text{OEt}_2)_2][\text{H}_2\text{N}(\text{B}(\text{C}_6\text{F}_5)_3)_2]$  in 0.2M  $[\text{Bu}_4\text{N}][\text{BF}_4]$ -  $\text{CH}_2\text{Cl}_2$  at  $100\text{mV s}^{-1}$ .

**Interaction with  $\text{Eu}(\text{fod})_3$ .**

The lanthanide complex  $\text{Eu}(\text{fod})_3$ , **Figure 2.26**, was once widely used as a paramagnetic shift reagent to resolve  $^1\text{H-NMR}$  spectra<sup>70</sup> before the advent of 400 MHz and above instruments. The complex functions as a Lewis acid with a potential to bind one, two or possible three ‘hard’ O or N donor atoms. The electronic spin of the Eu atom induces a local magnetic field shifting the resonances of protons close to where it binds.

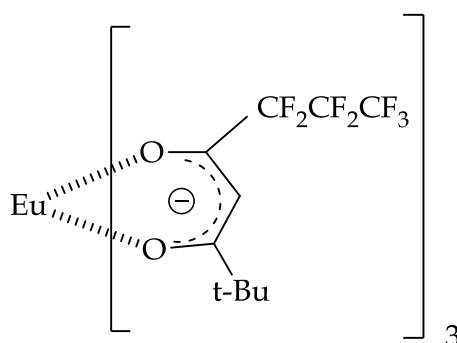


**Figure 2.26** Structure of the lanthanide complex  $\text{Eu}(\text{fod})_3$ .

It was thought that this reagent might be exploited to control the geometry of **Complex 1** in solution and this was indeed the case. The dramatic effect of  $\text{Eu}(\text{fod})_3$  on the redox isomerism is shown by cyclic voltammetry in **Figure 2.27** which was recorded in 0.2M  $[\text{Bu}_4\text{N}][\text{BF}_4]$  -  $\text{CH}_2\text{Cl}_2$ . Thus one equivalent of  $\text{Eu}(\text{fod})_3$  is sufficient to more or less ‘stop’ the isomerism in solution. The primary process associated with the  $\text{A}_1^+/\text{A}_1$  couple is lost whilst that process associated with the  $\text{B}_1^+/\text{B}_1$  couple is now the dominant process. In addition, this second process has enhanced reversibility consistent with

inhibition of the rearrangement of  $\mathbf{B1}^+$  to  $\mathbf{A1}^+$ . Simulation of the experimental data is shown in **Figure 2.28** together with the parameters used.

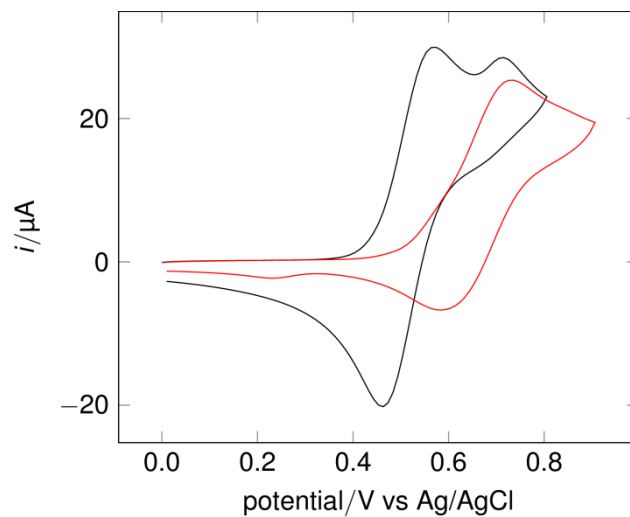


**Figure 2.27.** Cyclic voltammetry of 6.25 mM of **Complex 1** with 1eq of  $\text{Eu}(\text{fod})_3$  in 0.2M  $[\text{Bu}_4\text{N}][\text{BF}_4]$  in  $\text{CH}_2\text{Cl}_2$  recorded at a scan-rate of  $100\text{mVs}^{-1}$  and at 293K. Black curve before addition of  $\text{Eu}(\text{fod})_3$ , red curve is after addition.

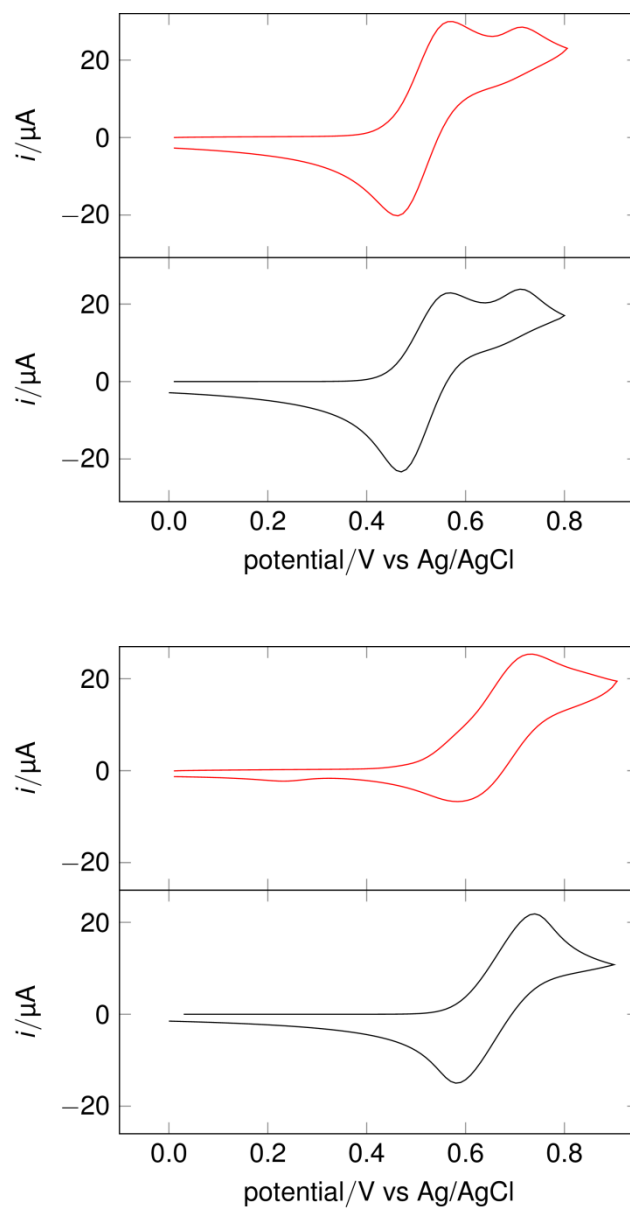
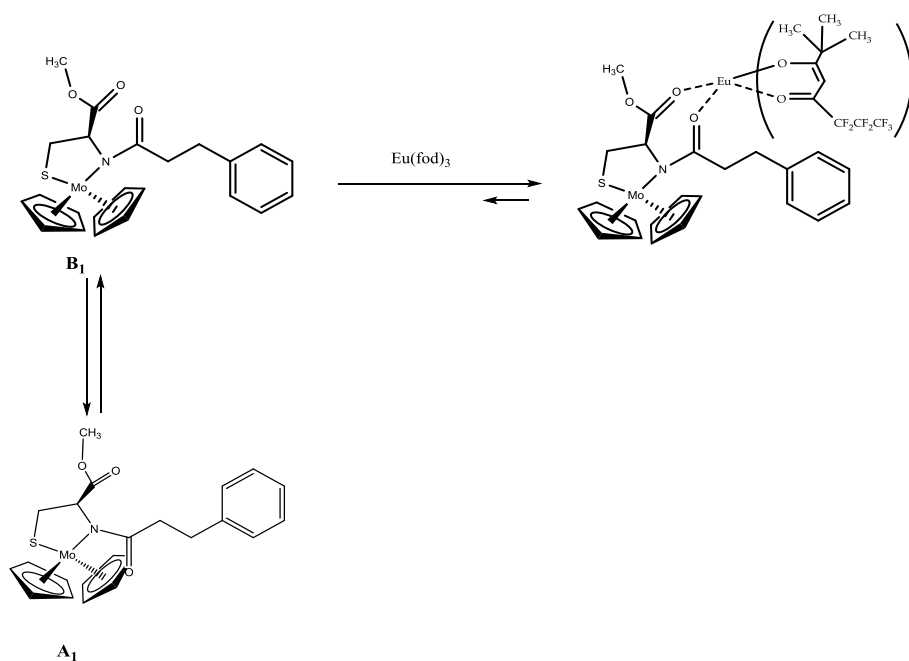


**Figure 2.28.** Cyclic voltammetry of 6.25 mM of **Complex 1** without  $\text{Eu}(\text{fod})_3$ , (above) and with 1 eq of  $\text{Eu}(\text{fod})_3$  (below) in 0.2M  $[\text{Bu}_4\text{N}][\text{BF}_4]$  in  $\text{CH}_2\text{Cl}_2$ . Experimental curves are red, simulated curves are black.

The explanation for the effect of  $\text{Eu}(\text{fod})_3$  on the isomer distribution is that binding to the amide oxygen occurs and this deploys the amide group away from the metal centre preventing dipolar interactions and stabilization of  $\mathbf{A}_1^+$ . That is the favourable rearrangement of the *trans*-rotamer  $\mathbf{B}_1^+$  to the *cis*-rotamer  $\mathbf{A}_1^+$  is inhibited as represented in **Scheme 2.8**. As discussed above,  $\text{Eu}(\text{fod})_3$  can expand its coordination sphere from 6 to 7 or 8 and it may be the case that co-binding to the ester group also occurs, **Figure 2.29**.  $^1\text{H-NMR}$  experiments discussed below lend support to the formation of a 1:1 adduct of the complex with  $\text{Eu}(\text{fod})_3$



**Scheme 2.8** Proposed interaction of  $\text{Eu}(\text{fod})_3$  with **Complex 1**.

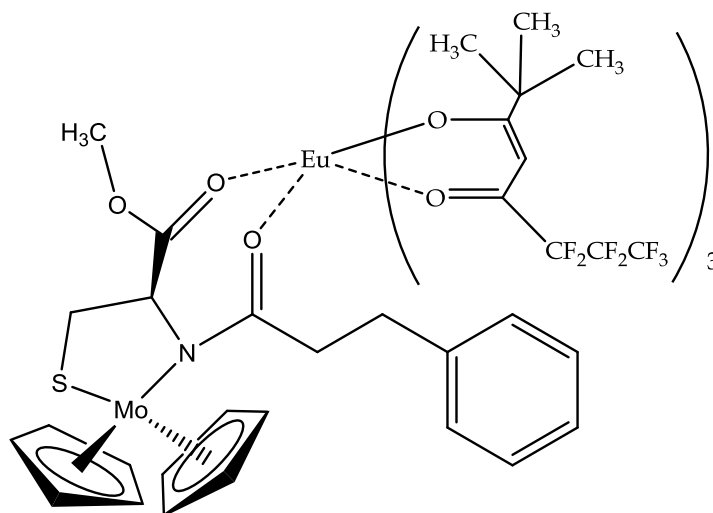


**Figure 2.29** A possible structure of  $[\text{Mo}(\eta\text{-C}_5\text{H}_5)_2\text{L1}(\text{Eu}(\text{fod})_3)]$ .

***<sup>1</sup>H NMR spectra of Complex 1 - Eu(fod)<sub>3</sub> adduct.***

The <sup>1</sup>H-NMR of the adduct of Eu(fod)<sub>3</sub> with **complex 1** in CD<sub>2</sub>Cl<sub>2</sub> was examined. The key features of the spectrum of the adduct is that the four resonances for the cyclopentadienyl rings observed in the absence of Eu(fod)<sub>3</sub> are reduced to two of equal intensity, **Figure 2.30**, each integrating to 5 protons with respect to the 27 tertiary butyl protons of Eu(fod)<sub>3</sub>. The cyclopentadienyl resonances are shifted substantially upfield to 9.53, 10.19 ppm consistent with the proximity of the paramagnetic centre and its electronic influence through the metallocyclic ring. The shift in the aromatic protons is minimal they are observed at 7.23 ppm as a single unresolved resonance integrating to 5 protons. The methyl protons of the ester in the adduct are assigned to the single resonance at 7.05 ppm consistent with close proximity to the paramagnetic centre. The

## CHAPTER 2 | INTRAMOLECULAR REDOX ISOMERISM

resonance at 3.29 possibly encompasses other aliphatic CH<sub>2</sub> protons. These results are reasonably consistent with interaction of Eu(fod)<sub>3</sub> with the amide and parallels the upfield shift observed in simpler systems. [71](#), [72](#)



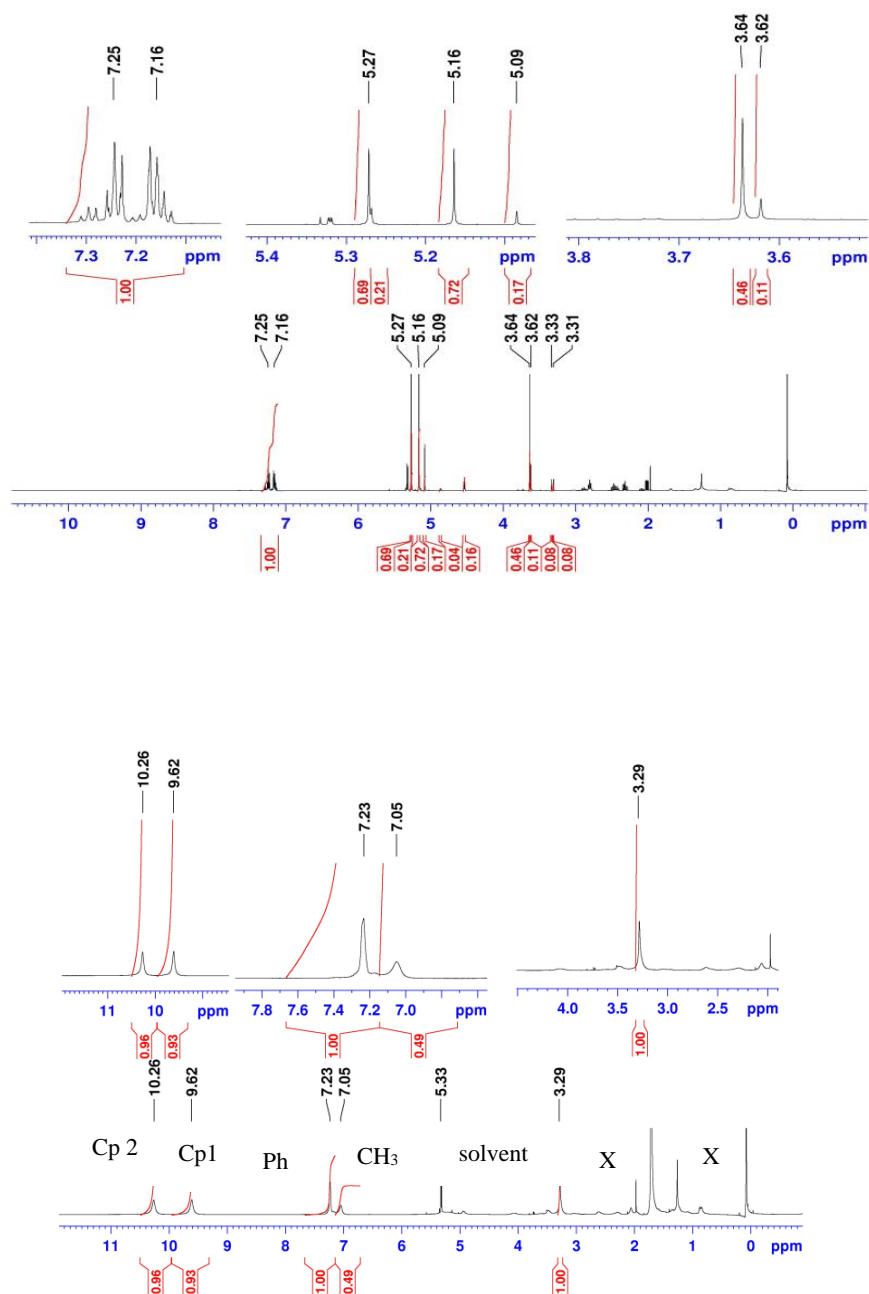


**Figure 2.30.**  $^1\text{H}$ NMR for **Complex 1** (above) without  $\text{Eu}(\text{fod})_3$  and (below) with  $\text{Eu}(\text{fod})_3$  in  $\text{CD}_2\text{Cl}_2$ .

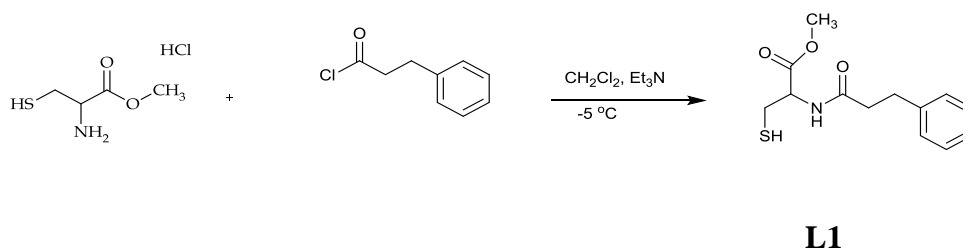
### 2.2.7 Final Remarks

In this Chapter it has been shown that the spectroscopy and electrochemistry of **Complex 1** involves interconverting redox isomers. This closely parallels the redox isomerism behavior first described for a closely related pyrrole system. The results support the explanation that intramolecular *cis/trans*-isomerism about an amide bond is involved in both systems. This is reinforced by the observation that the interaction of  $\text{Eu}(\text{fod})_3$  with **Complex 1** switches the system to a predominately single *trans*-isomer.

**Complex 1** in both isomeric forms is a closed-shell 18-electron complex, and similarly the oxidized isomers are both 17-electron complexes. The 18e/17e species can be considered as ‘frustrated’ with respect to accommodating an electron-pair, neither possessing a low lying vacant orbital. Thus the shift of 200mV between the redox potentials of the isomeric forms must largely be attributable to electrostatic/dipolar interactions.

## 2.3 Experimental

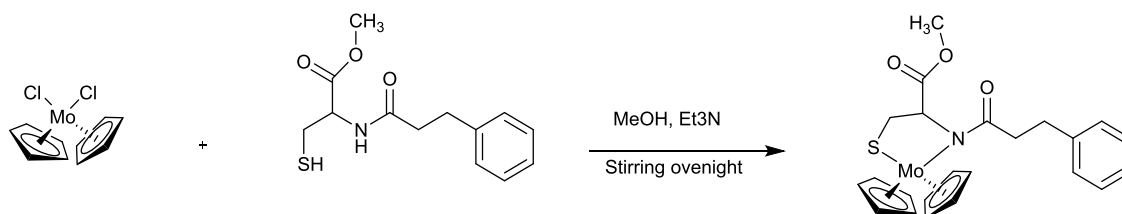
### 2.3.1 Synthesis of N-(3-phenylpropanoyl)-L-cysteine methyl ester (L1):



## CHAPTER 2 | INTRAMOLECULAR REDOX ISOMERISM

This ligand was synthesized by the literature method <sup>73</sup> A solution of 3-phenylpropanoyl chloride (4.6 g, 27 mmol) in (15 ml) distilled CH<sub>2</sub>Cl<sub>2</sub> was added dropwise to a solution of L- cysteine methyl ester hydrochloride (5 g, 29.12 mmol) in 50 ml CH<sub>2</sub>Cl<sub>2</sub> with triethylamine (8.08 ml, 57.6 mmol) at -5 °C. The mixture was stirred at -5 °C for 2 hours, then for two more hours at room temperature. 25ml of Ethyl acetate was added to the reaction mixture and the resulting organic layer removed and washed three times by a saturated solution of NaHCO<sub>3</sub> and brine 60 ml. The organic layer was dried over MgSO<sub>4</sub> overnight and filtered. Removal of the solvent gave the white product, 4.3 g (85 %) which was clean by TLC and had a <sup>1</sup>H-nmr according to that reported in the literature. <sup>73</sup>

### 2.3.2 Synthesis of Complex 1, bis(cyclopentadienyl)molybdenum(IV)-N-(3-phenylpropanoyl)-L-cysteine methyl ester:



**Complex 1**

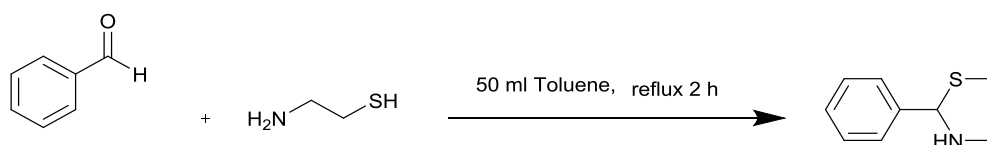
A solution of N-(3-phenylpropanoyl)-L-cysteine methyl ester (0.148 g, 0.552 mmol) dissolved in dried MeOH containing 4 equivalents of Et<sub>3</sub>N was added dropwise to a

solution of bis(cyclopentadienyl)molybdenum(IV) dichloride (0.164 g, 0.552 mmol) in MeOH. The orange red mixture of reaction was stirred at room temperature overnight. The resulting solution was filtered and concentrated. Storing at 2 °C gave red-orange single crystals suitable for X-ray diffraction. Anal. Found (calcd) for  $C_{23}H_{25}NO_3SMo$ : C, 56.21 (57.32); H, 5.09 (5.77); N 2.85 (2.56). IR (MeCN): 1743, 1728, 1581, 1574  $cm^{-1}$ .  $^1H$ -NMR (500 MHz;  $CD_2Cl_2$ ): 1.98-2.98 ppm *cis* and *trans* (m, 4 H of  $CH_2CH_2-Ph$ ), 3.20 and 3.23 ppm (d, 2H of  $SCH_2$ ), 3.54 and 3.56 ppm *cis* and *trans* (s, 3H of  $O-CH_3$ ), 4.5 and 4.8 ppm *cis* and *trans* (dd,  $SCH_2-CH-N-$ ), 5.08 and 5.19 ppm (s, 5 H of Cp), 7- 7.3 ppm *cis* and *trans* (m, 5 H of Ph).

### 2.3.4 Synthesis of 2-Benzyl amino ethanethiol:

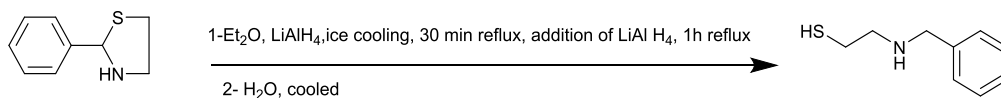
This compound was prepared following a literature method <sup>74</sup> by two steps.

*2-phenyl-1,3- thiazolidine:*

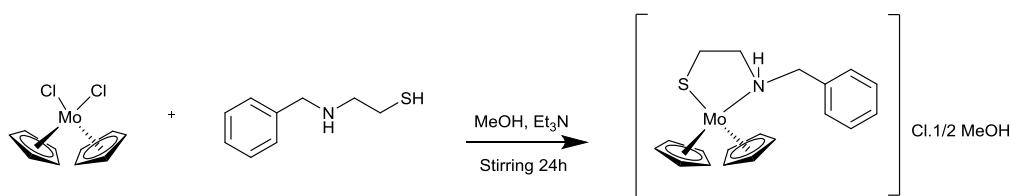


### L2

A solution of benzaldehyde (4.6 ml, 45 mmol) in fresh distilled toluene with 2-aminoethanethiol (3.5 g, 30 mmol) was refluxed until all water was removed. After the reaction mixture cool down, it was filtered and washed three time by dried diethyl ether.

*2-Benzyl amino ethanethiol:***L3**

Lithium aluminum hydride (0.184g) in dried ether was added dropwise to a 2-phenyl-1-3 thiazolidine (**L2**) in fresh distilled ether (5 ml ) under ice bath and the mixture was refluxed for one hour. 1 ml of degassed water was added to quench the reaction mixture in an ice bath and the solution was stirred for a further hour. The solid was filtered off and dissolved in (1N) sodium hydroxide solution and extracted with ethyl acetate (3 x 100 ml). The organic layer washed then dried over anhydrous magnesium sulfate then dried to give colorless oily product, (82%).

**Synthesis of Complex 2, [MoCp<sub>2</sub>(SCH<sub>2</sub>CH<sub>2</sub>NHBn)Cl.1/2 (MeOH)]:****Complex 2**

2-benzylaminoethanethiol (**L3**, 96 mg, 0.57 mmol) was dissolved in 10ml of freshly distilled MeOH with 4 eq of triethylamine. This was added dropwise to a solution of

bis(cyclopentadienyl)molybdenum(IV) dichloride (169mg, 0.57mmol) in 10 ml of methanol. The yellow orange solution was stirred for 24 hour under nitrogen atmosphere at room temperature. The reaction mixture was filtered and concentrated to give orange crystal at 2 °C suitable for single crystal X-ray diffraction. Yield: 78% (200mg). Elemental analysis calc. (Found) for  $C_{19}H_{22}NS, 0.5(CH_4O)Cl$ : C 52.85 (53.24); H 5.19(5.76); N 3.2(3.45).  $^1H$  NMR ( $CD_3Cl$ ): 2.31 ppm (dd, H), 2.34ppm (d,H), 3.19-3.7 (m,2H), 5.4 (s,5H), 5.5ppm (s,5H), 7.4(m,5H).

### 2.3.8 Electrochemical measurements

Cyclic voltammetry measurements were carried out in 0.2 M  $[Bu_4N][BF_4]$  – MeCN or  $CH_2Cl_2$  using a three compartment cell fitted with a glassy carbon working electrode (diameter 3 mm), a platinum counter electrode and a Ag/AgCl reference electrode interfaced with an Autolab PGSTAT302N potentiostat using the GPES software package. The electrolyte was prepared by a standard laboratory procedure <sup>47</sup> and the solvents were purified as described in the experimental section in **Chapter 1**.

### 2.3.9 Digital CV simulations

DigiElch was used for digital simulation and nonlinear optimization of the model parameters against the experimental data. Electrochemical Simulation Package E (redox potential),  $k_e$  (heterogeneous rate constant), and  $k_f$  and  $k_b$  (homogeneous chemical reaction rate constants for forward and reverse reactions, respectively) were optimized to fit the experimental data using the program-implemented procedure; the electron transfer coefficient  $\alpha$  was not optimized and was approximated as 0.5 for all

redox couples. The values for the solution resistance and double-layer capacitance were adjusted manually, and the same values were used for all fits. The electrode area is  $0.0707 \text{ cm}^2$ . The procedure was repeated for each temperatures separately, and the parameters that give satisfactory fits for all temperatures and scan-rates were selected and used for the simulations.

A/B		A <sup>+</sup> /B <sup>+</sup>					
T (K)	K <sub>eq</sub>	k <sub>f</sub>	k <sub>b</sub>	k <sub>f</sub> <sup>+</sup>	k <sub>b</sub> <sup>+</sup>	K <sub>eq</sub> <sup>+</sup>	Diffusion Coefficient, D / cm <sup>2</sup> s <sup>-1</sup>
293	0.7	0.5	0.71	0.007	113.79	6.15 x10 <sup>-5</sup>	9.6 x10 <sup>-6</sup>
270	0.6	0.08	0.13	0.005	594.1	8.4 x10 <sup>-6</sup>	6.8 x10 <sup>-6</sup>
231	0.57	0.04	0.07	5.0 x10 <sup>-5</sup>	0.74	6.8 x10 <sup>-5</sup>	3.0x10 <sup>-6</sup>
197	0.53	3.0 x10 <sup>-4</sup>	5.7 x10 <sup>-4</sup>	4.0x10 <sup>-7</sup>	0.03	1.49x10 <sup>-5</sup>	2.0 x10 <sup>-6</sup>
Experimental condition: Scan rate= 100 mV s <sup>-1</sup> , Electrode area= 0.0707 cm <sup>2</sup> , concentration of parent complex = 1 mM 0.2 M [Bu <sub>4</sub> N][BF <sub>4</sub> ] – CH <sub>2</sub> Cl <sub>2</sub> .				Simulation : Heterogeneous electron transfer 1000 cm/s E° (A <sup>+</sup> /A) =0.50 V , E° (B <sup>+</sup> /B) =0.71 V. R <sub>u</sub> = 700 Ω			

**Table 2.6** Parameters used for simulation of the variable temperature cyclic voltammetry of **complex 1** in CH<sub>2</sub>Cl<sub>2</sub>.



### 2.3.10 X-ray crystallography

#### *Crystal structure analysis of Complex 1*

*Crystal data:* C<sub>23</sub>H<sub>25</sub>MoNO<sub>3</sub>S,  $M = 491.4$ , Monoclinic, space group  $P2_1/c$ ,  $a = 8.1359(5)$  Å,  $b = 29.276(2)$  Å,  $c = 11.2937(5)$  Å,  $\beta = 131.466(3)^\circ$ ,  $V = 2015.8(2)$  Å<sup>3</sup>,  $Z = 4$ ,  $D_c = 1.619$  g cm<sup>-3</sup>,  $F(000) = 1008$ ,  $T = 100(2)$  K,  $\mu(\text{Mo-}K\alpha) = 0.780$  mm<sup>-1</sup>,  $\lambda(\text{Mo-}K\alpha) = 0.71073$  Å.

Crystals are orange plates. From a sample under oil, one, *ca.* 0.040 mm × 0.030 mm × 0.010 mm, was mounted on a glass fibre and fixed in the cold nitrogen stream on an Rigaku Saturn724+diffractometer equipped with Mo- $K\alpha$  radiation and confocal mirrors. Intensity data were measured by  $\omega$ -scans. Total no. of reflections recorded, to  $\theta_{\text{max}} = 27.5^\circ$ , was 24991 of which 4613 were unique ( $R_{\text{int}} = 0.073$ ); 4043 were 'observed' with  $I > 2\sigma_I$ .

Data were processed using the CrysAlisPro program.<sup>75</sup> The structure was determined by the direct methods routines in the SUPERFLIP program<sup>76</sup> and refined by full-matrix least-squares methods on  $F^2$  in SHELXL-2013.<sup>77</sup> The non-hydrogen atoms were refined with anisotropic thermal parameters. Hydrogen atoms were included in idealised positions and their  $U_{\text{iso}}$  values were set to ride on the  $U_{\text{eq}}$  values of the parent carbon atoms. At the conclusion of the refinement,  $wR_2 = 0.159$  and  $R_1 = 0.070$  for all 4613 reflections; for the 'observed' data only,  $R_1 = 0.060$ .

***Crystal structure analysis of Complex 2***

*Crystal data:* C<sub>19</sub>H<sub>21</sub>MoNS, 0.5(CH<sub>4</sub>O), Cl, *M* = 442.8, Monoclinic, space group *P*2<sub>1</sub>/*n*, *a* = 7.7667(5) Å, *b* = 15.7118(11) Å, *c* = 15.1693(10) Å, *β* = 93.502(3)°, *V* = 1847.6(2) Å<sup>3</sup>, *Z* = 4, *D*<sub>c</sub> = 1.592 g cm<sup>-3</sup>, *F*(000) = 904, *T* = 100(2) K, *μ*(Mo-*Kα*) = 0.971 mm<sup>-1</sup>, *λ*(Mo-*Kα*) = 0.71073 Å.

Crystals are orange plates. From a sample under oil, one, *ca.* 0.050 mm × 0.030 mm × 0.010 mm, was mounted on a glass fibre and fixed in the cold nitrogen stream on Rigaku Saturn724+ diffractometer equipped with Mo-*Kα* radiation and confocal mirrors. Intensity data were measured by *ω*-scans. Total no. of reflections recorded, to *θ*<sub>max</sub> = 27.5°, was 23838 of which 4234 were unique (*R*<sub>int</sub> = 0.067); 3496 were 'observed' with *I* > 2*σ*<sub>*I*</sub>.

Data were processed using the CrystalClear-SM Expert program.<sup>78</sup> The structure was determined by the direct methods routines in the Superflip program<sup>76</sup> and refined by full-matrix least-squares methods on *F*<sup>2</sup> in SHELXL-2013.<sup>77</sup> The non-hydrogen atoms were refined with anisotropic thermal parameters. Hydrogen atoms were included in idealised positions and their *U*<sub>iso</sub> values were set to ride on the *U*<sub>eq</sub> values of the parent carbon atoms. At the conclusion of the refinement, *wR*<sub>2</sub> = 0.119 and *R*<sub>1</sub> = 0.057 for all 4234 reflections; for the 'observed' data only, *R*<sub>1</sub> = 0.045.

## CHAPTER 3. INTERACTION OF $\text{Eu}(\text{fod})_3$ WITH COORDINATED CYANIDE IN AN ANALOGUE OF THE SUB-SITE OF [FeFe]- HYDROGENASE

### 3.1 Introduction:

#### 3.1.1 General aspects

This chapter is concerned with the second coordination sphere interactions of cyanide ligands with the lanthanide shift reagent  $\text{Eu}(\text{fod})_3$  which has Lewis acidic properties. Specifically, the cyanide species of interest is the dianion  $[\text{Fe}_2(\text{CO})_4(\text{CN})_2\text{pdt}]^{2-}$  [pdt = 1,3-propane dithiolate,  $(\text{CH}_2)(\text{CH}_2\text{S}^-)_2$ ]. This species is related to the diiron sub-site of the H-cluster of [FeFe]-hydrogenase. Notably, this synthetic complex, and related dianions with oxa or aza groups replacing the bridgehead  $\text{CH}_2$  of the pdt ligand, can be incorporated into an *apo*-enzyme lacking the sub-site.<sup>79</sup> In the case of reconstituting with the aza dithiolate species, it has been shown that an activity corresponding to that of the native enzyme can be attained.<sup>79</sup>

A general introduction to [FeFe]-hydrogenase chemistry is provided in the next section, this is relevant to both this chapter and **Chapter 4** which discusses hydrogen bonding interactions with the sub-site analogue. This is followed by brief a description of the synthesis, spectroscopy and chemistry of the dianion  $[\text{Fe}_2(\text{CO})_4(\text{CN})_2\text{pdt}]^{2-}$ . The chemistry and spectroscopy of  $\text{Eu}(\text{fod})_3$  has been described in **Chapter 2** in the context

of its use as a Lewis acid to modify the redox chemistry of a molybdenum rotamer system.

### 3.1.2 [FeFe]-hydrogenase chemistry

*The Hydrogenases.* The interconversion of  $\text{H}_2$ , protons, and electrons is mediated in Nature by a class of metalloenzymes known as hydrogenases. The hydrogenases are of major interest in the field of bioorganometallic chemistry and enzymatic catalysis.<sup>80-82</sup> This is because an understanding of their structure and function is seen as potentially important in technological production and utilization of dihydrogen for a hydrogen economy.<sup>83</sup> Especially relevant to this is the fact that the active sites of the enzymes are based on abundant elements (Fe or Fe and Ni, and sulfur) rather than platinum. Platinum is the best electrocatalyst for fuel and producer cells but certain of the hydrogenases can electrocatalyse these reactions at rate comparable to platinum on a per-site basis. Most of these enzymes are found in archaea and bacteria. Depending on the oxygen content of the environment, hydrogenase can remove reducing equivalents by production of  $\text{H}_2$  or provide energy for organisms by generating electrons from  $\text{H}_2$  in anaerobic environments. Three classes of hydrogenase are known: [NiFe]-hydrogenases; [FeFe]-hydrogenases; and iron-sulfur cluster-free hydrogenases<sup>84</sup> classified by the metals located at the active site. [FeFe]- and [NiFe]-hydrogenases have similar properties. Thus the active sites for both [FeFe]- and [NiFe]-hydrogenases feature Fe centers which are ligated by CO and  $\text{CN}^-$  ligands<sup>85, 86</sup>. The bimetallic centers are bridged by thiolate ligands with a vacant coordination site on at least one

metal center that binds substrate. In addition, both [FeFe]- and [NiFe]-hydrogenase have FeS clusters which are employed to transport electrons to and from the active site to the enzyme surface [87](#).

**Structure and function of [FeFe]-Hydrogenase.** The H-cluster and its immediate protein environment as obtained by Peters and coworkers [88](#) from a high resolution structure of an [FeFe]-hydrogenase isolated from *Clostridium pasteurianum* is shown in **Figure 3.1**. A ChemDraw representation which shows the key hydrogen bonding interactions of the protein backbone with the cyanide ligands is also shown in this figure. The cyanide ligand at the Fe proximal to the cluster is hydrogen bonded to proline (Pro 231) and serine (Ser 232), the cyanide at the Fe atom distal to the cluster is hydrogen bonded to proline (Pro 324), glutamine (Gln 325). [NiFe]-hydrogenase in which two cyanide ligands are coordinated to the Fe center also shows strong hydrogen bonding interactions with arginine (Arg 479) and serine (Ser 502) of the protein backbone. Hydrogen bonding interactions to the H-cluster probably serve several important functions. First, they must contribute to the binding of the subsite to the protein which is otherwise only held by a single cysteine bridging sulfur to the 4Fe4S cluster. Secondly, hydrogen bonding must hold the subsite in a *trans-(basal,basal)* orientation favouring the exposure of a substrate ( $\text{H}^+/\text{H}_2$ ) binding site. Thirdly, the hydrogen bonding must modify the electronic properties of the subsite by removing electron density from the Fe(I)Fe(II) - core. This would have the effect of making this unit easier to reduce. Finally, hydrogen bonding plays an important role in transporting

## CHAPTER 3 | INTERACTION OF $\text{Eu}(\text{fod})_3$ WITH COORDINATED CYANIDE IN AN ANALOGUE OF THE SUB-SITE OF $[\text{FeFe}]$ -HYDROGENASE

protons to and from the active site *via* the bridging 2-azapropane-1,3-dithiolate ligand (adt). The current view of the catalytic cycle which includes the role for the adt ligand in this proton relaying function is shown by **Scheme 3.1**. [89,90](#)

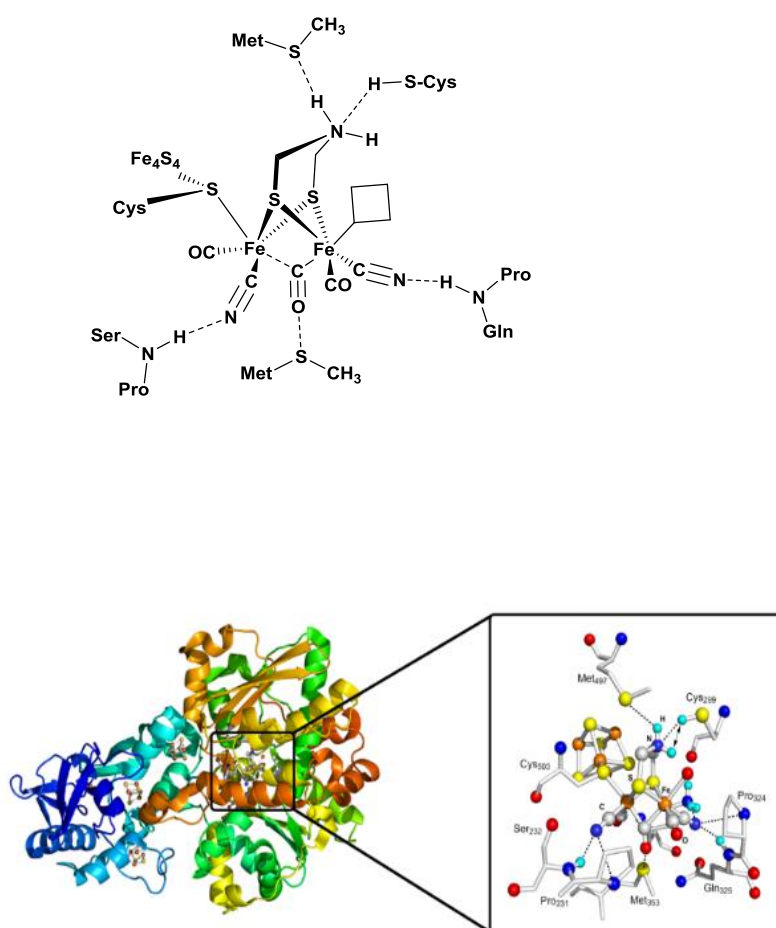
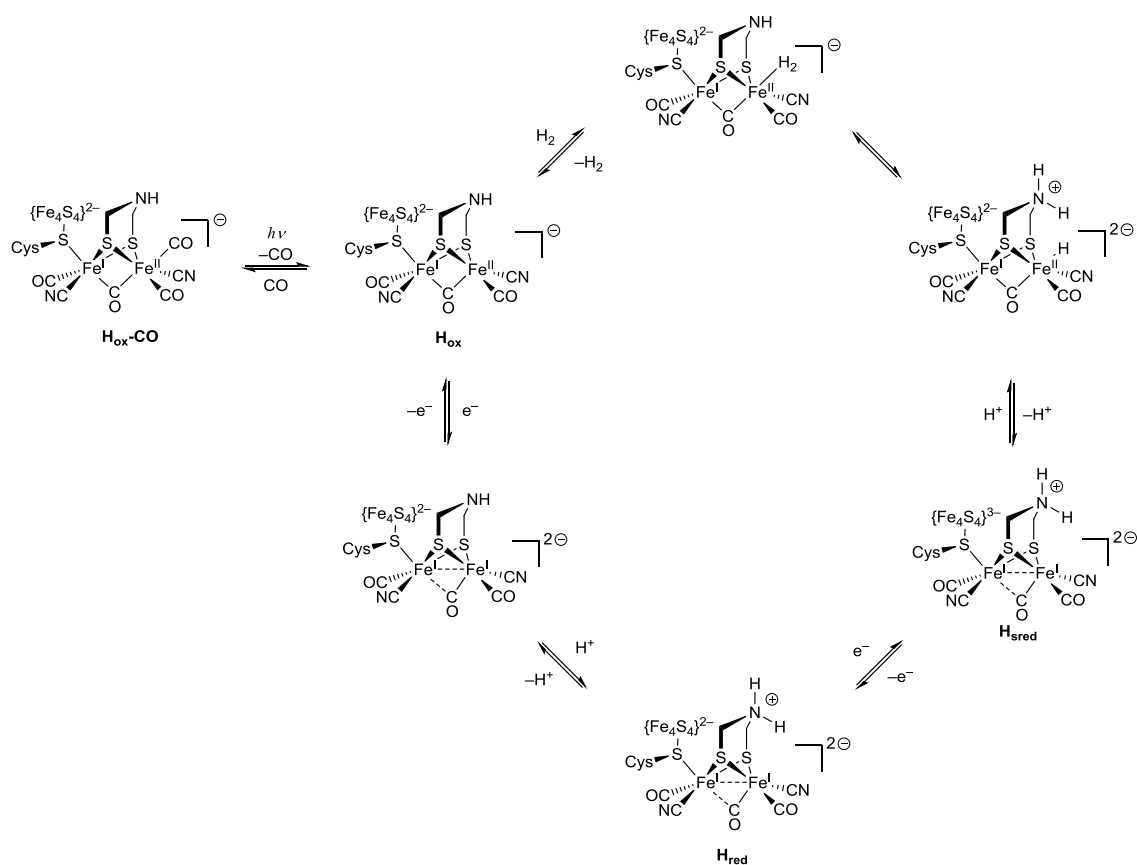


**Figure 3.1** Active site of  $[\text{FeFe}]$ -hydrogenase showing hydrogen bonding and other second coordination sphere interactions of the H-cluster in the hydrogenase from *Clostridium pasteurianum*. Reproduced from reference [91](#).

CHAPTER 3 | INTERACTION OF  $\text{Eu}(\text{fod})_3$  WITH COORDINATED CYANIDE  
IN AN ANALOGUE OF THE SUB-SITE OF  $[\text{FeFe}]$ -  
HYDROGENASE



**Scheme 3.1** States and proposed catalytic cycle of  $[\text{FeFe}]$ -Hydrogenase. Adapted from reference [92](#).

### 3.1.3 Synthesis, structural and spectroscopic aspects of the sub-site analogue $[\text{Fe}_2(\text{CO})_4(\text{CN})_2\text{pdt}]^{2-}$

The synthesis of the dianion  $[\text{Fe}_2(\text{CO})_4(\text{CN})_2\text{pdt}]^{2-}$  ( $\text{A}^{2-}$ ) as a tetraalkylammonium salt was first reported independently by three groups in 1999 [93-95](#). It was prepared by the reaction of  $[\text{Fe}_2(\text{CO})_6\text{pdt}]$  with the nucleophile  $\text{CN}^-$  in MeCN and isolated as a stable, water soluble, air sensitive salt [93-95](#), **Scheme 3.2**. An x-ray crystallographic study of  $[\text{Et}_4\text{N}]_2[\text{Fe}_2(\text{CO})_4(\text{CN})_2\text{pdt}]$  by Rauchfuss and co-workers showed that in the solid state the dianion  $\text{A}^{2-}$  was in the apical - basal isomeric conformation, **Figure 3.2**.

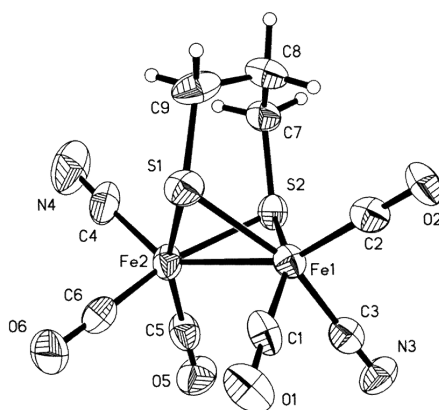
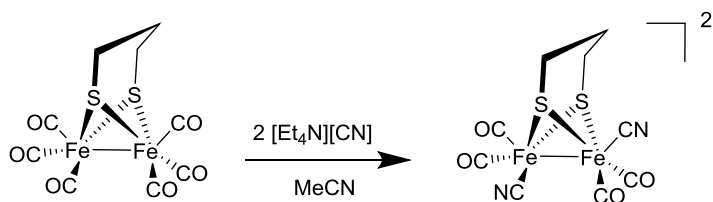


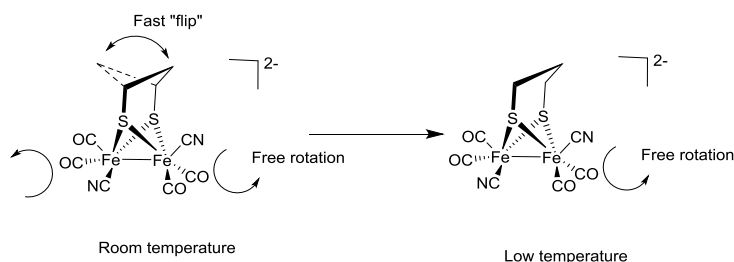
**Figure 3.2** Structure of  $(\text{Et}_4\text{N})_2[\text{Fe}_2(\text{CO})_4(\text{CN})_2\text{pdt}]$  [94](#).



**Scheme 3.2** Synthesis of  $(\text{Et}_4\text{N})_2[\text{Fe}_2(\text{CO})_4(\text{CN})_2\text{pdt}] \text{A}^{2-}$ .



This is clearly different from the disposition of the CN groups in the H-cluster which are deployed in the *trans* (*basal,basal*) configuration, **Figure 3.1**.  $^{13}\text{C}$  NMR spectroscopy at room temperature in MeCN showed a single resonance for ligated  $^{13}\text{CN}$  thus on the NMR time-scale the two cyanide ligands were in equivalent environments or averaged equivalent environments. This indicated that free turnstile rotation of the two  $[\text{Fe}(\text{CO})_2(\text{CN})]$  units must take place. However, on lowering the temperature to  $-40\text{ }^\circ\text{C}$  two cyanide resonances were observed.<sup>94</sup> This was explained as being consequence of the freezing-out of the fast ‘flip’ of the propanedithiolate bridge but not the turnstile rotation **Scheme 3.3**.



**Scheme 3.3** Effect of lowering temperature on the propanedithiolate bridge.

The solution infra-red of the complex in MeCN is shown in **Figure 3.3**. The pattern of this spectrum is essentially identical to that measured in  $\text{CH}_2\text{Cl}_2$ , in both solvents a single sharp cyanide band is observed near  $2075\text{ cm}^{-1}$ . Infra-red spectroscopy, unlike NMR is a fast technique and gives an ‘instantaneous’ measurement of the vibrational spectrum in solution. Four geometric isomers of  $\text{A}^{2-}$  are possible, these are the *trans*-

*(basal,basal)*, *cis-(basal,basal)*, *(apical,apical)* or *(apical-basal)* configurations. There has been no discussion of the nature of the distribution of geometric isomers present in solutions of  $\text{A}^{2+}$  in the literature. DFT calculations undertaken by Dr J. A Wright provided theoretical gas-phase IR data in the CO/CN region for the four isomers. The calculated spectra for these are illustrated in **Figure 3.4**. The best fit to the experimental pattern in the CO region is for the *cis-(basal, basal)* isomer.

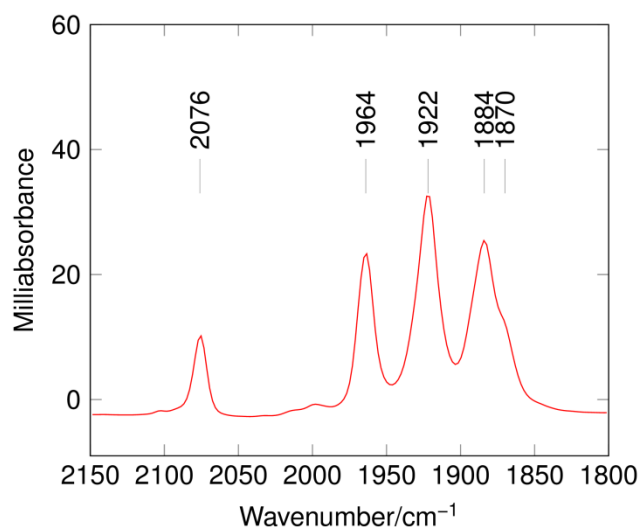


**Figure 3.3** IR of  $(\text{Et}_4\text{N})_2[\text{Fe}_2(\text{CO})_4(\text{CN})_2\text{pdt}]$  in MeCN.

CHAPTER 3 | INTERACTION OF  $\text{Eu}(\text{fod})_3$  WITH COORDINATED CYANIDE  
IN AN ANALOGUE OF THE SUB-SITE OF  $[\text{FeFe}]$ -  
HYDROGENASE

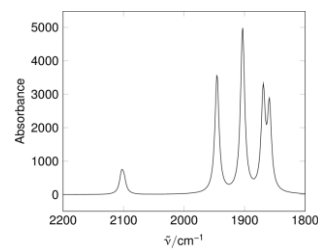
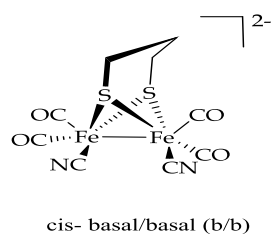
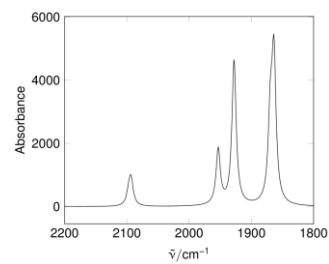
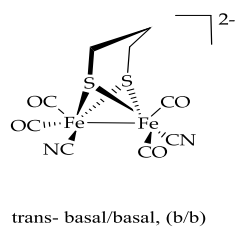
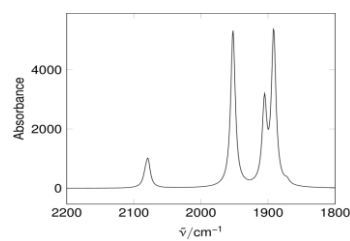
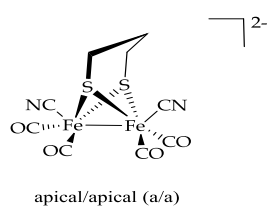
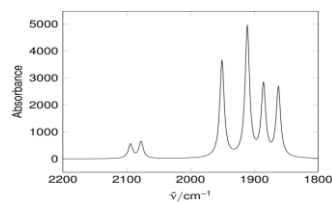
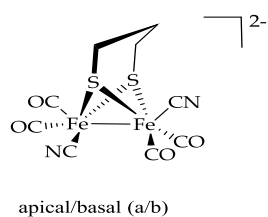


**Figure 3.4** IR spectra of isomers of  $[\text{Fe}_2(\text{CO})_4(\text{CN})_2\text{pdt}]^{2-}$  from DFT calculations.

### 3.1.4 Second coordination sphere interactions of [Fe<sub>2</sub>(CO)<sub>4</sub>(CN)<sub>2</sub>pdt]<sup>2-</sup> with triaryl boranes.

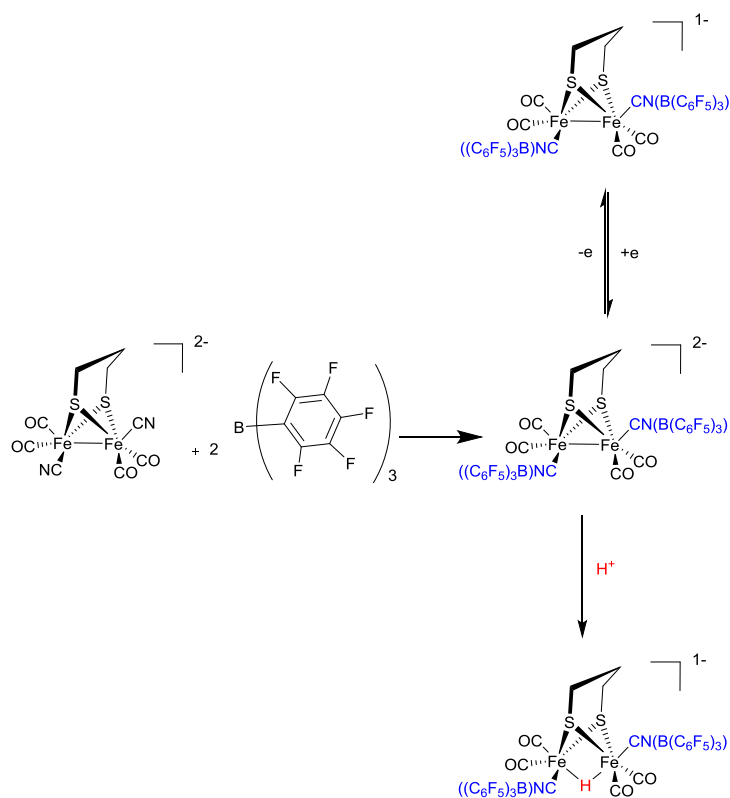
The general ability of coordinated cyanide to engage its nitrogen lone pair in bonding with another metal centre to form CN bridged structures has been introduced in **Chapter 1**. More specifically, the coordinated cyanide ligands in **A<sup>2-</sup>** possess a lone pair on their nitrogen atoms that is sufficiently basic to interact with protic solvents and to ion-pair with cations such as K<sup>+</sup>. Further consideration of hydrogen bonding to **A<sup>2-</sup>** is given in **Chapter 4**. In the context of the interactions of the Lewis acid Eu(fod)<sub>3</sub> that are discussed in this chapter, the reactions of **A<sup>2-</sup>** with boron based Lewis acids, as first reported by Rauchfuss and coworkers, is particularly relevant, **Scheme 3.4**. Notably, to date there are no reports of metal centred Lewis acid adducts of **A<sup>2-</sup>**.

The crystallographic structure of the adduct formed between **A<sup>2-</sup>** and two molecules of the triarylborane Lewis acid, B(C<sub>6</sub>F<sub>5</sub>)<sub>3</sub> is shown in **Figure 3.5**. In this structure the *apical basal* geometry of the parent dianion is retained. In addition, the CN, CO, FeFe bond lengths in the adduct are very similar to those in **A<sup>2-</sup>**. However, there is substantial shift in the CO and CN stretching frequencies observed in the solution FTIR spectrum. The  $\nu$  (CO) shifts to higher values which can be explained by the withdrawal of electron density from the iron atoms which reduces back bonding into the  $\pi^*$  antibonding orbitals of CO. The  $\nu$  (CN) stretches also shift to higher frequencies, this would also be consistent with diminished back donation into  $\pi^*$  antibonding orbitals of CN. Other triarylborane adducts with **A<sup>2-</sup>** were described and it was found that the shift in the CO

and CN frequencies to positive value was related to the Lewis acidity of the triarylborane. Thus the smallest shift observed was for  $\text{BPh}_3$  and the largest for  $\text{B}(\text{C}_6\text{F}_5)_3$ , see **Table 3.1** in **section 3.2**.

The formation of the triarylborane adducts has a considerable effect on the chemistry of the diiron unit. Whereas the protonation of  $\text{A}^{2-}$  leads to the formation of unstable species and to an insoluble coordination polymer <sup>96</sup>, protonation of the bis-(triarylborane) adducts can give stable bridging hydrides, **Scheme 3.4**. Similarly, whereas oxidation of  $\text{A}^{2-}$  is an irreversible process, the adduct  $[\text{Fe}_2(\text{CO})_4(\text{CN})_2\text{pdt}(\text{B}(\text{C}_6\text{F}_5)_3)_2]^{2-}$  undergoes a well-defined reversible one electron oxidation, **Scheme 3.4**.

CHAPTER 3 | INTERACTION OF  $\text{Eu}(\text{fod})_3$  WITH COORDINATED CYANIDE  
IN AN ANALOGUE OF THE SUB-SITE OF  $[\text{FeFe}]$ -  
HYDROGENASE



**Scheme 3.4** Binding of borane Lewis acid to cyanide ligands in a diiron dithiolate complex and the chemistry of this adduct. Adapted from reference 97. [97](#)

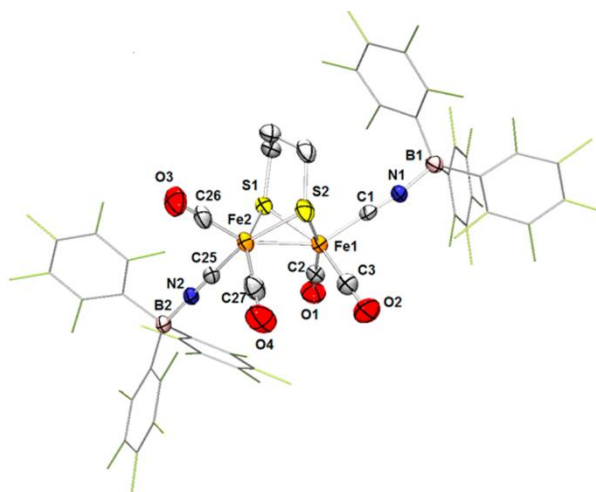


**Figure 3.5** Thermal ellipsoid plot of  $[\text{Fe}_2(\text{CO})_4(\text{CN})_2\text{pdt}(\text{BArF}_3)_2]^{2-}$  at 50% probability and with H atoms omitted for clarity. Pentafluorophenyl groups are deemphasized for clarity. Reported by Rauchfuss and co-workers <sup>97</sup>.

## 3.2 Results and discussion

### 3.2.1 The binding of Eu(fod)<sub>3</sub>, (tris -6,6,7,7,8,8,8-hepta-fluor-2,2-dimethyl-3,5-octanedionato-europium), to $[\text{Fe}_2(\text{CO})_4(\text{CN})_2(\text{pdt})]^{2-}$ , $\text{A}^{2-}$ .

#### 3.2.1.1 FTIR spectroscopy.

As discussed in **Chapter 2**, Eu(fod)<sub>3</sub> has Lewis acid properties and therefore we expected that it would bind to these cyanide ligands in  $\text{A}^{2-}$ . Evidence that this was the case was first obtained by FTIR spectroscopy.

**Figure 3.6** shows the evolution of the FTIR spectra in MeCN as the molar ratio of Eu(fod)<sub>3</sub> :  $\text{A}^{2-}$  is increased from 0.5 : 1 to 2.0 : 1. It can be seen that the carbonyl bands

are all shifted to higher frequencies whilst the single cyanide band initially present is split into two new bands after addition of two equivalents. A similar set of changes is observed when the titration is carried out in  $\text{CH}_2\text{Cl}_2$  as is shown by **Figure 3.7**. Note that there is very little change in the spectrum on increasing the ratio from 2 to 3 equivalents of  $\text{Eu}(\text{fod})_3$ . These results are fully consistent with the binding of two  $\text{Eu}(\text{fod})_3$  molecules to  $\text{A}^{2-}$ , with one  $\text{Eu}(\text{fod})_3$  at each of the cyanide ligands as represented in **Figure 3.8**.

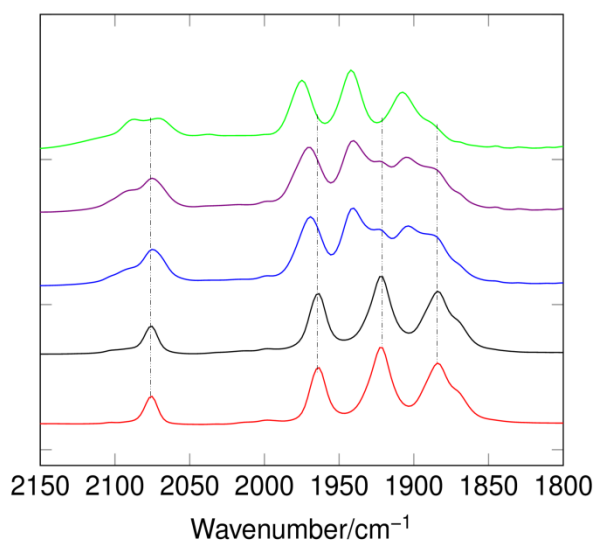


**Figure 3.6.** FTIR spectra of  $\text{A}^{2-}$ , red no  $\text{Eu}(\text{fod})_3$ , black 0.5 equivalents, blue 1 equivalents, violet 1.5 equivalents and green 2 equivalents of  $\text{Eu}(\text{fod})_3$  in MeCN.



CHAPTER 3 | INTERACTION OF  $\text{Eu}(\text{fod})_3$  WITH COORDINATED CYANIDE  
IN AN ANALOGUE OF THE SUB-SITE OF  $[\text{FeFe}]$ -  
HYDROGENASE

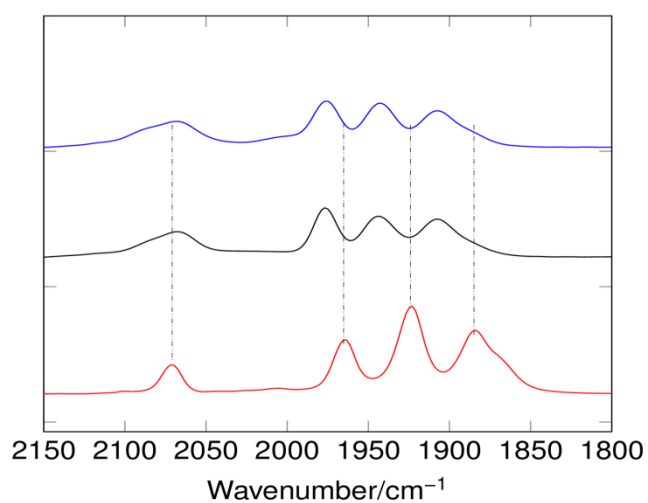


**Figure 3.7** FTIR spectra of  $\text{A}^{2-}$ , red no  $\text{Eu}(\text{fod})_3$ , black 2 equivalents and blue 3 equivalents of  $\text{Eu}(\text{fod})_3$  in  $\text{CH}_2\text{Cl}_2$ .

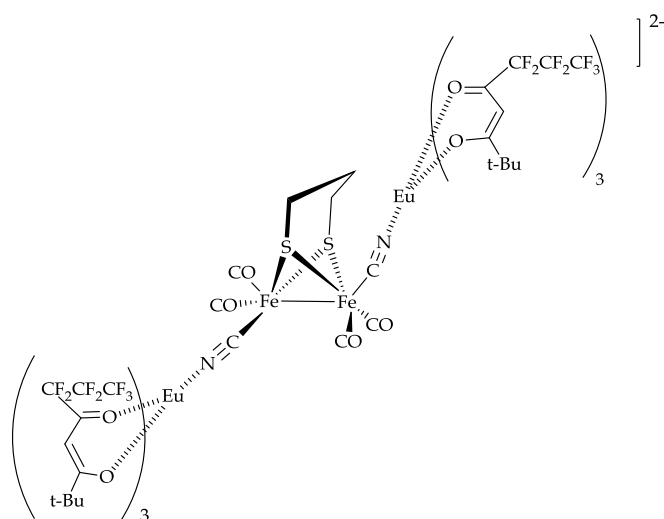


**Figure 3.8** . Proposed coordination arrangement of  $[\text{Fe}_2(\text{CO})_4(\text{CN})_2\text{pdt}]^{2-}$  with two equivalents of  $\text{Eu}(\text{fod})_3$ .

Further evidence that  $\text{Eu}(\text{fod})_3$  uniquely bound to the cyanide ligands was obtained by control experiments. **Figure 3.9** shows the FTIR spectra obtained for  $[\text{Fe}_2(\text{CO})_4(\text{PMe}_3)_2(\text{pdt})]$  alone and in the presence of two equivalents of  $\text{Eu}(\text{fod})_3$ . The spectra clearly superimpose showing that the Lewis acid does not interact with other basic sites in the molecule such as the metal-metal bond or the dithiolate sulfur ligands. Identical results were obtained using  $[\text{Fe}_2(\text{CO})_6(\text{pdt})]$ , no changes in the FTIR spectrum were observed in the presence of  $\text{Eu}(\text{fod})_3$ .

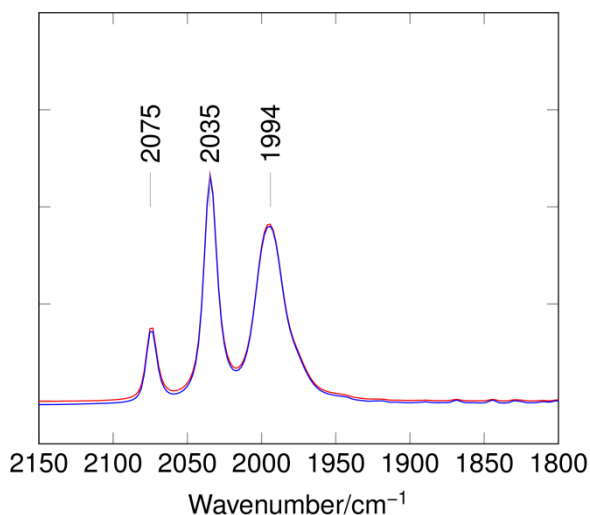


**Figure 3.9** IR Spectra of  $[\text{Fe}_2(\text{CO})_4(\text{PMe}_3)_2\text{pdt}]$  ; (blue) with and (red) without 2 equivalents of  $\text{Eu}(\text{fod})_3$  in MeCN.

**3.2.1.2 Isolation and characterisation of  $(\text{Et}_4\text{N})_2[\text{Fe}_2(\text{CO})_4(\text{CN})_2(\text{pdt})(\text{Eu}(\text{fod})_3)_2]$  by mass spectroscopy.**

As described in detail in the experimental section, the addition of one equivalent of the parent complex  $(\text{Et}_4\text{N})_2[\text{Fe}_2(\text{CO})_4(\text{CN})_2(\text{pdt})]$  in MeCN to two equivalents of  $\text{Eu}(\text{fod})_3$  in the same solvent at room temperature resulted in a rapid color change from dark red to orange. Reduction in the volume of the solvent and storage overnight at  $-20\text{ }^\circ\text{C}$  gave an orange powder. The elemental analysis (C,H,N) of this isolated material was consistent with the formulation  $(\text{Et}_4\text{N})_2[\text{Fe}_2(\text{CO})_4(\text{CN})_2(\text{pdt})(\text{Eu}(\text{fod})_3)_2]$  (see experimental).

Negative ion electrospray mass spectrometry from  $\text{CH}_2\text{Cl}_2/\text{MeOH}$  showed a high mass/charge set of peaks near 2565 as shown in **Figure 3.10**. The isotopic pattern is fully consistent with a monoanionic species containing both Eu and Fe isotopes in a ratio of 1:1. The mass distribution of the isotopes can be explained by loss of one counter ion  $[\text{Et}_4\text{N}]^+$ , 2 CO molecules and solvation by MeOH. Loss of CO is a common feature in the mass spectrometry of metal carbonyls.

### CHAPTER 3 | INTERACTION OF $\text{Eu}(\text{fod})_3$ WITH COORDINATED CYANIDE IN AN ANALOGUE OF THE SUB-SITE OF $[\text{FeFe}]$ -HYDROGENASE

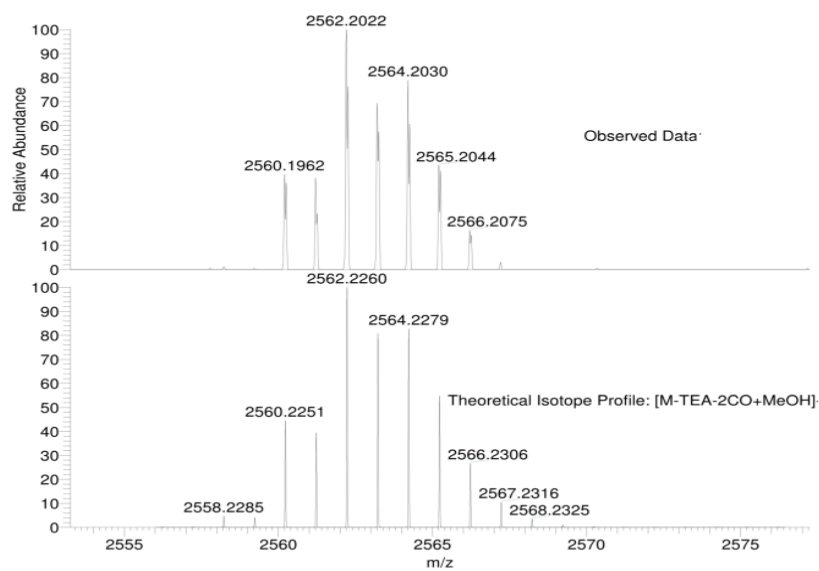
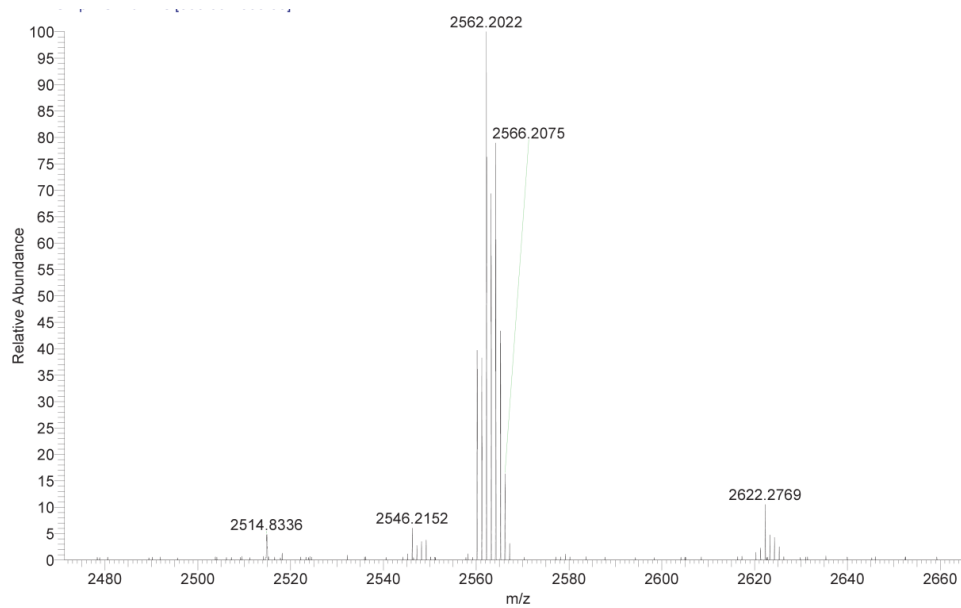


**Figure 3.10** Negative ion electrospray mass spectrum of  $(\text{Et}_4\text{N})_2[\text{Fe}_2(\text{CO})_4(\text{CN})_2(\text{pdt})(\text{Eu}(\text{fod})_3)_2]$ .

### 3.2.1.3 Further spectroscopic characterisations

#### of(Et<sub>4</sub>N)<sub>2</sub>[Fe<sub>2</sub>(CO)<sub>4</sub>(CN)<sub>2</sub>(pdt)(Eu(fod)<sub>3</sub>)<sub>2</sub>]

*NMR spectroscopy.* The <sup>1</sup>H NMR of the parent diiron dicyanide in CD<sub>3</sub>CN show peaks at 1.21 ppm for the 24 methyl protons of [(CH<sub>3</sub>CH<sub>2</sub>)<sub>4</sub>N]<sup>+</sup> and a peak at 3.17 ppm for 16 methylene protons of [(CH<sub>3</sub>CH<sub>2</sub>)<sub>4</sub>N]<sup>+</sup> in the cation. The protons for the the axial and equatorial SCH<sub>2</sub> in the propane dithiolate bridge of the complex [Fe<sub>2</sub>(CO)<sub>4</sub>(CN)<sub>2</sub>(pdt)] appear as a multiplet at 1.87 ppm (4H) and those for the methylene SCH<sub>2</sub>CH<sub>2</sub>CH<sub>2</sub>S protons show a multiplet at 1.68 ppm (2H) as shown in **Figure 3.11**. This is in accord with the reported literature data. <sup>93,94</sup> The <sup>1</sup>H NMR of Eu(fod)<sub>3</sub> recorded under the same conditions shows a sharp peak for the <sup>t</sup>Bu protons at -0.5ppm and a peak assigned to the methane protons at 7.3 ppm. On formation of the adduct of A<sup>2-</sup> with two equivalents of Eu(fod)<sub>3</sub> the chemical shifts of the [NEt<sub>4</sub>]<sup>+</sup> methyl and methylene protons are slightly shifted to 1.12 and 3.02 ppm respectively. This may reflect a change in the ion-pairing of the cation(s) and the dianion upon adduct formation. The <sup>t</sup>Bu and methine (CH) groups of Eu(fod)<sub>3</sub> are more significantly the affected former is shifted downfield to 0.69 ppm and the latter upfield to 3.31 ppm. This is in accord with observations made on dimeric [Eu(fod)<sub>3</sub>] linked by bidendate 2,2'-bipyrimidine ligands. <sup>98</sup> The methylene protons of the pdt ligand are no longer present at 1.87 and 1.68 ppm in the adduct. However a multiplet is observed at 3.12 ppm which overlaps with that for the [(CH<sub>3</sub>CH<sub>2</sub>)<sub>4</sub>N]<sup>+</sup> (2 x 8H) methylene protons, **Figure 3.11**. This resonance possibly results from a downfield shift of the SCH<sub>2</sub> and/or

CHAPTER 3 | INTERACTION OF  $\text{Eu}(\text{fod})_3$  WITH COORDINATED CYANIDE  
IN AN ANALOGUE OF THE SUB-SITE OF  $[\text{FeFe}]$ -  
HYDROGENASE

$\text{SCH}_2\text{CH}_2\text{CH}_2\text{S}$  protons. In summary, the dramatic changes observed in the  $^1\text{H}$  NMR when  $\text{Eu}(\text{fod})_3$  and  $\text{A}^{2-}$  are present in a 2:1 ratio provides further evidence for the formation of a tightly bound adduct  $[\text{Fe}_2(\text{CO})_4(\text{CN})_2(\text{pdt})(\text{Eu}(\text{fod})_3)_2]^{2-}$ .

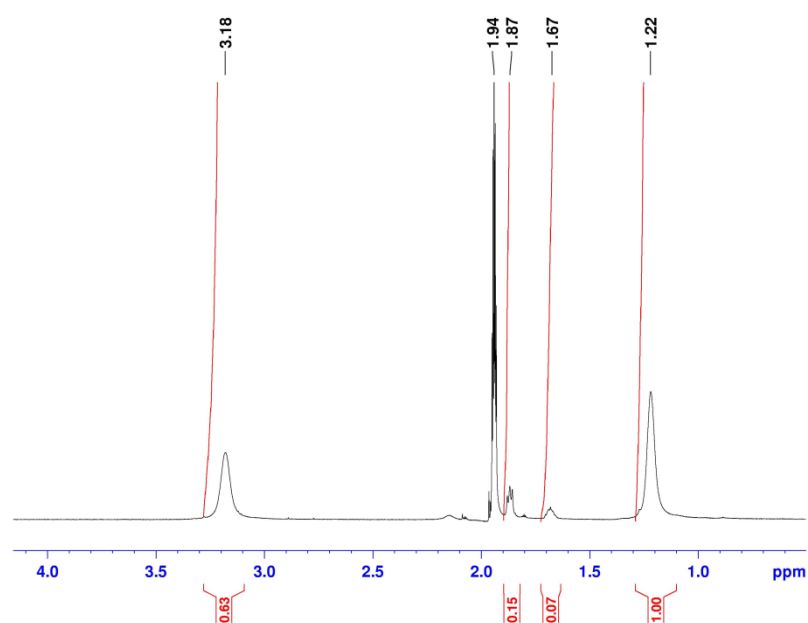


**Figure 3.11.** The  $^1\text{H}$  NMR of  $[\text{Fe}_2(\text{CO})_4(\text{CN})_2\text{pdt}]^{2-}$  in  $\text{CD}_3\text{CN}$ .

CHAPTER 3 | INTERACTION OF Eu(fod)<sub>3</sub> WITH COORDINATED CYANIDE  
IN AN ANALOGUE OF THE SUB-SITE OF [FeFe]-  
HYDROGENASE

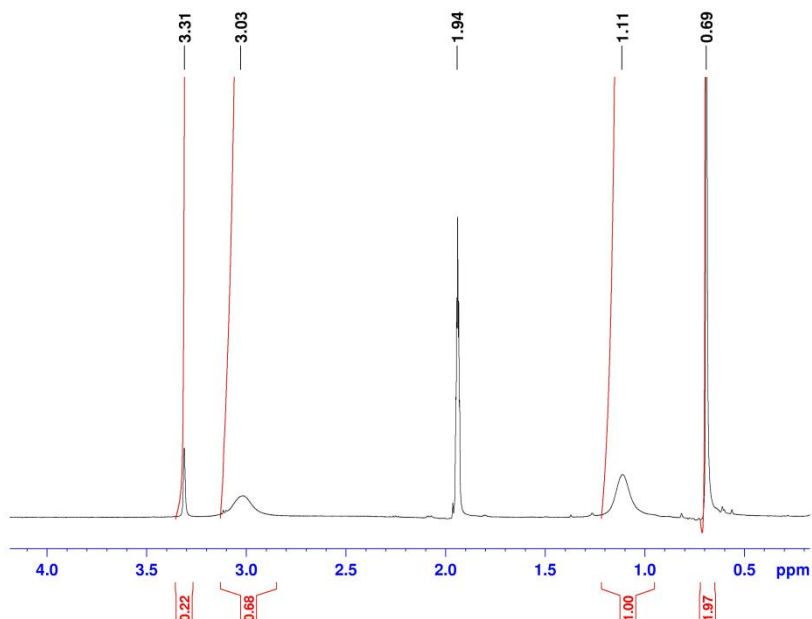


**Figure 3.12** The <sup>1</sup>H NMR of [Fe<sub>2</sub>(CO)<sub>4</sub>(CN)<sub>2</sub>pdt(Eu(fod)<sub>3</sub>)<sub>2</sub>]<sup>2-</sup> in CD<sub>3</sub>CN.

The (<sup>1</sup>H)<sup>19</sup>F - NMR for Eu(fod)<sub>3</sub> in CD<sub>3</sub>CN shows three peaks at -82.49 (3F, triplet), -127.32 (2F, multiplet) and -129.68 (broad singlet) ppm relative to CFC<sub>3</sub> which are assigned to the CF<sub>3</sub>CF<sub>2</sub>CF<sub>2</sub>, CF<sub>3</sub>CF<sub>2</sub>CF<sub>2</sub> and CF<sub>3</sub>CF<sub>2</sub>CF<sub>2</sub> fluorine groups respectively, **Figure 3.13 (a)**. This closely corresponds to previously reported experimental data shown in **Figure 3.13 (b)**.<sup>99</sup> After interaction with the cyanide complex in the ratio [Eu(fod)<sub>3</sub>] : [A<sup>2-</sup>] = 2 : 1, these resonances are slightly shifted to -81.62, -123.51 and -127.53 ppm respectively, **Figure 3.14**.

CHAPTER 3 | INTERACTION OF  $\text{Eu}(\text{fod})_3$  WITH COORDINATED CYANIDE  
IN AN ANALOGUE OF THE SUB-SITE OF  $[\text{FeFe}]$ -  
HYDROGENASE

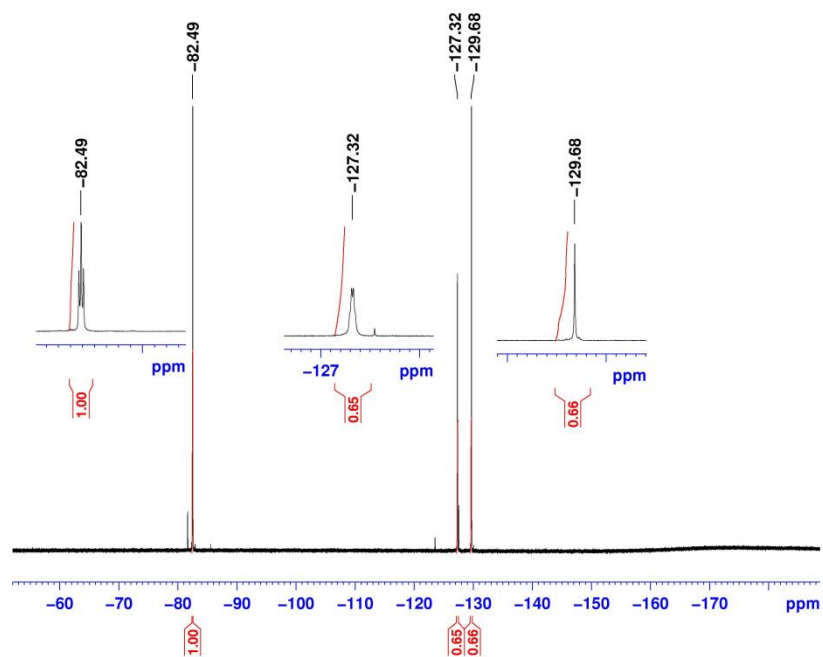


**Figure 3.13 (a)**  $^{19}\text{F}$  NMR of  $\text{Eu}(\text{fod})_3$  in  $\text{CD}_3\text{CN}$ .

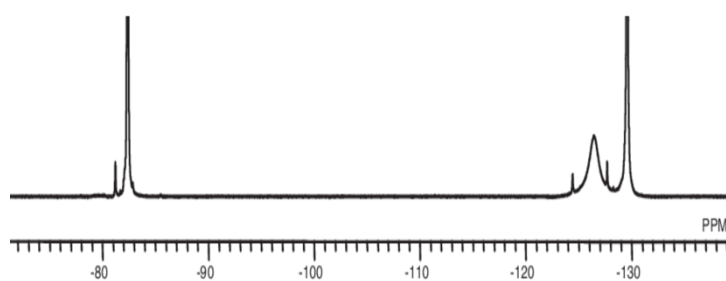


**Figure 3.13 (b)**  $^{19}\text{F}$  NMR of  $\text{Eu}(\text{fod})_3$  in  $\text{CD}_3\text{Cl}$ . Adapted from reference 98.<sup>99</sup>



CHAPTER 3 | INTERACTION OF  $\text{Eu}(\text{fod})_3$  WITH COORDINATED CYANIDE  
IN AN ANALOGUE OF THE SUB-SITE OF  $[\text{FeFe}]$ -  
HYDROGENASE

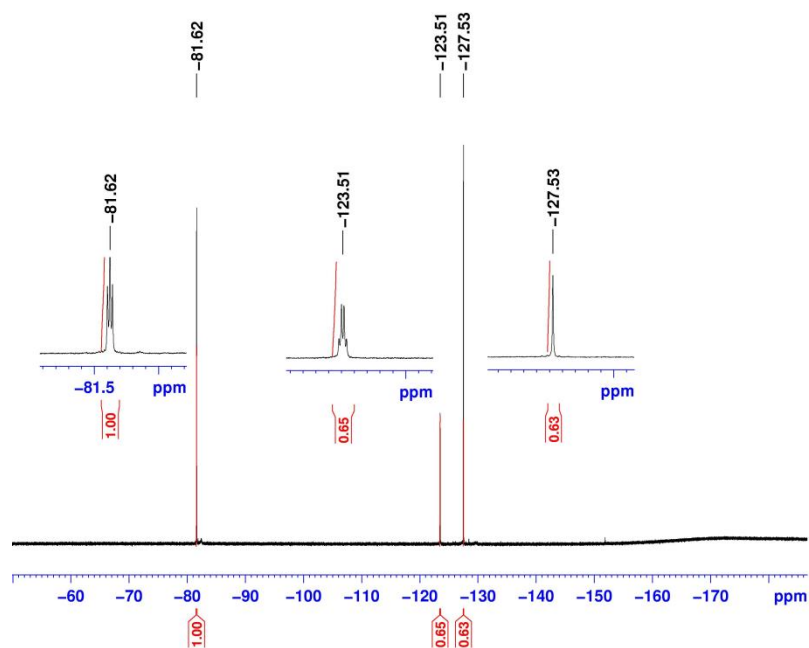


**Figure 3.14.**  $^{19}\text{F}$  NMR of  $[\text{Fe}_2(\text{CO})_4(\text{CN})_2\text{pd}(\text{Eu}(\text{fod})_3)_2]^{2-}$  in  $\text{CD}_3\text{CN}$ .

**UV-Visible spectroscopy.** A solution of Eu(fod)<sub>3</sub> in CH<sub>2</sub>Cl<sub>2</sub> has a strong absorption band at 296 nm with a molar extinction coefficient of  $1.912 \times 10^5 \text{ M}^{-1} \text{ cm}^{-1}$ . The complex [Fe<sub>2</sub>(CO)<sub>4</sub>(CN)<sub>2</sub>pdt]<sup>2-</sup>, **A**<sup>2-</sup>, shows a moderately strong absorption band at 355 nm with a corresponding molar extinction coefficient of  $1.25 \times 10^5 \text{ M}^{-1} \text{ cm}^{-1}$ , **Figure 3.15** and **Table 3.2**. The adduct formed in a CH<sub>2</sub>Cl<sub>2</sub> solution of 10 μM Eu(fod)<sub>3</sub> and 5 μM **A**<sup>2-</sup> (2: 1 molar ratio) shows the loss of the absorption at 355 nm associated with the parent diiron complex together with a small blue shift in the band of the Eu(fod)<sub>3</sub> chromophore to 293 nm. The band at 355 nm in the parent complex is associated with a transition from the HOMO which is the Fe-Fe bond to a Fe-Fe anti-bonding orbital ( $\delta \rightarrow \delta^*$ ), the LUMO or to a ligand based anti-bonding orbital.<sup>100</sup> The effect of adduct formation on this band can be explained by the removal of electron density from the diiron unit by the two Lewis acid Eu(fod)<sub>3</sub> groups which lowers the energy of the HOMO and thereby increases the energy gap between it and the acceptor orbital. This would result in a blue shift in the absorption peak which in our case is probably masked by the Eu(fod)<sub>3</sub> chromophore, **Figure 3.15**. The sensitivity of the energy of the transition to changes in the nature of the ligands around the Fe-Fe dithiolate core has been documented.<sup>101</sup> Thus it has been shown that replacing donor ligands by electron withdrawing ligands can result in a considerable blue shift. The sensitivity of the energy of the HOMO to changes in the coordination sphere has also been well-established by oxidation potential measurements.<sup>100</sup>

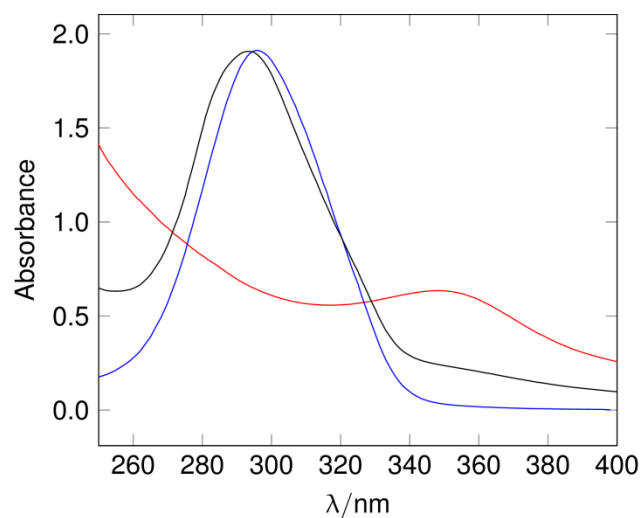


**Figure 3.15.** Absorption spectra of  $\text{Eu}(\text{fod})_3$ ,  $1.0 \times 10^{-5}$  M; (blue),  $[\text{Fe}_2(\text{CO})_4(\text{CN})_2\text{pdt}]^{2-}$ ,  $0.5 \times 10^{-5}$  M; (red) and  $[\text{Fe}_2(\text{CO})_4(\text{CN})_2\text{pdt}(\text{Eu}(\text{fod})_3)_2]^{2-}$ ; (1:2) (black) in  $\text{CH}_2\text{Cl}_2$ .

Compound	$\lambda_{\text{max}}$ /nm
$\text{Eu}(\text{fod})_3$	296
$[\text{Fe}_2(\text{CO})_4(\text{CN})_2\text{pdt}]^{2-}$	351
$[\text{Fe}_2(\text{CO})_4(\text{CN})_2\text{pdt}(\text{Eu}(\text{fod})_3)_2]^{2-}$	293

**Table 3.2** UV-Visible spectroscopic data.

**Fluorescence Spectroscopy.** The fluorescent spectroscopy of Eu(fod)<sub>3</sub> and other Eu(III) chelates has been widely studied [102,103, 104](#) and the general description of the electronic manifold associated with excitation and emission is represented by the Jablonski diagram shown in **Figure 3.16**. Thus after excitation to a vibrational level of the first excited singlet state, the Eu(III) chelate undergoes rapid internal conversion to lower vibrational levels through interaction with the solvent matrix. This excited singlet state can be deactivated radiatively (fluorescence), or undergoes intersystem crossing to the triplet system, which by internal conversion reaches the lowest triplet state. This state can combine radiatively with the ground state by means of a spin-forbidden transition giving rise to a typical long-lived molecular phosphorescence. Alternatively, the molecule can undergo a non-radiative transition from the triplet system to low lying f + f excited states. After this indirect excitation by energy transfer, the excited Eu(III) reaches the ground state by radiative or radiationless deactivation. Emission spectra correspond to the radiative deactivation of the <sup>5</sup>D<sub>0</sub> excited state to <sup>7</sup>F<sub>0-6</sub> ground states. The position of these lines is independent on the solvent but changes in relative intensities are solvent dependent. The experimental emission spectra of a 10 μM solution of Eu(fod)<sub>3</sub> in CH<sub>2</sub>Cl<sub>2</sub> after excitation at 296 nm gave four bands at 578, 588, 610 and 622 nm which are assigned to the f-f transitions <sup>5</sup>D<sub>0</sub>→<sup>7</sup>F<sub>0</sub>, <sup>5</sup>D<sub>0</sub>→<sup>7</sup>F<sub>1</sub>, <sup>5</sup>D<sub>0</sub>→<sup>7</sup>F<sub>2</sub>, and <sup>5</sup>D<sub>0</sub>→<sup>7</sup>F<sub>3</sub> respectively with the <sup>5</sup>D<sub>0</sub>→<sup>7</sup>F<sub>2</sub>, <sup>5</sup>D<sub>0</sub>→<sup>7</sup>F<sub>3</sub> emissions being the most intense. The corresponding emission spectrum of a 10 μM solution [Fe<sub>2</sub>(CO)<sub>4</sub>(CN)<sub>2</sub>pdt(Eu(fod)<sub>3</sub>)<sub>2</sub>]<sup>2-</sup> generated from **A**<sup>2-</sup> and two equivalents of

$\text{Eu}(\text{fod})_3$  is substantially changed. The emission bands for the adduct are observed at 535, 582, 588 (sh), 594 and 610 nm, **Figure3.17**.

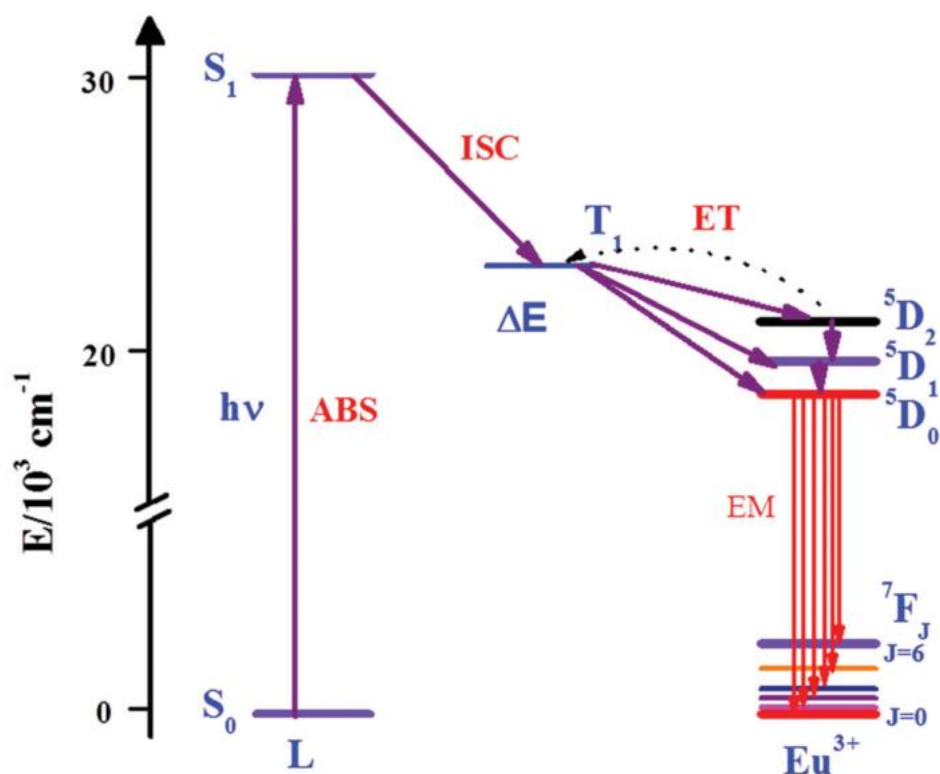


**Figure 3.16** Jablonski diagram for luminescent of  $\text{Eu}^{+3}$  complexes Taken from reference 101. [102](#).

In this case the emissions at 582 and 610 nm are the strongest and both of these are higher in intensity than the 588 and 610 nm bands in the parent  $\text{Eu}(\text{fod})_3$  emitter. Although we do not have an understanding of the observed changes in the emission spectrum it is evident that the loss in the intense emission at 588 nm in  $\text{Eu}(\text{fod})_3$  and its replacement by an intense emission at 582 nm signals the formation of the new 2:1 adduct.

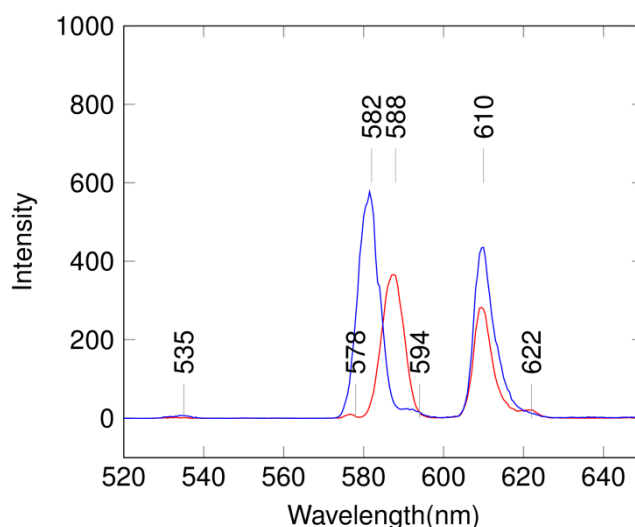


**Figure 3.17** Emission spectra of  $\text{Eu}(\text{fod})_3$  (red) and  $[\text{Fe}_2(\text{CO})_4(\text{CN})_2\text{pdt}(\text{Eu}(\text{fod})_3)_2]^{2-}$  (blue) 0.1 mM in  $\text{CH}_2\text{Cl}_2$ .

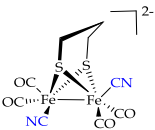
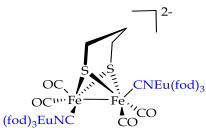
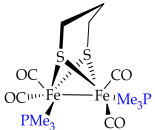
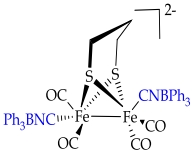
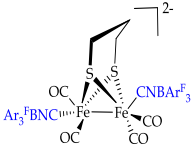
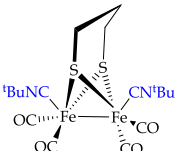
#### 3.2.1.4 Comparative infra-red spectroscopy

**Table 3.1** gives  $\nu(\text{CO})$  and (where measurable)  $\nu(\text{CN})$  data for di-iron dithiolate systems in which the terminal N of the cyanide is bound to an acceptor molecule. The effect on  $\nu(\text{CO})$  is first considered. It is evident that the addition of a Lewis acid to the

CHAPTER 3 | INTERACTION OF  $\text{Eu}(\text{fod})_3$  WITH COORDINATED CYANIDE  
IN AN ANALOGUE OF THE SUB-SITE OF [FeFe]-  
HYDROGENASE

nitrogen atom of ligated cyanide ligands in all the listed complexes invariably results in a shift of  $\nu(\text{CO})$  bands to higher frequencies. This is reasonably explained by the removal of electron-density from the FeFe core towards the N-bound Lewis acid which diminishes electron-density available for back-bonding from Fe  $d\pi$  orbitals into  $\text{CO } \pi^*$  orbitals and thus raises  $\nu(\text{CO})$ . The shift in  $\nu(\text{CO})$  to higher frequencies follows the order : none <  $\text{Eu}(\text{fod})_3$  <  $\text{BPh}_3$  <  $\text{B}(\text{C}_6\text{F}_5)_3$  <  ${}^t\text{Bu}^+$  corresponding to the expected increase in Lewis acidity - including, *in extremis*, the formation of the N-C covalent bond of the isocyanide  ${}^t\text{BuNC}$ . In terms of the average shift in  $\nu(\text{CO})$ , the effect of  $\text{Eu}(\text{fod})_3$  is quite similar to that of  $\text{BPh}_3$ , **Table 3.1**.

CHAPTER 3 | INTERACTION OF Eu(fod)<sub>3</sub> WITH COORDINATED CYANIDE  
IN AN ANALOGUE OF THE SUB-SITE OF [FeFe]-  
HYDROGENASE

Compound	Structure	$\nu$ CN cm <sup>-1</sup>	$\nu$ CO cm <sup>-1</sup>		
A <sup>2-</sup>		2076	1965	1923	1884 1872(sh)
(AEu(fod) <sub>3</sub> ) <sup>2-</sup>		2088 2069	1975	1945	1909
B <a href="#">105</a>			1979	1942	1898
(ABPh <sub>3</sub> ) <sup>2-</sup> <a href="#">97</a>		2137	1984	1946	1911
(ABAr <sup>F</sup> <sub>3</sub> ) <sup>2-</sup> <a href="#">97</a>		2136	1990	1954	1922
(A <sup>t</sup> Bu) <a href="#">18</a>		2145	1997	1972	1933

**Table 3.1** Infra-red  $\nu(\text{CN})$  and  $\nu(\text{CO})$  data for selected di-iron dithiolate species recorded in CH<sub>2</sub>Cl<sub>2</sub>.



The effect of binding an acceptor group to the terminal N-atom of ligated cyanide is now considered. In general terms, when a molecule  $\text{A}\equiv\text{B}-\text{M}$  (where M is a metal centre) coordinates to a metal  $\text{M}'$  centre (or other acceptor group) to give a complex  $\text{M}'-\text{A}\equiv\text{B}-\text{M}$ , two effects arise. Firstly, the frequency of  $\text{A}\equiv\text{B}$  stretching mode may increase due to mechanical coupling of the oscillators  $\text{M}'-\text{A}$  and  $\text{A}\equiv\text{B}$  which is usually referred to as kinematic coupling whereby the CN stretching vibration is impeded by the connection to two atoms. Secondly, the frequency of the  $\text{A}\equiv\text{B}$  stretching mode may decrease due to coordination, as a consequence of the weakening of the  $\text{A}\equiv\text{B}$  bond. Depending upon the factor which predominates, the  $\text{A}\equiv\text{B}$  stretching frequency of the coordinating molecule may decrease or increase. It has been argued that the bond weakening effect generally predominates resulting in a *decrease* in the  $\text{A}\equiv\text{B}$  stretching frequency. <sup>106</sup>

However, when the bond weakening is very small, kinematic coupling probably is the dominant factor resulting in an *increase* in the  $\text{A}\equiv\text{B}$  stretching frequency. Considering the experimental data given in **Table 3.1** a shift in  $\nu(\text{CN})$  to *higher* frequencies from that of  $\text{A}^{2+}$  is observed for all the complexes, *except* that of the  $\text{Eu}(\text{fod})_3$  adduct, and this parallels the order observed for  $\nu(\text{CO})$  which is  $\text{BPh}_3 < \text{B}(\text{C}_6\text{F}_5)_3 < \text{}^t\text{Bu}^+$ . It might therefore be argued that kinematic coupling predominates. However, this is unlikely to be the only contribution to the raising of  $\nu(\text{CN})$  since the order parallels that of Lewis acidity indicative of an electronic effect. It is perhaps more reasonable to argue that removal of electron density from the core diiron dithiolate assembly onto the Lewis acid, through the  $\sigma$  bonding framework of CN and Fe, diminishes back-bonding from

Fe  $d\pi$  into CN  $\pi^*$  anti-bonding orbitals, thereby raising  $\nu(\text{CN})$ . This explains the parallel order with  $\nu(\text{CO})$ . It is remarkable that in contrast to the other Lewis acids,  $\text{Eu}(\text{fod})_3$  adduct formation results in a lowering of  $\nu(\text{CN})$  from that of the parent cyanide, in addition two closely spaced bands are evident, **Table 3.1** and **Figure 3.6**. The presence of two  $\nu(\text{CN})$  stretches is explained by the adduct in solution being in basal-apical configuration. Eu(III) has ‘buried’ f-orbitals which are considered to be too low in energy to partake in covalent bonding to ligands and it is generally believed that bonding is predominately electrostatic in character. Polarisation across the Fe-C $\equiv$ N unit towards +Fe=C=N- would weaken the CN bond and lower  $\nu(\text{CN})$ , **Figure 3.3**. This polarization of charge would also explain the observed raising of  $\nu(\text{CO})$  as a consequence of diminished negative charge on iron leading to weaker backbonding interactions. There are several examples of cyanide bridged systems which show a lowering of  $\nu(\text{CN})$  relative to the unbridged parent cyanide. For example, the complexes  $[\text{Fe}_4\text{S}_4(\text{NCM}(\text{CO})_5)_4]^{2-}$  where M = Cr, Mo or W show  $\nu(\text{CN})$  decreased by 40-70  $\text{cm}^{-1}$  relative to that in the parent  $[\text{M}(\text{CO})_5(\text{CN})]^-$  complex.<sup>107</sup>

### 3.2.1.5 Electrochemistry studies

The cyclic voltammetry of  $[\text{Fe}_2(\text{CO})_4(\text{CN})_2\text{pdt}]^{2-}$  in MeCN - 0.2M  $[\text{Bu}_4\text{N}][\text{BF}_4]$  at a vitreous carbon electrode shows a major irreversible oxidation process with  $E_{p/2} = -0.17$  V *versus* Ag/AgCl followed by further secondary oxidation processes arising from products of the primary step. At a more positive potential near +1.3V a further major

irreversible oxidation is observed, **Figure 3.18**.  $\text{Eu}(\text{fod})_3$  was examined by cyclic voltammetry under similar conditions and was found to be electrochemically inactive over the potential range -0.50 to + 2.00 V *versus* Ag/AgCl .

In the presence of two equivalents of  $\text{Eu}(\text{fod})_3$  the primary irreversible oxidation of  $[\text{Fe}_2(\text{CO})_4(\text{CN})_2\text{pdt}]^{2-}$  is no longer observed. Instead, a new partially reversible one-electron process at  $E^\circ = 0.64$  V replaces the two electron oxidation step of the parent molecule, **Figure 3.19**. This is consistent with formation of the adduct  $[\text{Fe}_2(\text{CO})_4(\text{CN})_2\text{pdt}(\text{Eu}(\text{fod})_3)]^{2-}$ ,  $(\text{AEu}(\text{fod})_3)^{2-}$ . The shift in the oxidation process to a more positive potential is explained by lowering the energy of the HOMO by removal of charge from the diiron unit as has been observed for the borane adducts.<sup>97</sup> Similarly the  $\text{B}(\text{C}_6\text{F}_5)_3$  and other borane adducts also show an enhanced electrochemical reversibility for the primary oxidation as is observed with  $\text{Eu}(\text{fod})_3$ . Generally as the oxidation potential of a metal complex becomes more positive then resulting one-electron oxidized species is less stable as it more susceptible to nucleophilic attack. In the case of the Lewis acid adducts the converse appears to be true. This is possibly because adduct formation increases steric hindrance around the di-iron unit inhibiting attack by solvent, water or other nucleophiles. Examination of the cyclic voltammetry of  $(\text{AEu}(\text{fod})_3)^{2-}$  when it is generated in a  $\text{CH}_2\text{Cl}_2$  electrolyte reveals a well-defined reversible one-electron oxidation couple at  $E^\circ = -0.047$  V which is followed by a broad ill-defined feature near 0.33V and further oxidation process at 0.89V, **Figure 3.20** and **Figure 3.21**. The disparity between the oxidation potentials measure for  $(\text{AEu}(\text{fod})_3)^{2-}$

CHAPTER 3 | INTERACTION OF  $\text{Eu}(\text{fod})_3$  WITH COORDINATED CYANIDE  
IN AN ANALOGUE OF THE SUB-SITE OF  $[\text{FeFe}]$ -  
HYDROGENASE

in the two solvents is surprising and suggests the nature of the HOMO is remarkably solvent dependent. The small shift in the oxidation potential of  $(\text{AEu}(\text{fod})_3)^{2-}$  in  $\text{CH}_2\text{Cl}_2$  relative to the parent complex  $\text{A}^{2-}$  is perhaps more consistent with the small shift in  $\nu(\text{CO})$  to higher values observed in the FTIR spectrum.

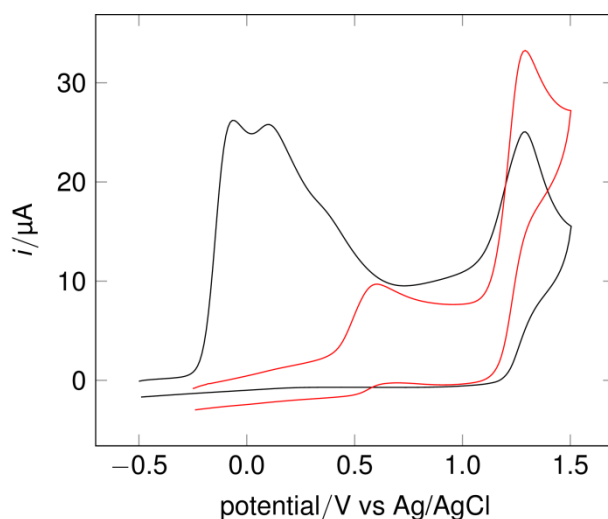


**Figure 3.18.** Cyclic voltammetry of 4.29 mM of  $[\text{Fe}(\text{CO})_4(\text{CN})_2\text{pdt}]^{2-}$  no  $\text{Eu}(\text{fod})_3$  (black), with 2eq of  $\text{Eu}(\text{fod})_3$  (red) in 0.2M  $[\text{Bu}_4\text{N}][\text{BF}_4]$  in MeCN. Scan rate = 100  $\text{mV s}^{-1}$ . electrode area =  $0.0707 \text{ cm}^2$ .

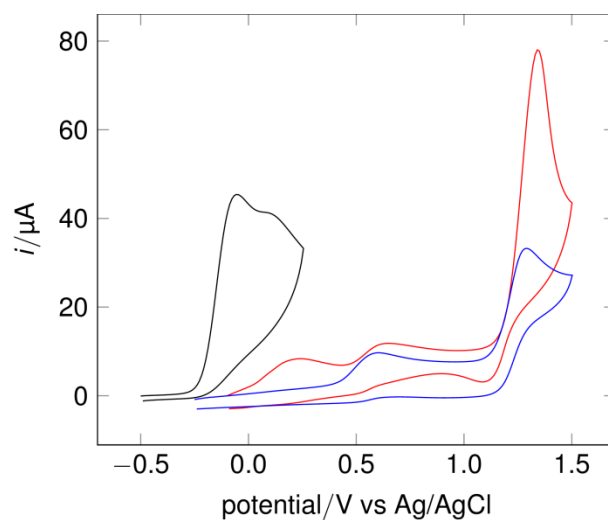


**Figure 3.19.** Cyclic voltammetry of 4.29 mM of  $\text{A}^{2-}$  no  $\text{Eu}(\text{fod})_3$  (black), with 2eq of  $\text{Eu}(\text{fod})_3$  1min (red) and 2eq of  $\text{Eu}(\text{fod})_3$  2 min (blue) in 0.2M  $[\text{Bu}_4\text{N}][\text{BF}_4]$ - MeCN. Scan rate =  $100 \text{ mVs}^{-1}$  ; electrode area =  $0.0707 \text{ cm}^2$ .

CHAPTER 3 | INTERACTION OF  $\text{Eu}(\text{fod})_3$  WITH COORDINATED CYANIDE  
IN AN ANALOGUE OF THE SUB-SITE OF  $[\text{FeFe}]$ -  
HYDROGENASE

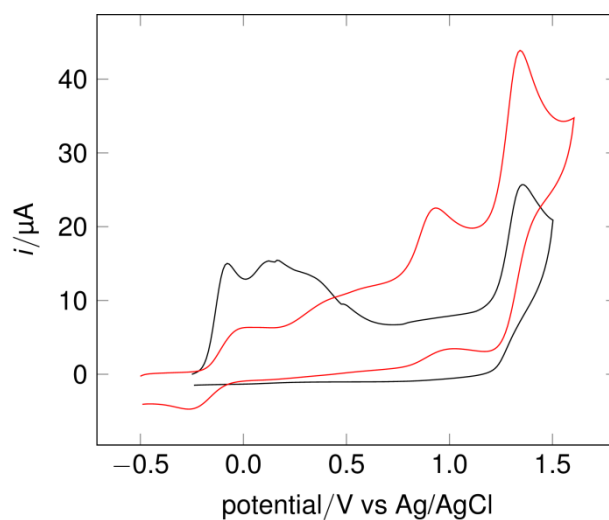


**Figure 3.20.** Cyclic voltammetry of 4.37 mM of  $\text{A}^{2-}$ , black before  $\text{Eu}(\text{fod})_3$  and red after 2eq of  $\text{Eu}(\text{fod})_3$  at  $100\text{mV s}^{-1}$  in  $0.2\text{M} [\text{Bu}_4\text{N}][\text{BF}_4] \text{-CH}_2\text{Cl}_2$ .

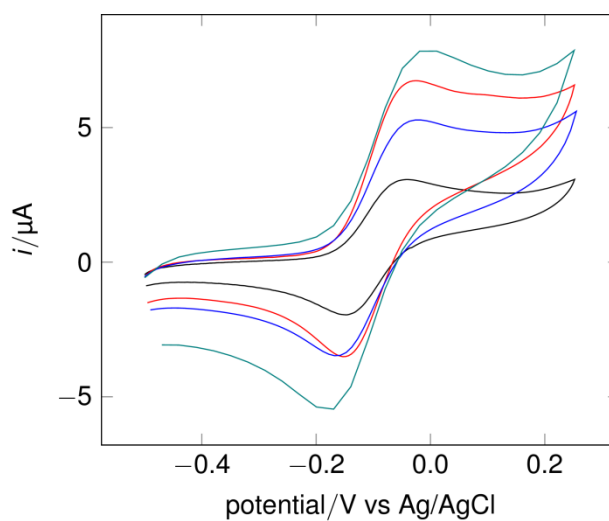


**Figure 3.21.** Cyclic voltammetry of 4.37 mM of  $(\text{AEu}(\text{fod})_3)^{2-}$  scan rate 25, 50, 100, 200  $\text{mV s}^{-1}$  in  $0.2\text{M} [\text{Bu}_4\text{N}][\text{BF}_4]$  in  $\text{CH}_2\text{Cl}_2$ .

		[Fe <sub>2</sub> (CO) <sub>4</sub> (CN) <sub>2</sub> pdt] <sup>2-</sup>	[Fe <sub>2</sub> (CO) <sub>4</sub> (CN) <sub>2</sub> pdt(Eu(fod) <sub>3</sub> ) <sub>2</sub> ] <sup>2-</sup>		
Solvent	E	E1(V)	E2 (V)	E3 (V)	
MeCN	-0.09	0.242	0.64	1	
CH <sub>2</sub> Cl <sub>2</sub>	-0.076	-0.047	0.33	0.89	

**Table 4.4** The CV data For (AEu(fod)<sub>3</sub>)<sup>2-</sup> in MeCN and CH<sub>2</sub>Cl<sub>2</sub>

### 3.2.1.6 Protonation of [Fe(CO)<sub>4</sub>(CN)<sub>2</sub>pdt(Eu(fod)<sub>3</sub>)<sub>2</sub>]<sup>2-</sup>

In earlier synthetic studies it was shown that protonation of **A**<sup>2-</sup> led to decomposition and clean product(s) could not be isolated, only an insoluble CO - free material thought to be a coordination polymer<sup>96</sup>. Stopped-flow studies with HBF<sub>4</sub>.Et<sub>2</sub>O in MeCN led to CO loss *unless* restricted to a narrow acid range of 2-3 equivalents at concentrations of 2-3 mM after mixing. A more extensive description of the stopped flow behavior of **A**<sup>2-</sup> with HBF<sub>4</sub>.Et<sub>2</sub>O in MeCN is provided in **Chapter 4**.

The effect of coordinating the cyanide ligands in **A**<sup>2-</sup> with Eu(fod)<sub>3</sub> has a dramatic effect on its reaction with HBF<sub>4</sub>.Et<sub>2</sub>O. The protection of the CN ligands by formation of [Fe<sub>2</sub>(CO)<sub>4</sub>(CN)<sub>2</sub>pdt(Eu(fod)<sub>3</sub>)<sub>2</sub>]<sup>2-</sup> allows stopped-flow protonation studies with a ten-fold excess of acid (0.5mM complex: 5mM acid), that is conditions which are close to being *pseudo*-first order in acid, without significant decomposition taking place.

However, at higher concentrations of acid considerable decomposition took place insofar as CO band intensities were considerably diminished. **Figure 3.22** shows a typical difference spectra obtained by stopped-flow FTIR upon mixing  $(\text{AEu}(\text{fod})_3)^{2-}$  and the acid. It is clearly seen that with increasing time (blue to red) the bands of the parent ‘cyanide protected’ Eu adduct at 1910, 1945, 1975  $\text{cm}^{-1}$  ( $\nu\text{CO}$ ) and 2071 and 2088  $\text{cm}^{-1}$  ( $\nu\text{CN}$ ) are depleted as shown by the negatively increasing absorbance bands in **Figure 3.22**. Correspondingly new bands progressively grow in intensity in the positive absorbance spectra of **Figure 3.22**. These bands are all at higher frequency than those of the parent complex  $(\text{AEu}(\text{fod})_3)^{2-}$  and occur at 1999, 2036, 2054  $\text{cm}^{-1}$  ( $\nu\text{CO}$ ) and 2132  $\text{cm}^{-1}$  ( $\nu\text{CN}$ ). The shift to higher frequency of the carbonyl bands and the band pattern is very similar to that observed upon protonation of well-defined di-iron dithiolate systems which give crystallographically characterized bridging hydride products. [55](#), [100](#), [108](#) For example, **Figure 3.23** shows the stopped-flow difference FTIR spectrum obtained for protonation of the thioether complex **D** under similar conditions in MeCN. Complex **D** has an apical arrangement of the thioether ligand with the  $\text{PMe}_3$  group in a basal position and this configuration is retained upon protonation to give the  $\mu$ -hydride  $(\text{D H})^+$ , **Figure 3.24**.



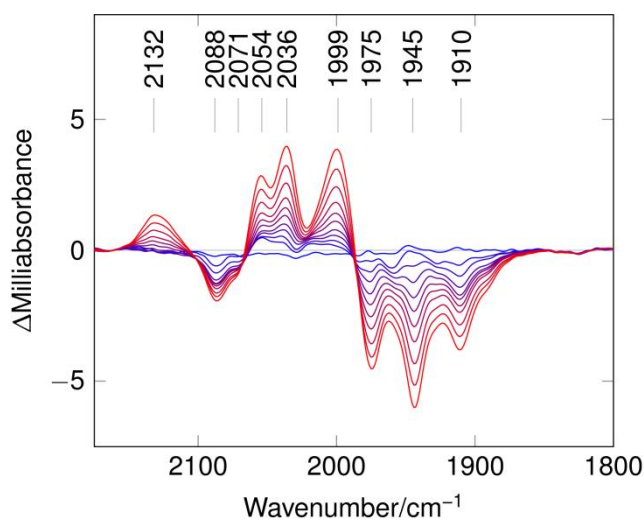


**Figure 2.22** Difference spectrum for stopped flow IR data for products of protonation of  $(\text{AEu}(\text{fod})_3)^{2-}$  0.5mM by  $\text{HBF}_4 \cdot \text{Et}_2\text{O}$  5mM (time scale 90ms) in MeCN.

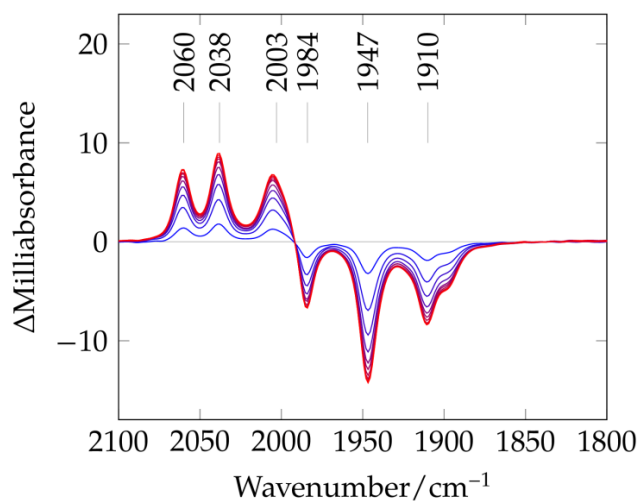


**Figure 3.23** Difference spectrum for stopped-flow IR data in the time range 80ms; **D** 0.05mM,  $[\text{HBF}_4 \cdot \text{Et}_2\text{O}]$  50mM in MeCN. Taken from reference 110. [55](#)

CHAPTER 3 | INTERACTION OF  $\text{Eu}(\text{fod})_3$  WITH COORDINATED CYANIDE  
IN AN ANALOGUE OF THE SUB-SITE OF  $[\text{FeFe}]$ -  
HYDROGENASE

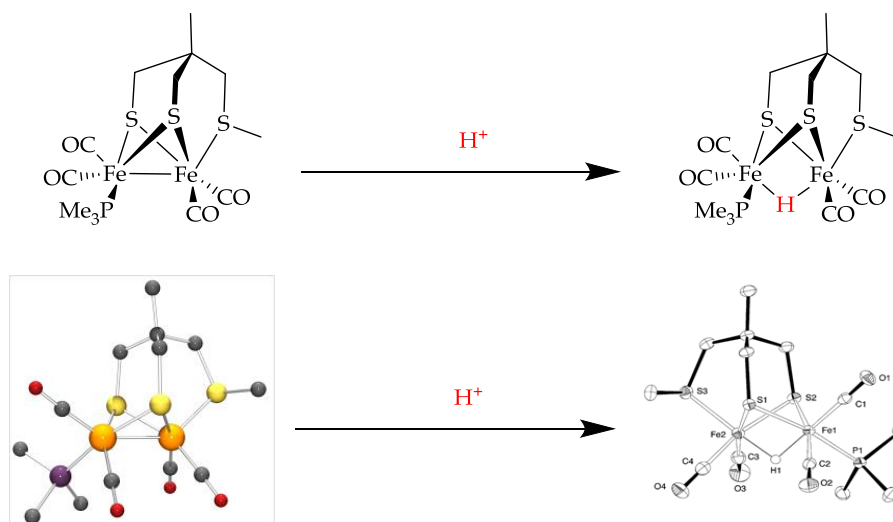


**Figure 3.24.** Protonation of **D** with x-ray structures. [55](#), [108](#)

This protonation product  $(\text{DH})^+$  has an infrared finger print closely similar to the spectrum generated on protonation of  $(\text{AEu}(\text{fod})_3)^{2-}$  (except of course CN bands are absent) **Table 3.5**, and we thus conclude that an analogous  $\mu$ -hydride  $(\text{AEu}(\text{fod})_3\text{H})^+$  is formed as represented by the reaction in **Figure 3.25**. **Table 3.5** also provides FTIR data for the protonation of some other diiron dithiolate systems. It is notable that protonation of the bis( $\text{PMe}_3$ ) complex **B** (**Table 3.5**) has been shown to proceed to give initially the *apical, basal*  $\mu$ -hydride  $(\text{BH})^+$  [109](#), [110](#) as in the formation of  $(\text{AEu}(\text{fod})_3\text{H})^+$  and  $(\text{DH})^+$ . However, on a longer timescale this rearranges to the *trans, basal-basal* isomer, **Figure 3.26**. [110](#) a process not observed in the stopped – flow protonation studies of  $(\text{AEu}(\text{fod})_3)^{2-}$  and **D**.

CHAPTER 3 | INTERACTION OF  $\text{Eu}(\text{fod})_3$  WITH COORDINATED CYANIDE  
IN AN ANALOGUE OF THE SUB-SITE OF  $[\text{FeFe}]$ -  
HYDROGENASE

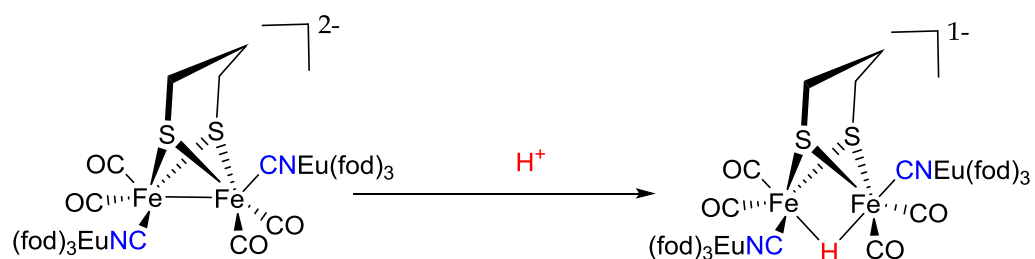


**Figure 3.25** Protonation of  $(\text{AEu}(\text{fod})_3)_2^{2-}$ .

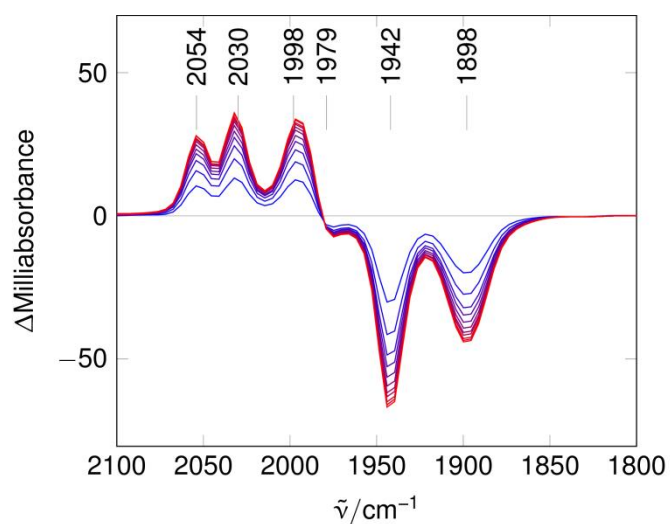


**Figure 3.26** Difference spectrum for stop-flow IR for product of protonation of **B** in the time range over time range 0.072 s,  $[\text{HBF}_4 \cdot \text{Et}_2\text{O}]$  25.0 mM. Adapted from reference 110. [110](#)

The time course data for the depletion infrared band at  $1910\text{ cm}^{-1}$  that is observed upon protonation of  $(\text{AEu}(\text{fod})_3)^{2-}$  is shown in **Figure 3.27**. The curve is bi-phasic and can be fit to a double exponential corresponding to two *pseudo* first-order rate constants of  $4.9 \pm 0.5 \times 10^{-3}\text{ s}^{-1}$  and  $1.8 \pm 0.2 \times 10^{-1}\text{ s}^{-1}$ . If we reasonably assume a first-order dependence on acid and a first-order dependence on complex then the second-order rate constants for the two processes are  $0.98 \pm 0.1\text{ M}^{-1}\text{s}^{-1}$  and  $36 \pm 4\text{ M}^{-1}\text{s}^{-1}$  respectively. The fast protonation step a value identical within error to that measured for the dithiolate thioether complex **D** this is perhaps not surprising as the electronic condition of the diiron unit as reflected by values of  $\nu(\text{CO})$  in the two structurally distinct molecules are very close, **Table 3.5**.

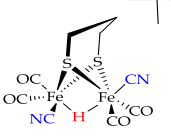
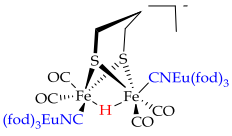
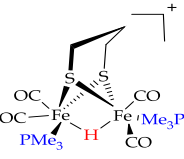
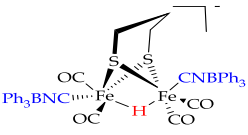
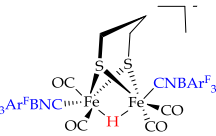
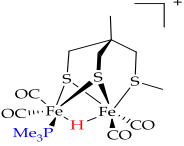
The growth of the band at  $2132\text{ cm}^{-1}$  follows the same bi-phasic pattern as that for the decay of the band at  $1910\text{ cm}^{-1}$  and this provides two corresponding second – order rate constants of  $0.97 \pm 0.1\text{ M}^{-1}\text{s}^{-1}$  and  $20 \pm 4\text{ M}^{-1}\text{s}^{-1}$ .

The second-order rate constants determined for the bi-phasic growth and decay of other bands in the stopped-flow FTIR spectrum of  $(\text{AEu}(\text{fod})_3)^{2-}$  following protonation are given in **Table 3.6**. They are consistent with formation of a single product concerted with the consumption of  $(\text{AEu}(\text{fod})_3)^{2-}$  in both the fast and slow processes. Although no intermediate species which builds up to a significant level was detected, small depletion bands at  $1959$  and  $1926\text{ cm}^{-1}$  are evident in the early stages of the reaction. It is possible that some reversible protonation at a basic sulfur site on the di-iron unit or at a basic oxygen site(s) on the  $\text{Eu}(\text{fod})_3$  unit occurs and that this results in a decrease

in basicity at the Fe-Fe bond, giving rise to the slower protonation step and the higher frequency depletion bands, **Figure 3.22**.

Earlier data on the reaction of  $\text{A}^{2-}$  with acid at low concentration shows that protonation of a cyanide ligand first takes place giving rise to  $\nu(\text{CO})$  bands at 1914, 1948 and 1979  $\text{cm}^{-1}$  which converts slowly to a  $\mu$ -hydride with  $\nu(\text{CO})$  bands at 1981, 2024, 2044  $\text{cm}^{-1}$  (see **Chapter 4** for more details). None of these bands match those observed in the stopped-flow protonation studies of  $(\text{AEu}(\text{fod})_3)^{2-}$  and we therefore conclude that decoordination of  $\text{Eu}(\text{fod})_3$  in the presence of acid to expose unprotected cyanide sites or the loss of  $\text{Eu}(\text{fod})_3$  following protonation do not occur. The results discussed here are therefore fully consistent with conservation of the attached  $\text{Eu}(\text{fod})_3\text{NCFe}$  units upon protonation of the Fe-Fe bond.

CHAPTER 3 | INTERACTION OF Eu(fod)<sub>3</sub> WITH COORDINATED CYANIDE  
IN AN ANALOGUE OF THE SUB-SITE OF [FeFe]-  
HYDROGENASE

Compound	Structure	$\nu$ CN cm <sup>-1</sup>	$\nu$ CO cm <sup>-1</sup>
AH <sup>-</sup>		2119	2044 2024 1983 <sup>a</sup>
(AEu(fod) <sub>3</sub> H) <sup>-</sup>		2132	2054 2036 1998 <sup>a</sup>
(BH) <sup>+</sup> <sup>105</sup>			2029 1989 <sup>b</sup>
(ABPh <sub>3</sub> H) <sup>-</sup> <sup>97</sup>		2180	2064 2043 2009 <sup>b</sup>
(ABAr <sup>F</sup> <sub>3</sub> H) <sup>-</sup> <sup>97</sup>		2185	2071 2051 2022 <sup>b</sup>
(DH) <sup>+</sup> <sup>55</sup>			2060 2038 2003

**Table 3.5** Infra-red  $\nu$ (CN) and  $\nu$ (CO) data for selected di-iron dithiolate product of protonation recorded in a (MeCN) or b (CH<sub>2</sub>Cl<sub>2</sub>) .

CHAPTER 3 | INTERACTION OF Eu(fod)<sub>3</sub> WITH COORDINATED CYANIDE  
IN AN ANALOGUE OF THE SUB-SITE OF [FeFe]-  
HYDROGENASE

Peak	t1 (s)	t2 (s)
1911	210	5.6
1999	240	8.4
2087	196	2.3
2132	206	9.9

**Table 4.6.** Kinetic Analysis for  $[\mu\text{HFe}_2(\text{CO})_4(\text{CN})_2\text{pdt}(\text{Eu}(\text{fod})_3)_2]^-$

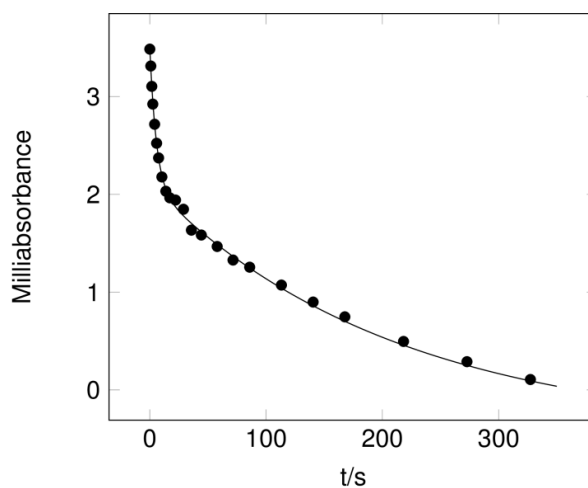


**Figure 3.27** Decay of IR band at  $1910\text{ cm}^{-1}$  over time following protonation of  $[\text{Fe}_2(\text{CO})_4(\text{CN})_2\text{pdt}(\text{Eu}(\text{fod})_3)_2]^{2-}$  0.5 mM,  $[\text{HBF}_4\cdot\text{Et}_2\text{O}]$  5 mM in MeCN (circles); pseudo-second order fit (line).

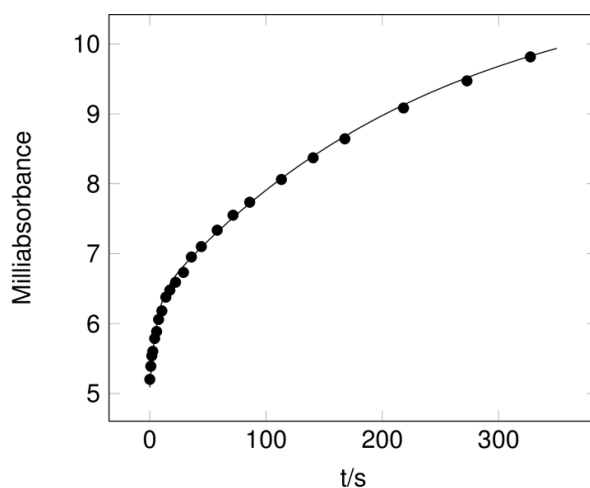


**Figure 3.28:** Growth of IR band at  $1999\text{ cm}^{-1}$  over time following protonation of  $[\text{Fe}_2(\text{CO})_4(\text{CN})_2\text{pdt}(\text{Eu}(\text{fod})_3)_2]^{2-}$   $0.5\text{ mM}$ ,  $[\text{HBF}_4\cdot\text{Et}_2\text{O}]$   $5\text{ mM}$  in MeCN (circles); pseudo-second order fit (line).

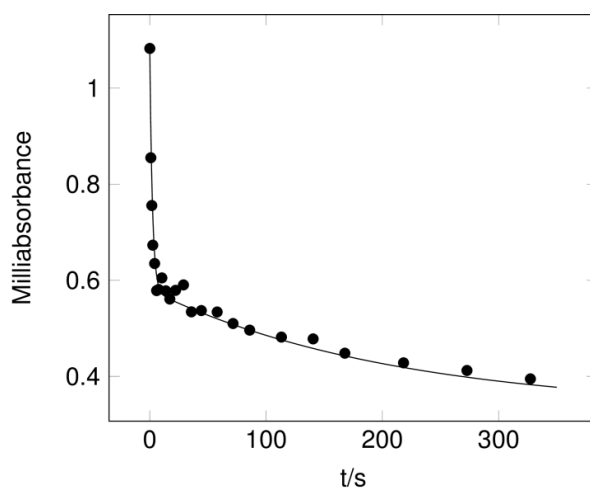


**Figure 3.29 .** Decay of IR band at  $2078\text{ cm}^{-1}$  over time following protonation of  $[\text{Fe}_2(\text{CO})_4(\text{CN})_2\text{pdt}(\text{Eu}(\text{fod})_3)_2]^{2-}$   $0.5\text{ mM}$ ,  $[\text{HBF}_4\cdot\text{Et}_2\text{O}]$   $5\text{ mM}$  in MeCN . (circles); pseudo-second order fit (line).



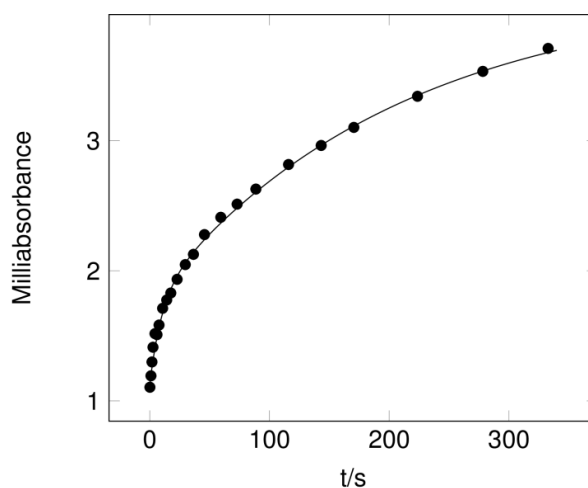


**Figure 3.30** Growth of IR band at  $2132\text{ cm}^{-1}$  over time following protonation of  $[\text{Fe}_2(\text{CO})_4(\text{CN})_2\text{pdt}(\text{Eu}(\text{fod})_3)_2]^{2-}$   $0.5\text{ mM}$ ,  $[\text{HBF}_4\cdot\text{Et}_2\text{O}]$   $5\text{ mM}$  in  $\text{MeCN}$ . . (circles); pseudo-second order fit (line).

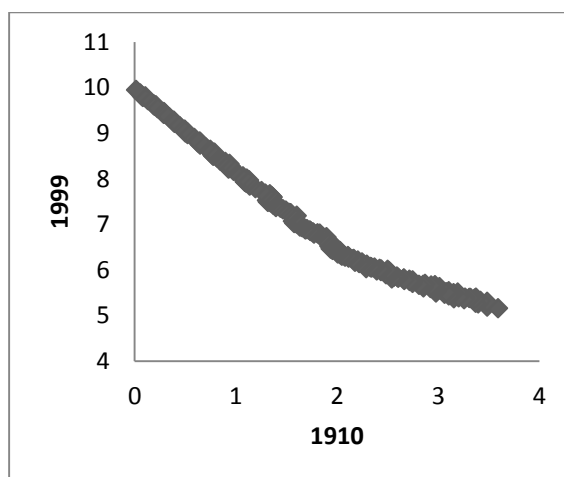


**Figure 3.31** Plot of peaks at  $1910\text{ cm}^{-1}$  against  $1999\text{ cm}^{-1}$ .

CHAPTER 3 | INTERACTION OF  $\text{Eu}(\text{fod})_3$  WITH COORDINATED CYANIDE  
IN AN ANALOGUE OF THE SUB-SITE OF  $[\text{FeFe}]$ -  
HYDROGENASE

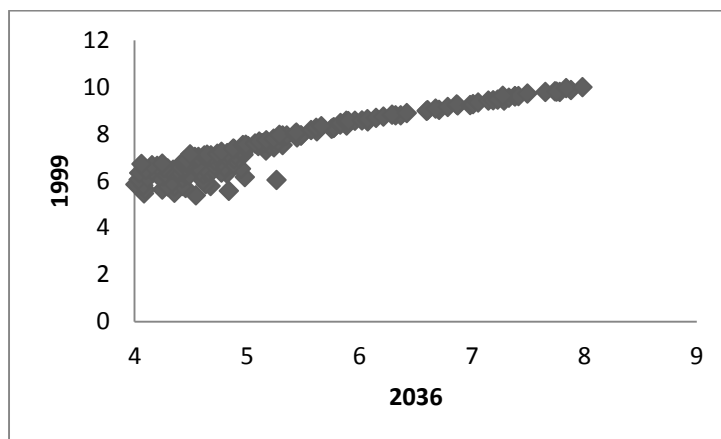


**Figure 3.32** Plot of peaks at  $2036 \text{ cm}^{-1}$  against  $1999 \text{ cm}^{-1}$ .

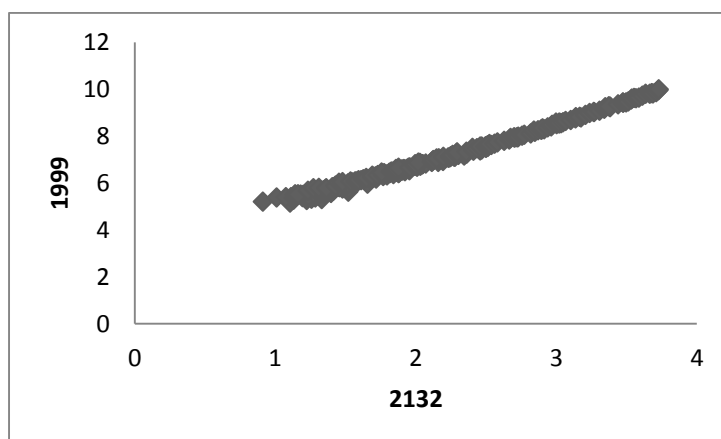


**Figure 3.33** Plot of peaks at  $2132 \text{ cm}^{-1}$  against  $1999 \text{ cm}^{-1}$ .

### 3.3 Experimental:

All experimenters were carried out under an atmosphere of nitrogen using standard Schlenk and cannula techniques or in a conventional nitrogen-filled glove-box. Dichloromethane and acetonitrile were refluxed over calcium hydride, all solvents were freshly distilled and degassed prior to use.  $\text{Eu}(\text{fod})_3$  was purchased from Sigma Aldrich and complex  $[\text{Et}_4\text{N}]_2[\text{Fe}_2(\text{CO})_4(\text{CN})_2\text{pdt}]$ , ( $[\text{Et}_4\text{N}]_2\text{A}$ ) complex was synthesized following the literature procedures. [93](#), [94](#) [111](#)

#### 3.3.2 Synthesis of $(\text{Et}_4\text{N})_2[\text{Fe}_2(\text{CO})_4(\text{CN})_2\text{pdt}(\text{Eu}(\text{fod})_3)_2]$

A solution of  $\text{Eu}(\text{fod})_3$  (0.150 g, 0.145 mmole) in fresh distilled dichloromethane was added to a solution of  $(\text{Et}_4\text{N})_2[\text{Fe}_2(\text{CO})_4(\text{CN})_2\text{pdt}]$  (0.0324g, 0.050 mmole) in dichloromethane. The resulting solution was stirred and cool down at  $-20\text{ }^\circ\text{C}$  then filtrated; the orange product was washed with hexane to give 0.165g (90%). Anal. Calcd for  $\text{C}_{85}\text{H}_{106}\text{N}_4\text{F}_{42}\text{O}_{16}\text{S}_2\text{Fe}_2\text{Eu}_2$  (found): C %, 37.55 (38.16); H %, 3.93 (3.91); N %, 1.89 (2.06). IR (MeCN): 2088, 2071, 1975, 1945, 1910  $\text{cm}^{-1}$ .  $^1\text{H-NMR}$  ( $\text{CD}_3\text{CN}$ ):  $\delta$  0.69 ppm (s, 54H), 1.12 ppm (s, 16 H), 3.02 ppm (s, 16H), 3.31ppm (s, 6H).  $^{19}\text{F NMR}$  ( $\text{CD}_3\text{CN}$ ):  $\delta$  -81 ppm, 62 (t), -123.51 ppm (t), -127.53 ppm (s). Mass [M-TEA-2CO + MeOH] 2562.2022 found (2562.2260).

#### 3.3.3 Stopped flow measurements

Stock solutions for stopped flow were prepared in a Belle Technology glove box (oxygen concentration  $< 10$  ppm), and were adjusted by dilution with acetonitrile. IR

measurements were carried out using a Tgk stopped-flow drive interfaced to a Bruker Vertex 80 spectrometer equipped with a custom-built flow cell (path length = 50  $\mu\text{m}$ ) fitted with  $\text{CaF}_2$  windows (Tgk Scientific). The drive unit was located inside the glove box, with the reagents carried to the cell prior to mixing via a flexible conduit. The cell itself was mounted in a miniature anaerobic chamber fixed inside the sample compartment of the IR instrument. The conduit and cell were set to  $21.0 \pm 0.2$  °C using a Thermo Scientific recirculating bath. Mixing of the two solutions occurred in a chamber within the cell body. The initial concentration of substrate was typically 0.50 mM after mixing. A Northumbria Optical Coatings filter (pass band 4.76 to 5.60  $\mu\text{m}$ ) was fitted in front of the cell, within the sample chamber. The stopped-flow system was controlled using the Tgk KinetaDrive and Bruker Opus 3D packages. IR data was processed and analysed using the Fit\_3D application and curve fitting was carried out using SciDAVis. Data were normally collected at 4  $\text{cm}^{-1}$  resolution. Typically between 60 and 180 time points were recorded for each experiment.

#### **3.3.4 NMR experiments:**

NMR spectra were recorded on Bruker Ascend 500 MHz spectrometers at 298 K; chemical shifts are referenced to the residual proton impurity of the deuterated solvent ( $^1\text{H}$  NMR/  $^{19}\text{F}$  NMR)

The NMR solvents were purchased from Cambridge isotope, stored under nitrogen over molecular sieves.

### 3.3.5 Electrochemical measurements

Cyclic voltammetry measurements were carried out in 0.2 M  $[\text{Bu}_4\text{N}][\text{BF}_4] - \text{MeCN}$  using a three compartment cell fitted with a glassy carbon working electrode (diameter 3 mm), a platinum counter electrode and a Ag/AgCl reference electrode interfaced with an Autolab PGSTAT302N potentiostat using the GPES software package.

### 3.3.6 UV-Vis Absorption Spectroscopy

UV-Vis absorption experiment was performed on UV-VIS-NIR spectrophotometer *Varian Cary 500* in double beam mode. All experiments were performed at room temperature ( $\sim 25^\circ\text{C}$ ).  $\text{Eu}(\text{fod})_3$  was dissolved in  $\text{CH}_2\text{Cl}_2$ .

## CHAPTER 4. HYDROGEN BONDING INTERACTIONS OF TRIS AND BIS UREA AND THIOUREAS WITH CYANIDE LIGANDS IN AN ANALOGUE OF THE SUB-SITE OF [FeFe]-HYDROGENASE

### 4.1 Introduction

#### 4.1.1 General aspects

The wider context of hydrogen-bonding in chemical systems was discussed in the Introduction, **Chapter 1** together with specific hydrogen-bonding interactions of cyanide ligands at the diiron subsite of [FeFe]-hydrogenase. This chapter is concerned with how such hydrogen -bonding interactions can be introduced around synthetic diiron subsites by substituted di- and tri (thio) ureas anion receptors and how this perturbs the electronic and spectroscopic properties of the di-iron unit.

In the simple cyanide complex  $K_4[Fe(CN)_6]$  a well-defined solid state structure has been reported which shows the capacity of cyanide ligands to engage in hydrogen bonding to a macrocyclic amine molecule, **Figure 4.1** [112](#).

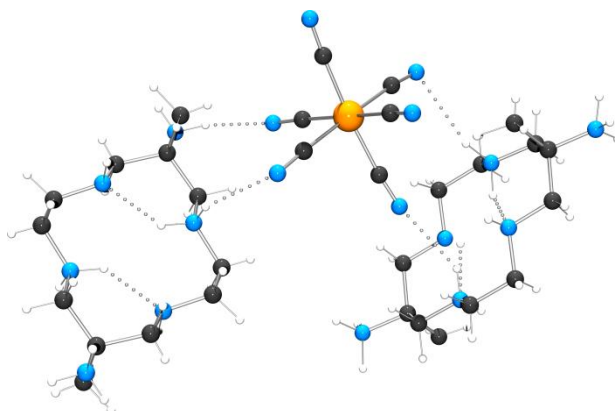


**Figure 4.1.** Solid state structure of hydrogen bonding of cyanide ligands to a macrocyclic amine molecule . Reproduced from reference 112 (white spheres H; blue spheres N; black spheres C; orange sphere Fe)<sup>112</sup>

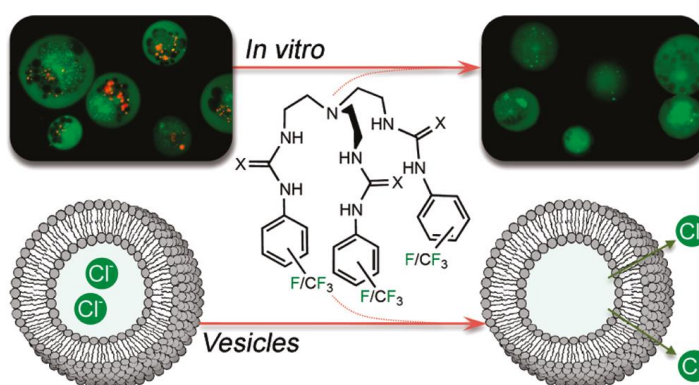
However, hydrogen bonding interactions with cyanide in [FeFe]-subsite analogues have not reported, although Lewis acid binding has been demonstrated by Rauchfuss and coworkers using various triaryl boranes acceptors<sup>97</sup>, this is discussed in more detail in **Chapter 3**.

#### 4.1.2 Hydrogen bonding of substituted (thio)ureas to simple anions.

The specific approach taken in this work was to explore the potential binding properties of certain bis- and tris- (thio)ureas to the synthetic subsite analogue  $[\text{Fe}_2(\text{CO})_4(\text{CN})_2\text{pdt}]^{2-} \text{A}^{2-}$  for the following reasons.

It was reported by the group of Gale and coworkers that certain tris -ureas and – thioureas can very tightly bind anionic ligands such as chloride, nitrate, and sulphate and this provided a means for transporting these ions across bi-lipid membranes, as

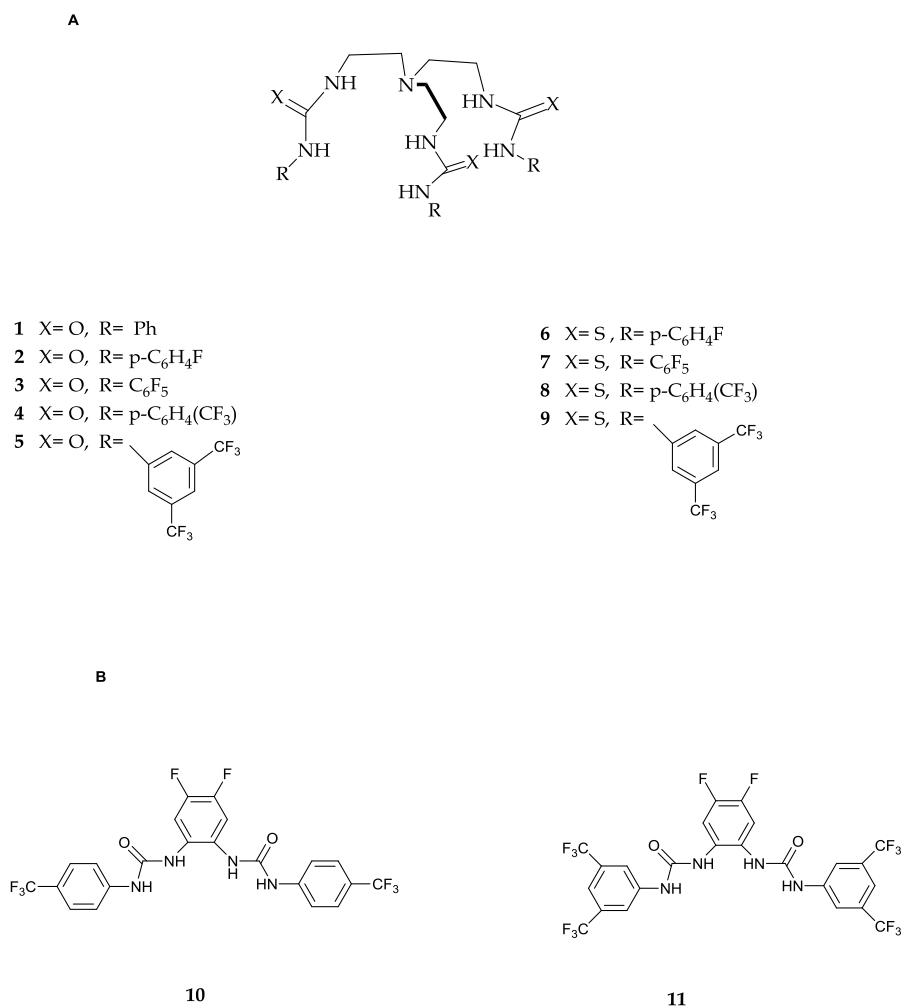
illustrated in **Scheme 4.1** <sup>113</sup>. Particularly effective in transporting such anions were tris- and bis (thio)ureas receptors possessing electron-withdrawing fluoro-substituent groups. It was therefore thought that such molecules might also be able to interact with *ligated* cyanide(s) in the dianionic synthetic subsite. We are indebted to Professor Gale for supplying us with a wide range of tris- and bis-(thio)ureas the structures of which are shown in **Scheme 4.2** together with the annotation of the formula.



**Scheme 4.1.** Anion transport across bi-lipid membranes facilitated by urea and thioureas <sup>113</sup>.



CHAPTER 4 | HYDROGEN BONDING INTERACTIONS OF TRIS AND BIS UREA AND THIOUREAS WITH CYANIDE LIGANDS IN AN ANALOGUE OF THE SUB-SITE OF [FeFe]-HYDROGENASE



**Scheme 4.2.** General structure of the substituted tris- (thio)ureas (A) and bis- ureas (B) compounds studied in this work.

The range of binding modes of tris(thio) ureas to simple anions based upon the X-ray crystallographic structures are shown in **Figure 4.2.** <sup>113</sup> Notably the structural data

shows that oxy-anion binding can involve 1 or 2 (thio)ureas. What is also clear from the structural data is the multiple H-bonding interactions occur. This is not surprising in the case of the carbonate, sulphate and nitrate oxyanions, but the ‘wrapping-up’ of the chloride ligand was especially attractive in terms of possible interactions of the ‘pseudo-halide’ cyanide in the [FeFe]-hydrogenase subsite analogue.

The strength of hydrogen bonding in an arrangement YH...X is generally considered to parallel the acidity of the YH bond. Thus increasing electron-withdrawing groups on the (thio)urea backbone might be expected to enhance hydrogen bonding. [114,115](#) Gale and co-workers have obtained extensive information on the binding of chloride and other anions to the (thio)ureas by NMR studies. [113](#) **Table 4.1** summarises the binding (association) constant data ( $K_a$ ) for  $\text{Cl}^-$  with a range of (thio)ureas in water. Two general observations are evident from this data. First,  $K_a$  for the ureas has a relatively narrow range of less than one order of magnitude (166 – 882)  $\text{M}^{-1}$  with the least acidic (unsubstituted) urea binding more tightly. Secondly, although the NH groups in thioureas experimentally more acidic than are their urea analogues [116,117, 118](#), they are significantly less tightly binding to  $\text{Cl}^-$  [113](#).

CHAPTER 4 | HYDROGEN BONDING INTERACTIONS OF TRIS AND BIS UREA AND THIOUREAS WITH CYANIDE LIGANDS IN AN ANALOGUE OF THE SUB-SITE OF [FeFe]-HYDROGENASE

Thio(urea)	Association Constants $K_a(M^{-1})$
1	882
2	575
3	166
4	405
5	517
6	179
7	128
8	156
9	-

**Table 4.1.** Association constants  $K_a$  ( $M^{-1}$ ) for the binding of (thio)urea receptors with  $Cl^-$  in DMSO- $d_6$  and water. [113](#)

The explanation for the lack of correlation of  $K_a$  with acidity probably lies with the equilibrium involving breaking water-urea  $NH\dots OH_2$  hydrogen bonds, these are likely to be stronger the greater the acidity of the (thio)urea [119,120,121](#) and thus the net free-energy involved upon  $Cl^-$  bonding will be decreased. [113](#)

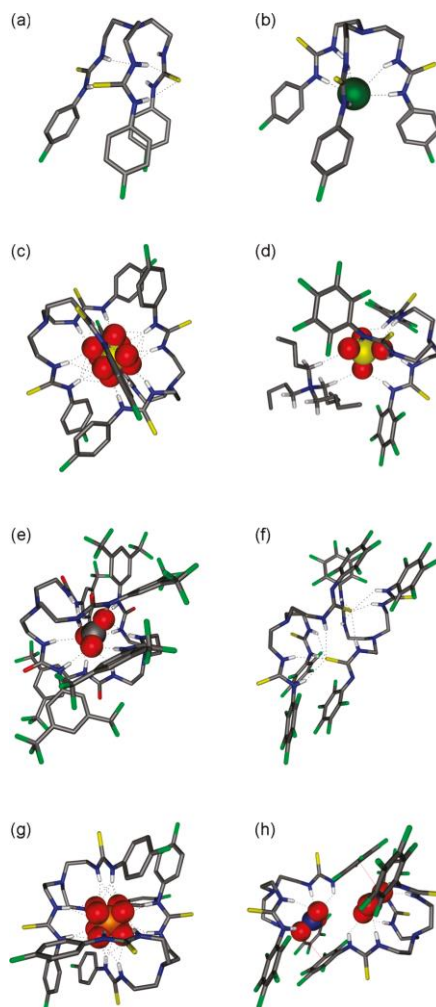


**Figure 4.2.** X-ray crystal structures of **5**, **6**, and **7** with a variety of anionic guests. C (gray), H(white), N(blue), S (yellow), O(red), F (green), Cl(dark green), P (orange). (a) **6**; (b) **6** ⊃ Cl; (c) (**6**)<sub>2</sub> ⊃ SO<sub>4</sub><sup>2-</sup>; (d) **7** ⊃ SO<sub>4</sub><sup>2-</sup> .TBA (e) (**5**)<sub>2</sub> ⊃ CO<sub>3</sub><sup>2-</sup>; (f) (**7-H**)<sub>2</sub>; (g) (**6**)<sub>2</sub> ⊃ HPO<sub>4</sub><sup>2-</sup>; (h) (**8**⊃NO<sub>3</sub>)<sub>2</sub>. [113](#)

The ability of these ligands to coordinate by multiple hydrogen bonds, due to the nature the acidic of NH, is one of the most important properties of these compounds [122,123,124,125, 126](#).

### 4.1.3 Probing H-bonding interactions by FTIR spectroscopy:

FTIR spectroscopy provides a useful way of probing second coordination sphere effects on synthetic subsite analogues, specifically  $[\text{Fe}_2(\text{CO})_4(\text{CN})_2\text{pdt}]^{2-}$  because both  $\nu(\text{CN})$  and  $\nu(\text{CO})$  are sensitive to changes in the distribution of electron-density within the dianion. As charge is removed towards 'acidic' hydrogen bonding groups this can have the effect of diminishing backbonding to the  $\pi$ -acid CO ligands, raising the frequency of their vibrations. Shifts in  $\nu(\text{CN})$  to higher frequencies can also occur as back bonding is diminished but CN is also sensitive to charge removed through the sigma bonding framework which can *weaken* the CN triple bond and thereby lower the stretching frequency. The balance of weakening back-donation *versus* weakening the  $\sigma$ -bond can thus lead to shifts in  $\nu(\text{CN})$  to lower or higher frequencies [127,128, 129](#). A classic example of how the electron-density on a complex can perturb  $\nu(\text{CN})$  is shown by the change observed between tetra-anionic ferrocyanide and tri-anionic ferricyanide, in the solid state the former shows  $\nu(\text{CN})$  at  $2041\text{ cm}^{-1}$  the latter shows  $\nu(\text{CN})$  at  $2116\text{ cm}^{-1}$  [130](#).

Before hydrogen bonding effects of the various ureas and thioureas on FTIR spectra are interpreted, it was important to determine general solvent effects on  $\nu(\text{CN})$  and  $\nu(\text{CO})$ , particularly how aqueous and non-aqueous protic and aprotic solvents affect the stretching frequencies of the coordinated diatomic ligands in the subsite analogue.

## 4.2 Result and discussion

### 4.2.1 Solvent effects on $\nu(\text{CN})$ and $\nu(\text{CO})$ in $[\text{Et}_4\text{N}]_2[\text{Fe}_2(\text{CO})_4(\text{CN})_2\text{pdt}]$ .

**Figure 4.3** shows a typical spectrum in the  $\nu(\text{CO}) / \nu(\text{CN})$  region for  $[\text{Fe}_2(\text{CO})_4(\text{CN})_2\text{pdt}]^{2-}$ ,  $\text{A}^{2-}$ , recorded in MeCN. In all solvents, the basic pattern for the  $\nu(\text{CO})$  stretches are similar, three strong bands are observed together with small shoulder on the lowest frequency absorption, in MeOH this shoulder is not resolved.

**Table 4.1** lists FTIR  $\nu(\text{CN})$  and  $\nu(\text{CO})$  data all of which have been independently measured. Those in MeCN <sup>93</sup> and  $\text{CH}_2\text{Cl}_2$  <sup>97</sup> are concordant with previously reported data. It is evident that in the weakly hydrogen bonding solvents DMF, MeCN and  $\text{CH}_2\text{Cl}_2$  the differences in  $\nu(\text{CN})$  and  $\nu(\text{CO})$  frequencies are relatively small,  $\leq 5 \text{ cm}^{-1}$ , but nevertheless significant.

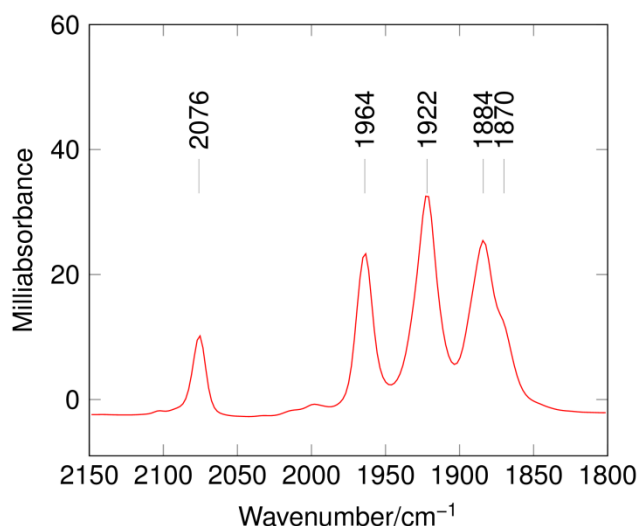


**Figure 4.3.** FTIR spectra of  $\text{A}^{2-}$  in MeCN.

$[\text{Fe}_2(\text{CO})_4(\text{CN})_2\text{pdt}]^{2-}, \text{A}^{2-}$					
Solvent	$\nu\text{CN cm}^{-1}$	$\nu\text{CO cm}^{-1}$			
H <sub>2</sub> O	2052	1984	1950	1914	1870(sh)
D <sub>2</sub> O	2065	1978	1947	1909	1870(sh)
MeOH	2054	1977	1941	1906	not resolved
DMF	2077	1962	1917	1882	1865(sh)
CH <sub>3</sub> CN	2076	1964	1922	1884	1870(sh)
CH <sub>2</sub> Cl <sub>2</sub>	2071	1965	1923	1884	1869(sh)
CH <sub>3</sub> CN/HBF <sub>4</sub>	2105	1980	1950	1916	1900(sh) <sup>96</sup>

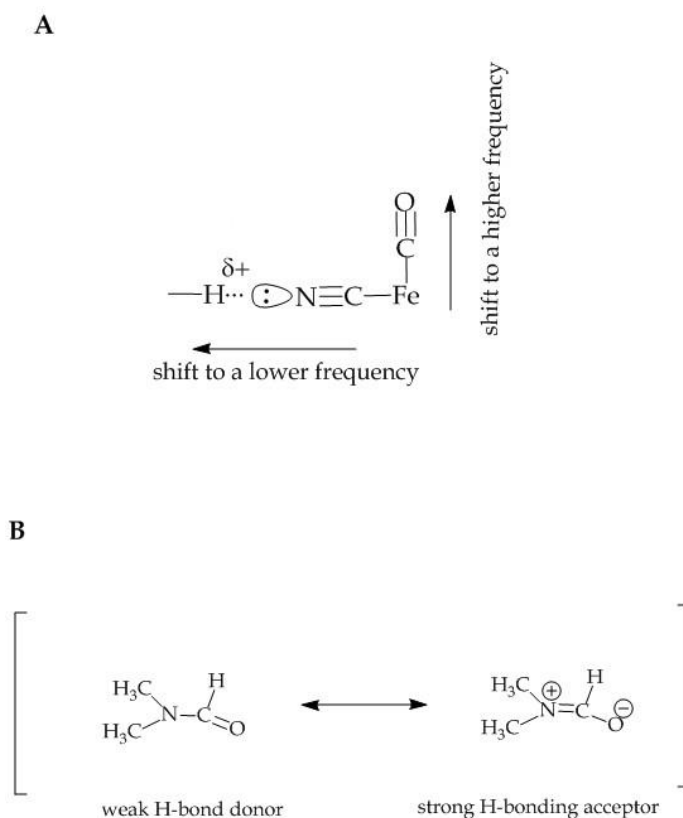
**Table 4.2.** FTIR data for  $\text{A}^{2-}$  in protic and aprotic solvents.

The  $\nu(\text{CN})$  in H<sub>2</sub>O is broad and weak and at 2052 cm<sup>-1</sup>, that observed in D<sub>2</sub>O is strong at 2065 cm<sup>-1</sup>. In both cases the frequencies are substantially lower than in CH<sub>2</sub>Cl<sub>2</sub>, or the other aprotic solvents MeCN and DMF, **Table 4.2**, as is consistent with the weakening of the cyanide bond-strength by a drift of electron density from the  $\sigma$ - bond to the hydrogen bond involving the lone-pair of electrons on the N-atom. In the protic solvents water and methanol, the perturbation of the  $\nu(\text{CO})$  bands relative to those in

the aprotic solvents is also dramatic, **Table 4.2**. For example, in water the  $\nu(\text{CO})$  bands are shifted to higher frequencies relative to those in  $\text{CH}_2\text{Cl}_2$  by an average of  $+25 \text{ cm}^{-1}$  and this is indicative of strong hydrogen bonding to the cyanide ligands in the complex. In  $\text{D}_2\text{O}$  the average shift in  $\nu(\text{CO})$  is less,  $+17 \text{ cm}^{-1}$ , consistent with  $\text{D}_2\text{O}$  being a weaker acid. Within the group of aprotic solvents,  $\nu(\text{CO})$  frequencies are on average lower in DMF than in MeCN or  $\text{CH}_2\text{Cl}_2$ .

The picture which emerges from the observed effects is that stronger hydrogen bonding raises  $\nu(\text{CO})$  and lowers  $\nu(\text{CN})$  probably by the bonding mechanism represented in **Scheme 4.3 A**. It is at first sight surprising that DMF is apparently poorer at hydrogen bonding to cyanide than  $\text{CH}_2\text{Cl}_2$ . However, the canonical form in **Scheme 4.3 B** must contribute substantially to its resonance structure, DMF is consequently a weak hydrogen bond donor but a strong hydrogen bond acceptor.





**Scheme 4.3** A : Representation of effect of H-bonding on  $\nu(\text{CN})$  and  $\nu(\text{CO})$ ; B canonical structures of DMF showing H-bonding acceptor behaviour.

The general trend of hydrogen bonding to cyanide increasing  $\nu(\text{CO})$  and decreasing  $\nu(\text{CN})$  is shown graphically by the plot of  $\nu(\text{CO})_{\text{average}}$  versus  $\nu(\text{CN})$  in **Figure 4.4** which has a correlation coefficient  $r^2$  of 0.976.

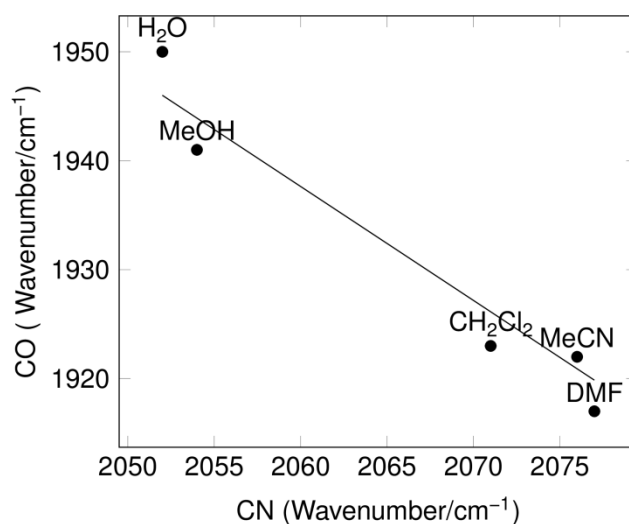


**Figure 4.4.** Major  $\nu(\text{CO})$  absorption band *versus*  $\nu(\text{CN})$  band in various solvents. The corresponding plot of  $\nu(\text{CO})_{\text{average}}$  *versus*  $\nu(\text{CN})$  is similar ( $r^2 = 0.976$ )

The effect of ‘full’ protonation at cyanide in  $[\text{Fe}_2(\text{CO})_4(\text{CN})_2(\text{pdt})]^{2-}$  by two equivalents of  $\text{HBF}_4$  in MeCN is also given in **Table 4.2**. This data is from a previously reported stopped-flow FTIR study <sup>96</sup>. The protonated product is unstable but the expected shift of  $\nu(\text{CO})$  to higher frequencies is observed and a broad peak for ligated HNC is observed near  $2105 \text{ cm}^{-1}$ . Notably linearly coordinated MeNC shows  $\nu(\text{CN})$  stretches in region  $2110\text{-}2165 \text{ cm}^{-1}$  but ‘bent’ coordinated HNC at electron-rich Re centres shows  $\nu(\text{CN})$  at  $1725 \text{ cm}^{-1}$  <sup>131</sup>. It is therefore reasonable to conclude that HNC is coordinated in a linear fashion.

## 4.2.2 Interaction of $A^{2-}$ with substituted tris-(thio)ureas **5** and **9**

### 4.2.2.1 The binding of $A^{2-}$ to 1,1',1''-(nitrilotris(ethane-2,1-diyl))tris(3-(3,5-bis(trifluoromethyl)phenyl) urea), **5** and its thiourea analogue **9**.

In preliminary investigations it was found that the bis- $CF_3$  urea **5** and thiourea **9**, **Figure 4.5**, showed the most dramatic effect on the FTIR spectra of  $A^{2-}$  in MeCN and DMF. It was therefore decided to probe the interactions of these molecules in detail. A range of other ureas and thioureas as listed in **Table 4.3** were also studied and general effects are discussed in subsequent sections. The notation  $A^{2-} \supset n$  (where  $n = 1, 2, \dots$  etc) is used to represent the binding of the diiron unit to a particular (thio)urea receptor  $n$  as defined in **Table 4.3**.

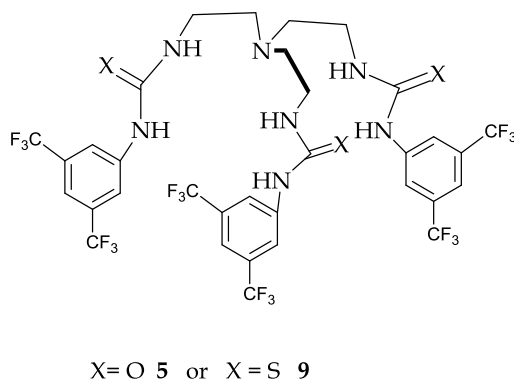


**Figure 4.5.** Structures of **5** and **9**.

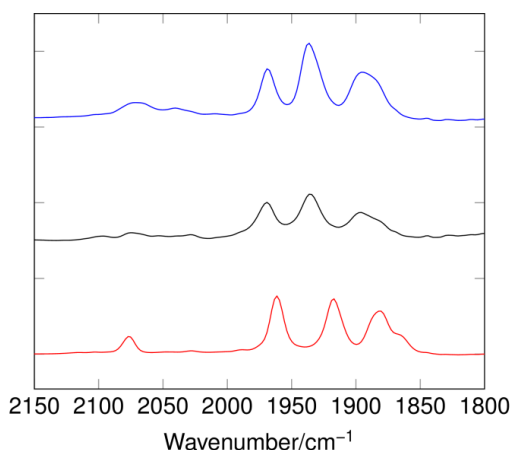


**Figure 4.6.** IR spectra of  $A^{2-}$  red(5.90mM),  $A^{2-} \supset 5$  black (3.41mM) and  $A^{2-} \supset 9$  blue (5.28mM) in DMF.

The basic pattern of the spectrum in the carbonyl region upon binding to either receptor **5** or **9** remains similar to that of  $A^{2-}$ . However, the frequencies are substantially shifted from that of the parent as summarised in **Table 4.3** and illustrated in **Figure 4.6**. In addition, the relative intensities of the absorptions are changed. Thus the  $\nu(\text{CO})$  stretches are raised in frequency as is consistent with hydrogen bonding to CN causing a shift in electron-density from the Fe centres which consequently diminishes back-bonding to CO. The well-defined  $\nu(\text{CN})$  band in the parent complex is lost with both receptors and is replaced by broad features in the cyanide stretching region. In the carbonyl region the  $\nu(\text{CO})$  stretches are at a slightly higher frequency for the thiourea acceptor **9** than for its urea analogue **5** *ca*  $1 - 2\text{cm}^{-1}$ . Oxygen is more electronegative than sulfur and it might be expected that the NH groups are consequently more acidic and that the urea **5** would give the higher  $\nu(\text{CO})$  stretches. That the opposite is true can

be explained by weak outer-sphere solvent or ion-pairing interactions. Whatever the reason the differences are small.

The geometric isomers possible for  $A^{2-}$  are summarised by **Figure 4.7**. The barrier for rotation of CO and CN groups at each iron is low for the parent complex in solution with the *trans-(basal, basal)* isomer probably the dominant form, as is observed for the related complex  $[Fe_2(CO)_4(PMe_3)_2(pdt)]$ . With a receptor bound to each cyanide it is likely that rotation is restricted and this may favour the *apical, basal* isomer. If a single receptor binds tightly to both cyanides then rotation is likely to be fully restricted. The rather ill-defined and broad nature of the CN bands in the thio(urea) adducts makes it difficult to determine whether one or more isomers are present, this is discussed in more detail below.

CHAPTER 4 | HYDROGEN BONDING INTERACTIONS OF TRIS AND BIS UREA AND THIOUREAS WITH CYANIDE LIGANDS IN AN ANALOGUE OF THE SUB-SITE OF [FeFe]-HYDROGENASE

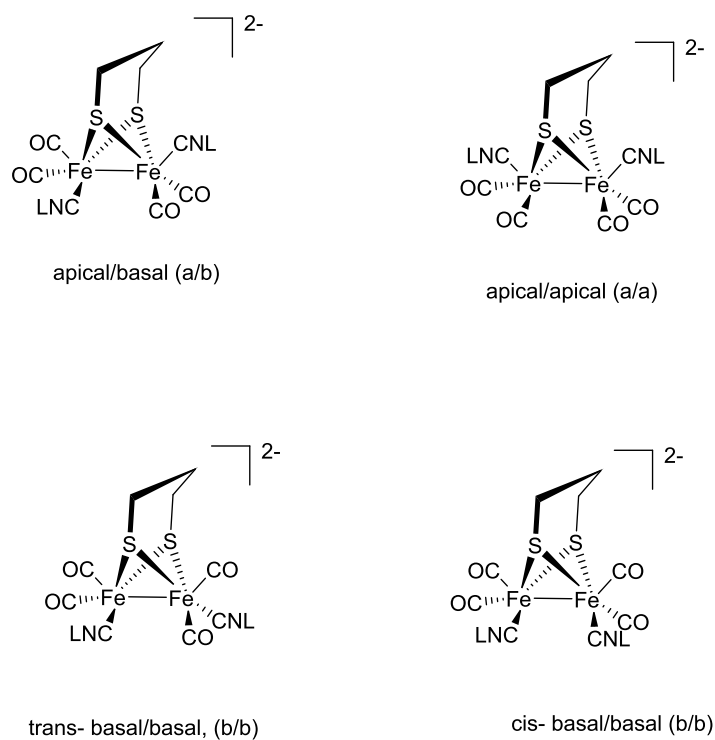


**Figure 4.7.** Possible isomers of  $A^{2-} \supset n$  where L represents the receptor. The receptor may bind to a single cyanide or to both cyanides in the complex.

#### 4.2.2.2. Spectroscopic studies of the binding of $A^{2-}$ to 1,1',1''-(nitrilotris(ethane-2,1-diyl))tris(3-(3,5-bis(trifluoromethyl)phenyl)thiourea), **9**.

In order to probe the binding of the receptors to  $A^{2-}$  in more detail, particularly the stoichiometry of binding and whether intermediates might be detected, FTIR stopped-flow studies, UV-visible and  $^1H$ -nmr experiments were undertaken.

*Stopped-flow FTIR experiments.* These experiments were performed in an inert atmosphere glove box using a Tgk Scientific stopped-flow drive equipped with a custom built flow cell fitted with  $CaF_2$  windows and thermostated at  $21 \pm 0.2$  °C (see Experimental Section). The response time of the instrumental set-up using a maximum frequency limit of  $2150\text{ cm}^{-1}$  and a peak resolution of  $4\text{ cm}^{-1}$  is 79 ms. This is determined by the analogue to digital conversion of the Fourier Transform rather than the mixing time in the flow cell which is 15ms.

**Figure 4.8** shows the stopped-flow spectrum obtained 80ms after mixing  $A^{2-}$  and **9** in MeCN in a molar ratio of 1:5. The FTIR bands are essentially identical in pattern to those that were observed in DMF in static experiments with  $A^{2-}$  and **9** (minutes timescale 1:2 ratio). There is a small solvent shift of  $2 - 6\text{ cm}^{-1}$  to higher frequencies in MeCN relative to DMF, **Table 4.3**. The spectrum is produced ‘instantaneously’ with respect to the time-resolution of the instrumental set-up, *ie* 79 ms and remains unchanged over a three minute time-scale. Thus product growth/reactant depletion spectra were not observed and no intermediate(s) was detected. This is consistent with a high kinetic affinity of the receptor **9** for the complex  $A^{2-}$ .

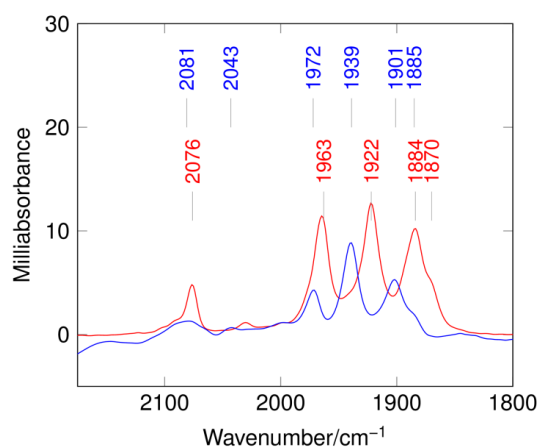


**Figure 4.8** . Stopped-flow FTIR of the reaction of  $A^{2-}$  with **9** in MeCN recorded after 84s. Concentration after mixing:  $A^{2-} = 0.5$  mM ; **9** = 2.5 mM.

**Figure 4.9** shows spectra obtained using different molar ratios of complex and receptor,  $A^{2-} : \mathbf{9}$  which were 1:1 ; 1:2 and 1:5. These results show that the spectra obtained at ratios of 1:2 and 1:5 are essentially superimposable whilst the major carbonyl peak  $1939\text{ cm}^{-1}$  at 1:1 is *ca* 95% of that measured at the 1:5 ratio.



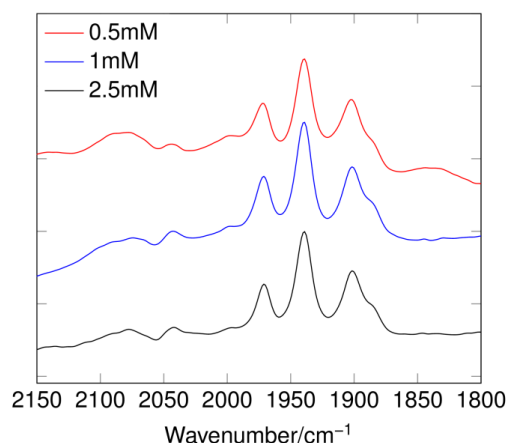


**Figure 4.9.** FTIR for the reaction of  $A^{2-}$  with **9** in MeCN recorded after 80 ms. Concentrations, after mixing :  $A^{2-} = 0.5 \text{ mM}$ ; **9** = 0.5 mM, 1:1 complex: receptor (red spectrum), 1.0mM 1:2 complex: receptor (blue spectrum), 2.5mM (black spectrum).

*Uv – visible spectroscopy.* The uv-visible spectrum of the parent complex  $A^{2-}$  is shown in **Figure 4.10** (purple curve). It shows an absorption band at 351nm with a corresponding molar extinction coefficient of  $2.3 \times 10^5 \text{ M}^{-1} \text{ cm}^{-1}$  together with a tail from the uv into the visible region. The 351 nm has been attributed to a transition from the HOMO which is metal-metal bond in character to the LUMO which is has metal-metal anti-bonding character. The receptor shows two major absorption bands at 280 and 248 nm with extinction coefficients of  $1.6 \times 10^5 \text{ M}^{-1} \text{ cm}^{-1}$  and  $2.9 \times 10^5 \text{ M}^{-1} \text{ cm}^{-1}$  respectively, **Figure 4.10** (black curve). The uv-visible spectrum resulting from a *ca* 1 : 1 mixture of  $A^{2-}$  (6  $\mu\text{M}$ ) and **9** ( 6.26  $\mu\text{M}$ ) is shown **Figure 4.10** by the blue curve. It is evident that the absorption at 351 nm is essential absent after the addition of one equivalent and that the tail from the uv into the visible region is substantially reduced. There is a small shift in the higher energy band of the receptor to lower energy

upon complexation. In a the *ca* 1:2 ratio of the complex (3  $\mu\text{M}$ ) to the receptor the (6.26  $\mu\text{M}$ ) the spectrum fits excellently to the linear combination of 3  $\mu\text{M}$  [ $\text{A}^{2-} \supset \mathbf{9}$ ] + 3.26  $\mu\text{M}$   $\mathbf{9}$  as is shown by **Figure 4.11**. This is in full accord with a stoichiometry of 1:1 and tight binding of the receptor to the diiron complex.

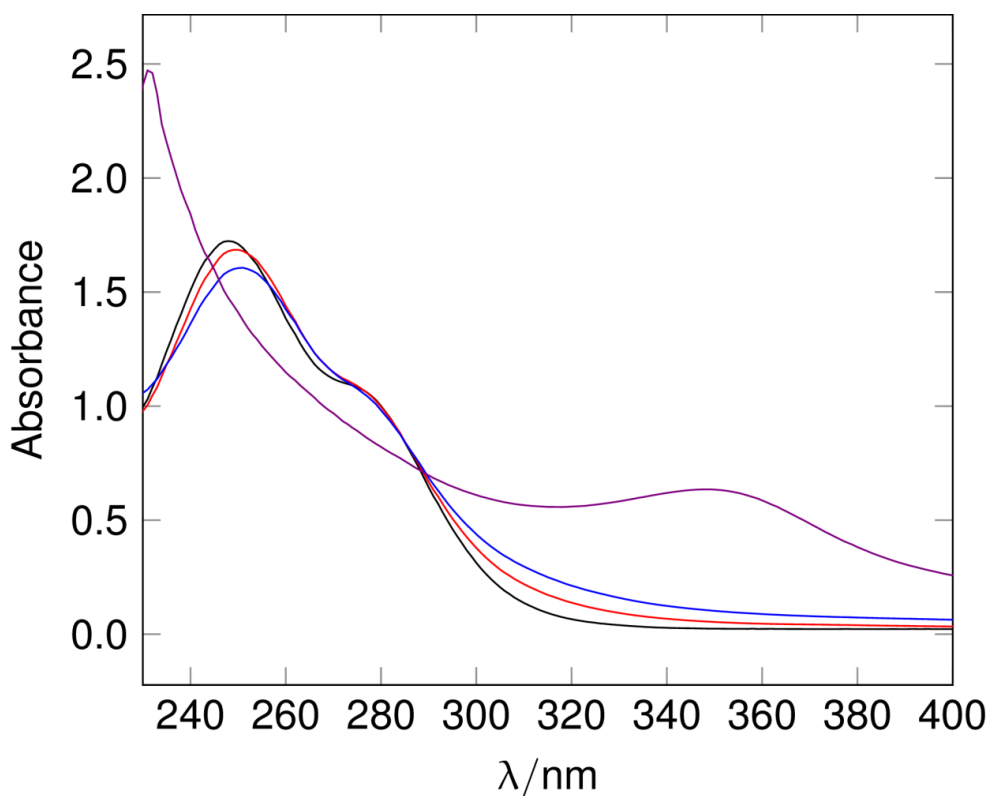


**Figure 4.10.** Absorption spectra of  $\text{A}^{2-}$  (violet),  $\mathbf{9}$  (black) and  $\text{A}^{2-} \supset \mathbf{9}$  with ratio (1:2) (red) and (1:1) (blue) in MeCN. The concentration of the receptor was 6.26  $\mu\text{M}$  in all of the experiments and that of the complex 6  $\mu\text{M}$  (blue) and 3  $\mu\text{M}$  (red) spectra.

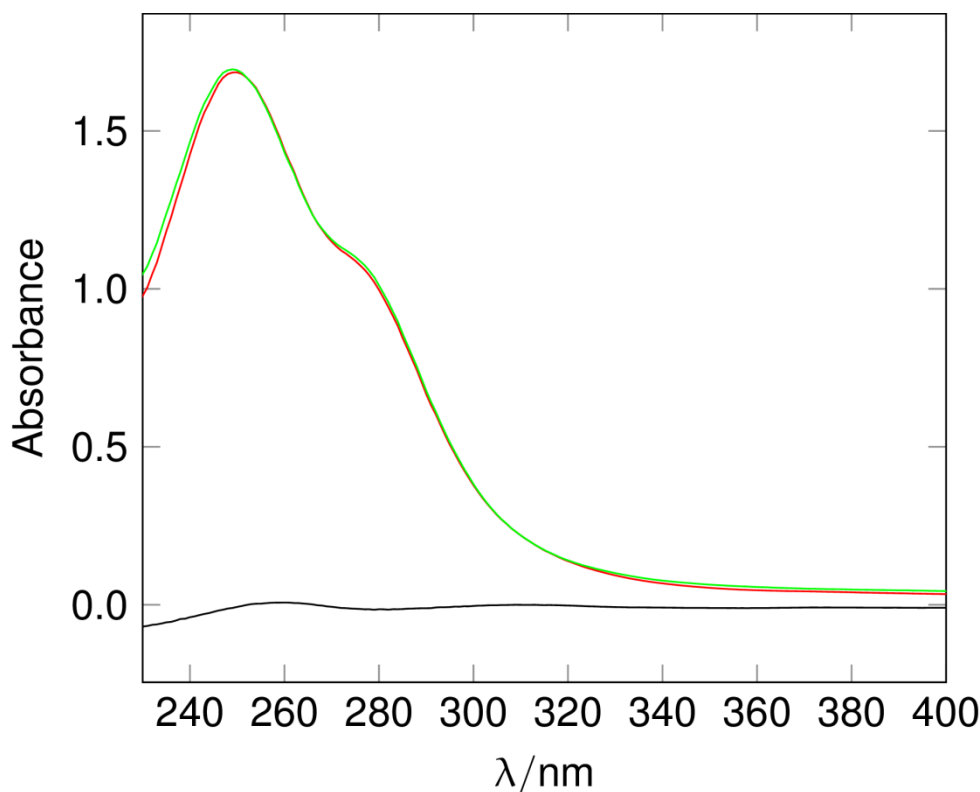


**Figure 4.11:** The red curve is the experimental curve for the 1:2 ratio of  $A^{2-} : 9$  shown in **Figure 4.10** and the superimposed green curve is that calculated from the linear combination  $\frac{1}{2}$  (blue curve, **Figure 4.10**) + 3.26/6.26 (black curve, **Figure 4.10**). The closeness of the fit is shown by the residues black plot ( red curve – green curve).

**$^1H$  NMR and  $^{19}F$  NMR studies of  $A^{2-} \rightarrow 9$ .** The  $^1H$  NMR for the ligand **9** in  $CD_2Cl_2$  shows a resonance at 2.82 ppm for six protons of  $(HN-CH_2-\underline{CH_2}-N-)$ , 3.89 ppm for the six protons of  $((HN-\underline{CH_2}-CH_2-N-)$  while phenyl proton peaks appear at 7.50ppm for three *para*-protons and at 7.86 ppm for the six *ortho*-protons. In addition, three amide protons for  $CH_2\underline{NH}$  are observed at 7.13ppm and three amide protons for the

CHAPTER 4 | HYDROGEN BONDING INTERACTIONS OF TRIS AND BIS  
UREA AND THIOUREAS WITH CYANIDE LIGANDS IN AN  
ANALOGUE OF THE SUB-SITE OF [FeFe]-HYDROGENASE

3,5-(CF<sub>3</sub>)<sub>2</sub>C<sub>6</sub>H<sub>3</sub>NH group appear at 9.16 ppm. These resonances shown in **Figure 4.12** are fully in accord with the reported literature spectrum. [113](#)

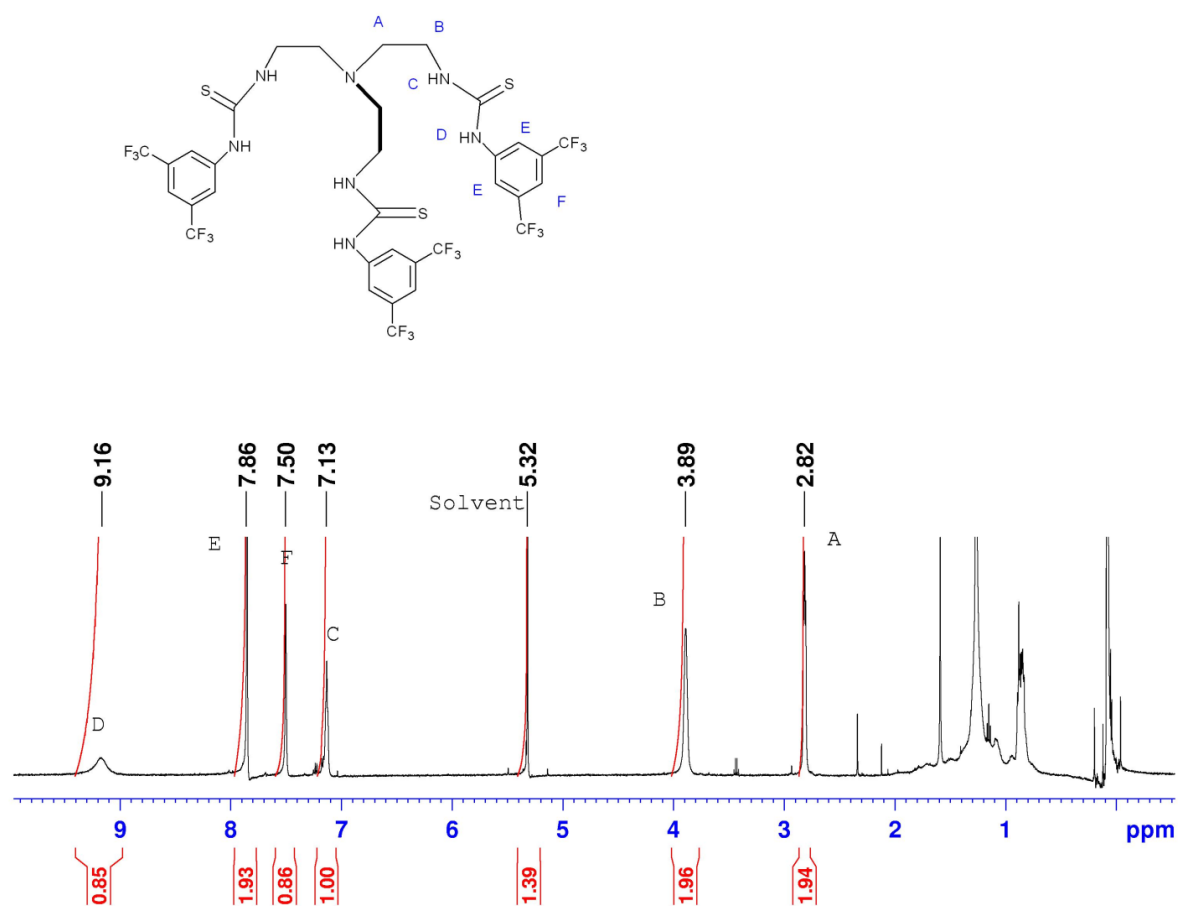


**Figure 4.12** <sup>1</sup>H NMR of ligand **9** in CD<sub>2</sub>Cl<sub>2</sub>.

The diiron complex  $[\text{Et}_4\text{N}]_2[\text{A}]$  in the same solvent shows resonances at 1.36 and 3.36 ppm for the tetraethylammonium cation together with broad resonances at 1.70 and 1.90 which are attributable to the propane dithiolate  $\text{CH}_2\text{CH}_2\text{CH}_2$  and  $\text{SCH}_2$  protons. The dithiolate bridge is known to flip rapidly at room temperature interconverting axial and equatorial protons. The integration of these resonances correspond to six protons in total, **Figure 4.13**

There are significant changes in the  $^1\text{H}$  NMR following the formation of  $\text{A}^{2-} \rightleftharpoons \mathbf{9}$ . Firstly, the resonances for the NH protons become very broadened. This has been observed with NH bonding interactions of these type of receptors with anions, notably in the work of Hageman<sup>116</sup>, Alamgir Hossain<sup>119</sup> and Gale<sup>113</sup> and their coworkers, and is consistent with strong H-bonding interactions of the receptor with the complex, **Figure 4.14**

Secondly, the aromatic protons in the N-substituted thiourea are shifted in the  $\text{A}^{2-} \rightleftharpoons \mathbf{9}$  adduct relative to those in the receptor alone. The *ortho* – protons, E, are shifted downfield,  $\Delta=0.22$  ppm, whilst the *para* – protons are shifted upfield,  $\Delta=0.13$  ppm, **Figure 4.14**. This is analogous phenyl proton shifts reported by Boiocchi *et al* for the receptor 1,3-bis(4-nitrophenyl)urea upon binding acetate. They observed that the *ortho*-protons close to the C=O urea group shift downfield whilst the *meta*-protons shifted upfield, see **Figure 4.16**).<sup>132</sup> The explanation was that H-bonding leads to an increased electron density on the aromatic ring through the bonding system and this leads to a shielding effect and an upfield shift of the *para*-H. On the other hand, a

through space polarization of the *ortho*-H atoms by an electrostatic interaction causes a deshielding effect and a shift in the resonance downfield. The electrostatic effect falls off rapidly with distance and its influence on the *para*-H atoms is small.

As might be expected, there are also other effects on the receptor alkyl CH<sub>2</sub> resonances which shift upfield upon H-bonding of the receptor **9** to A<sup>2-</sup> and can be explained by an increase in electron-density in the receptor framework. The resonances for the alkylammonium counter ion are also surprisingly shifted upfield as are those for the propanedithiolate ligand. This might be explained by a decrease in electrostatic ion-pairing interactions as the receptor wraps around A<sup>2-</sup> increasing the distance between A<sup>2-</sup> and Et<sub>4</sub>N<sup>+</sup>. In terms of the <sup>19</sup>F NMR, no change was observed on <sup>19</sup>F NMR for the ligand with and without diiron dicyanide ( see **Figure 4.18 and 4.19**).

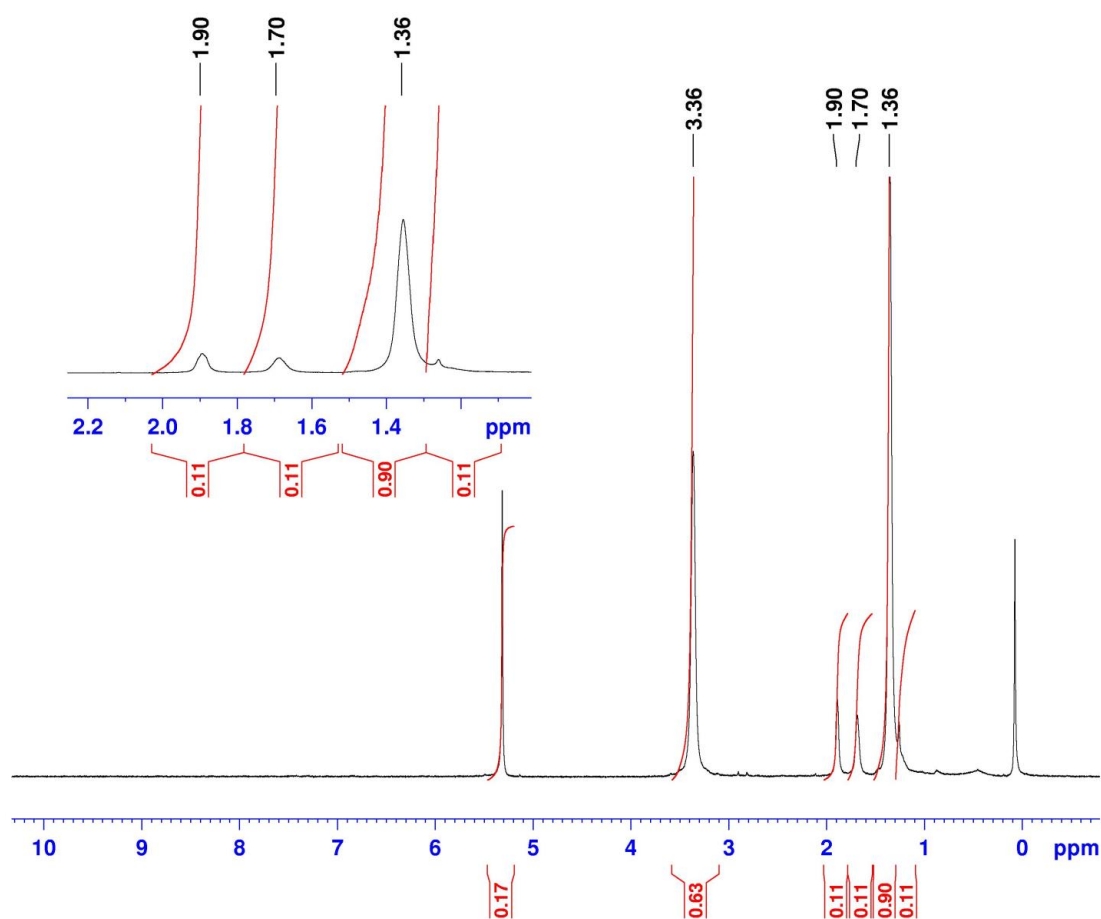


**Figure 4.13**  $^1\text{H}$  NMR of  $[\text{Et}_4\text{N}]_2[\text{A}]$  in  $\text{CD}_2\text{Cl}_2$

CHAPTER 4 | HYDROGEN BONDING INTERACTIONS OF TRIS AND BIS  
UREA AND THIOUREAS WITH CYANIDE LIGANDS IN AN  
ANALOGUE OF THE SUB-SITE OF [FeFe]-HYDROGENASE

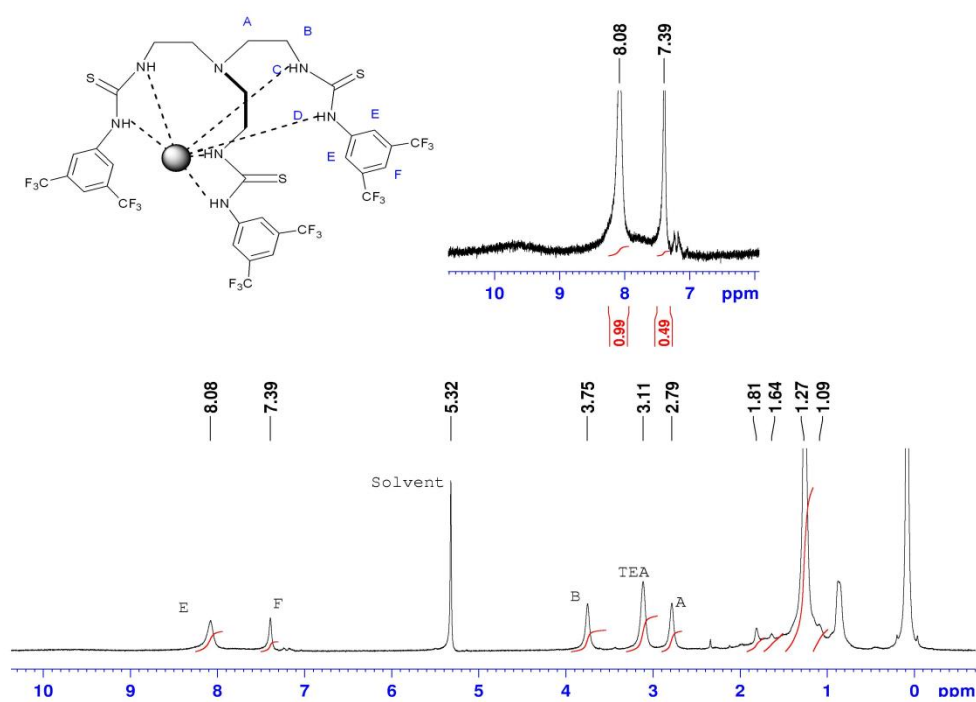


**Figure 4.14** The  $^1H$  NMR of  $A^{2-} \rightarrow 9$  in  $CD_2Cl_2$ .



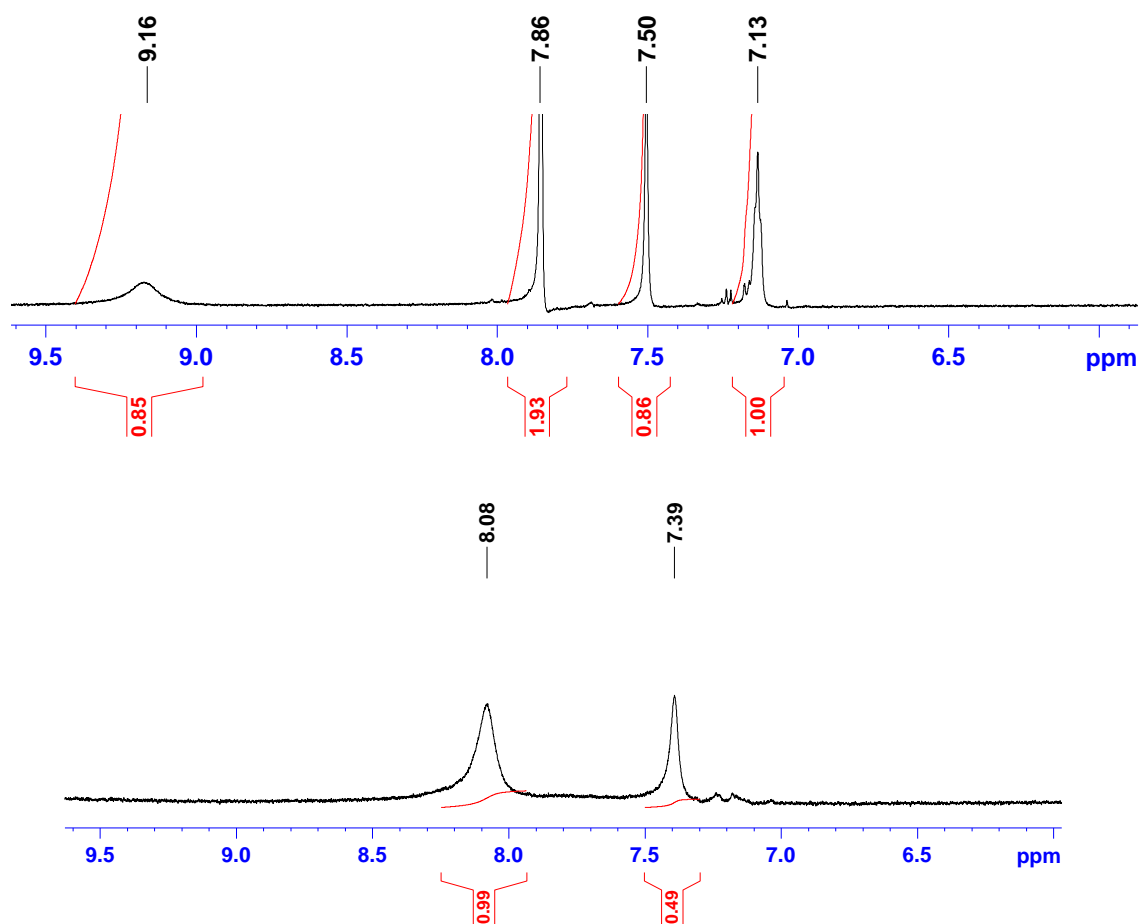


**Figure 4.15.** <sup>1</sup>H NMR of **9** before and after interaction with A<sup>2-</sup> in CD<sub>2</sub>Cl<sub>2</sub>, for Ph and NH protons region

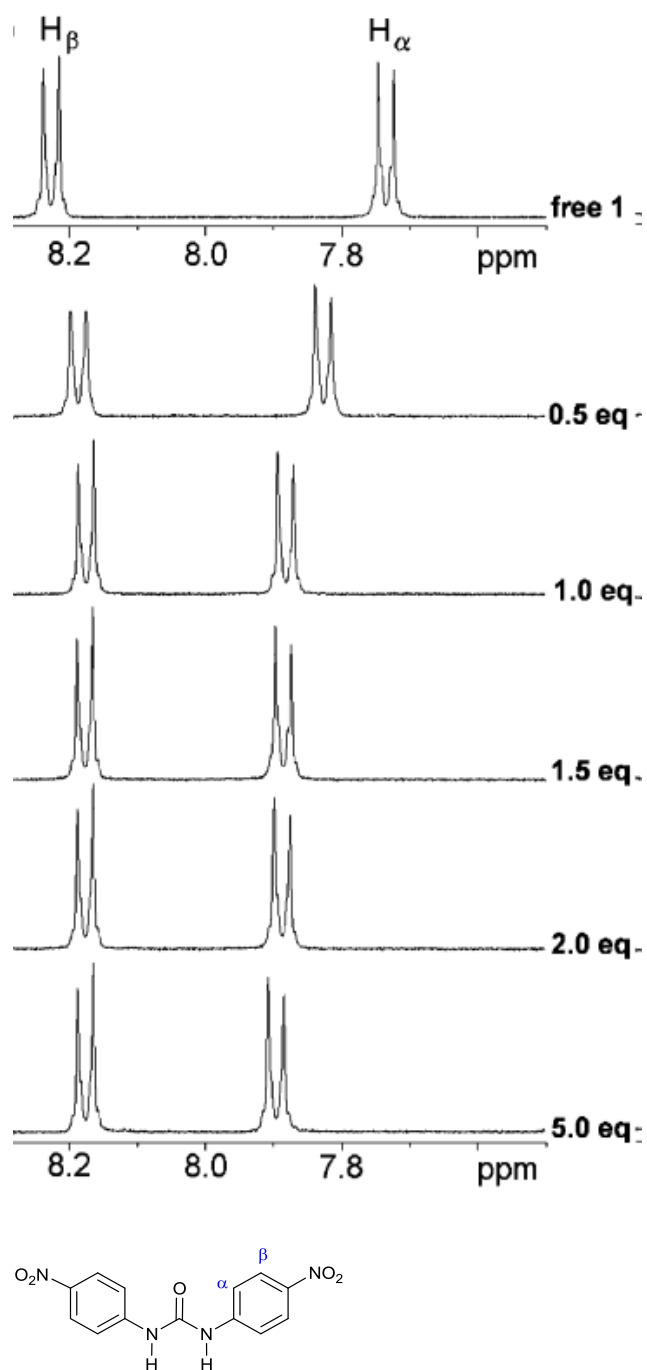


**Figure 4.16.**  $^1\text{H}$  NMR of interaction between 1,3-bis(4-nitrophenyl)urea and  $[\text{CH}_3\text{COO}]^-$  in  $\text{DMSO-}d_6$  reproduced from paper of Boiocchi *et al* [132](#).

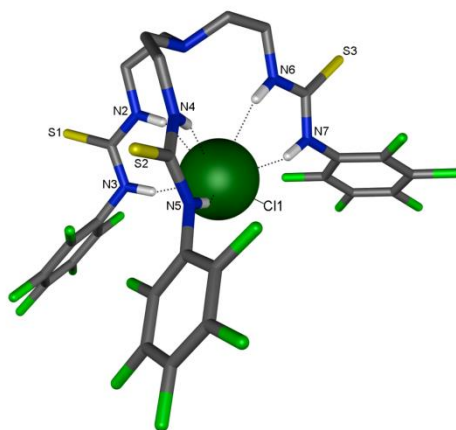


**Figure 4.17.** Schematic representation of the hydrogen bonds in the crystal of (7 ⊃ Cl·(Et<sub>4</sub>N)). Reported by reference 113. [113](#).

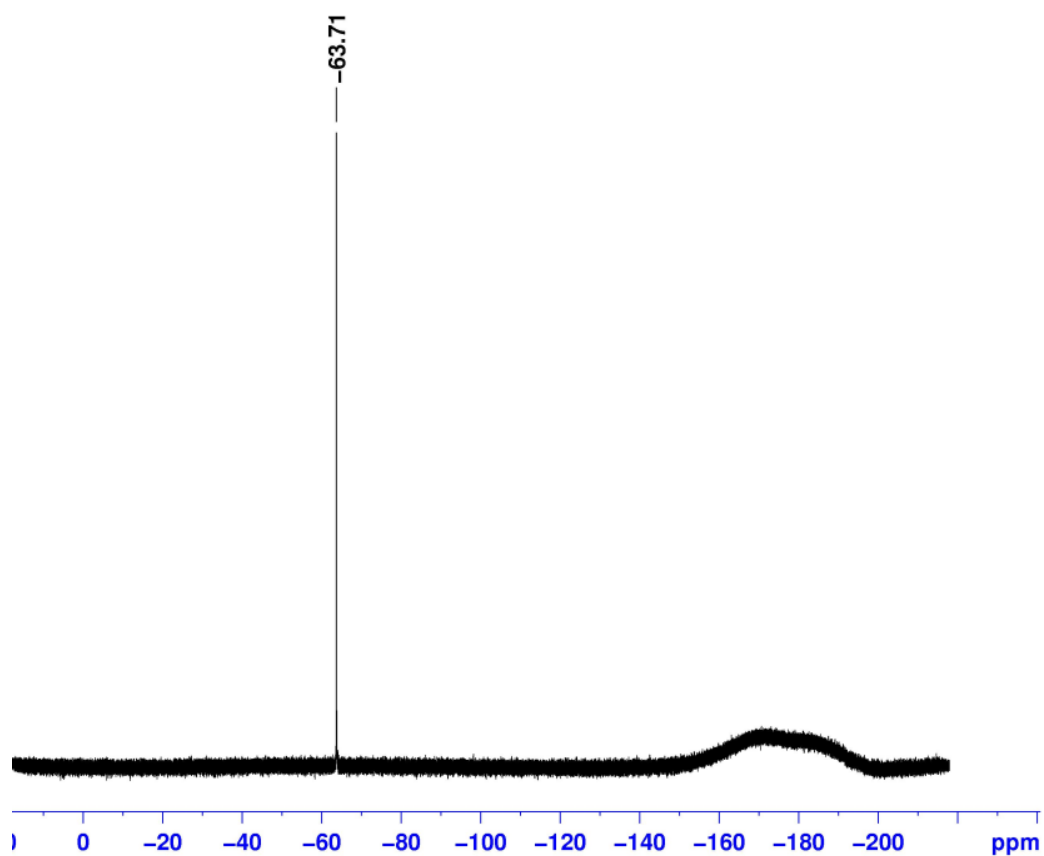


**Figure 4.18.**  $^{19}\text{F}$  NMR of **9** in  $\text{CD}_2\text{Cl}_2$

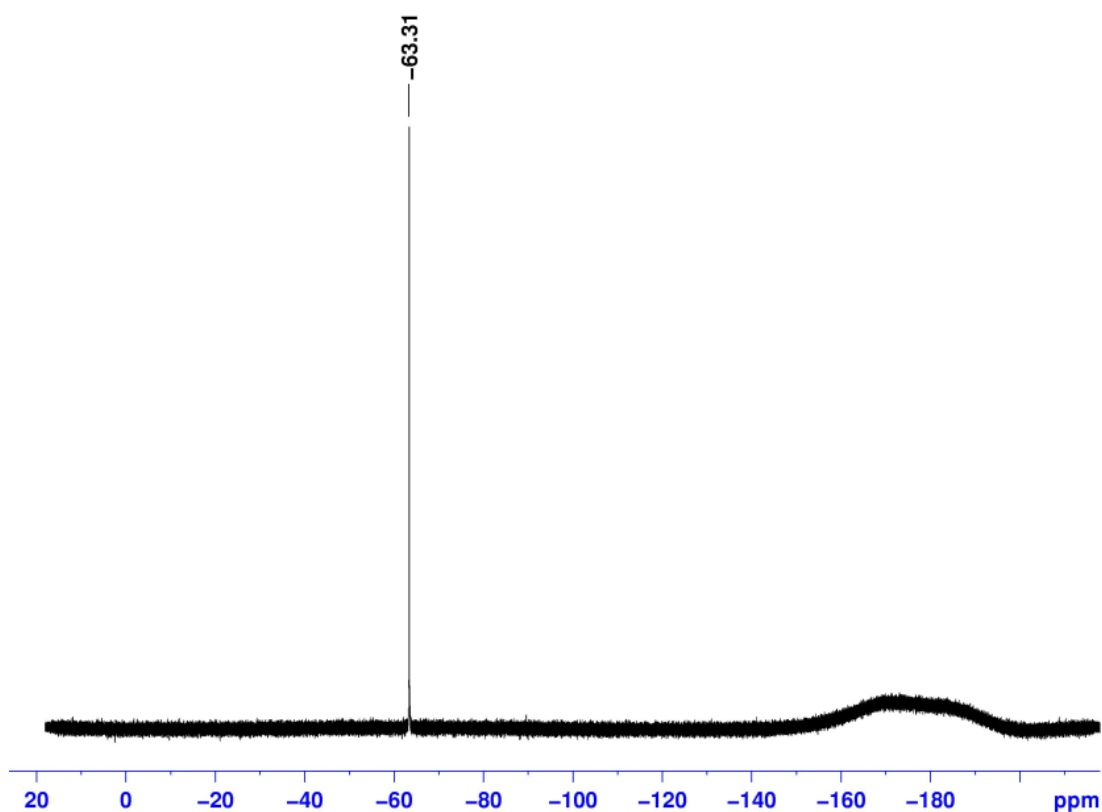


**Figure 4.19.**  $^{19}\text{F}$  NMR of **9** in  $\text{CD}_2\text{Cl}_2$

*The nature of the  $\text{A}^{2-} \rightarrow \mathbf{9}$  H-bonding interactions.* The evidence presented so far suggests that (1) the receptor **9** and, by analogy the receptor **5**, interact with  $\text{A}^{2-}$  in a one to one stoichiometry (2) that this interaction involves hydrogen-bonding and (3) that this hydrogen-bonding is to one, or possibly both cyanide ligands. Attempts were made to isolate crystalline materials for X-ray characterization but these have been so far proved unsuccessful, the long term stability of the materials in various solvent mixtures has been problematic. It was therefore thought that DFT calculations on

$A^{2-} \supset 9$  might helpfully provide information on the type of stable structures which could be expected. Dr Joseph Wright undertook these calculations with input from the author. The approach was to take known structural data for **9** and for  $A^{2-}$  which were then docked to allow cyanide thiourea NH interactions. Calculations were performed using the Gaussian 09 computational package<sup>133</sup>. Geometry optimisation and frequency calculations were carried out using the Tao-Perdew-Staroverov-Scuseria (TPSS) density functional<sup>134</sup>. Iron and sulphur were described using the Hay and Wadt LANL2DZ<sup>135</sup> basis set; all other elements used the 6-31G basis set. Structures were geometry optimised in the gas phase with the default convergence criteria and confirmed as minima through frequency calculations. The calculated structure resulting from this procedure is shown in **Figure 4.20**. Most notably, one cyanide ligand of  $A^{2-}$  is hydrogen bonded to two of the arms of the tris(thiourea) receptor with the third arm providing two NH hydrogen bonds to the other coordinated cyanide. Thus all the urea units are engaged in bonding to the cyanides of the diiron unit which adopts a *apical basal* configuration as shown in **Figure 4.20**. Inspection of the calculated structure shows that it would be difficult to accommodate an additional receptor.

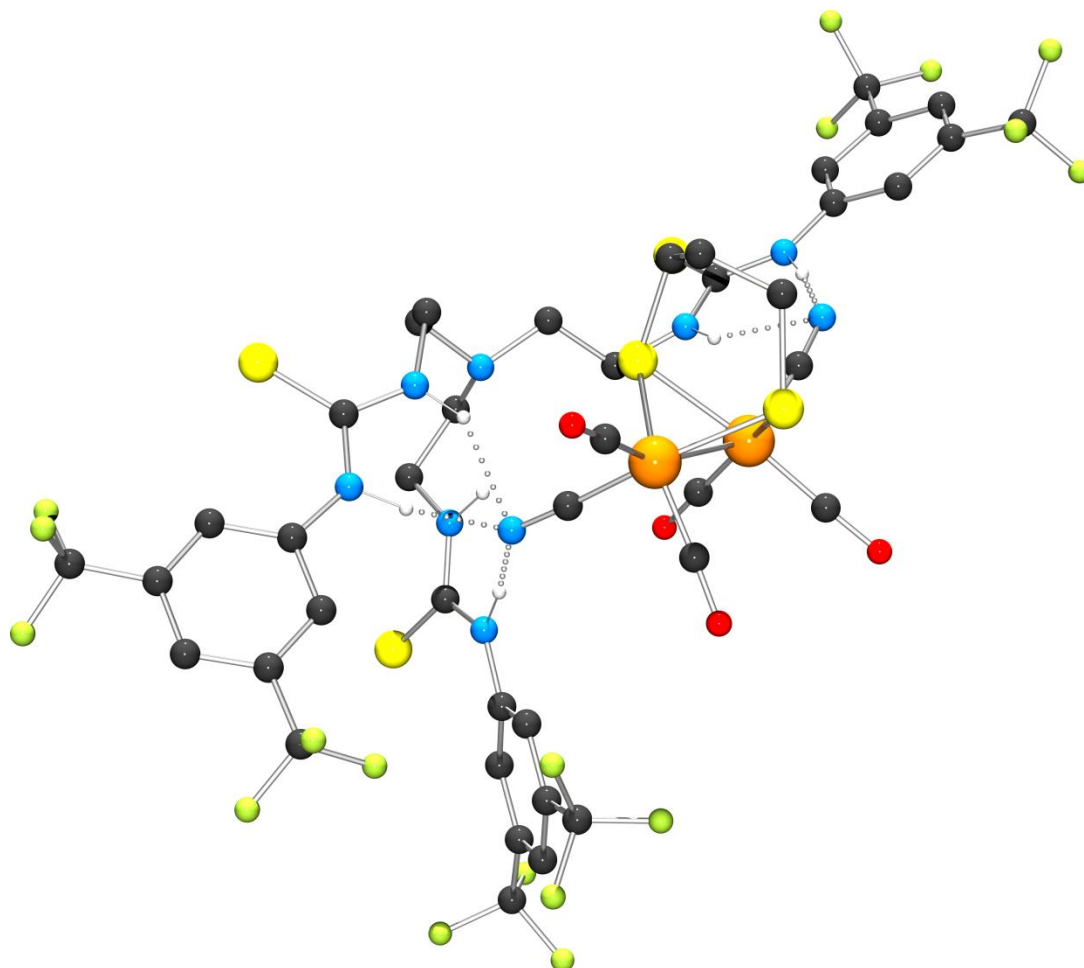


**Figure 4.20** The calculated structure resulting from the DFT calculations for  $\mathbf{A}^{2-} \supset \mathbf{9}$  .

White spheres H; blue spheres N; black spheres C; red spheres O; orange spheres Fe;  
yellow spheres S; green spheres F.

### 4.2.3 The interaction of $A^{2-}$ with other urea and thiourea receptors.

The FTIR spectra of  $A^{2-}$  in the presence of two equivalents of the various receptors listed in **Scheme 4.2** were surveyed in DMF. The IR data obtained is listed in **Table 4.3**. Several trends emerge.

It is only the receptors with electron-withdrawing groups that show significant shifts in the carbonyl and cyanide frequencies. The phenyl substituted urea **1** does not significantly perturb the spectrum although there is small shift in the major CO band of  $2\text{ cm}^{-1}$  to a higher frequency. In contrast, the *para*-fluoro- (**2, 6**), *para* – trifluoromethyl (**4,8**) and pentafluoro (**3,7**) substituted receptors show shifts in this major  $\nu(\text{CO})$  band of  $11\text{-}14\text{ cm}^{-1}$  to higher wave numbers. The 3,5-bis (trifluoromethyl) substituted receptors (**5,9**) show the most dramatic shift of  $20\text{ - }22\text{ cm}^{-1}$  as has been discussed in more detail above.

There is a small but consistent difference in  $\nu(\text{CO})$  for the corresponding urea and thiourea receptors. Thus the thiourea receptors show a shift of  $1\text{ - }3\text{ cm}^{-1}$  to higher values relative to their urea counterparts. However, it is the lowest frequency  $\nu(\text{CN})$  band that is more sensitive to whether the receptor is a urea or thiourea, this is shifted to lower frequencies by  $5\text{ - }11\text{ cm}^{-1}$  on switching from C=O to C=S implying a weakening of the CN bond either by removal of electron density from bonding orbitals or by increasing back donation into  $\pi^*$  antibonding orbitals. The general observation that the single relatively strong  $\nu(\text{CN})$  band in the parent complex is replaced in all cases, except for the pentafluoro-receptors, by three bands is now considered. With two

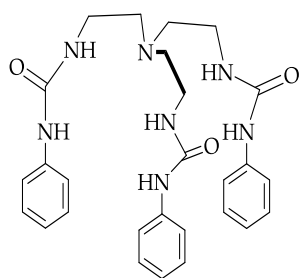


cyanides in an apical-basal arrangement two distinct CN stretches would be expected. In a trans-basal arrangement the asymmetric arrangement of the hydrogen – bonding would also be expected to lead to two distinct absorptions. This is because two arms of the receptor are predicted to bind to one cyanide by four H-bonds and the other arm to bind to the CN on the other iron atom via two H-bonds. It is possible that both isomers are present but the trans-basal (or cis– basal) geometries are unlikely because of steric crowding. DFT indicates these are likely to be less stable than a trans-basal arrangement. It seems more probable that the observation of three bands might best be explained by ‘receptor’ based isomerism with partial disassociation of one arm of the tris –thiourea.

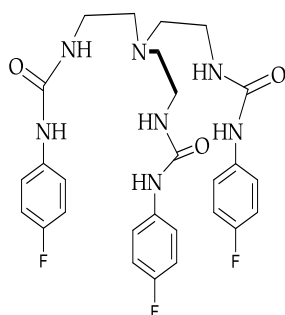
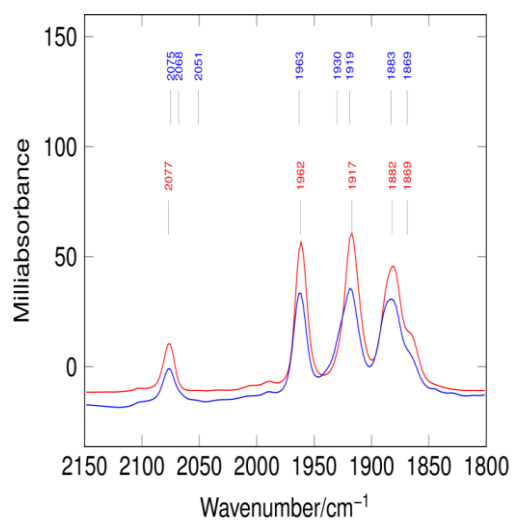
The nature of the thio(urea) receptor is also important in determining the affinity for  $A^{2-}$ . As a measure of the extent of interaction the variation of the intensity of the parent peak at  $1917\text{ cm}^{-1}$  relative to the ‘shifted’ peak at a 1:2 ratio of  $A^{2-}$  : receptor was qualitatively examined. The extent of binding of the tris(urea) series followed the order **1**(Ph) < **3**( $C_6F_5$ ) ~ **4** [*p*-  $C_6H_4$  ( $CF_3$ )] < **2** (*p*-  $C_6H_4F$ ) < **5** [*3,5*- $C_6H_3$  ( $CF_3$ )<sub>2</sub>]. That for the thio(urea) series followed the order **6** (*p*-  $C_6H_4F$ ) < **7** ( $C_6F_5$ ) < **8** [*p*-  $C_6H_4$  ( $CF_3$ )] < **9** [*3,5*- $C_6H_3$  ( $CF_3$ )<sub>2</sub>]. Certainly for the thio(urea) data the trend is clearly that the more electron-withdrawing the substituents on the phenyl rings the greater is the extent of binding. The trend for the urea data is difficult to rationalize although the weakest electron-withdrawing system **1** shows the least affinity whilst that with the strongest electron-withdrawing substituents **5** shows greatest affinity. The FTIR data upon which

## CHAPTER 4 | HYDROGEN BONDING INTERACTIONS OF TRIS AND BIS UREA AND THIOUREAS WITH CYANIDE LIGANDS IN AN ANALOGUE OF THE SUB-SITE OF [FeFe]-HYDROGENASE

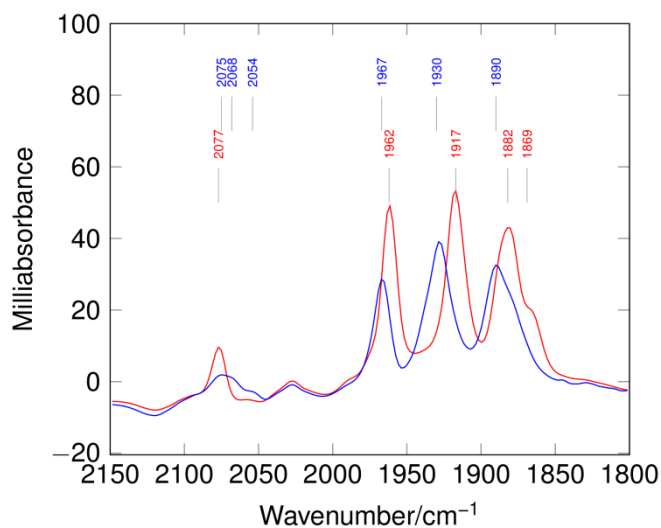
these qualitative deductions are based is shown by the two panels of spectra for the urea and thiourea receptors in **Figures 3.21** and **3.22** respectively.



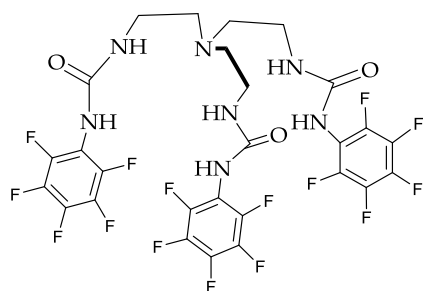
**1**



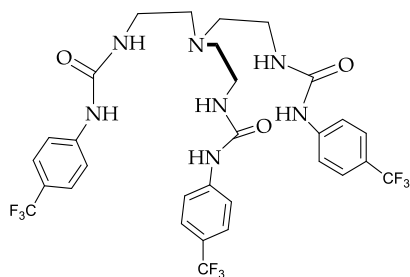
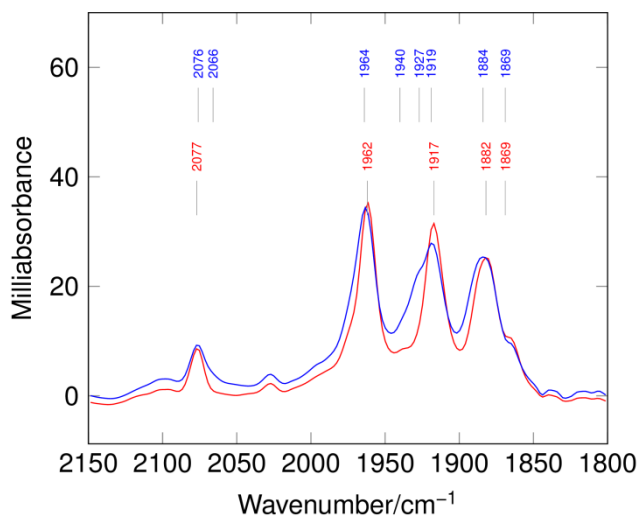
**2**



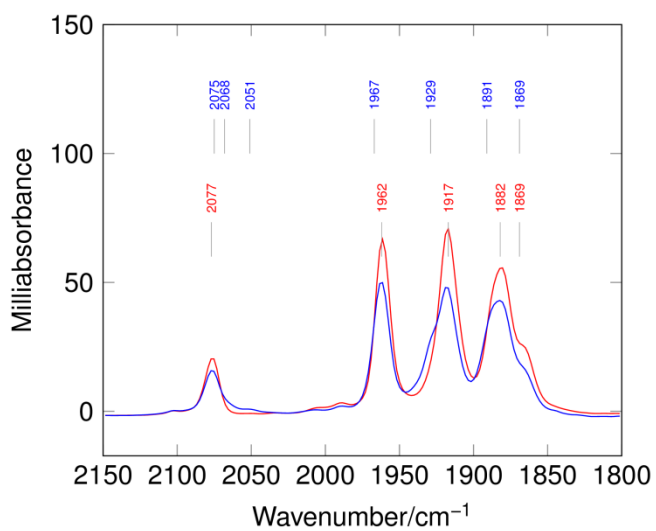
CHAPTER 4 | HYDROGEN BONDING INTERACTIONS OF TRIS AND BIS UREA AND THIOUREAS WITH CYANIDE LIGANDS IN AN ANALOGUE OF THE SUB-SITE OF [FeFe]-HYDROGENASE



3



4



CHAPTER 4 | HYDROGEN BONDING INTERACTIONS OF TRIS AND BIS UREA AND THIOUREAS WITH CYANIDE LIGANDS IN AN ANALOGUE OF THE SUB-SITE OF [FeFe]-HYDROGENASE

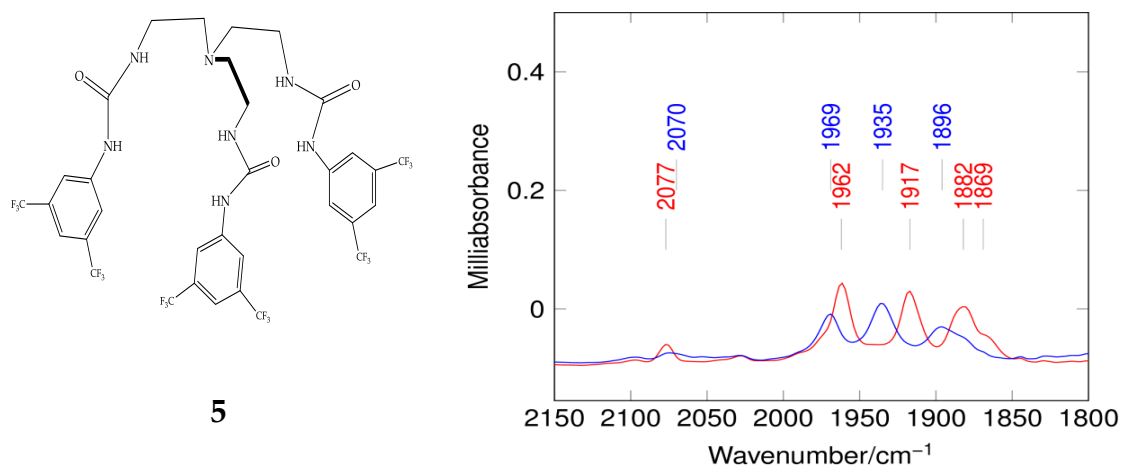
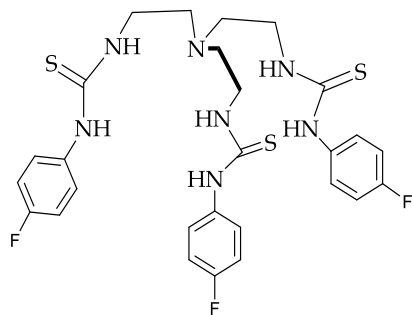
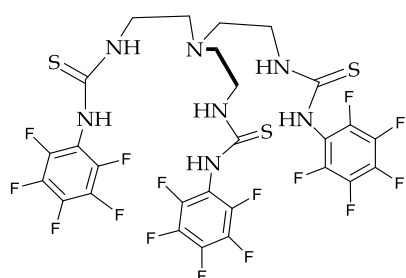
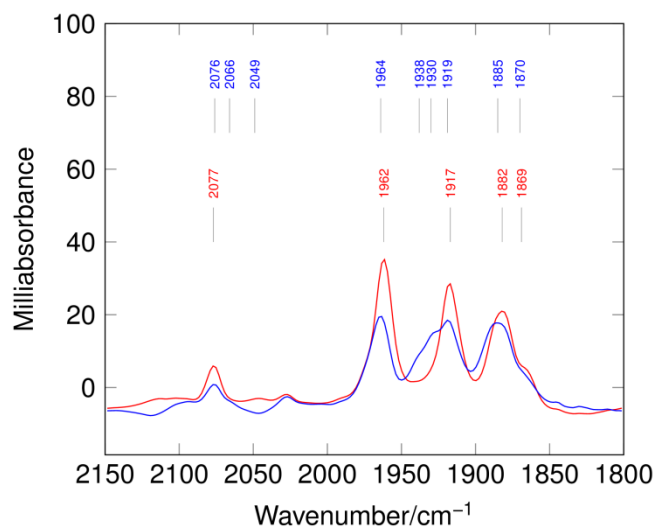


Figure 4.21. FTIR spectra of A<sup>2-</sup> red and A<sup>2-</sup> tris-ureas blue in DMF.

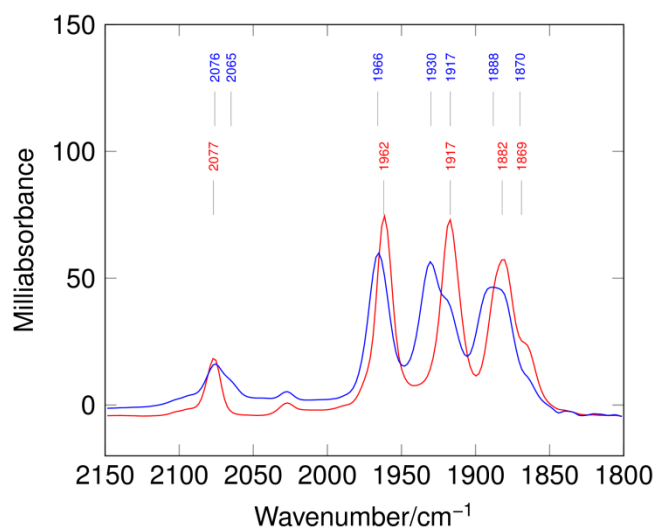
CHAPTER 4 | HYDROGEN BONDING INTERACTIONS OF TRIS AND BIS UREA AND THIOUREAS WITH CYANIDE LIGANDS IN AN ANALOGUE OF THE SUB-SITE OF [FeFe]-HYDROGENASE



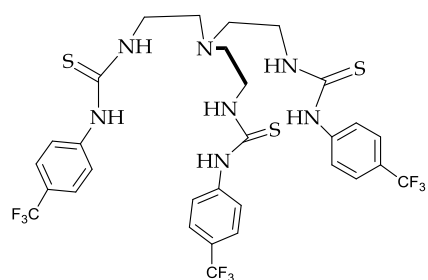
6



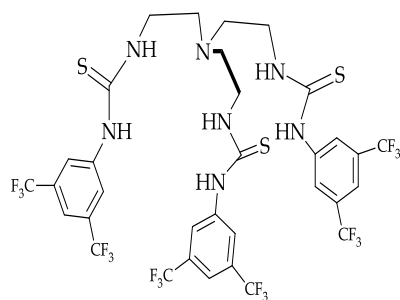
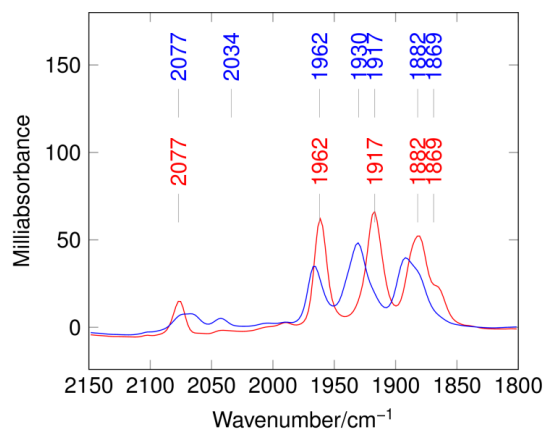
7



CHAPTER 4 | HYDROGEN BONDING INTERACTIONS OF TRIS AND BIS UREA AND THIOUREAS WITH CYANIDE LIGANDS IN AN ANALOGUE OF THE SUB-SITE OF [FeFe]-HYDROGENASE



8



9

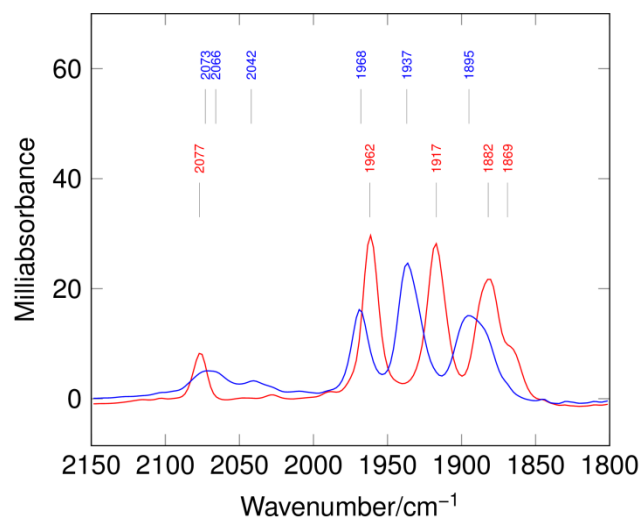
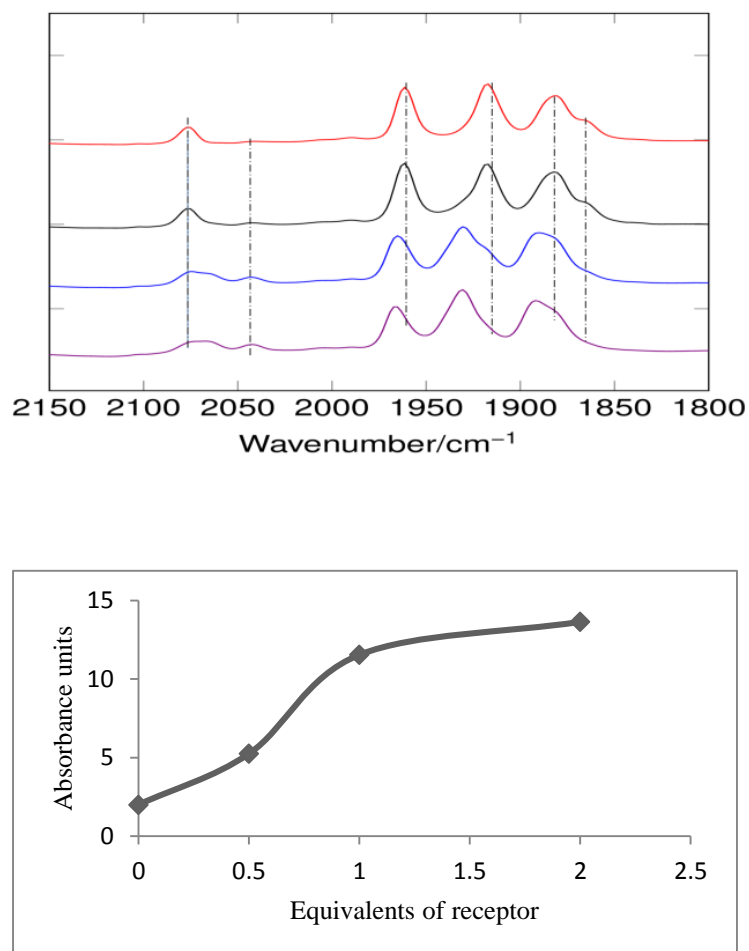


Figure 4.22. FTIR spectra of  $A^{2-}$  red and  $A^{2-}$  tris-thioureas blue in DMF.

Whereas the 3,5-bis(trifluoromethyl) thiourea **9** shows a tight 1:1 binding to  $\mathbf{A}^{2-}$ , the corresponding mono(trifluoromethyl) thiourea receptor **8** shows evidence for somewhat weaker binding. **Figure 4.23(a)** illustrates the evolution of the FTIR spectrum at increasing ratios of receptor to complex and **Figure 4.23(b)** the corresponding plot of the absorbance at  $1931\text{ cm}^{-1}$  *versus* the molar ratio of complex to receptor. The shape is consistent with 1:1 binding but conversion is approximately 80% complete at a 1:1 molar ratio and this is indicative of an association constant  $K_a$  of the order of  $20\text{ M}^{-1}$ . A similar calculation for the association of  $\mathbf{A}^{2-}$  with **9** using the stopped flow data from **Figure 4.9** gives  $K_a$  of ca  $380\text{ M}^{-1}$ . Some caution needs to be placed on the interpretation of the association constants as it seems likely from the observation of two new cyanide bands and the presence of a band close to that of the parent complex that an equilibrium involving two or more isomeric forms may be involved.



**Figure 4.23 (a)** FTIR spectra of  $A^{2-}$  (red) and  $A^{2-} \cdots \mathbf{8}$  with ratio of complex to receptor of (1:0.5) (black), (1:1) (blue) and (1:2) (violet) in DMF. (b). plot of the absorbance at  $1931\text{ cm}^{-1}$  versus the molar ratio of complex to receptor.

During the later stages of this study two bis(urea)s possessing p- $CF_3$  (**10**) and 3,5 -  $(CF_3)_2$  (**11**) substituents were made available by the Professor Gales's group<sup>136</sup>. Preliminary studies showed both receptors interact with  $A^{2-}$ . As is evident from **Figure**



CHAPTER 4 | HYDROGEN BONDING INTERACTIONS OF TRIS AND BIS UREA AND THIOUREAS WITH CYANIDE LIGANDS IN AN ANALOGUE OF THE SUB-SITE OF [FeFe]-HYDROGENASE

4.24 the binding of **11** is as expected tighter than **10** when 1:2 ratios of complex to receptor are compared.

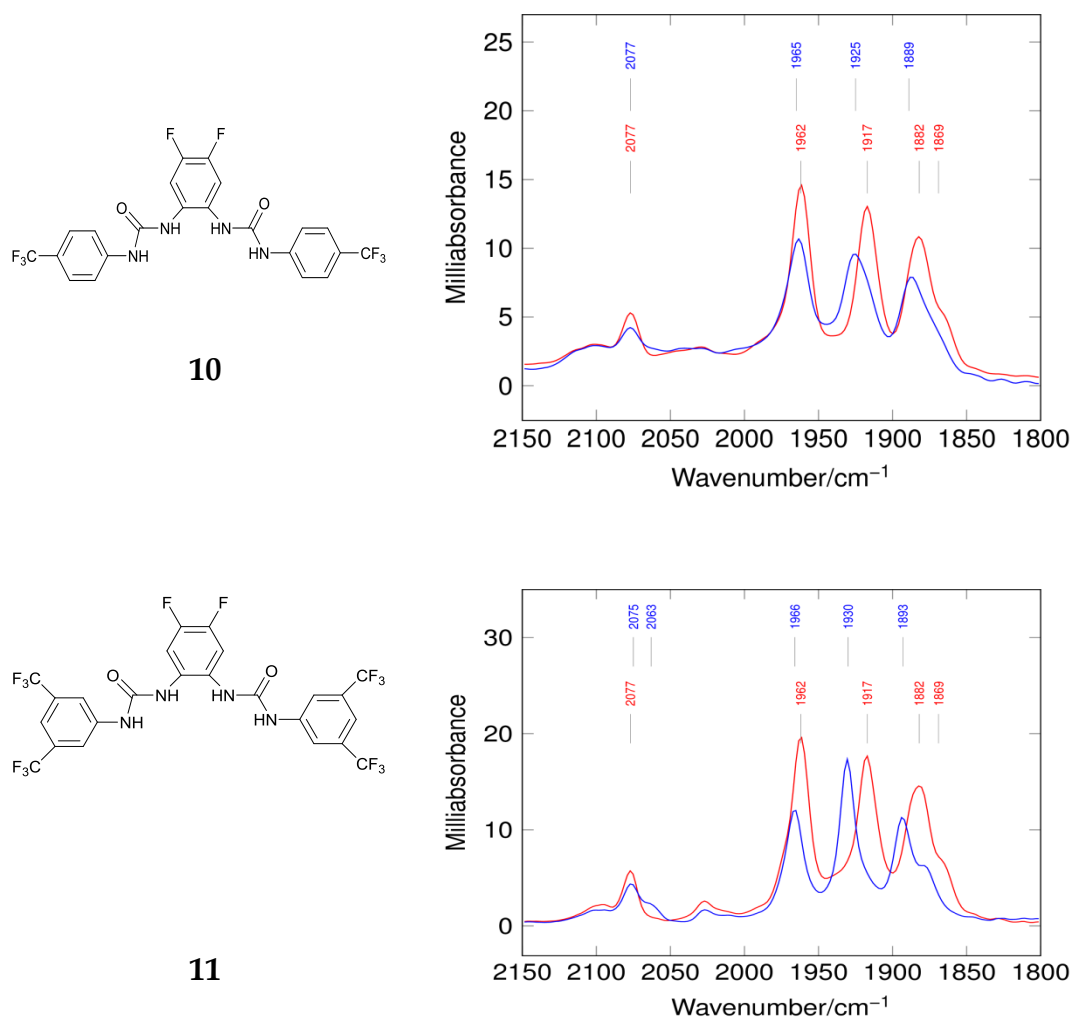


Figure 4.24. FTIR spectra of  $A^{2-}$  red and  $A^{2-} \rightleftharpoons$  bis-ureas blue in DMF

CHAPTER 4 | HYDROGEN BONDING INTERACTIONS OF TRIS AND BIS UREA AND THIOUREAS WITH CYANIDE LIGANDS IN AN ANALOGUE OF THE SUB-SITE OF [FeFe]-HYDROGENASE

Compound	$\nu\text{CN cm}^{-1}$	$\nu\text{ CO cm}^{-1}$			
$\text{A}^{2-}$	2077	1962	1917	1882	1869(sh)
$\text{A}^{2-} \supset \mathbf{1}$	2077	1963	1919	1883	
$\text{A}^{2-} \supset \mathbf{2}$	2075,2068,2054	1967	1928	1890	
$\text{A}^{2-} \supset \mathbf{6}$	2076,2066, 2049	1964	1929	1885	
$\text{A}^{2-} \supset \mathbf{3}$	2076 , 2066	1964	1927	1884	
$\text{A}^{2-} \supset \mathbf{7}$	2076 , 2065	1966	1930	1888	
$\text{A}^{2-} \supset \mathbf{4}$	2075,2068, 2051	1967	1929	1891	
$\text{A}^{2-} \supset \mathbf{8}$	2073, 2066, 2044	1966	1931	1992	
$\text{A}^{2-} \supset \mathbf{5}$	2075, 2068, 2053	1969	1935	1896	
$\text{A}^{2-} \supset \mathbf{9}$	2073, 2066, 2042	1968	1937	1895	
$\text{A}^{2-} \supset \mathbf{9^a}$	2090,2077 ,2043	1972	1939	1901	

**Table 4.3** IR data for (thio)urea -  $[\text{Fe}_2(\text{CO})_4(\text{CN})_2\text{pdt}]^{2-}$  interactions. Recorded in DMF, except for entry  $\mathbf{9^a}$  which was measured for comparison in MeCN. Data obtained for

2:1 ratio of receptor to  $A^{2-}$ . In the *para*-fluoro and pentafluorophenyl substituted (thio)urea systems peaks attributable to the parent complex were also present but are not listed in the Table.

#### 4.2.4. Stopped – flow FTIR studies of the protonation of $A^{2-} \rightarrow 9$ with $HBF_4 \cdot (Et_2O)_2$ in MeCN.

In earlier synthetic studies it was shown that protonation of  $A^{2-}$  led to decomposition and clean product(s) could not be isolated, only an insoluble CO - free material thought to be a coordination polymer<sup>96</sup>. Stopped-flow studies with  $HBF_4 \cdot Et_2O$  in MeCN led to CO loss *unless* restricted to a narrow acid range of 2-3 equivalents at concentrations of 2-3 mM after mixing. In this acid range the reaction of  $A^{2-}$  showed several ill-resolved bands on the short time-scale of < 100ms which after *ca* 1.5 minutes resolved into a spectrum with a pattern similar to that of the parent material but with the carbonyl peaks shifted to higher frequencies, **Figure 4.25 and 4.26**. The sharp cyanide band in the parent complex at  $2076\text{ cm}^{-1}$  was replaced by a broad feature at  $2101\text{ cm}^{-1}$ . The magnitude of the shift of the carbonyl peaks upon protonation from 1884, 1922, 1965  $\text{cm}^{-1}$  in the parent compound to 1914, 1948, and 1979  $\text{cm}^{-1}$  upon reaction with acid is not consistent with protonation at the Fe-Fe bond. The argument against protonation of the Fe-Fe bond is that complex **B**, **Table 4.4** is protonated at the Fe-Fe bond and this results in a greater shift in CO frequencies from 1898, 1943 and 1980  $\text{cm}^{-1}$  to 1990, 2031  $\text{cm}^{-1}$  (two bands). The initial site of protonation of  $A^{2-}$  was therefore suggested to be a cyanide ligand.

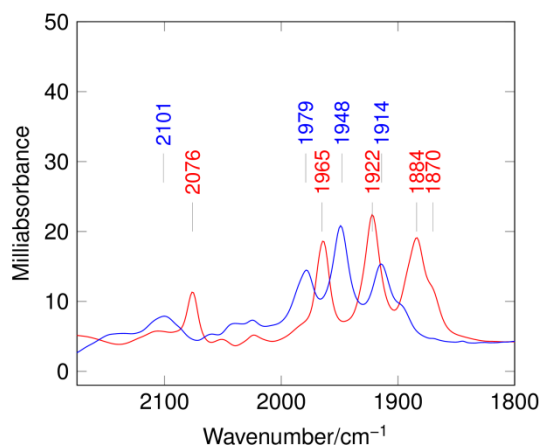


**Figure 4.25** Stopped-flow FTIR of the reaction of  $A^{2-}$  (0.5mM) ,( red) with  $HBF_4 \cdot Et_2O$  (2.5 mM) in MeCN , blue , 86 s , Reproduced from data provided by Dr Joseph Wright from reference [96](#).

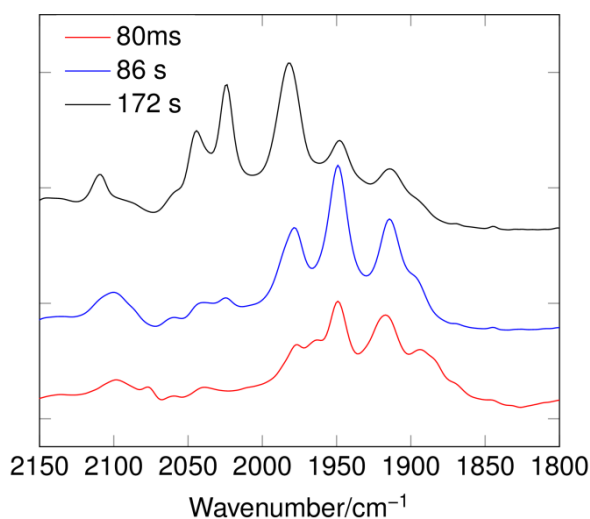


**Figure 4.26** Stopped-flow FTIR of the reaction of  $A^{2-}$  (0.5mM) with  $HBF_4 \cdot Et_2O$  (2.5 mM) in MeCN , red = short time, 80ms, blue = mid time, 86 s , black = long time 172 s. Reproduced from data provided by Dr Joseph Wright from reference [96](#).

The complexity of the spectrum at short time is probably because  $A^{2-}$  exists in solution as an equilibrium of (*trans, basal, basal*), (*cis basal, basal*), (*apical, basal*) and (*apical, apical*) isomers with protonation giving a distribution of CNH isomers which slowly convert to the thermodynamically favoured *trans, basal, basal* CN, CNH isomeric form. Over a longer period of 1.5 - 3 minutes further substantial changes in the spectra were found to occur. Thus the bands observed at 1914, 1948, and 1979  $cm^{-1}$  diminished and new carbonyl bands grew in at 1981, 2024, 2044  $cm^{-1}$  together with a well resolved cyanide band at 2110  $cm^{-1}$ . These larger magnitude changes in carbonyl stretching frequencies were interpreted as protonation on the Fe-Fe bond either by intramolecular migration of the proton on a cyanide ligand or by protonation of the Fe-Fe bond concerted with de-protonation of the CNH ligand to give  $\mu HA^{1-}$ , **Table 4.4** [137](#).

The effect of encapsulation  $A^{2-}$  by the receptor **9** has a pronounced effect on its reaction with  $HBF_4 \cdot Et_2O$  compared with that observed for protonation of the complex alone. **Figure 4.27** illustrates the spectral change observed before and 79ms after protonation of  $A^{2-} \supset 9$  with five equivalents of the acid at 5mM concentration. Compared with protonation of  $A^{2-}$  alone, a relatively clean spectrum is obtained. The shifts in  $\nu(CO)$  bands are relatively small, **Table 4.4**, which is again consistent with protonation not taking place on the Fe-Fe bond. The most likely site of initial protonation is the basic tertiary amine group of the tris-thioamide receptor as shown in **Scheme 4.4**, this 'third' coordination sphere interaction to give a positive aminium centre will increase the acidity of the thiourea NH groups, remove electron density from the Fe atoms and thus diminish back-bonding to the CO ligands. Thus the 'clean' spectrum obtained upon

initial protonation of  $\mathbf{A}^{2-} \supset \mathbf{9}$  can be explained by (i) protection of the CN ligands from protonation by hydrogen bonding (ii) the existence of only one basic amine site that can be protonated and (iii) the tris-thioamide locking the conformation of the complex in a single *apical-basal* form. This protonation product is subsequently labelled  $\mathbf{A}^{2-} \supset \mathbf{9NH}^+$ .

**Figure 4.28(a)** shows the evolution of the spectral changes from 79ms - 360s. On the longer time-scale higher frequency bands are clearly evident and a corresponding decrease in intensity of the bands associated with  $\mathbf{A}^{2-} \supset \mathbf{9NH}^+$  is observed. This is more clearly shown by the difference spectrum **Figure 4.28(b)**. The new CO bands at 2001, 2038, 2055  $\text{cm}^{-1}$  together with a broad band assigned to CN at 2130  $\text{cm}^{-1}$  are considerably shifted from those of the parent  $\mathbf{A}^{2-} \supset \mathbf{9NH}^+$ , it is therefore reasonable to attribute these to a subsequent slow protonation taking place on the Fe-Fe bond to give a bridging hydride species,  $\mu\mathbf{HA}^{1-} \supset \mathbf{9NH}^+$ , **Scheme 4.4** and **Table 4.4**. This contrasts with  $\nu(\text{CO})$  bands at 1981, 2024, 2044  $\text{cm}^{-1}$  and  $\nu(\text{CN})$  at 2110  $\text{cm}^{-1}$  for  $\mu\mathbf{HA}^{1-}$ . The higher frequencies observed for  $\mu\mathbf{HA}^{1-} \supset \mathbf{9NH}^+$  are clearly attributable to the retention of the protonated receptor which removes electron density from the FeFe core.

CHAPTER 4 | HYDROGEN BONDING INTERACTIONS OF TRIS AND BIS  
UREA AND THIOUREAS WITH CYANIDE LIGANDS IN AN  
ANALOGUE OF THE SUB-SITE OF [FeFe]-HYDROGENASE

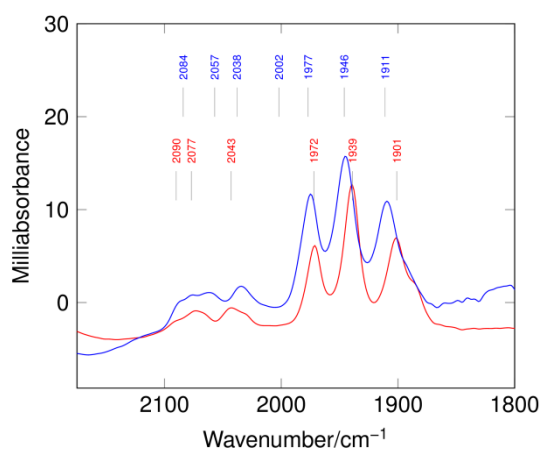


**Figure 4.27.** IR Stopped-flow FTIR of the reaction of  $\mathbf{A}^{2-} \rightarrow \mathbf{9}$  (0.5mM) with  $\text{HBF}_4 \cdot \text{Et}_2\text{O}$ , 5mM. Red spectrum: before reaction; blue spectrum: 79 ms after reaction with the acid.

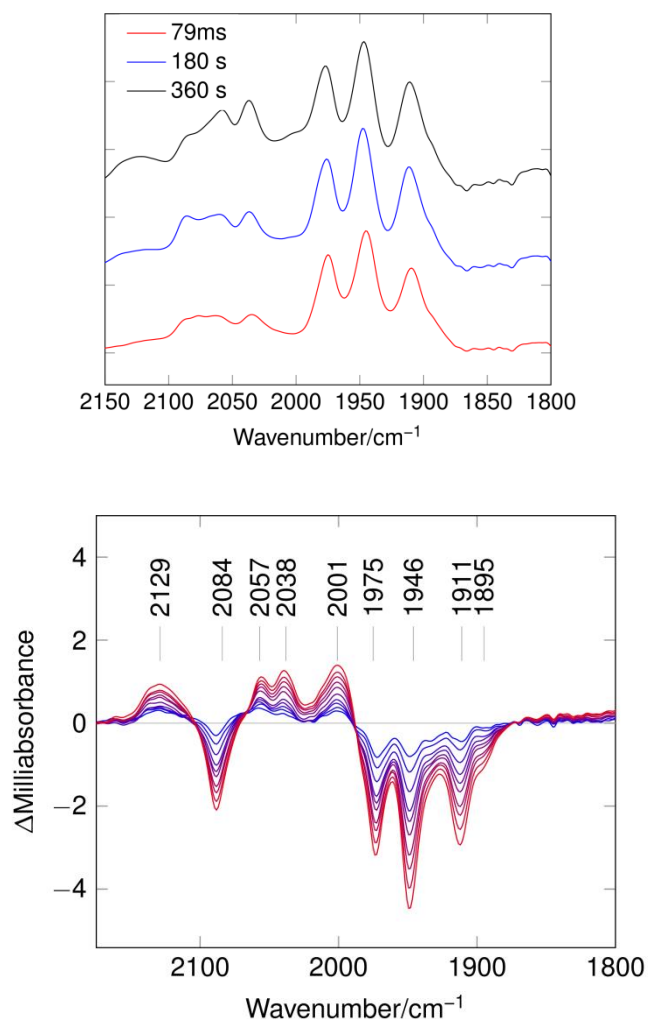


**Figure 4.28** (a) IR Stopped-flow FTIR of the reaction of  $A^{2-} \supset 9$  (0.5mM) with an acid concentration of (5 mM) in MeCN, red = short time scan 70ms, blue = mid time =180 s, black=long time scan 360 s, black. (b). Difference spectrum showing conversion of the initial protonated species  $A^{2-} \supset 9NH^+$  to  $\mu HA^{1-} \supset 9NH^+$



As discussed above, the protonation of  $\mathbf{A}^{2-}$  has been interpreted as involving fast diffusion-controlled protonation at cyanide followed by slow intramolecular transfer of a proton to the Fe-Fe bond to give the thermodynamic product. A first-order rate constant of *ca*  $k_1 = 8 \times 10^{-3} \text{ s}^{-1}$  <sup>109</sup> was determined for this step but only over a very limited low acid regime. At longer times it is also clear that the primary product of reaction of the encapsulated complex,  $\mathbf{A}^{2-} \rightarrow \mathbf{9NH}^+$  also undergoes further chemistry to give the bridging hydride, of  $\mu\mathbf{HA}^{1-} \rightarrow \mathbf{9NH}^+$ , **Figure 4.28**. Absorption data for the peak at  $1948 \text{ cm}^{-1}$  was fitted to a single exponential decay **Figure.4.29** which gave a  $k_{\text{observed}} = 6 \times 10^{-3} \text{ s}^{-1}$ . This is of a similar magnitude to the first-order rate constant attributed to the intramolecular migration of a proton coordinated to a cyanide in  $\mathbf{A}^{2-}$ . That it is somewhat slower may be attributed to the receptor inhibiting the migration of the proton to the Fe-Fe bond or protecting it from further protic attack. However, caution must be exercised in this comparison. Whereas, formation of  $\mu\mathbf{HA}^{1-}$  is likely to involve proton loss or migration from the  $\text{CNH}^+$  site in an overall 1<sup>st</sup> order step, the corresponding reaction of  $\mathbf{A}^{2-} \rightarrow \mathbf{9NH}^+$  need not involve proton loss from the remote amine.

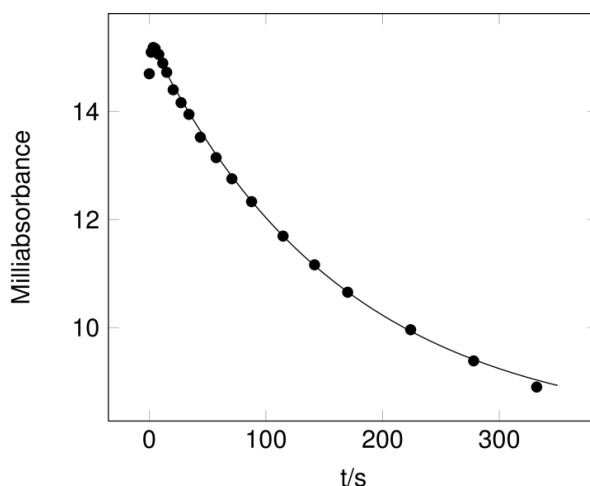


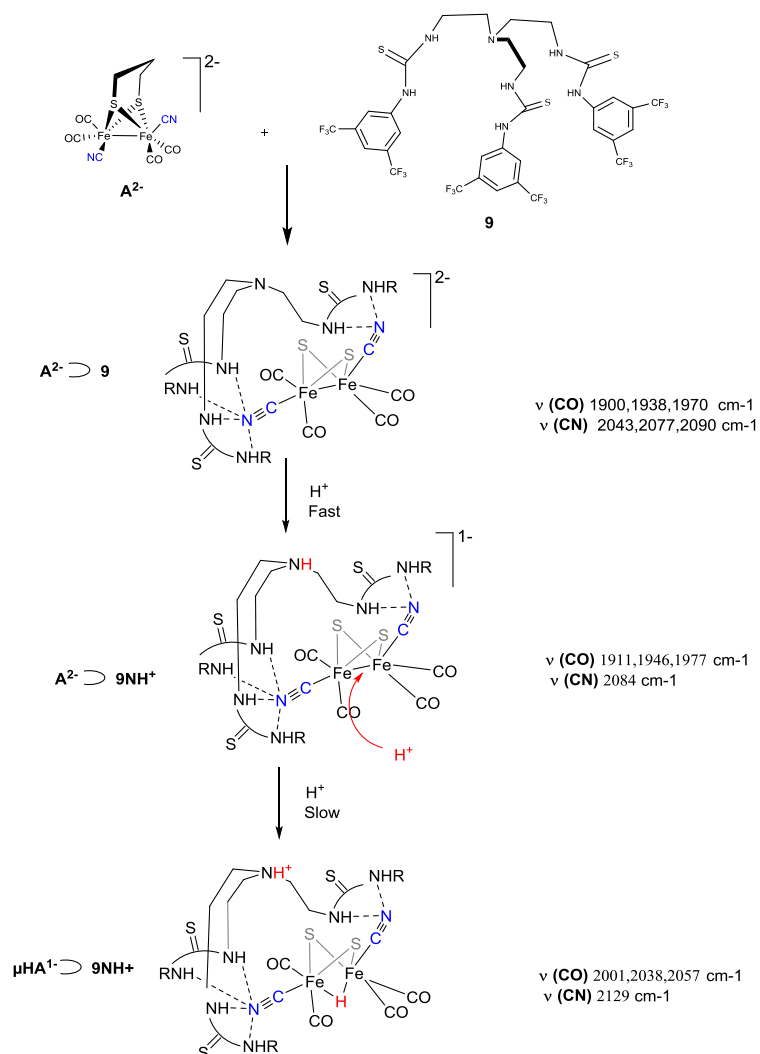
**Figure.4.29** Decay of IR band at  $1948\text{ cm}^{-1}$  over time on protonation of  $\mathbf{A}^{2-} \supset \mathbf{9}$  ; 0.5 mM,  $[\text{HBF}_4 \cdot \text{Et}_2\text{O}]$  ;5 mM in MeCN(circles); pseudo-first order fit (line).

If formation of  $\mu\text{HA}^{1-} \supset \mathbf{9NH}^+$  is a proton dependent second-order reaction then the second-order rate constant estimated from a single acid concentration is *ca*  $1.2\text{ M}^{-1}\text{s}^{-1}$ .

**Table 4.4** lists protonation data for several known systems, together with that for the two steps of the  $\mathbf{A}^{2-} \supset \mathbf{9}$  protonation. It can be seen that the  $\nu(\text{CO})$  data for the complex **D** before and after protonation is remarkably similar to that obtained for  $\mathbf{A}^{2-} \supset \mathbf{9H}^+$  before and after protonation. This reinforces the conclusion that the second protonation step of  $\mathbf{A}^{2-} \supset \mathbf{9}$  is at the metal-metal bond since the structure of **DH**<sup>+</sup> is crystallographically and spectroscopically unequivocally established as a bridging hydride. The second order rate constant of *ca*  $1\text{ M}^{-1}\text{s}^{-1}$  estimated for the reaction of  $\mathbf{A}^{2-} \supset \mathbf{9H}^+$  with proton compares with  $36\text{ M}^{-1}\text{s}^{-1}$  measured for the protonation of **D** under similar conditions. There is a linear free energy relationship between the energy of the HOMO which is a measure of the basicity of the Fe-Fe bond and  $\log k_2$ , the second

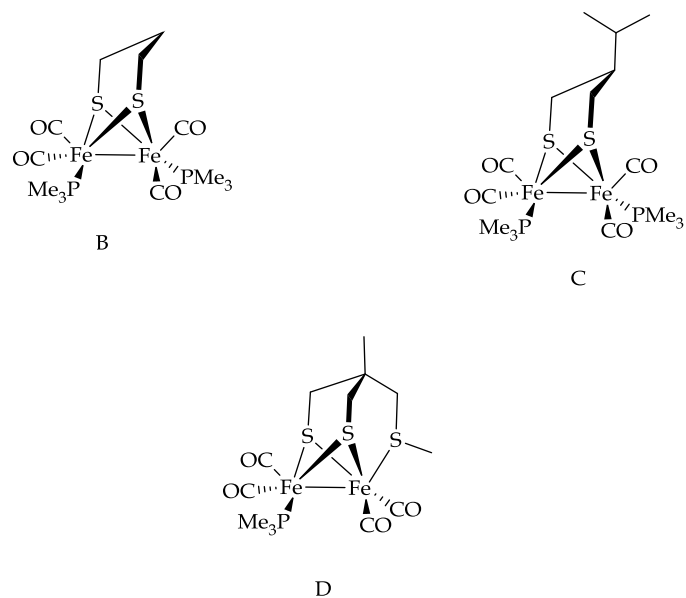
order rate for protonation, Given the similarity of the FTIR data for  $\mathbf{A}^{2-} \supset \mathbf{9H}^+$  and  $\mathbf{D}$  the energy of the Fe-Fe bond must also be quite similar. Thus the order of magnitude difference in rate might be attributable to the receptor sterically inhibiting protic attack at the Fe-Fe bond rather than it having a lower basicity. However, given the very limited kinetic data, this is largely conjecture.

CHAPTER 4 | HYDROGEN BONDING INTERACTIONS OF TRIS AND BIS UREA AND THIOUREAS WITH CYANIDE LIGANDS IN AN ANALOGUE OF THE SUB-SITE OF [FeFe]-HYDROGENASE



**Scheme 4.4.** Encapsulation of  $A^{2-}$  by **9** and the proposed protonation reactions of  $A^{2-} \supset 9$ . The 1,3-propane dithiolate bridge is omitted for clarity.

CHAPTER 4 | HYDROGEN BONDING INTERACTIONS OF TRIS AND BIS  
 UREA AND THIOUREAS WITH CYANIDE LIGANDS IN AN  
 ANALOGUE OF THE SUB-SITE OF [FeFe]-HYDROGENASE



**Scheme 4.5.** Structures of diiron dithiolate complexes , which use to compare with complex examined in **Tables 4.4**

CHAPTER 4 | HYDROGEN BONDING INTERACTIONS OF TRIS AND BIS  
UREA AND THIOUREAS WITH CYANIDE LIGANDS IN AN  
ANALOGUE OF THE SUB-SITE OF [FeFe]-HYDROGENASE

Compound	$\nu$ $\text{cm}^{-1}$
$\text{A}^{2-}$	1884 1922 1965 2076
$\mu\text{HA}^{1-}$	1981 2024 2044 2110
$\text{A}^{2-} \supset \mathbf{9}$	1900 1938 1970 2043 2077 2090
$\text{A}^{2-} \supset \mathbf{9NH}^+$	1911 1946 1977 2084
$\mu\text{HA}^{1-} \supset \mathbf{9NH}^+$	2001 2038 2057 2129
<b>D</b>	1910 1947 1984 <sup>55</sup>
<b>DH</b> <sup>+</sup>	2003 2038 2060 <sup>55</sup>
<b>C</b>	1899 1943 1980 <sup>55</sup>
<b>CH</b> <sup>+</sup>	1995 2032 2054 <sup>55</sup>
<b>B</b>	1898 1943 1980
<b>BH</b> <sup>+</sup>	1990 2031 <sup>110</sup>

**Table 4.4.** FTIR data assigned for  $\text{A}^{2-} \supset \mathbf{9}$  ,  $\text{A}^{2-} \supset \mathbf{9H}^+$  and  $\mu\text{HA}^{1-} \supset \mathbf{9NH}^+$  together with data reported for related compounds in literature.

#### 4.2.5 Cyclic voltammetry of receptor complexes.

Preliminary cyclic voltammetry studies for certain tris and bis urea were explored in MeCN and DMF. As noted in **Chapter 3**,  $A^{2-}$  oxidises irreversibly. Encapsulation of the complex results in a shift in the peak oxidation potential to more positive values, but no increase in reversibility of the system is observed for the three adducts studied, **Table 4.5**. The positive shift is as expected since H-bonding will remove electron-density and lower the energy of the HOMO thereby making the system more difficult to oxidise.

**Figure 4.30 (a)** shows the effect of increasing the concentration of the receptor **4** on the cyclic voltammetric response at a scan-rate of  $100\text{mVs}^{-1}$ . The peak current decreases towards a minimum at two equivalents of the receptor with  $i_p$  about one half of that in the absence of **4**, **Figure 4.30 (b)**. In addition, the peak position is progressively shifted positive **Figure 4.30 (a)** as increasing amounts of **4** are added. The decrease in the peak current is explained as follows. If the oxidation is an *ece* process with the initial one electron – step,  $e$ , followed by a chemical reaction,  $c$ , and a further one-electron oxidation,  $e$ , then the magnitude of the total peak current will depend on the rate of the intervening chemical step and the scan-rate. If the chemical step is very slow (on the time-scale of the potential scan) then the system will appear to be a reversible one-electron process . [138](#), [139](#) If it is fast then the peak current will approach that for an irreversible two electron process. At intermediate rates peak currents will lie between these extremes. With two equivalents of **4** the extent of formation of  $A^{2-} \rightleftharpoons 4$

approaches completion and the lower peak current can be explained by a decrease in the rate of the chemical step *c*, in the *ece* process. This chemical step may be inhibited by the receptor protecting the Fe centres from nucleophilic attack. For  $A^{2-} \supset 5$  in which the receptor aryls are 3,5-(CF<sub>3</sub>)<sub>2</sub> substituted, *ie* twice as many electron-withdrawing substituents as in  $A^{2-} \supset 4$ , the shift in the peak potential is larger,  $\Delta E = 239\text{mV}$ . Similarly, with the bis- urea receptor **11** which has backbone F and 3,5-CF<sub>3</sub> aryl substituents, **Figure 4.24**, a positive shift in the peak potential for  $A^{2-} \supset 11$  of 245mV is observed. The shifts observed for the adducts of  $A^{2-}$  with the receptors **4**, **5** and **11** parallel the trend in the frequencies measured for  $\nu(\text{CO})$ .



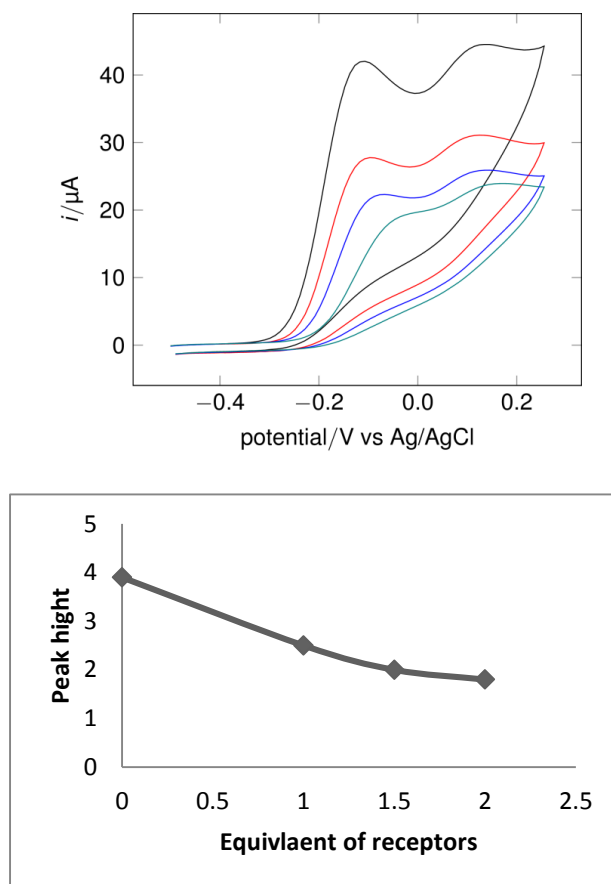


**Figure 4.30 . (a)** Cyclic voltammety of 8.93 mM of  $[\text{Fe}(\text{CO})_4(\text{CN})_2\text{pdt}]^{2-}$ , black before receptor **4**, red with one eq of receptor **4**, blue with 1.5 of receptor **4**, green with 2eq of receptor **4** at  $100\text{mV s}^{-1}$  in 0.2M  $[\text{Bu}_4\text{N}][\text{BF}_4]$  in DMF.

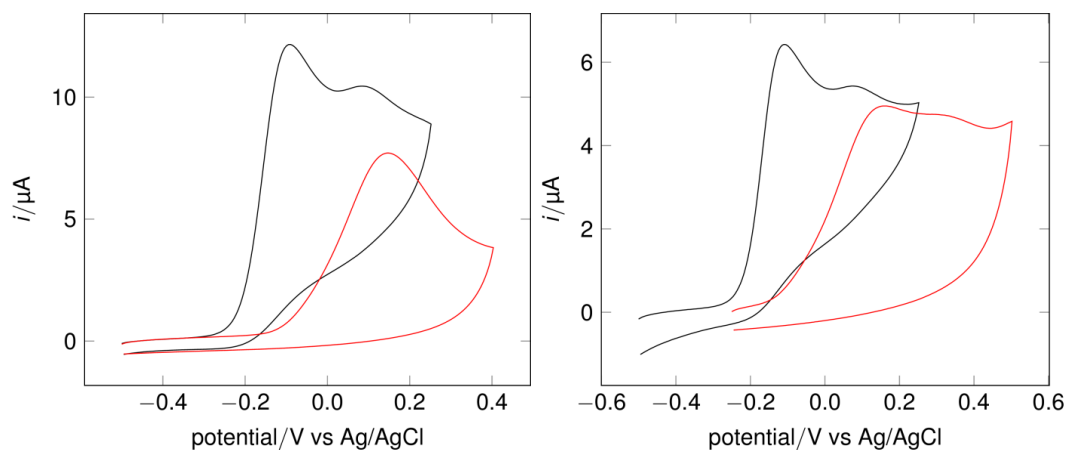


**Figure 4.31 . (a)** Cyclic voltammetry of 2.08 mM of  $\mathbf{A}^{2-}$ , black before receptor **5**, red with 2 eq of receptor **5** at  $50 \text{ mV s}^{-1}$  in 0.2M  $[\text{Bu}_4\text{N}][\text{BF}_4]$  in MeCN. **(b)** Cyclic voltammetry of 1 mM of  $[\text{Fe}(\text{CO})_4(\text{CN})_2\text{pdt}]^{2-}$ , black before receptor **11**, red with 2 eq of receptor **11** at  $50 \text{ mV s}^{-1}$  in 0.2M  $[\text{Bu}_4\text{N}][\text{BF}_4]$  in MeCN.

Complex	$E_p$ V	$\Delta E_p$ mV	$E_{1/2}/V$
$A^{2-}$	-0.09 <sup>a</sup> , 0.092(sh)		-0.163
$A^{2-}$	-0.11 <sup>b</sup> , 0.134(sh)		-0.176
$A^{2-} \supset 4$	-0.027 <sup>b</sup> , 0.143(sh)	83	-0.132
$A^{2-} \supset 5$	0.149 <sup>a</sup>	239	0.015
$A^{2-} \supset 11$	0.155 <sup>a</sup>	245	0.009

**Table 4.5.** Electrochemical data for oxidation of complex  $A^{2-}$  in (a) MeCN or (b) DMF containing 0.2 [NBu<sub>4</sub>][BF<sub>4</sub>] at a vitreous carbon electrode together with those of its adduct with receptors **4**, **5** and **11**. Potentials are reported *versus* Ag/AgCl at scan-rates of 100mV s<sup>-1</sup> in DMF or 50mV s<sup>-1</sup> in MeCN.  $\Delta E_p$  is the shift observed upon forming the receptor adduct with  $A^{2-}$  in the presence of two equivalents of the receptor.

### 4.3 Experimental:

All experiments were carried out under an atmosphere of nitrogen using standard Schlenk and cannula techniques or in a conventional nitrogen-filled glove-box. Dichloromethane and acetonitrile were refluxed over calcium hydride, all solvents were freshly distilled and degassed prior to use.  $\text{Eu}(\text{fod})_3$  was purchased from Sigma Aldrich and complex  $[\text{Et}_4\text{N}]_2[\text{Fe}_2(\text{CO})_4(\text{CN})_2\text{pdt}]$ , ( $[\text{Et}_4\text{N}]_2\mathbf{A}$ ) complex was synthesized following the literature procedures. [93](#), [94](#) [95](#), [111](#)

#### 4.3.1 Stopped flow measurements

Stock solutions for stopped flow were prepared in a Belle Technology glove box (oxygen concentration < 10 ppm), and were adjusted by dilution with acetonitrile. IR measurements were carried out using a Tgk stopped-flow drive interfaced to a Bruker Vertex 80 spectrometer equipped with a custom-built flow cell (path length = 50  $\mu\text{m}$ ) fitted with  $\text{CaF}_2$  windows (Tgk Scientific). The drive unit was located inside the glove box, with the reagents carried to the cell prior to mixing via a flexible conduit. The cell itself was mounted in a miniature anaerobic chamber fixed inside the sample compartment of the IR instrument. The conduit and cell were set to  $21.0 \pm 0.2$  °C using a Thermo Scientific recirculating bath. Mixing of the two solutions occurred in a chamber within the cell body. The initial concentration of substrate was typically 0.50 mM after mixing. A Northumbria Optical Coatings filter (pass band 4.76 to 5.60  $\mu\text{m}$ ) was fitted in front of the cell, within the sample chamber. The stopped-flow system was controlled using the Tgk KinetaDrive and Bruker Opus 3D packages. IR data was

processed and analysed using the Fit\_3D application and curve fitting was carried out using SciDAVis. Data were normally collected at  $4\text{ cm}^{-1}$  resolution. Typically between 60 and 180 time points were recorded for each experiment.

#### 4.3.2 Electrochemical measurements

Cyclic voltammetry measurements were carried out in 0.2 M  $[\text{Bu}_4\text{N}][\text{BF}_4]$  – MeCN or DMF using a three compartment cell fitted with a glassy carbon working electrode (diameter 3 mm), a platinum counter electrode and a Ag/AgCl reference electrode interfaced with an Autolab PGSTAT302N potentiostat using the GPES software package. The electrolyte was prepared by a standard laboratory procedure and the solvents were purified as described in the experimental section in **Chapter 1**.

## CHAPTER 5. CONCLUDING REMARKS

### 5.1 The redox isomerism system.

The results presented in **Chapter 2** provide support for the unequivocal observation of a square – scheme intramolecular isomerism system being explained by the rotation about the C-N amide bond resulting in deployment of the amide O towards or away from the metal centre and the polarity of this group vicinal to the metal influencing the redox potential. Future work on modifying the basic structure could provide further information. A clear target would be the synthesis of the W analogue. Attempts in this direction were frustrated by the greater oxophilicity of W over Mo which led to the isolation of a methoxy bridged species. The unstable paramagnetic isomers **A<sub>1</sub><sup>+</sup>** and **B<sub>1</sub><sup>+</sup>** should be amenable to study by EPR spectroscopy at low temperature and <sup>13</sup>C labelling of the amide carbon might provide further structural information.

### 5.2 Interactions of cyanide in [FeFe]-hydrogenase subsite models.

The demonstration that Eu(fod)<sub>3</sub> binds to cyanide in the subsite analogue has prompted further work in the group on the construction of other metal Lewis acid adducts. In particular, a Ru – NC-Fe complex bearing a bipyridyl/tripyridyl photoreceptor has been synthesized and structurally characterized (James Woods, personal communication).

The now established hydrogen – bonding interactions of tris- and bis- amides with the sub-site cyanide ligands is undoubtedly a potentially fruitful further avenue of research. Designing linked bis-amides which control the stereochemistry of the subsite is particularly attractive and the possibility of ‘nesting’ the subsite with apical-basal

## CHAPTER 5 | CONCLUDING REMARKS

deployment of CN may provide a means of promoting protonation to give a terminal hydride as in certain systems with bulky phosphine ligands.

## Uncategorized References

1. C. C. Scully, P. Jensen and P. J. Rutledge, *Journal of Organometallic Chemistry*, 2008, 693, 2869-2876.
2. D. J. Mercer and S. J. Loeb, *Chemical Society Reviews*, 2010, 39, 3612-3620.
3. D. R. Alston, P. R. Ashton, T. H. Lilley, J. F. Stoddart, R. Zarzycki, A. M. Z. Slawin and D. J. Williams, *Carbohydrate Research*, 1989, 192, 259.
4. R. L. Shook and A. Borovik, *Inorganic Chemistry*, 2010, 49, 3646-3660.
5. M. Formica, V. Fusi, M. Micheloni, R. Pontellini and P. Romani, *Coordination Chemistry Reviews*, 1999, 184, 347-363.
6. M. Mitewa and P. R. Bontchev, *Coordination Chemistry Reviews*, 1994, 129, 135-136.
7. J. W. Steed, *Coordination Chemistry Reviews*, 2001, 215, 171-221.
8. J. L. Atwood, L. J. Barbour, M. J. Hardie and C. L. Raston, *Coordination Chemistry Reviews*, 2001, 222, 3-32.
9. P. R. Ashton, C. G. Claessens, W. Hayes, J. F. Stoddart, S. Menzer, A. J. White and D. J. Williams, *Angewandte Chemie International Edition in English*, 1995, 34, 1862-1865.



10. Z. Liu, S. T. Schneebeli and J. F. Stoddart, *CHIMIA International Journal for Chemistry*, 2014, 68, 315-320.
11. S. E. Sherman and S. J. Lippard, *Chemical Reviews*, 1987, 87, 1153-1181.
12. M. C. Fyfe, P. T. Glink, S. Menzer, J. F. Stoddart, A. J. White and D. J. Williams, *Angewandte Chemie International Edition in English*, 1997, 36, 2068-2070.
13. C. Pederson, *Angewandte Chemie International Edition*, 1988, 27, 1021-1027.
14. D. Cram, *Angewandte Chemie International Edition English*, 1988, 27, 1009-1020.
15. J. Lehn, M, *Angewandte Chemie International Edition English*, 1988, 27, 89-112.
16. H. M. Colquhoun, J. F. Stoddart and D. J. Williams, *Journal of the Chemical Society, Chemical Communications*, 1981, 849-850.
17. M. S. Goodman, V. Jubian and A. D. Hamilton, *Tetrahedron letters*, 1995, 36, 2551-2554.
18. N. Alcock, E. Rybak-Akimova and D. Busch, *Acta Crystallographica Section C: Crystal Structure Communications*, 1997, 53, 1385-1387.
19. A. Mohamadou, G. A. van Albada, I. Mutikainen, U. Turpeinen, J. Marrot and J. Reedijk, *Polyhedron*, 2009, 28, 2813.
20. M. C. Etter, *Accounts of Chemical Research*, 1990, 23, 120-126.

21. E. L. Hegg, *European journal of Biochemistry*, 1997, 250, 625-629.
22. A. Orpen, L. Brammer, F. Allen, O. Kennard, D. Watson and R. Taylor, eds. I. Tables and f. Crystallography, Wilson, AJC., : Kluwer Academic Publishers: Dordrecht The Netherlands, 1995, vol. c, pp. 707-791.
23. L. C. Blasiak, F. H. Vaillancourt, C. T. Walsh and C. L. Drennan, *Nature*, 2006, 440, 368-371.
24. L. G. Beauvais and J. R. Long, *Journal of the American Chemical Society*, 2002, 124, 2110-2111.
25. K. J. Nelson, I. D. Giles, W. W. Shum, A. M. Arif and J. S. Miller, *Angewandte Chemie International Edition*, 2005, 40, 3129-3132.
26. P. Roder, A. Ludi, G. Chapuis, K. Schenk, D. Scjwarzembach and K. Hodgson, *Inorganica Chimica Acta*, 1979, 34, 113-117.
27. A. Figuerola, C. Diaz, J. Ribas, V. Tangoulis, C. Sangregorio, D. Gatteschi, M. Maestro and J. Mahía, *Inorganic Chemistry*, 2003, 42, 5274-5281.
28. J.-R. Li, L.-Z. Cai, R.-Q. Zou, G.-W. Zhou, G.-C. Guo, X.-H. Bu and J.-S. Huang, *Acta Crystallographica Section E*, 2002, 58, m686-m687.
29. D. F. Mullica, J. M. Farmer, B. P. Cunningham and J. A. Kautz, *Journal of Coordination Chemistry*, 2000, 49, 239-250.

30. K. Nakamoto, *Infrared and Raman Spectra of Inorganic and Coordination Compounds, Applications in Coordination, Organometallic, and Bioinorganic Chemistry*, Wiley, 1997.
31. S. Eller and R. D. Fischer, *Inorganic Chemistry*, 1990, 29, 1289-1290.
32. W. M. Laidlaw and R. G. Denning, *Journal Of The Chemical Society, Dalton Transactions*, 1994, 1987-1994.
33. S. F. Kettle, G. L. Aschero, E. Diana, R. Rossetti and P. L. Stanghellini, *Inorganic Chemistry*, 2006, 45, 4928-4937.
34. K. D. Karlin, *Progress in Inorganic Chemistry*, Wiley, 2009.
35. I. S. Lee and J. R. Long, *Dalton Transactions*, 2004, 3434-3436.
36. N. G. Connelly and A. G. Orpen, *Chemical Communications*, 1998, 517-518.
37. R. J. Parker, L. Spiccia, B. Moubaraki, K. S. Murray, D. C. Hockless, A. D. Rae and A. C. Willis, *Inorganic Chemistry*, 2002, 41, 2489-2495.
38. F. Bonadio, M.-C. Senna, J. Ensling, A. Sieber, A. Neels, H. Stoeckli-Evans and S. Decurtins, *Inorganic Chemistry*, 2005, 44, 969-978.
39. M. Flay, V. Comte and H. Vahrenkamp, *Zeitschrift Fur Anorganische Und Allgemeine Chemie*, 2003, 629, 1147-1152.
40. H. O. H.Oshio, O.Tamada,H.Mizutani,T.Hikichi and T. Ito, *Chemistry - A European Journal*, 2000, 2523.

41. T. Sheng and H. Vahrenkamp, *Inorganica Chimica Acta*, 2004, 357, 2121-2124.
42. M. Shatruk, A. Dragulescu-Andrasi, K. E. Chambers, S. A. Stoian, E. L. Bominaar, C. Achim and K. R. Dunbar, *Journal of the American Chemical Society*, 2007, 129, 6104-6116.
43. Z.-G. Gu, Q.-F. Yang, W. Liu, Y. Song, Y.-Z. Li, J.-L. Zuo and X.-Z. You, *Inorganic Chemistry*, 2006, 45, 8895-8901.
44. G. Berggren, A. Adamska, C. Lambertz, T. Simmons, J. Esselborn, M. Atta, S. Gambarelli, J.-M. Mouesca, E. Reijerse and W. Lubitz, *Nature*, 2013, 499, 66-69.
45. W. L. Armarego and C. L. L. Chai, *Purification of laboratory chemicals*, Butterworth-Heinemann, Amstrdam; London, 5th edn., 2003.
46. G. S. Girolami, T. B. Rauchfuss and R. J. Angelici, *Synthesis and Technique in inorganic chemistry A laboratory manual*, University Science Books, 1999.
47. S. K. Ibrahim, Ph.D., University of Sussex, 1992.
48. J. Keeler and P. Wothers, *Chemical structure and reactivity : an integrated approach*, Oxford University Press, Oxford, 2008.
49. F. A. Cotton and G. Wilkinson, *Advanced inorganic chemistry*, Wiley, New York, 5th ed. edn., 1988.
50. Q. Hu, R. J. Noll, H. Li, A. Makarov, M. Hardman and R. Graham Cooks, *Journal of Mass Spectrometry*, 2005, 40, 430-443.

51. A. J. B. W. Clegg, R. O. Gould, P. Main, *Crystal Structure Analysis Principles and Practice*, Oxford Science Publications, 2001.
52. A. J. White, K. Drabble and C. W. Wharton, *Biochem. J.*, 1995, 306, 843-849.
53. K. M. Alenezi, PhD.thesis, University of East Anglia, 2013.
54. L. Webster, PhD thesis, University of East Anglia, 2014.
55. A. Jablonskyte, PhD Thesis, University of East Anglia 2014.
56. A. C. Fisher, *Electrode Dynamics*, Oxford 1996.
57. A. J. B. L. R. Faulkner, *Electrochemical Methods: Fundamentals and Applications*, John Wiley & Sons 2nd edn., 2001.
58. , ElchSoft, Kleinromstedt, Germany, 4 edn.
59. J. S. D. Sholl, *Density Functional Theory: A Practical Introduction*, Wiley, 2009.
60. M. C. Durrant, S. A. Fairhurst, D. L. Hughes, S. K. Ibrahim, M. Passos, C. J. Pickett and A. Queiros, *Chemical Communications*, 1997, 2379-2380.
61. C. Prior, L. R. Webster, S. K. Ibrahim, J. A. Wright, A. F. Alghamdi, V. S. Oganessian and C. J. Pickett, *Dalton Transactions*, 2016, 45, 2399-2403.
62. T. T. Wooster, W. E. Geiger and R. D. Ernst, *Organometallics*, 1995, 14, 3455-3460.

63. A. J. Pombeiro, M. F. C. G. da Silva and M. A. N. Lemos, *Coordination Chemistry Reviews*, 2001, 219, 53-80.
64. A. Erxleben, *Inorganic Chemistry*, 2005, 44, 1082-1094.
65. P. Zanello, *Inorganic electrochemistry: theory, practice and applications*, Royal Society of Chemistry, 2003.
66. D. R. Crow, *Principles and Applications of Electrochemistry, 4th Edition*, Taylor & Francis, 1994.
67. *In addition, the magnitude of the peak current is proportional to  $D^{1/2}$  thus minor differences in  $D$  are 'flattened' when square-rooted. .*
68. T. Adachi, M. D. Durrant, D. L. Hughes, C. J. Pickett, R. L. Richards, J. Talarmin and T. Yoshida, *Journal of the Chemical Society, Chemical Communications*, 1992, 1464-1467.
69. S. J. Lancaster, A. Rodriguez, A. Lara-Sanchez, M. D. Hannant, D. A. Walker, D. H. Hughes and M. Bochmann, *Organometallics*, 2002, 21, 451-453.
70. G. Montaudo and P. Finocchiaro, *The Journal of Organic Chemistry*, 1972, 37, 3434-3439.
71. R. Sievers, *Nuclear Magnetic Resonance Shift Reagents*, Elsevier Science, 2012.
72. M. B. Sporn, *The Retinoids*, Elsevier Science, 2012.

73. A. Sakakura, R. Kondo and K. Ishihara, *Organic letters*, 2005, 7, 1971-1974.
74. T. N. Matsumoto, Hiroyuki; Shirai, junya: Kusumoto, Tomokazu, in *SciFinder Scholar*, ed. T. P. C. limited, Takeda Pharmaceutical Company limited, Japan, 2009, vol. WO 2009063993, ch. WO 2009063993
75. CrysAlisPro, Agilent Technologies, Abingdon, UK, 2012.
76. L. Palatinus and G. Chapuis, *Journal of Applied Crystallography*, 2007, 40, 786–790.
77. G. M. Sheldrick, *Acta Crystallographica Section A: Foundations of crystallography*, 2008, 64, 112–122
78. CrystalClear-SM Expert, Rigaku, 2014.
79. J. Esselborn, C. Lambertz, A. Adamska-Venkatesh, T. Simmons, G. Berggren, J. Noth, J. Siebel, A. Hemschemeier, V. Artero and E. Reijerse, *Nature Chemical Biology*, 2013, 9, 607-609.
80. J. W. Peters, W. N. Lanzilotta, B. J. Lemon and L. C. Seefeldt, *Science*, 1998, 282, 1853-1858.
81. Y. Nicolet, C. Piras, P. Legrand, C. E. Hatchikian and J. C. Fontecilla-Camps, *Structure*, 1999, 7, 13-23.
82. D. J. Evans and C. J. Pickett, *Chemical Society Reviews*, 2003, 32, 268-275.
83. M. Winter and R. J. Brodd, *Chemical Reviews*, 2004, 104, 4245-4270.

84. P. M. Vignais, B. Billoud and J. Meyer, *FEMS Microbiology Reviews*, 2001, 25, 455-501.
85. A. J. Pierik, M. Hulstein, W. R. Hagen and S. P. Albracht, *European Journal of Biochemistry*, 1998, 258, 572-578.
86. A. J. Pierik, W. Roseboom, R. P. Happe, K. A. Bagley and S. P. Albracht, *Journal of Biological Chemistry*, 1999, 274, 3331-3337.
87. J. C. Fontecilla-Camps, A. Volbeda, C. Cavazza and Y. Nicolet, *Chemical Reviews*, 2007, 107, 4273-4303.
88. A. S. Pandey, T. V. Harris, L. J. Giles, J. W. Peters and R. K. Szilagyi, *Journal of the American Chemical Society*, 2008, 130, 4533-4540.
89. C. Tard and C. J. Pickett, *Chemical Reviews*, 2009, 109, 2245-2274.
90. B. J. Lemon and J. W. Peters, *Biochemistry*, 1999, 38, 12969-12973.
91. T. R. Simmons, G. Berggren, M. Bacchi, M. Fontecave and V. Artero, *Coordination Chemistry Reviews*, 2014, 270, 127-150.
92. N. T. Hunt, J. A. Wright and C. Pickett, *Inorganic Chemistry*, 2015.
93. A. Le Cloirec, S. C. Davies, D. J. Evans, D. L. Hughes, C. J. Pickett and S. P. Best, *Chemical Communications*, 1999, 2285-2286.
94. M. Schmidt, S. M. Contakes and T. B. Rauchfuss, *Journal of the American Chemical Society*, 1999, 121, 9736-9737.



95. E. J. Lyon, I. P. Georgakaki, J. H. Reibenspies and M. Y. Darensbourg, *Angewandte Chemie International Edition*, 1999, 38, 3178-3180.
96. J. A. Wright, L. Webster, A. Jablonskytè, P. M. Woi, S. K. Ibrahim and C. J. Pickett, *Faraday Discussions*, 2011, 148, 359-371.
97. B. C. Manor, M. R. Ringenberg and T. B. Rauchfuss, *Inorganic Chemistry*, 2014, 53, 7241-7247.
98. M. Irfanullah and K. Iftikhar, *Journal of Photochemistry and Photobiology A: Chemistry*, 2011, 224, 91-101.
99. H. Iwanaga, A. Amano and M. Oguchi, *Japanese Journal Of Applied Physics*, 2005, 44, 3702.
100. A. Jablonskyte, L. R. Webster, T. R. Simmons, J. A. Wright and C. J. Pickett, *Journal of the American Chemical Society*, 2014, 136, 13038-13044.
101. S. J. George, Z. Cui, M. Razavet and C. J. Pickett, *Chemistry-A European Journal*, 2002, 8, 4037-4046.
102. M. Reddy, V. Divya and R. Pavithran, *Dalton Transactions*, 2013, 42, 15249-15262.
103. L. Norel, E. Di Piazza, M. Feng, A. Vacher, X. He, T. Roisnel, O. Maury and S. P. Rigaut, *Organometallics*, 2014, 33, 4824-4835.

104. M. Tropiano, N. L. Kilah, M. Morten, H. Rahman, J. J. Davis, P. D. Beer and S. Faulkner, *Journal of the American Chemical Society*, 2011, 133, 11847-11849.
105. X. Zhao, I. P. Georgakaki, M. L. Miller, R. Mejia-Rodriguez, C.-Y. Chiang and M. Y. Darensbourg, *Inorganic Chemistry*, 2002, 41, 3917-3928.
106. D. N. Sathyanarayana, *Vibrational Spectroscopy: Theory and Applications*, New Age International (P) Limited, 2015.
107. N. Zhu, R. Appelt and H. Vahrenkamp, *Journal of Organometallic Chemistry*, 1998, 565, 187-192.
108. A. Jablonskytė, J. A. Wright, S. A. Fairhurst, L. R. Webster and C. J. Pickett, *Angewandte Chemie International Edition*, 2014, 53, 10143-10146.
109. A. Jablonskytė, J. A. Wright and C. J. Pickett, *Dalton Transactions*, 2010, 39, 3026-3034.
110. J. A. Wright and C. J. Pickett, *Chemical Communications*, 2009, 5719-5721.
111. F. Gloaguen, J. D. Lawrence, M. Schmidt, S. R. Wilson and T. B. Rauchfuss, *Journal of the American Chemical Society*, 2001, 123, 12518-12527.
112. P. Bernhardt, G. Lawrance, B. Skelton and A. White, *Australian Journal of Chemistry*, 1989, 42, 1035-1043.
113. N. Busschaert, M. Wenzel, M. E. Light, P. Iglesias-Hernández, R. Pérez-Tomás and P. A. Gale, *Journal of the American Chemical Society*, 2011, 133, 14136-14148.

114. B. E. Smart, *Journal of Fluorine Chemistry*, 2001, 109, 3-11.
115. C. A. Hunter, *Angewandte Chemie International Edition*, 2004, 43, 5310-5324.
116. W. K. Hagmann, *Journal of Medicinal Chemistry*, 2008, 51, 4359-4369.
117. H. J. Böhm, D. Banner, S. Bendels, M. Kansy, B. Kuhn, K. Müller, U. Obst-Sander and M. Stahl, *ChemBioChem*, 2004, 5, 637-643.
118. S. Purser, P. R. Moore, S. Swallow and V. Gouverneur, *Chemical Society Reviews*, 2008, 37, 320-330.
119. M. E. Khansari, C. R. Johnson, I. Basaran, A. Nafis, J. Wang, J. Leszczynski and M. A. Hossain, *RSC Advances*, 2015, 5, 17606-17614.
120. F. G. Bordwell, *Accounts of Chemical Research*, 1988, 21, 456-463.
121. A.-F. Li, J.-H. Wang, F. Wang and Y.-B. Jiang, *Chemical Society Reviews*, 2010, 39, 3729-3745.
122. V. Amendola, L. Fabbrizzi and L. Mosca, *Chemical Society Reviews*, 2010, 39, 3889-3915.
123. R. Custelcean, B. A. Moyer and B. P. Hay, *Chemical communications*, 2005, 5971-5973.
124. C. Caltagirone and P. A. Gale, *Chemical Society Reviews*, 2009, 38, 520-563.

125. M. A. Hossain, R. A. Begum, V. W. Day and K. Bowman-James, in *Supramolecular Chemistry*, John Wiley & Sons, Ltd, 2012, DOI: 10.1002/9780470661345.smc063.
126. L. S. Evans, P. A. Gale, M. E. Light and R. Quesada, *New Journal of Chemistry*, 2006, 30, 1019-1025.
127. R. H. Crabtree, *The Organometallic Chemistry of the Transition Metals*, Wiley, 2014.
128. F. P. Pruchnik, *Organometallic Chemistry of the Transition Elements*, Springer US, 2013.
129. J. Li, B. C. Noll, C. E. Schulz and W. R. Scheidt, *Angewandte Chemie International Edition*, 2009, 48, 5010-5013.
130. T. A. Scott, C. P. Berlinguette, R. H. Holm and H.-C. Zhou, *Proceedings of the National Academy of Sciences of the United States of America*, 2005, 102, 9741-9744.
131. J. J. R. F. d. M. F. C. Guedes da Silva, A. J. L. and M. A. P. Pombeiro, A. Tiripicchio,, *Journal of the Chemical Society. Dalton transactions*, 1996, 2763 - 2772
132. M. Boiocchi, L. Del Boca, D. E. Gómez, L. Fabbrizzi, M. Licchelli and E. Monzani, *Journal of the American Chemical Society*, 2004, 126, 16507-16514.
133. [http://www.gaussian.com/g\\_tech/g\\_ur/m\\_citation.htm](http://www.gaussian.com/g_tech/g_ur/m_citation.htm) (we use revision C.01).

134. J. Tao, J. P. Perdew, V. N. Staroverov and G. E. Scuseria, *Physical Review Letters*, 2003, 91, 146401.
135. P. J. Hay and W. R. Wadt, *Journal of Chemical Physics*, 1985, 82, 270-298
136. L. E. Karagiannidis, C. J. Haynes, K. J. Holder, I. L. Kirby, S. J. Moore, N. J. Wells and P. A. Gale, *Chemical Communications*, 2014, 50, 12050-12053.
137. S. Tschierlei, S. Ott and R. Lomoth, *Energy & Environmental Science*, 2011, 4, 2340-2352.
138. J. Wang, *Analytical Electrochemistry*, Wiley, 2006.
139. P. H. Rieger, *Electrochemistry*, Springer Netherlands, 2012.